Low-temperature thermochronology from tunnel and surface samples in the Central and Western Alps

Dissertation

zur Erlangung des Grades eines Doktors der Naturwissenschaften

der Geowissenschaftlichen Fakultät
der Eberhard-Karls-Universität Tübingen

vorgelegt von
Christoph Glotzbach
aus Haltern

2008

Tag der mündlichen Prüfung: 11. Juli 2008

Dekan: Prof. Dr. Peter Grathwohl

1. Berichterstatter: Prof. Dr. Cornelia Spiegel

2. Berichterstatter: Prof. Dr. Wolfgang Frisch

3. Berichterstatter: o. Univ. Prof. Dr. Franz Neubauer

Acknowledgements

This work was supported by a research grant from the German Science Foundation within the project „Perturbation of isotherms below topography: constraints from tunnel transects through the Alps“.
First of all I like to thank Cornelia Spiegel, Meinert Rahn and Wolfgang Frisch for giving me the chance to work on this interesting project. Thanks also for the chance to participate numerous conferences and field trips. Conny, thank you for introducing me into the world of thermochronology and assistance during preparation of my manuscripts. Wolfgang Frisch is thanked for his support during my work here in Tübingen, especially during the time of application for prolongation of this project. Meinert Rahn is gratefully thanked for sampling parts of the study areas and providing the sample aliquots. Martin Danišík is thanked for his supervision during the work with the He-line. Sorry Martin, for the extra labour and time, which were essential for the success of the measurements. John Reinecker is thanked for numerous productive discussions about the geodynamics of the Alps. In addition, thanks go to Christian, John and Martin for sampling in rugged mountainous areas and carrying heavy samples. I like to thank Paul Bons for introduction into and support with the modelling. Thanks go also to the technical assistances (Mrs. Kost, Höckh, Mühlbayer-Renner) for the mineral separation, and to Annett Weisheit for hours of picking under the binocular microscope. Thanks also to Thomas Wenzel for his assistance with the electron microprobe analysis.
I also like to thank M. Zattin, P. van der Beek, E. Sobel and T. Ehlers for constructive reviews of my manuscripts.
Andreas Wölfler and Christian Dekant are thanked for a successful excursion in the Alps, and discussion and activations beyond the geology. Thanks to the whole working group including Horst Hann, Achim Kuhlemann, Ingrid Krumrei and Volker Schuller for the nice time in Tübingen.
Thanks to my parents for supporting me all the time. I like to thank my Merina for her daily support. Merina, you enriched my everyday life and gave me motivation to succeed all occurring problems.

Low-temperature thermochronology from tunnel and surface samples in the Central and Western Alps

Christoph Glotzbach

Abstract
Low-temperature thermochronology owns the unique potential to derive rates of cooling, exhumation and denudation (erosional and tectonic). Furthermore it bears information about palaeotopography. This thesis comprises five low-temperature thermochronological studies conducted in the Western and Central Alps, i.e., one study in the eastern Lepontine dome and four studies along orogen-perpendicular transects through the Western and Central Alps. Main objectives of these studies are:
(1) To unravel the structural-kinematic and exhumation history of the investigated regions, and (2) to estimate the shape of palaeo-isotherms under given boundary conditions.
Three transects along tunnels (Mont Blanc, Lötschberg and Gotthard) and corresponding surface profiles were sampled in the external crystalline massifs (ECM) of the Mont Blanc, Aar and Gotthard. Sampling of the Lepontine dome was applied on a broader spatial scale. Samples were dated with the apatite and zircon fission track method (AFT and ZFT, respectively) and with the apatite (U-Th)/He method (AHe), which record the cooling of rocks between 330 and 40°C. The resulting two-dimensional sample transects along the tunnels were used to estimate the shape of palaeo-isotherms and to derive lateral and temporal differences in exhumation rates.
Thermochronological data, especially from near vertical age-elevation profiles, were used to derive the Late Neogene exhumation history of the investigated regions in the external massifs and of the Lepontine dome. The exhumation histories were compared with estimates for adjacent regions and used to investigate the impact of climatic and tectonic forcing on the evolution and exhumation of the Alpine orogen. Main conclusions from the individual studies are:

Mont Blanc transect
Thermal modeling of AFT and AHe data suggests that the Mont Blanc massif (MBM) was exhumed episodically, with rapid exhumation (2.5±0.5 km/Myr) before 6 Ma, followed by an episode of slow exhumation and again a period of fast exhumation (>1 km/Myr) after ~3 Ma. The MBM is the only ECM that experienced fast exhumation at ~6.5 Ma, possibly related to NW and minor SE directed thrusting of the MBM. I propose that the acceleration in exhumation rates of the MBM after ~3 Ma is caused by rapid valley incision related to beginning Alpine glaciation, implying that the recent relief of the MBM is a young feature.

Lötschberg transect
The data show a constant exhumation of the SW Aar massif with a rate of ~0.5 km/Myr for the last 10 Myr, increasing only in the southern area close to the Rhône-Simplon fault around 3.5 Ma to values up to 1.2 km/Myr. Acceleration of exhumation in the south is most likely triggered by increased orogen-perpendicular extension causing tectonic denudation along the south dipping Rhône-Simplon fault. Climatic forcing, especially the intensification of Alpine glaciation around 0.9 Ma has also contributed to the observed exhumation, but the magnitude of this impact can not be resolved with the data.

Gotthard transect
Thermochronological ages along the sampled Gotthard transect are very uniform, suggesting that vertical movements along distinct fault structures within and between the Aar massif

(AM) and Gotthard massif (GM) can be neglected since ~15 Ma. Age-elevation profiles of ZFT and AFT data of the central AM and GM suggest fast exhumation (~1 km/Myr) around 15 Ma decreasing to a steady, uniform and moderate exhumation with a rate of ~0.5 km/Myr since ~9 Ma. Fast exhumation at ~15 Ma is probably related to continuing indentation of the Adriatic wedge, which resulted in thrusting and exhumation of the external massifs. Since ~9 Ma, the central AM and GM are maybe in a long-term exhumational steady state. Isostatic movements caused by unloading effects due to glacier retreat and/or enhanced erosion, however, led to short term fluctuations of rock uplift rates, not resolvable by our data.
Thermochronological data (ZFT, AFT) within the Gotthard tunnel show no correlation with topography, suggesting that (palaeo-) topography-induced perturbations of isotherms were small under given boundary conditions (i.e., topographic wavelength = 12 km, relief = 1.7 km, exhumation rate = 0.5 km/Myr).
A new 3D thermal model was developed and used for investigating the potential impact of different input parameters (topography, conductivities, heat production, exhumation rates) on shape of isotherms and resulting thermochronological data. Modelling reveals a strong dependence of the shape of isotherms and thermochronological ages on spatial variable heat production and exhumation rates. In the case of the Gotthard transect the influence of the topography can be neglected for the interpretation of thermochronological data, as well as in most other regions in the Alps with similar relief.

Lepontine dome
Thermochronological data of the eastern Lepontine dome was used to investigate the exhumation history and activity of the Forcola fault. The data reveal episodic exhumation of the eastern Lepontine dome with fast exhumation from ~23-16 Ma, 12-10 Ma and 5-4 Ma. The exhumation is directly linked to the onset of Miocene lateral extension and related activation of the Forcola fault. Fast exhumation between 5 and 4 Ma coincide with an increase in foreland basin deposits. Slowing down of exhumation after 4 Ma is consistent with the proposed transition from orogenic construction to orogenic destruction and related shift of active deformation into the interior of the Alpine orogen.

To sum up, all three sampled tunnel transects show no correlation of palaeo-isotherms with topography. This observation has to be interpreted in terms of the topography induced perturbation of isotherms, taking into account that obviously the present topography and relief is a very young feature (< 3 Ma). Accompanied thermal modelling additionally demonstrates that other parameters (exhumation rate, heat production), beside topography, also strongly influence the shape of near-surface isotherms. Reasons why no correlation of palaeo-isotherms with recent topography is observable are different for the tunnel transects: The relief along the **Mont Blanc tunnel** was less pronounced at the time given by the thermochronometer. Along the **Lötschberg tunnel** strong spatial differences in exhumation rates control the thermochronological age pattern, and consequently the topographic effect is not observable. Along the **Gotthard tunnel** ages are controlled by several spatially varying parameters (including topography, exhumation and heat production), which result in apparent flat palaeo-isotherms.
Comparing exhumation histories from the appended studies, complemented by published exhumation histories of adjacent regions, I conclude that:
(1) Comparing the exhumation rates of all ECM shows that the Messinian base level drop (~5.5 Ma) and the intensification of precipitation caused by an increase in the Atlantic Gulf Stream (~4.6 Ma) did not affect the exhumation rates of the external Alps.
(2) All ECMs, except the central Aar and Gotthard massifs, show an increase in exhumation rates at ~3 Ma. I interpret this as the result of beginning Alpine glaciation and normal faulting along orogen-parallel faults.

Niedrig-Temperatur Thermochronologie von Tunnel- und Oberflächenproben in den zentralen und westlichen Alpen

Christoph Glotzbach

Zusammenfassung

Niedrig-Temperatur-Thermochronologie erlaubt es Raten der Abkühlung, Exhumation und der Denudation (durch Erosion und Tektonik) zu bestimmen. Außerdem lassen sich Informationen über die Paläo-Topographie ableiten. Die vorliegende Doktorarbeit beinhaltet fünf Niedrig-Temperatur-Thermochronologische Arbeiten über die westlichen und zentralen Alpen, d.h. eine Arbeit im Lepontine Dome und vier Arbeiten entlang orogen-senkrechter Profile in den westlichen und zentralen Alpen. Zielsetzungen dieser Arbeiten waren:
(1) Die Exhumationsgeschichte der untersuchten Arbeitsgebiete zu rekonstruieren, und (2) den Verlauf von Paläo-Isothermen unter gegebenen Rahmenbedingungen abzuschätzen.
Drei Tunnelprofile (Mont Blanc, Lötschberg und Gotthard) und ihre entsprechenden Oberflächenprofile wurden in den externen Kristallin-Massiven (ECM) des Mont Blanc, Aar und Gotthard beprobt. Die Beprobung im Lepontine Dome erfasste ein größeres Areal. Die Proben wurden mit der Apatit und Zirkon Spaltspurmethode (AFT und ZFT) und mit der Apatit (U-Th)/He Methode (AHe) datiert, mit welchen sich die Abkühlung von Gesteinen von 330 auf 40°C rekonstruieren lässt. Die resultierenden zwei dimensionalen Probenprofile entlang der Tunnel wurden dazu benutzt, um den Verlauf von Paläo-Isothermen abzuschätzen und laterale und temporale Unterschiede in Exhumationsraten zu bestimmen.
Thermochronologische Daten, besonders von fast vertikalen Alters-Höhen-Profilen, wurden benutzt um die Spät-Neogene Exhumationsgeschichte der Untersuchungsgebiete in den ECM um im Lepontine Dome herzuleiten. Die resultierenden Exhumationsgeschichten wurden mit denen benachbarter Gebiete verglichen, um den Einfluss von klimatischen und tektonischen Kräften auf die Entstehung und die Exhumation des alpinen Orogens zu quantifizieren. Die wichtigsten Schlussfolgerungen der Einzelarbeiten sind:

Mont Blanc Profil

Thermische Modellierung von AFT und AHe Daten zeigen, daß das Mont Blanc Massiv (MBM) episodisch exhumiert wurde: sehr schneller Exhumation (2.5±0.5 km/Myr) vor 6 Ma, gefolgt von einer Phase sehr langsamer Exhumation und wiederum gefolgt von einer Phase schneller Exhumation (>1 km/Myr) nach ~3 Ma. Das MBM ist das einzige ECM, welches diese sehr schnelle Exhumation um etwa 6.5 Ma zeigt, die vermutlich im Zusammenhang mit NW und SE Überschiebung des MBM steht. In dieser Arbeit schlage ich vor das die beschleunigte Exhumation seit ~3 Ma in Zusammenhang mit einer schnellen Taleintiefung steht, die durch die beginnende alpine Vergletscherung verursacht wurde. Damit ist das Relief des MBM sehr jung.

Lötschberg Profil

Die Daten zeigen eine konstante Exhumation des SW Aar Massivs mit einer Rate von ~0.5 km/Myr für die letzen 10 Myr an, welche nur im südlichen Teil des Profils nahe der Rhône-Simplon Störung um 3.5 Ma auf Raten bis 1.2 km/Myr anstiegen. Dieser Anstieg in den Exhumationsraten wurde vermutlich durch orogen-senkrechte Extension ausgelöst, die zu tektonischer Denudation entlang der Rhône-Simplon Störung führte. Klimatische Kräfte, besonders die Intensivierung der alpinen Vergletscherung um 0.9 Ma haben ebenfalls zur beobachten Exhumationsgeschichte beigetragen, allerdings kann ihr Anteil an den Exhumationsraten nicht mit den vorliegenden Daten quantifiziert werden.

Gotthard Profil
Thermochronologische Alter entlang des Gotthard Profils sind sehr einheitlich, was nahe legt das seit ~15 Ma vertikale Bewegungen entlang von Störzonen innerhalb und zwischen dem Aar Massiv (AM) und dem Gotthard Massiv (GM) vernachlässigbar klein sind. ZFT und AFT Alters-Höhen Profile im zentralen AM und GM zeigen ein schnelle Exhumation (~1 km/Myr) um 15 Ma an, welche mit der Zeit abnahm und seit etwa 9 Ma konstant bei ~0.5 km/Myr lag. Die schnelle Exhumation um 15 Ma hängt vermutlich mit der andauernden Einrückung des adriatischen Keils zusammen, welche zu einer Überschiebung und Exhumation der ECM führte. Vermutlich seit ~9 Ma sind die Exhumationsraten im zentralen AM und GM in einem stationären Zustand. Allerdings verursachten isostatische Bewegungen induziert von Entlastungen (Gletscher Rückgang, gesteigerte Erosion) kurzzeitige Schwankungen in Hebungsraten, die nicht mit unseren Daten aufgelöst werden können.
Die thermochronologischen Daten (AFT und ZFT) entlang des Gotthard Tunnels zeigen keine Korrelation mit der Topographie, welches andeutet das die (paläo-) topographisch-induzierte Aufwölbung von Isothermen gering war unter den gegebenen Rahmenbedingungen (d.h., topographische Wellenlänge = 12 km, Relief = 1.7 km, Exhumationsrate = 0.5 km/Myr).
Ein neues drei-dimensionales thermisches Model wurde entwickelt und für die Abschätzung des möglichen Einflusses verschiedener thermischer Parameter (Topography, Konduktivität, Wärmeproduktion, Exhumationsrate) auf die Aufwölbung von Isothermen und resultierender thermochronologischen Ater benutzt. Die Modellierungen zeigen einen großen Einfluss auf den Verlauf von Isothermen in Abhängigkeit von räumlich variierender Wärmproduktions- und Exhumationsraten. Im Falle des Gotthard Profils kann der Einfluss der Topographie auf die Isothermen und damit auf die Interpretation von thermochronologischen Daten vernachlässigt werden, genau wie in den meisten alpinen Gebieten mit ähnlichen Relief.

Lepontine Dome
Thermochronologische Daten vom östlichen Lepontine Dome wurden benutzt um die Aktivität der Forcola Störung und die Exhumationsgeschichte des Untersuchungsgebietes zu untersuchen. Die Daten zeigen eine episodische Exhumation des östlichen Lepontine Domes an, mit schneller Exhumation zwischen ~23-16 Ma, 12-10 Ma und 5-4 Ma. Die Exhumation ist direkt mit der Miozänen lateralen Extension und der Aktivität der Forcola Störung gekoppelt. Schnelle Exhumation zwischen 5 und 4 Ma deckt sich zeitlich mit einem Anstieg in Vorlandbecken-Ablagerungen. Verlangsamte Exhumation nach 4 Ma ist im Einklang mit einem postulierten Übergang von orogenen Konstruktion zu orogenen Destruktion and damit in Zusammenhang stehender Verschiebung der aktiven Deformationsfront ins Innere des alpinen Orogens.

Zusammenfassend läßt sich sagen, daß abgeleitete Paläo-Isothermen der drei untersuchten Tunnelprofile keine Korrelation mit der Topographie zeigen. Für die Interpretation dieser Beobachtung bezüglich des Einflusses der Topographie auf die Aufwölbung von Isothermen muß berücksichtigt werden, daß die heutige Topographie und das heutige Relief sehr jung sing (< 3 Ma). Die begleitende Modellierung zeigte außerdem, daß andere Parameter außer der Topographie (z.B. Exhumation und Wärmeproduktion), einen starken Einfluß auf den Verlauf von oberflächennahen Isothermen haben. Die Gründe weshalb keine Korrelation zwischen den Paläo-Isothermen und der heutigen Topographie gefunden wurde sind verschieden für die einzelnen Tunnelprofile: Das Relief am **Mont Blanc Tunnel** war weniger stark ausgeprägt während der Zeit als die Proben die für die benutzten Thermochronometer sensitiven Isothermen durchliefen. Entlang des **Lötschberg Tunnels** kontrollierten stark räumlich variierende Exhumationsraten die thermochronologische Altersverteilung, und folglich ist der Effekt der Topographie nicht zu erkennen. Die Alter entlang des **Gotthard**

Tunnels sind das Resultat von verschiedenen räumlich variierenden Parameter (Topographie, Exhumation und Wärmeproduktion), die zu scheinbaren flachen Paläo-Isothermen führten.
Vergleicht man die Exhumationsgeschichte aus den untersuchten Arbeitsgebieten, ergänzt durch publizierte Exhumationsgeschichten benachbarter Gebiete, so kann man folgende Schlußfolgerungen ziehen:
(1) Alle ECM zeigen das die Messininsche Salinitätskrise (~5.5 Ma) und die Intensivierung der Niederschlags verursacht durch einen erhöhten Atlantischen Golfstrom (~4.6 Ma) keinen Einfluß auf die Exhumationsraten der externen Alpen haben.
(2) Mit Ausnahme des zentralen AM und GM zeigen alle ECM eine Steigerung in den Exhumationsraten um 3 Ma. Diese Steigerung resultiert aus der beginnenden alpinen Vergletscherung und abschiebender Bewegungen entlang von orogen-parallelen Störungen.

Contents

Appendix

1. Introduction

1.1 Aim of the study

This thesis has two main aims:

(1) The first aim is to measure and model the perturbation of isotherms below topography. Exhumation rates are routinely derived from low-temperature thermochronological data using (near-) vertical age-elevation profiles. The resulting slope of the age-elevation relationship equals the exhumation rate in the case of flat isotherms. Perturbed isotherms led to an overestimation of derived exhumation rates. Active orogens with high relief are most likely affected by the topography-induced perturbation of isotherms, which magnitude needs to be quantified for the given boundary conditions. For this purpose, the Gotthard, Lötschberg and Mont Blanc tunnels and their corresponding surface lines were sampled. Low-temperature thermochronology (fission track dating on apatite and zircon, and (U-Th)/He dating on apatite) were applied to these two dimensional profiles.
This sample strategy allows to interpolate isochrones of each thermochronological system, and thus to get information about the shape of the palaeo-isotherms. The shape of the palaeo-isotherms is used to test existing thermal models. In addition, I implement a three dimensional finite difference thermal model to investigate the impact of different parameters (e.g. topography, thermal conductivity, heat production) on near surface isotherms. Both, derived palaeo-isotherms and modelled isotherms are used to provide a geological benchmark for the significance of the perturbation of isotherms due to thermal relevant parameters.

(2) The second aim is to unravel the Neogene exhumation history of the following areas: Aar, Gotthard and Mont Blanc massifs and Lepontine dome. These areas are chosen because they are characterised by high relief up to 3 km, high recent rock uplift rates up to 1.5 mm/y and very young thermochronological ages, well suited for the investigation of the latest Neogene exhumation history of the Central and Western Alps. Near vertical elevation profiles in combination with the horizontal tunnel transects allowed to derive corrected exhumation rates. Deduced spatial and temporal cooling/exhumation rates were compared to adjacent regions and used to test different geodynamic models explaining the Neogene exhumation history of the Western and Central Alps. Of particular importance was the question: What is the contribution of climatic and tectonic forcing to the observed exhumation history?

1.2 The European Alps

During Cenozoic times continent-continent collisions associated with the closure of the Tethys and marginal seas led to formation of a chain of orogens ranging from the Himalayas in the east to the western Mediterranean region (e.g., Frisch and Meschede, 2005). The European Alps are part of this orogenic chain, which formed in response to ongoing compressional movements in the Mediterranean region and closure of ocean basins during Mesozoic and Cenozoic times.
First continent-continent collision in the European Alps happened in Cretaceous (Eoalpine) times during the closure of a marginal sea of the Tethys (Vardar Ocean), in which the Austroalpine units were subducted and partly metamorphosed up to eclogite facies. A second continent-continent collision is related to the closure of the Penninic oceans (South and North

Penninic oceans), which is kinematically linked to the breakup of the Pangaea supercontinent and formation of the Atlantic ocean. Rifting in the South Penninic ocean (Piedmont-Ligurian ocean) started in Middle Jurassic and separated the European continent in the north from the Austro- and Southalpine units in the south. The opening of the North Penninic (Valais) ocean in Early Cretaceous times led to the separation of a crustal terrane, known as Middle Penninic (Briançonnais) micro continent, from the European continent (Frisch, 1979). Southward subduction of the Penninic units started in the Late Cretaceous and led to collision of the Austroalpine with the Middle Penninic and subsequent collision with the passive European continental margin (Helvetic units) in the Palaeogene. Penninic units including oceanic relics were squeezed in between the colliding continents, and thus heavily deformed and partly metamorphosed up to ultrahigh-pressure conditions with formation of coesite. Ongoing collision led to northward/westward migration of deformation and thrusting, and a change in the sedimentation in the flexural foreland from flysch to molasse sediments (Molasse basin). In Oligocene times a slab-breakoff and subsequent indentation of the Adriatic wedge occurred (von Blanckenburg and Davies, 1995), which led to increased uplift and erosion in the Alps. This was accompanied by magmatic intrusions along the Periadriatic line (e.g. Bergell and Adamello bodies). In Oligocene to recent times the Western and Central Alps are kinematically controlled by the indentation of the Adriatic wedge (Schmid et al., 2004). Continuous northward movement of this indenter shifted the deformation front to more external zones, thus the Alpine orogen (Western and Central Alps) enters a phase of orogen construction (Willett et al., 2006). This led to nappe stacking in the external massifs and thrusting of the Jura Mountains and related inversion and erosion of the Molasse basin and retro-wedge deformation in the Southern Alps. Afterwards the European Alps passed into a phase of destruction, and concentration of deformation in more internal zones (Willett et al., 2006), emphasised by a stop of thrusting in the Southern Alps and in the Jura Mountaints before 4 Ma (e.g., Becker, 2000).

The Neogene orogen-parallel extension and extrusion plays a major role for the evolution of the Alps (e.g., Frisch et al., 2000). The extension led to the formation of the Tauern window in the Eastern Alps (Ratschbacher et al., 1991) and the Lepontine dome in the Central Alps (e.g., Grasemann and Mancktelow, 1993). Uplift and exhumation of the Lepontine dome was controlled by the initiation and continuing activity of the Simplon shear zone in the W and the Forcola fault in the E. In the Western Alps a change from orogen-parallel to orogen-perpendicular extension occurred in the Pliocene, which led to tectonic denudation in the footwall of orogen-parallel faults, e.g. at the Penninic frontal thrust. The resulting geology of the Alps is presented in a simplified map in Figure 1. For details about the tectono-metamorphic evolution of the European Alps see, e.g., Schmid et al. (2004), Steck and Hunziker (1994).

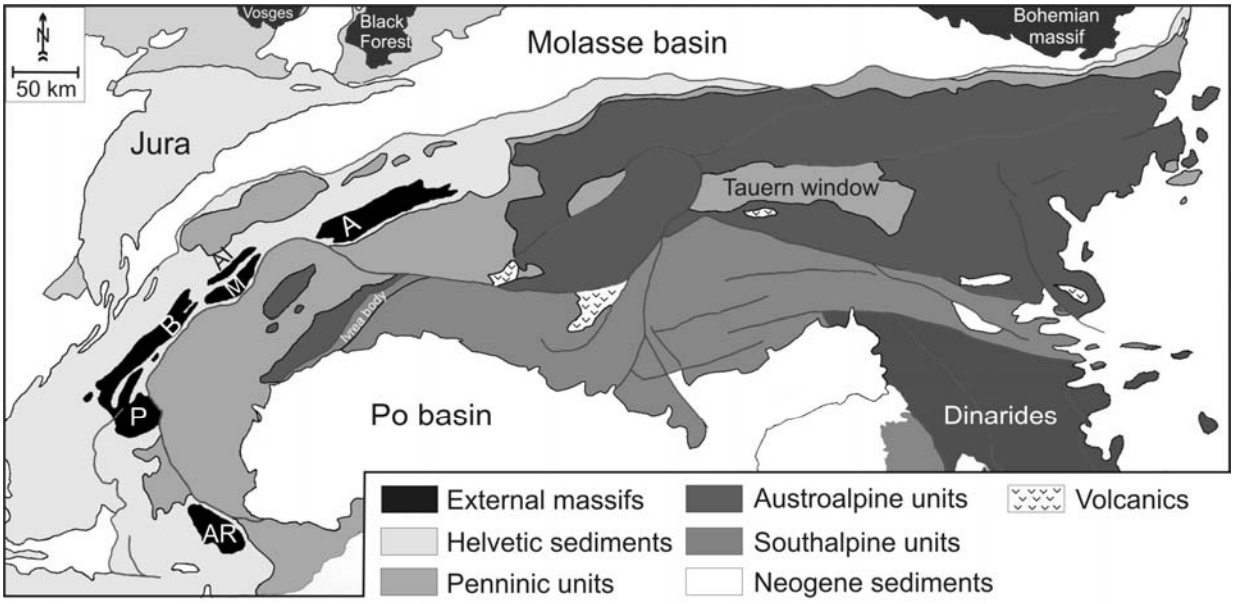

Fig. 1: Simplified geological map of the European Alps (modified from Schmid et al., 2004). External massifs are abbreviated as: A = Aar, M = Mont Blanc, AI = Aiguilles Rouges, B = Belledone, P = Pelvoux, AR = Argentera.

In this study four study areas have been investigated (Fig. 2), including three tunnel transects, which are all located in the external Alps: (1) the Mont Blanc road tunnel, (2) the Lötschberg railway tunnels and (3) the Gotthard road tunnel. The Mont Blanc tunnel is 12 km long and is located in the Western Alps crossing the central Mont Blanc massif at an elevation of ~1.3 km. The Lötschberg tunnels cross the SW Aar massif and their sedimentary cover at elevations of ~1.2 and ~0.7 km, respectively. The old Lötschberg railway tunnel is about 15 km long, whereas the new base-tunnel is ~35 km long. The Gotthard road tunnel is about 16 km long and crosses parts of the southeastern Aar massif and the whole central Gotthard 'massif' in the Central Alps at the elevation of ~1.1 km. The Aar, Gotthard and Mont Blanc massifs are orogen-parallel oriented bodies of basement rocks originating from the distal European continental margin (e.g., Schmid et al., 2004), also known as external crystalline massifs (ECM). These tunnel studies are complemented by a study in the eastern Lepontine dome. Detailed geological introductions are given in each of the appended manuscripts.

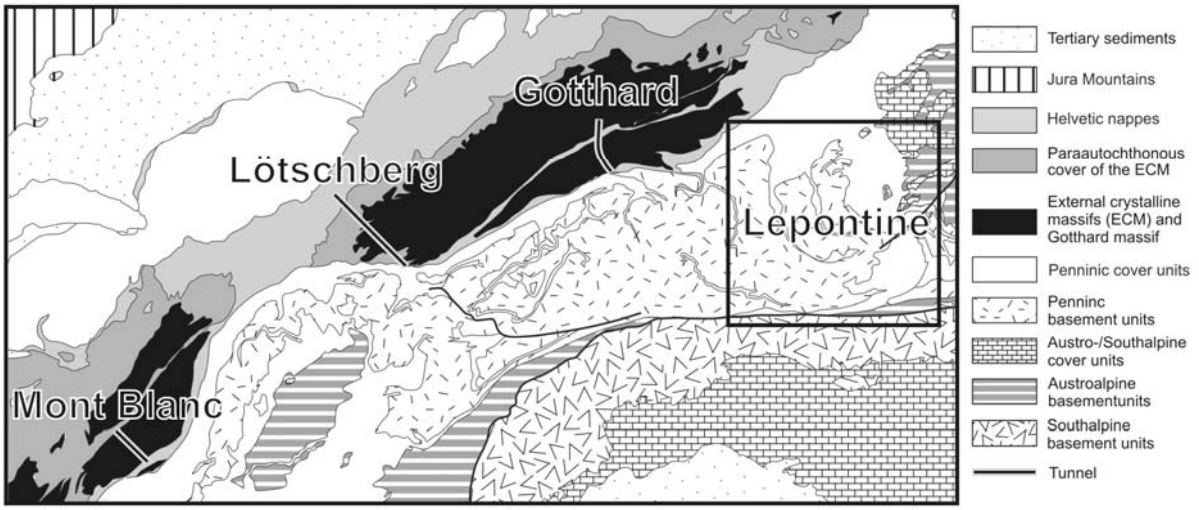

Fig. 2: Geological map of the NW European Alps, showing the location of the study areas.

1.3 Thermochronology

Thermochronology owns the unique potential to derive the low-temperature cooling history of rocks, and to derive rates of surface processes. In this thesis different thermochronological methods were used, and are described in more detail below.

1.3.1 Fission track thermochronology

In this chapter a brief introduction of the methodology and analytical procedure is given for the apatite and zircon fission track dating method. For detailed methodical information the reader is referred to, for instance, Wagner and Van den Haute (1992), Tagami and O'Sullivan (2005), Gallagher et al. (1998) or Reiners et al. (2005).

Fission track formation

The apatite and zircon fission track (AFT and ZFT, respectively) method is based on the accumulation of fission tracks, caused by decay of heavy elements (Price and Walker, 1962a; Price and Walker, 1962b). Spontaneous decay is restricted to elements with an atomic number $\geq$90 and a mass number $\geq$230, thus only the actinides are affected. Of these elements only ^{232}Th, ^{235}U and ^{238}U occur in measurable amounts in rocks, whereas ^{238}U cause almost all tracks in natural samples, due to the abundance and half life (Tagami and O'Sullivan, 2005; Wagner and Van den haute, 1992).
Fission releases two daughter particles, some neutrons and energy of 210 MeV (with E_{kin} = 160-190 MeV). The emerged neutrons can induce new fissions. The relation of the masses of the daughter particles are in the range of 1.4 and in extreme conditions exceed 2 (Wagner and Van den haute, 1992). After fission the heavy charged particles moved in opposite direction and interact with the lattice, in the form of electronic and nuclear interactions, which leads to ionization and resulting vacancies in the lattice (Tagami and O'Sullivan, 2005; Wagner and Van den haute, 1992). Unetched fission tracks are only observable by transmission electron microscopy (Fig. 3). Because both particles get the same kinetic energy, the lighter particle causes ionization over a longer distance. The crystal lattice is completely destroyed in the track core and the end of tracks shows broad zones of damage.

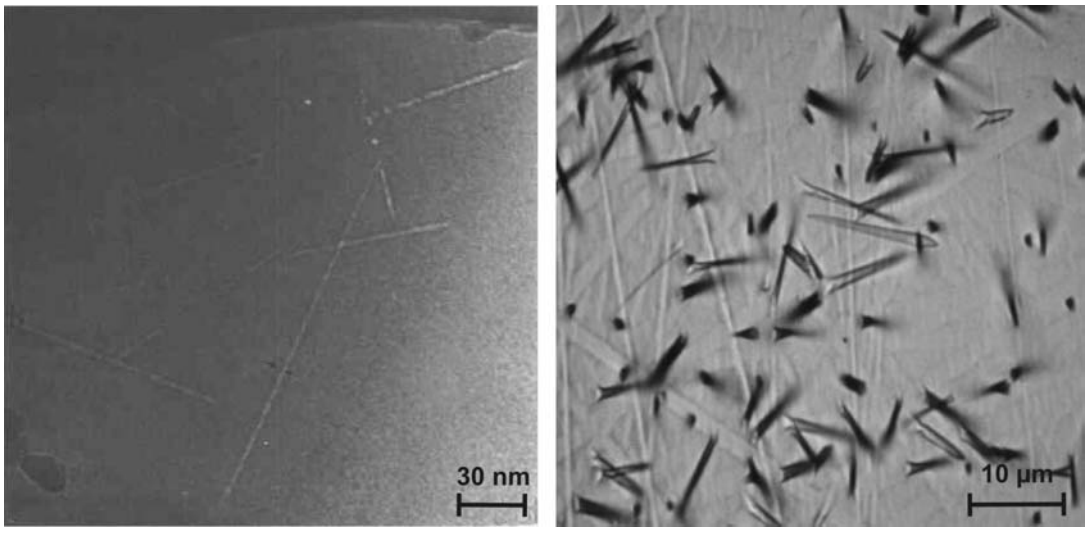

Fig. 3:(a) Unetched induced fission tracks in fluorapatite imaged with transmission electron microscope (modified from Paul and Fitzgerald (1992)). (b) Etched fission track in Durango apatite (modified from Geotrack website: www.geotrack .com.au).

Age determination

The most widely used and accepted AFT age calculation method is the external detector method (EDM). For this method the age can be calculated from counting spontaneous tracks in crystals (e.g. apatite or zircon) and induced tracks in an external detector (low uranium mica), held in close contact with the crystal during irradiation (e.g., Donelick et al., 2005; Wagner and Van den haute, 1992). The density of spontaneous fission tracks per unit area is positively correlated with U content and the time elapsed since the individual crystal cooled under the temperature, at which fission track formation exceeds the annealing process (e.g., Wagner and Van den haute, 1992). The fission track dating method can be described by the basic equation for isotopic dating:

$$N_D = N_P \cdot (e^{\lambda \cdot t} - 1)$$

in which N_D is the number of daughter particles (N_s), N_P is the number of parent particles (^{238}U) and λ is the decay constant. The parent particles decays not only by spontaneous fission (λ_f) but also by α-decay (λ_α = 1.55125*10^{-10} yr^{-1}), thus the total decay (λ_d) constant is composed of $\lambda_d = \lambda_\alpha + \lambda_f$. Because the α-decay is much more frequent ($\lambda_f \approx \lambda_\alpha * 10^7$), the resulting age equation solved for t is:

$$t = \frac{1}{\lambda_\alpha} \cdot \ln\left(\frac{\lambda_\alpha}{\lambda_f} \cdot \frac{N_s}{^{238}U} + 1\right)$$

The concentration of ^{238}U is determined by irradiation with thermal neutrons, which induced fissioning of ^{235}U:

$$N_i = {}^{235}U \cdot \sigma \cdot \Phi$$

In which σ is the cross section of ^{235}U for induced fission with thermal neutrons (580.2*10^{-24} cm²) and Φ is the neutron flux (typically in the range of 10^{15} tracks per cm²). Because the ratio of $^{235}U/^{238}U$ is constant in nature (7.2527*10^{-3}) we get:

$$N_i = {}^{238}U \cdot I \cdot \sigma \cdot \Phi$$

Finally we get the equation developed by Price and Walker (1963) for the fission track dating method:

$$t = \frac{1}{\lambda_\alpha} \cdot \ln\left(\frac{\lambda_\alpha}{\lambda_f} \cdot \frac{N_s}{N_i} \cdot I \cdot \sigma \cdot \Phi + 1\right)$$

In practical terms, during fission track counting we determine the density of etched tracks in an internal surface (ρ_s and ρ_i) of the crystal and not the number of tracks per volume (N_s and N_i). Therefore $N_{s,i}$ is substituted by $\rho_{s,i}$ in the following equations, for details see Wagner and Van den haute (1992).

A major problem is the accurate measuring of the decay constant for fission track, where individual determinations range around 7 to 8.5*10^{-17} y^{-1} (cf. compilation in Wagner and Van den haute (1992)). In addition, uncertainties are related to the determination of the thermal neutron flux (Hurford and Green, 1982), which is determined by using glass monitors from the National Institute of Standards and Technology (NIST) with known uranium

concentration. To overcome the uncertainty about the value of λ_f, Fleischer and Hart (1972) introduced the ζ- dating method, which affords to determine the personal calibration factor ζ for every individual dating method (e. g. apatite and zircon). Single ζ-values are determined with the following equation (Hurford and Green, 1983):

$$\zeta = \frac{e^{\lambda_\alpha \cdot t_s}}{\lambda_\alpha \cdot \frac{\rho_s}{\rho_i} \cdot G \cdot \rho_d}$$

In which t_s is the age of the analysed standard, and ρ_s (ρ_i, ρ_d) is the spontaneous (induced, dosimeter) track density and G the geometry factor, which is for an external surface 0.5. A mean of all analysed age standards (Fish Canyon Tuff Durango apatite) is used to calculate samples with unknown ages:

$$t = \frac{1}{\lambda_\alpha} \cdot \ln\left(\lambda_\alpha \cdot \frac{\rho_s}{\rho_i} \cdot \rho_d \cdot G \cdot \zeta + 1 \right)$$

This equation allows to determine the age of samples from a simple ratio of track density (Wagner and Van den haute, 1992). The track density of the glass monitor ρ_d is proportional to the fluence of $\Phi = B\rho_m$, where B is the factor expressing the proportionality of neutrons and tracks. Personal ζ-values are between 290 and 390 yr/cm² for the AFT system. Widely used age standards are the Fish Canyon tuff for apatite and zircon with an independent age of 27.8±0.2 Ma (biotite Ar/Ar age) and apatite MTL of 15.35±0.06 μm and Durango apatite with and age of 31.4±0.6 Ma (K-Ar) and a MTL of 14.47±0.06 μm (e.g., Hurford and Gleadow, 1977). Enkelmann et al. (2005) clearly showed that only Fish Canyon Tuff and Durango apatites are useful and accepted age standards for AFT method.
The external detector method yields an individual age for each analysed grain. Resulting single grain ages show a variation, which dispersion depends mainly on the age, U-content, sample quality, kinetic parameters and cooling history. Age calculations of the sample assume a Poissonian distribution of single grain ages, which is statistically checked by a modified χ^2-test. A χ^2 probability of >5% is representative for a single age population. The age of the sample can be calculated in different ways (e.g., mean, weighted, pooled, central). In this thesis only central ages are reported with 1σ error, for details on calculation see Galbraith and Laslett (1993).

Fission track annealing and modeling

Fission led to formation of an unstable zone of damage in solid crystals, which are affected by fading depending mainly on time and temperature (e.g., Fleischer et al. (1965)). This process, also known as annealing, led to a reduction of the length and density of fission tracks, making it a unique tool to derive the time temperature (tT) history of rocks (Wagner and Van den haute, 1992).
Annealing of fission tracks depend mainly on the cooling rate and the kinetic properties of single crystals, which must be approximated to derive reliable tT history predictions. Apatite owns a wide variety of composition with coupled substitution within the cations and anions position. The interrelationship of composition and structure leads to a complex behaviour of FT annealing (Carlson et al., 1999).
Zircons contain up to several thousands ppm U and Th, hence they are strongly affected by radioactive decay, causing radiation damage of the crystal lattice and transformation from the crystalline to the metamict state (Nasdala et al., 2001). The amount of radiation damage in

zircon affects the annealing behaviour: in grains with low radiation damage tracks anneal at higher temperatures than in grains with higher damage. Therefore annealing is not only a function of cooling rate, but is strongly depending on the amount of radiation damage (Garver, 2006). The colour of zircons depends on the trace-element composition, but is also related to the amount of radiation damage. Most zircons fall into two general colour series of increasing radiation damage: (a) a common pink series that ranges between pink, rose, red, purple (‘‘hyacinth’’), and black; (b) a less common yellow series that ranges between pale yellow, straw, honey, brown, and black (Gastil et al., 1967). Raman spectroscopy demonstrates that pink/purple grains have lower crystallinity values caused by higher amounts of radiation damage, and thus have lower temperatures of track retention (Riley and Garver, 2006).

Radiation damage and thus colour disappear in the temperature range between 350-400°C, called Colour Removal Zone (CRZ) (Garver and Kamp 2002). Gastil et al. (1967) concluded that colour loss is primarily a function of maximum temperature rather than thermal duration. The practical implication is that after an initial cooling event, zircons accumulate radiation damage at rates proportional to their U content. Subsequent reheating leads to annealing of low radiation damaged zircons (Garver et al. 2005).

Regarding the annealing of FT in apatites, annealing experiments clearly show that AFT lengths of compositional different samples are shortened by different amounts (Barbarand et al., 2003a). This behaviour represents the summed effect of the type and amount of elemental substitution, linked together with the substitution sites. These directly affect the apatite unit cell, resulting in different FT annealing rates. Barbarand et al. (2003a) found a clear correlation (positive for cell parameter a, negative for cell parameter c) between the level of annealing and the unit-cell size ($r>0.8$). Thus the unit cell parameter is a key indicator of the response to annealing in apatite (Barbarand et al., 2003a). Substitution on the anion site has a major influence on apatite cell parameters (9.367 to 9.628 Å for parameter a from F-apatite to Cl-apatite) (e. g., Sudarsanan et al., 1972). Thus cell parameter variations can be partly explained by levels of chlorine substitution. This correlation is most significant for Cl contents above 0.35 wt.%. The influence of the hydroxyl ion is small. Barbarand et al. (2003a) found that the REE concentration cause variations in cell parameters for samples with minor Cl content (< ~ 0.4 wt.%). Other substitutions (Ca, P, Sr) show less correlation with unit cell size.

This indicates that no single substitution can explain the bulk change in lattice parameters. An alternative approach for describing the annealing properties of apatite is to use its solubility, as a proxy for the bulk composition. For that reason the D_{par} of each crystal is measured, where D_{par} is the mean length of well-defined etch pits of outcropping fission tracks parallel to the crystallographic c-axis (Burtner et al., 1994). D_{par} values vary according to the apatite composition (Barbarand et al., 2003a). D_{par} values shows a positive correlation with cell parameter a and MTL. Green et al. (2005), however, proposed that even for fluorine-apatite a good correlation between annealing and wt.% Cl exists.

Annealing kinetics of single grains can be determined by microprobe analyses measuring apatite compositions or by D_{par} measurements. Annealing experiments and field observations show that chlorine-apatite is more resistant to annealing than pure fluorine-apatite. The same correlation can be observed for D_{par} values. D_{par} values usually vary around 1.5 µm for apatites that are less resistant to annealing, and reach up to 5.0 µm for apatites that are often most resistant to annealing (Carlson et al., 1999; Ketcham et al., 1999). AFT conducted on boreholes show that end member F-Apatites are fully annealed at a current down-hole temperature of 92°C, and apatites with 2.2 wt% Cl retain tracks until temperatures above 124°C (e.g., Green et al., 1989).

The concept of closure temperature (T_c) cannot be easily applied to fission track dating: (1) there is no geologically reasonable temperature at which annealing is negligible (Donelick et

al. 1990, Spiegel et al., 2007); (2) fission tracks anneal at relative low temperatures near the surface and thus many samples have experienced a complicated history. Therefore, Wagner et al. (1972) introduced the concept of the partial annealing zone (PAZ), which accounts for the fact that annealing happened over a range of temperatures. The PAZ ranges from 60 to 120°C and 230 to 330°C for AFT and ZFT, respectively (Garver et al., 1999; Hurford, 1986; Tagami and Shimada, 1996; Wagner and Van den haute, 1992).
Track length data can be used to derive information about the tT history of analysed samples. Implemented annealing models are used for inverse and forward modelling of possible tT path. To account for the differences in annealing kinetics, which are not limited to sedimentary rocks but are also found in igneous rocks, Ketcham et al. (2007b) implemented a multikinetic inversion model, requiring kinetic parameters of each grain, e.g. D_{par} values.
Fission track annealing in apatite is anisotropic, and strongly controlled by the track orientation relative to the crystallographic c-axis (Barbarand et al., 2003a), which has an impact on track length distributions. C-axis projection of measured track lengths can be used to correct for this bias (Ketcham et al., 2007a).

Length measurements

Track lengths are routinely measured on confined tracks. There are two types of confined tracks: (1) tracks in track (TINTs) and (2) tracks in cleavage (TINCLEs) (Wagner and Van den haute, 1992). There is a clear trend to longer tracks in TINCLEs (Barbarand et al., 2003), resulting from several sources of bias: (1) a TINCLE is more likely to intersect a fracture if its angle to the fracture is higher, resulting in a non-uniform distribution. (2) Fractures may be widened during polishing and etching. (3) Fractures exhibit higher etching rates, because the echant can access the confined tracks more easily. Therefore, for reducing the bias of track length data and thus for more reliable tT reconstructions, only TINTs were measured.
Another problem in length measurements is that the amount of shorter tracks will always be underestimated, because tracks between 5 and 2 μm are difficult to observe and for tracks <2 μm it is impossible to distinguish between a confined track and etch pits (Barbarand et al., 2003). Chemical properties of the etchant (e. g. concentration) cause different track revelation (e.g. in apatite with concentrated or diluted HNO_3 as etchant) (Wagner and Van den haute, 1992). The etched tracks can be identified by some distinct characteristics: (1) line defects of limited length (<20 μm), (2) straight, (3) exhibit no preferred orientation and (4) disappear after suitable heating. Irradiation with a collimated beam of heavy ions (e.g. ^{252}Cf) results in an increased proportion of TINTs thus improving the analytical precision. For aliquots with MTL <14 μm there is a slight systematic shift to longer values for Cf-irradiated samples, which is within the standard error for replicate measurements.
Interlaboratory comparisons show that length measurements of the same sample often yield differences of 20 % (Wagner and Van den haute, 1992). It is of great importance to ensure that annealing models used by different analysts are comparable to each other. Recent investigations show that there are large variations in AFT length distributions both intra- and interlaboratory, which can be up to ~ 30 % in extreme cases for samples with short mean track length measured by different analysts (Barbarand et al., 2003; Zattin et al., 2007). The reliability of the deduced tT history from AFT data depends mainly on the size of the dataset, especially the amount of the measured track lengths. For complex thermal histories a minimum value of 100 length measurements is required, whereas simple tT histories can be reliably deduced from ~50 length measurements (Barbarand et al., 2003).
X-ray diffraction (XRD) measurement of unit cell is attractive, but impractical as a routine tool. Alternatively there are two approaches: (1) Electron probe micro-analyser (EPMA) measurements can rapidly determine the chemical composition of apatite. (2) Etch pit measurements provide a clear correlation with cell parameter a and MTL values. Barbarand et

al. (2003) demonstrated that the etch-pit size is a valuable estimator of annealing properties of individual apatite grains, only limited by the precision of measurement.

Analytical procedure

Samples were disaggregated and minerals separated using standard magnetic and gravimetric techniques: crushing, sieving and electromagnetic and heavy liquid separation (sodium polytungstate and diiodmethane). Apatites were mounted in epoxy and zircons in PFA Teflon^{TM}, and their surfaces were ground and polished. The apatite mounts were etched with 5M HNO_3 for 20s at 20°C and the zircon mounts with a eutectic melt of KOH-NaOH for 27-130 hours at 215°C (Zaun and Wagner, 1985). Irradiation was carried out at the FRM-II reactor in Garching (TU München, Germany). Mica detectors were etched to reveal induced tracks using 40% HF at 20°C for 40 min. Fission track counting was carried out with an optical microscope (Axioscope 1, Zeiss) under 1000x magnification using a dry objective for apatite and an oil objective for zircon. Samples were dated by the external detector method (Gleadow, 1981; Naeser, 1978) using the zeta calibration approach (Hurford and Green, 1982; Hurford and Green, 1983). AFT zeta values of 354±7 (C. Glotzbach), 373±8 (C. Spiegel) and 390±8 yr/cm² (J. Reinecker) for dosimeter glass CN5 were determined from Durango and Fish Canyon Tuff apatite age standards. ZFT zeta values of 126±4 (C. Glotzbach) and 116±2 yr/cm² (C. Spiegel) for dosimeter glass CN2 were determined from Buluk Tuff, Tardree standard, and Fish Canyon Tuff zircon age standards. Age calculation, visualization and statistics were carried out with the Trackkey 4.2g program (Dunkl, 2000). More details about the used analytics are described in the attached manuscripts.
Because of low uranium contents and young ages, most apatite samples were irradiated by a ^{252}Cf source in Melbourne (Australia), to enhance the number of etchable confined tracks. Measured Dpar values (mean of 4 measurements of each crystal) were complemented by electron microprobe analysis (University of Tübingen, Germany) on selected crystals, using a JEOL Superprobe with a beam current of 30 nA, an acceleration voltage of 15 kV and a beam diameter of 10 μm.
Predicted time-temperature (tT) paths for individual samples were used for forward modeling of AFT and AHe data. Modeling was carried out with the program HeFTy v. 1.3c (Ketcham, 2005) based on the multikinetic annealing model of Ketcham et al. (2007b) and with c axis projected track length data (Ketcham et al., 2007a). tT paths were statistically evaluated and categorized by a value of goodness of fit (GOF), in which a 'good' result corresponds to a value of 0.5, an 'acceptable' result corresponds to a value of 0.05, and a GOF of 1 is the optimum. For details we refer to Ehlers et al. (2005) and Ketcham (2005).
The input parameters for each sample used in this study are its central FT age with 1σ error, the predicted tT path, and, if available, the c axis projected track length distribution, the single-grain AHe ages and, as a kinetic parameter, the D_{par} value.

1.3.2 **Apatite (U-Th)/He thermochronology**

In the last decade apatite (U-Th)/He thermochronology has become an important tool for quantifying the latest cooling history of rocks (Ehlers and Farley, 2002). Because of their low T_c this technique bridges the gap between the AFT method and methods applied on the surface (e.g. cosmogenic exposure dating). It is applicable to interdisciplinary investigations, including landform evolution, structural geology, and geodynamics.

He production and ingrowth

(U-Th)/He dating is based on the retention of ^{4}He in the crystal, which is produced by decay of ^{238}U, ^{235}U, ^{232}Th and ^{147}Sm (e.g., Ehlers and Farley, 2002):

$$^4He = 8 \cdot {}^{238}U \cdot (e^{\lambda 238 \cdot t} - 1) + 7 \cdot {}^{235}U \cdot (e^{\lambda 235 \cdot t} - 1) + 6 \cdot {}^{232}Th \cdot (e^{\lambda 232 \cdot t} - 1) + 1 \cdot {}^{147}Sm \cdot (e^{\lambda 147 \cdot t} - 1)$$

To solve the equation the amount of mother (U, Th and Sm) and daughter (He) particles have to be measured. Typically, this is done by a two-stage analytical procedure involving heating and degassing of crystals and gas-source mass spectrometry and subsequent inductive-coupled plasma mass spectrometry on the same crystal to measure their U, Th and Sm contents. In contrast to other dating techniques no limitation on the range of accessible ages exist (e. g. few 100 ka – 4.56 Ga).

Alpha recoil

Decay of U, Th and Sm nuclei emit alpha particles with high kinetic energies (4-8 MeV), which travel through the solid lattice of the grain before they come to rest. The travel distance, known as stopping distance, varies between ~11 and ~34 μm, with mean distances of 19.68, 22.83 and 22.46 μm for ^{238}U, ^{235}U and ^{232}Th, respectively (Farley et al., 1996). Accordingly, ^{4}He is lost at the crystals edges or injected by surrounding grains. Therefore correction for geometry has to be done. Prerequisites for applying this alpha-ejection correction are that He implantation from the surroundings are negligible, and that U, Th, and Sm are homogenously distributed in apatite. Most crystals determined have diameters between 75-170 μm, and ages without correction are underestimated by 15-33 %. Commonly the physical dimension of a crystal is measured to correct for alpha ejection. A problem within He dating is that grains with homogenous U and Th distributions are rare. Instead, apatite often shows different amounts of zonation, and this also reduces the reproducibility.

Sensitivity

Laboratory heating experiments provide the necessary information for understanding thermally activated volume diffusion (Wolf et al., 1996). Diffusion experiments show a remarkably similar diffusion behaviour for a wide variety of analysed apatites (Wolf et al., 1996). Retention and diffusion of ^{4}He is controlled by several factors: crystal size and geometry, tT history, distribution of mother isotopes and radiation damage of the crystal lattice (e.g., Shuster et al., 2006). These parameters control the temperature zone at which accumulation exceeds the diffusive loss of ^{4}He, called partial retention zone (PRZ). The apatite PRZ is estimated to be between 40 and 85°C (Wolf et al., 1996), but even at temperatures around 10°C or less, small amounts of ^{4}He loss are expected (Green and Duddy, 2006). The slower the cooling rate, the greater the sensitivity of the He age to subtle factors controlling He loss, like zonation, grain size, and variability in kinetic parameters. In contrast, Wolf et al. (1996) found no affect of chemical composition and grain size, suggesting that a

single T_c of 75±7°C is applicable to a wide range of samples. The most important impact on the T_c has the cooling rate (Wolf et al., 1996). For instance, Fitzgerald et al. (2006) found that samples that cooled quickly have less variation, whereas samples that cooled slowly or resided within the PRZ prior to more rapid cooling have a comparatively greater variation in ages, because of the increased importance of diffusion.

(U-Th)/He analytical procedure

Helium analyses were carried out in the thermochronological laboratory at the University of Tübingen (Germany). Apatite crystals were hand-picked under a stereomicroscope taking into account morphology, size and purity of the crystals (Farley, 2002). Crystals were inspected at 200x magnification under cross-polarized light for inclusions (all dated crystals were apparently free of visible inclusions). Each selected crystal was digitally photographed parallel and partly also perpendicular to its crystallographic c axis and measured. The crystals were loaded into Pt tubes and degassed by laser or furnace. U-Th analyses were conducted at the Scottish Universities Environmental Research Centre (SUERC) in East Kilbride (Scotland), and U-Th-Sm analyses were conducted at the University of Melbourne (Australia). Details about instrumentation and analytics are given in Danišík (2005).
The total analytical uncertainty (TAU) was computed as the square root of the sum of squares of weighted uncertainties on U, Th, (Sm), and He measurements. TAU was usually less than ~4% (1σ) and used to calculate errors of raw (U-Th)/He ages. For the raw (U-Th)/He ages an alpha-ejection correction was applied (Farley, et al., 1996). A value of 10% was adopted as the uncertainties of alpha-ejection corrections and used to calculate the error of corrected (U-Th)/He ages.

1.4 References

Barbarand, J., Carter, A., Wood, I. and Hurford, T., 2003a. Compositional and structural control of fission-track annealing in apatite. Chemical Geology, 14171: 1-31.

Barbarand, J., Hurford, T. and Carter, A., 2003b. Variation in apatite fission-track length measurement: implications for thermal history modelling. Chemical Geology, 14170: 1-30.

Becker, A., 2000. The Jura Mountains - an active foreland fold-and-thrust belt? Tectonophysics, 321: 381-406.

Burtner, R.L., Nigrini, A. and Donelick, R.A., 1994. Thermochronology of Lower Cretaceous source rocks in the Idaho-Wyoming thrust belt. AAPG Bulletin, 78(10): 1613-1636.

Carlson, W.D., Donelick, R.A. and Kecham, R.A., 1999. Variability of apatite fission-track annealing kinetics: I. Experimental results. American Mineralogist, 84: 1213-1223.

Donelick, R.A., O'Sullivan, P.B. and Ketcham, R.A., 2005. Apatite Fission-Track Analysis. Reviews in Mineralogy & Geochemistry, 58: 49-94.

Dunkl, I., 2000. Trackkey: a windows program for calculation and graphical presentation of fission track data. Computers & Geosciences, 28(1): 3-12.

Ehlers, T.A. et al., 2005. Computational tools for low-temperature thermochronometer interpretation. Reviews in Mineralogy & Geochemistry, 58: 589-622.

Ehlers, T.A. and Farley, K.A., 2002. Apatite (U-Th)/He thermochronometry: methods and applications to problems in tectonic and surface processes. Earth and Planetary Science Letters, 206(1-2): 1-14.

Enkelmann, E., Jonckheere, R. and Wauschkuhn, B., 2005. Independent fission-track ages (?-ages) of proposed and accepted age standards and a comparison of ?-, Z-, ?- and ?0-ages: Implications for method calibration. Chemical Geology, 222: 232-248.

Farley, K.A., Wolf, R.A. and Silver, L.T., 1996. The effects of long alpha-stopping distances on (U-Th)/He dates. Geochemica et Cosmochimica Acta, 60: 4223-4229.

Fitzgerald, P.G., Baldwin, S.L., Webb, L.E. and O'Sullivan, P.B., 2006. Interpretation of (U-Th)/He single grain ages from slowly cooled crustal terranes: A case study from the Transantarctic Mountains of southern Victoria Land. Chemical Geology, 225: 91-120.

Fleischer, R.L. and Hart, H.R., 1972. Fission track dating: techniques and problems. In: W.W. Bishop, D.A. Miller and S. Cole (Editors), Proc. Burg Wartenstein Conf. on Calibration of Hominoid Evolution. Scott. Acad. Press, Edinbourgh, pp. 135-170.

Fleischer, R.L., Price, P.B. and Walker, R.M., 1965. Effects of temperature, pressure, and ionization of the formation and stability of fission tracks in minerals and glasses. Journal of Geophysical Research, 70: 1497-1502.

Frisch, W., 1979. Tectonic progradation and plate tectonic evolution of the Alps. Tectonophysics, 60: 121-139.

Frisch, W., Dunkl, I. and Kuhlemann, J., 2000. Post-collisional orogen-parallel large-scale extension in the Eastern Alps. Tectonophysics, 327: 239-265.

Frisch, W. and Meschede, M., 2005. Plattentektonik und Gebirgsbildung. Wissenschafltiche Buchgesellschaft, Darmstadt, 208 pp.

Galbraith, R.F. and Laslett, G.M., 1993. Statistical models for mixed fission track ages. Nuclear Tracks and Radiation measurements, 21: 459-470.

Gallagher, K., Brown, R. and Johnson, C., 1998. Fission Track analysis and its application to geological problems. Annual Reviews Earth Planetary Science, 26: 519-572.

Garver, J.I., 2006. The significance of radiation damage in zircon for fission track dating. In: B. Ventura and F. Lisker (Editors), European Conference on Thermochronology. Schriftenreihe der Deutschen Gesellschaft für Geowissenschaften, Bremen, Germany, pp. 56-58.

Garver, J.I., Brandon, M.T., Roden-Tice, M. and Kamp, P.J.J., 1999. Exhumation history of orogenic highlands determined by detrital fission-track thermochronology. In: U. Ring, M.T. Brandon, G.S. Lister and S.D. Willet (Editors), Exhumation Processes: Normal Faulting, Ductile Flow and Erosion. Geological Society, London, Special Publications, London, pp. 283-304.

Gleadow, A.J.W., 1981. Fission-track dating methods: What are the real alternatives? Nuclear Tracks and Radiation measurements, 5(1/2): 3-14.

Grasemann, B. and Mancktelow, N.S., 1993. Two-dimensional thermal modelling of normal faulting: the Simplon Fault Zone, Central Alps, Switzerland. Tectonophysics, 225: 155-165.

Green, P.F. and Duddy, I.R., 2006. Interpretation of apatite (U-Th)/He ages and fission track ages from cratons. Earth and Planetary Science, 244: 541-547.

Green, P.F., Duddy, I.R. and Hegarty, K.A., 2005. Comment on "Compositional and structural control of fission track annealing in apatite" by J. Barbarand, A. Carter, I. Wood and A.J. Hurford, Chemical Geology, 198 (2003) 107-137. Chemical Geology, 214: 351-358.

Green, P.F. et al., 1989. Thermal annealing of fission tracks in apatite. Chemical Geology, 79: 155-182.

Hurford, A.J., 1986. Cooling and uplift patterns in the Lepontine Alps South Central Switzerland and an age of vertical movement on the Insubric fault line. Contributions to Mineralogy and Petrology, 92: 413-427.

Hurford, A.J. and Gleadow, A.J.W., 1977. Calibration of fission track dating parameters. Nuclear track detection, 1: 41-48.

Hurford, A.J. and Green, P.F., 1982. A users' guide to fission track dating calibration. Earth and Planetary Science Letters, 59: 343-354.

Hurford, A.J. and Green, P.F., 1983. The Zeta age calibration of fission-track dating. Chemical Geology (Isotope Geoscience Section), 41: 285-317.

Ketcham, R.A., 2005. Forward and inverse modelling of low-temperature thermochronology data. Reviews in Mineralogy & Geochemistry, 58(275-314).

Ketcham, R.A., Carter, A., Donelick, R.A., Barbarand, J. and Hurford, A.J., 2007a. Improved measurement of fission-track annealing in apatite using c-axis projection. American Mineralogist, 92: 789-798.

Ketcham, R.A., Carter, A., Donelick, R.A., Barbarand, J. and Hurford, A.J., 2007b. Improved modeling of fission-track annealing in apatite. American Mineralogist, 92: 799-810.

Ketcham, R.A., Donelick, R.A. and Carlson, W.D., 1999. Variability of apatite fission-track annealing kinetics: III. Extrapolation to geological time scales. American Mineralogist, 84: 1235-1255.

Naeser, C.W., 1978. Fission track dating. U.S. Geological Survey Open-File Report: 76-190.

Nasdala, L. et al., 2001. Meamictisation of natural zircon: accumulation versus thermal annealing of radioactivity-induced damage. Contributions to Mineralogy and Petrology, 141: 125-144.

Paul, T.A. and Fitzgerald, P.G., 1992. Transmission electron microscopic investigation of fission tracks in fluorapatite. American Mineralogist, 77: 336-344.

Price, P.B. and Walker, R.M., 1962a. A new track detector for heavy particle studies. Physics Letters, 3(3): 113-115.

Price, P.B. and Walker, R.M., 1962b. Observations of Charged -Particle Tracks in Solids. Journal of Applied Physics, 33(12): 3400-3406.

Price, P.B. and Walker, R.M., 1963. Fossil tracks of charged particles in mica and the age of minerals. Journal of Geophysical Research, 68: 4847-4862.

Ratschbacher, L., Frisch, W. and Linzer, H.-G., 1991. Lateral extrusion in the Eastern Alps, Part 2: structural analysis. Tectonics, 10: 257-271.

Reiners, P.W., Ehlers, T.A. and Zeitler, P.K., 2005. Past, present and future of Thermochronology. Reviews in Mineralogy & Geochemistry, 58: 1-18.

Riley, B.C.D. and Garver, J.I., 2006. Controls on low-temperature resetting of natural damaged detrital zircons: case study from Arizona. In: B. Ventura and F. Lisker (Editors), European Conference on Thermochronology. Schriftenreihe der Deutschen Gesellschaft für Geowissenschaften, Bremen, Germany, pp. 125-127.

Schmid, S.M., Fügenschuh, B., Kissling, E. and Schuster, R., 2004. Tectonic map and overall architecture of the Alpine orogen. Eclogae Geologicae Helvetiae, 97: 93-117.

Shuster, D.L., Flowers, R.M. and Farley, K.A., 2006. The influence of natural radiation damage on helium diffusion kinetics in apatite. Earth and Planetary Science, 249(3-4): 148-161.

Steck, A. and Hunziker, J., 1994. The Tertiary structural and thermal evolution of the Central Alps - compressional and extensional structures in an orogenic belt. Tectonophysics, 238: 229-254.

Sudarsanan, K., Mackie, P.E. and Young, R.A., 1972. Comparision of synthetic and mineral fluorapatite, Ca5(PO4)3F, in crystallographic detail. Mater. Res. Bull., 7: 1331-1338.

Tagami, T. and O'Sullivan, P.B., 2005. Fundamentals in Fission-Track Thermochronology. Reviews in Mineralogy & Geochemistry, 58: 19-47.

Tagami, T. and Shimada, C., 1996. Natural long-term annealing of the zircon fission track system around a granitic pluton. Journal of Geophysical Research, 101: 8245-8255.

von Blanckenburg, F. and Davies, J.H., 1995. Slab breakoff: A model for syncollisional magmatism and tectonics in the Alps. Tectonics, 14: 120-131.

Wagner, G. and Van den haute, P., 1992. Fission-Track Dating. Solid earth sciences library, 6. Enke Verlag, 285 pp.

Wagner, G.A., 1972. The geological interpretation of fission track ages. Transactions of the American Nuclear Society, 15.

Willett, S.D., Schlunegger, F. and Picotti, V., 2006. Messinian climate change and erosional destruction of the central European Alps. Geology, 34: 613-616.

Wolf, R.A., Farley, K.A. and Silver, L.T., 1996. Helium diffusion and low-temperature thermochronometry of apatite. Geochemica et Cosmochimica Acta, 60: 4231-4240.

Zattin, M. et al., 2007. Low temperature thermochronology: applications and interlaboratory calibration, Notes from the first workshop of the IGCP543.

Zaun, P.E. and Wagner, G., 1985. Fission-track stability in zircons under geological conditions. Nucl. Tracks Radiat. Meas., 10: 303-307.

1.5 List of enclosed manuscripts

A1 Glotzbach C., J. Reinecker, M. Danišík, M. Rahn, W. Frisch and C. Spiegel (2008): Neogene exhumation history of the Mont Blanc massif, Western Alps. – Tectonics, doi:10.1029/2008TC002257, in press.
Own contribution: 1. Idea: 30%, 2. Data generation: 90%, 3. Interpretation: 70%, 4. Writing: 60%.

A2 Glotzbach C., C. Spiegel, J. Reinecker, M. Rahn and W. Frisch (2008): What perturbs isotherms? An assessment using fission track thermochronology and thermal modelling along the Gotthard transect, Central Alps. – in Lisker et al. (eds): Thermochronological methods: from paleotemperature constraints to landscape evolution models, Geological Society of London, Special Publications, in press.
Own contribution: 1. Idea: 30%, 2. Data generation: 90%, 3. Interpretation: 70%, 4. Writing: 60%.

A3 Reinecker J. M. Danišík, C. Schmid, C. Glotzbach, M. Rahn, W. Frisch and C. Spiegel (in review): Tectonic control on the late stage exhumation of the Aar Massif (Switzerland): Constraints from apatite fission track and (U-Th)/He data. – Tectonics, doi:10.1029/2007TC002247R.
Own contribution: 1. Idea: 10%, 2. Data generation: 10%, 3. Interpretation: 20%, 4. Writing: 10%.

A4 Dörr N., C. Spiegel, M. Danišík, C. Glotzbach, M. Rahn and W. Frisch (in review): Neogene activity along the Forcola normal fault: implications for the late-stage exhumation history of the Central Alps (Switzerland). – Tectonics, doi:10.1029/2008TC002279.
Own contribution: 1. Idea: 5%, 2. Data Generation: 5%, 3. Interpretation: 10%, 4. Writing: 10%.

A5 Glotzbach C., J. Reinecker, M. Danišík, M. Rahn, W. Frisch and C. Spiegel (to be submitted): Exhumation history of the central Gotthard and Aar massifs (Switzerland): Constraints from low temperature thermochronology.
Own contribution: 1. Idea: 30%, 2. Data generation: 90%, 3. Interpretation: 70%, 4. Writing: 60%.

Neogene exhumation history of the Mont Blanc massif, Western Alps

C. Glotzbach[1,*], J. Reinecker[1], M. Danišík[1], M. Rahn[2], W. Frisch[1] and C. Spiegel[3]

[1] Institute of Geosciences, University of Tübingen, Germany
[2] Institute of Mineralogy-Geochemistry, University of Freiburg, Germany
[3] FB 5 – Geosciences, University of Bremen, Germany

Abstract

The contribution of climate and tectonic to the Neogene exhumation history of the European Alps is studied in the Mont Blanc (MB) massif using low-temperature thermochronology. Apatite fission track and (U-Th-[Sm])/He data suggest that the MB massif was exhumed episodically: Rapid exhumation (2.5±0.5 km/Myr) before 6 Ma is followed by an episode of slow exhumation and a period of accelerated exhumation (>1 km/Myr) after ~3 Ma. Comparing the exhumation rates of the MB massif with reported exhumation rates of all other external crystalline massifs (ECM) shows that the MB massif is the only ECM that experienced rapid exhumation before 6 Ma, which is possibly related to NW and minor SE directed thrusting of the MB massif. The data demonstrate that the Messinian base level drop (~5.5 Ma) and the increase in atmospheric moisture caused by an intensification of the Atlantic Golf Stream (4.6 Ma) did not affect the exhumation of the external Alps. All ECM, except the Gotthard massif, show an increase in exhumation rates at ~3 Ma. We interpret this as the result of normal faulting along orogen-parallel faults and beginning Alpine glaciation. The relative impact of these processes on the exhumation of the ECM can vary spatially and temporally, mainly depending on differences in geology and geomorphology. In the case of the MB massif we propose that the acceleration in exhumation rates at ~3 Ma is caused by rapid valley incision related to glaciation, and that the recent relief of the MB massif is thus a young feature.

1 Introduction

Endogenic and exogenic processes control the rate at which a rock volume is uplifted, eroded and exhumed [e.g., *Ring et al.*, 1999; *Molnar*, 2004], and thus determine the evolution of relief and topography [*England and Molnar*, 1990; *Willett et al.*, 2006]. Exhumation histories are particularly suitable for investigating the relation between exogenic and endogenic processes and their role for topography and relief evolution.
For the European Alps, an increase in exhumation has been reported for the Late Neogene [*Bogdanoff et al.*, 2000; *Kuhlemann*, 2000]. The relative contributions of climatic and tectonic processes to this increase are currently debated in the literature [*Cederbom et al.*, 2004; *Champagnac et al.*, 2006a; *Willett et al.*, 2006]. The external crystalline massifs (ECM) show very young exhumation and became exposed during the latest Neogene [e.g., *Michalski and Soom*, 1990; *Seward and Mancktelow*, 1994]. All ECM are characterized by high local relief, and most of them reveal similar exhumation histories [*Bogdanoff et al.*, 2000], which would argue for a climatic control of exhumation.

[*] Corresponding author. Institute of Geosciences, University of Tübingen, Sigwartstr. 10, D-72076 Tübingen, Germany. Tel. +49 7071 2975240. Fax +49 7071 5059.
E-mail addresses: christoph.glotzbach@uni-tuebingen.de (C. Glotzbach), martin.danisik@uni-tuebingen.de (M. Danišík), john.reinecker@uni-tuebingen.de (J. Reinecker), Meinert.Rahn@hsk.ch (M. Rahn), frisch@uni-tuebingen.de (W. Frisch), cornelia.spiegel@uni-bremen.de (C. Spiegel)

With a summit elevation of 4807 m a.s.l., the Mont Blanc (MB) massif is the highest of the ECM. Its Neogene kinematic and structural evolution is still not clear. *Leloup et al.* [2005] proposed a polyphase tectonic evolution with deformation mainly localized along two major shear zones: the Mont Blanc shear zone, a SE dipping reverse fault active between ~12 and 4 Ma, and the Mont Blanc back thrust, a NW dipping reverse fault active after 4 Ma (Figure 1). *Rolland et al.* [2007], by contrast, suggested that deformation was accommodated by numerous anastomozing shear zones, and that major shear zones are also present in the central part of the MB massif. They proposed a one-phase continuous model with east vergent motions, resulting in a transpressive pop-up system and continuous exhumation of ~1 km/Myr since ~16 Ma.

The aim of this study is to unravel the Late Neogene exhumation history of the MB massif by low-temperature thermochronology (apatite fission track and (U-Th-[Sm])/He thermochronology). Our new data will be used to test the different structural and kinematic evolution models by *Leloup et al.* [2005] and *Rolland et al.* [2007]. Furthermore, we compare the exhumation history of the MB massif with that of other ECM and discuss potential relations with tectonic and climatic processes. Finally, we propose a model for the relief evolution of the MB massif during the last 6 Ma.

For this purpose the MB road tunnel as well as the corresponding surface line were sampled, including a steep profile at the NW flank of the MB massif with a vertical sample elevation distance of ~2.5 km. This sampling strategy allows (1) to observe horizontal and vertical age trends across the MB massif, (2) to directly derive exhumation rates from the age elevation relationship, and (3) to test whether derived exhumation rates are affected by isotherm perturbation below topography.

2 Geological setting

The Western Alps formed during Paleogene southward subduction of the Penninic ocean [e.g., *Frisch*, 1979]. During continent-continent collision the European continental margin (Helvetic domain) was overthrust by the African continental margin (Austroalpine domain), while continental and oceanic crust fragments of the Penninic domain were squeezed in-between [e.g., *Steck and Hunziker*, 1994; *Schmid et al.*, 1996]. Penninic and Helvetic units were thrust northwestward, resulting in the burial of the now exposed ECM, e.g. the MB massif was buried to a depth of 15-20 km [*Leloup et al.*, 2005].

The ECM (Aar, Gotthard, Mont Blanc, Aiguilles Rouges, Belledone, Argentera, Pelvoux massifs) consist of pre-Variscan polymetamorphic basement intruded by late Variscan granitoids and covered by Paleozoic to lower Tertiary sedimentary rocks [Labhart, 1977; *von Raumer and Neubauer*, 1993]. All ECM are presently exposed as orogen-parallel bodies in the footwall of the Penninic frontal thrust (PFT) (Figure 1) and reveal similar Neogene exhumation histories [*Bogdanoff et al.*, 2000]. Repeated precise levelings show similar present day rock uplift rates around 1 mm/y for the Aar, Gotthard, Belledone, Aiguilles Rouges and MB massif [*Jouanne et al.*, 1995; *Kahle*, 1997].

An increase of the Alpine metamorphic grade from anchizonal conditions in the Aiguilles Rouges massif to lower greenschist facies metamorphism in the MB massif can be observed [*Frey and Mählmann Ferreiro*, 1999]. The MB massif is bordered by major fault structures: the dextral Chamonix line to the NW [*Hubard and Mancktelow*, 1992] and the PFT to the SE (Figure 1) [*Seward and Mancktelow*, 1994; *Fügenschuh and Schmid*, 2003]. Both structures were reactivated in the Neogene by dextral transpressional movements [*Seward and Mancktelow*, 1994; *Perello et al.*, 1999].

The Western Alps are characterized by orogen-parallel and orogen-perpendicular Neogene extensional movements (Figure 1) [*Sue et al.*, 2007]. Most prominent are the normal displacements along the Rhône-Simplon fault [e.g., *Keller et al.*, 2006] and the reactivation of

orogen-parallel thrusts (PFT, Briançonnais front, Internal Houiller fault) as faults with a normal component [*Sue et al.*, 1999; *Bistacchi and Massironi*, 2000; *Bistacchi et al.*, 2000; *Sue and Tricart*, 2002; *Malusà et al.*, 2005; *Champagnac et al.*, 2006b]. Orogen-parallel extension was active in the Miocene-Pliocene followed by a change to orogen-perpendicular extension in the Pliocene [*Sue et al.*, 2007], in accordance with the reactivation of the Internal Houiller fault as a normal fault after 5 Ma [*Fügenschuh and Schmid*, 2003]. Seismotectonic analyses confirm that normal movements along these faults are still active [*Sue et al.*, 1999]. *Champagnac et al.* [2006b] concluded that the Western Alps are currently in a state of post-orogenic collapse.

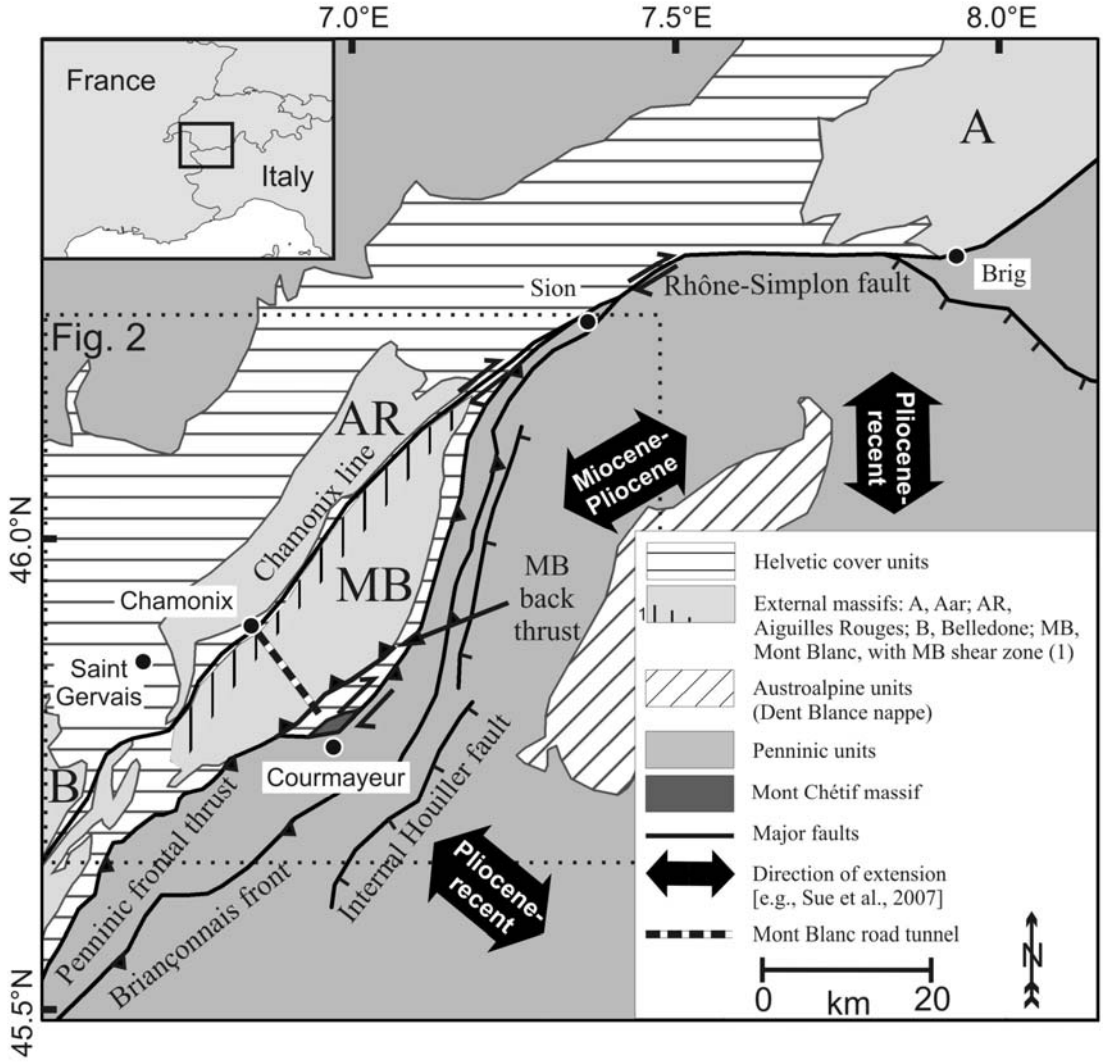

Fig. 1: Geological sketch map of the MB massif and the surrounding region, for location see inset.

3 Available thermochronological constraints

Previously published apatite fission track (AFT) ages from the MB massif range from 1.4 to 9.3 Ma, whereas zircon fission track (ZFT) ages vary between 11.2 and 15.7 Ma (Figure 2) [*Michalski and Soom*, 1990; *Seward and Mancktelow*, 1994; *Rahn*, 2001; *Fügenschuh and Schmid*, 2003; *Leloup et al.*, 2005]. All published datasets are largely consistent, except for the data of *Carpéna* [1992], who reported much older ages, e.g. AFT ages in the tunnel of 11 Ma. She used the activation method for FT analysis, which may explain the discrepancy to the other results. Because of this disagreement, her data will not be considered in our interpretation. AFT ages of the adjacent Aiguilles Rouges massif are similar to those of the

MB massif and vary between 2.7 and 8.9 Ma [*Michalski and Soom*, 1990; *Seward and Mancktelow*, 1994; *Rahn*, 2001; *Leloup et al.*, 2005]. ZFT ages of the Aiguilles Rouges massif show a large variation, ranging from 17.2 to 229 Ma [*Michalski and Soom*, 1990] and indicate a partially reset status for the ZFT system at the NW margin of the massif. AFT ages on both sides of the Chamonix line between these two massifs (Figures 2 and 3) are concordantly around 4 Ma, and show that the Chamonix line has not undergone vertical displacements since that time [*Rahn*, 2001; *Leloup et al.*, 2005].

A compilation of fission track data from the MB massif shows a broad correlation of ages with respect to elevation with a steeper slope for the AFT ages than for the ZFT ages, indicating accelerated cooling and exhumation since ~10 Ma as it was also found in other ECM [*Fügenschuh and Schmid*, 2003]. *Leloup et al.* [2005] sampled an age elevation profile along the MB tunnel transect over a vertical distance of ~4 km, suggesting an episodic exhumation history.

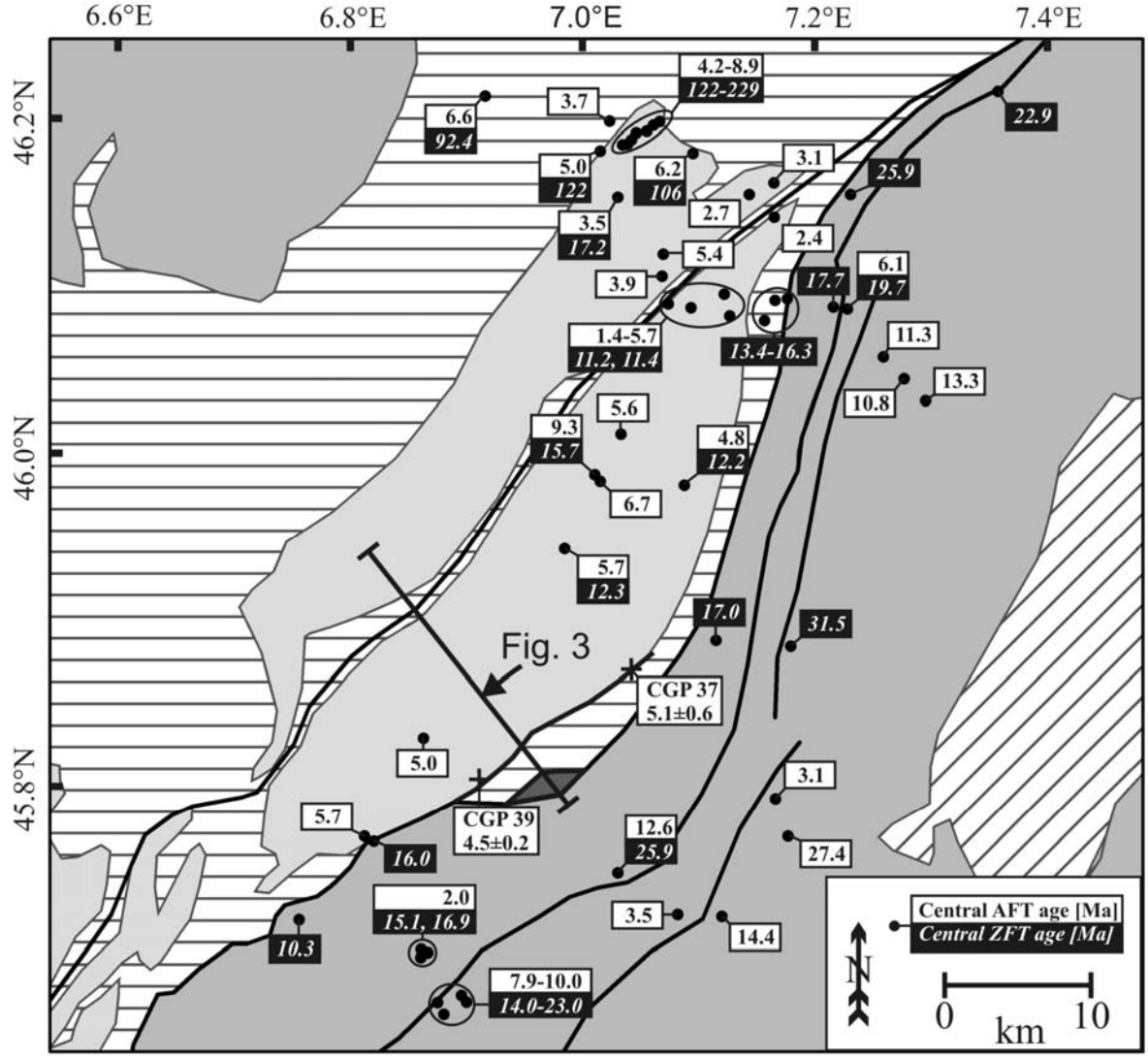

Fig. 2: Published surface AFT and ZFT ages in the MB massif and surrounding regions [*Michalski and Soom*, 1990; *Seward and Mancktelow*, 1994; *Fügenschuh and Schmid*, 2003; *Leloup et al.*, 2005; *Malusà et al.*, 2005]. Location of own samples outside the tunnel transect (CGP 37 and 39) are displayed with their central AFT age ±1σ error.

4 Results

4.1 AFT thermochronology

AFT ages were measured on 29 samples (Table 1, Figure 3). All AFT ages are displayed as central ages and errors as ±1σ [*Galbraith and Laslett*, 1993]. Dpar obtained for measured samples are narrow and relatively uniform, varying between 1.3 and 1.7 μm (Table 1). Microprobe analyses of 20 samples have been carried out, demonstrating that all samples are close to a F apatite end member (Table 2). Furthermore, analyzed elements such as Si, Ce and Sr do not show any significant variation, suggesting that apatites are kinetically uniform.
AFT ages range from 2.6 to 7.7 Ma. All samples are characterized by high chi-square probabilities (47-100) and low dispersions (0.00-0.14), indicating that all ages represent single age populations (Table 1). Ages along the MB tunnel with sample elevations around 1.3 km range from 3.4 to 5.3 Ma. Surface samples from elevations between 1.3 and 3.8 km yielded AFT ages between 2.6 and 7.7 Ma (Figure 3).
Fission track length data are mainly available for the NW part of the sampled transect. Mean unprojected track lengths (MTL) range from 12.0±2.7 to 13.7±1.7 μm, with a trend to shorter lengths toward the SE along the tunnel (Figure 3). *Seward and Mancktelow* [1994] reported track length data for three samples between 13.0±1.5 and 13.6±1.7 μm (RS 4, RS 5, and RS 14) which are nearly identical to our data from locations close-by. At elevations >2 km MTL are >13.5 μm, whereas below they are reduced up to 12.0±2.7 μm. All track length distributions are narrowly shaped, with the exception of samples CGP 25 and 2903, which show a pronounced tailing towards short track lengths (Figure 3).

4.2 (U-Th-[Sm])/He thermochronology

48 single apatite crystals from 8 surface and 4 tunnel samples were analyzed by (U-Th-[Sm])/He thermochronology (Table 3). Single-grain AHe ages older than the corresponding AFT age were excluded from our interpretation. We assume that 'too old' AHe ages are ascribed to micro-inclusions not detectable under 200x magnification. For AHe ages younger than corresponding AFT ages, averaged AHe ages with standard deviation were calculated weighting the single-grain ages with their analytical error. Samples which left over only one AHe age, single-grain AHe ages with analytical error are reported (Table 3). Two samples (PK 4250 and 5406) yield two reproducible age components. In the following interpretation we will use the younger age component, which fits better to the overall trend in AHe ages and the deduced thermal history.
Some scatter in the resulting data can be attributed to the difference in (U-Th)/He and (U-Th-Sm)/He ages. (U-Th-[Sm])/He dating of single-grain apatites reveals that He produced by Sm results in AHe ages that are on average 12% younger (max. 24%) compared to conventional (U-Th)/He dating (Table 3). Even in crystals with high U concentrations (up to 50 ppm) the Sm contribution to the [U-Th-Sm]/He age is more than 5 % (Figure 4). The analyzed Durango apatites show only a slight difference in age of 2%. The contribution of He produced from Sm decay to the AHe age is positively correlated to the ratio of Sm/U+Th (Figure 4).
AHe ages from surface samples are between 1.7 and 6.4 Ma, and are positively correlated with elevation (Figure 3). Tunnel samples have ages between 1.4 and 1.7 Ma (incorporating sample CGP 26 from the NW Tunnel portal), with one exceptional age of 2.7 Ma (sample 5406).

Table 1: AFT data from the Mont Blanc massif.

Sample	Tectonic unit	Coordinates		Elevation [m]	# grains	ρs	Ns	ρi	Ni	ρd	Nd	P(χ^2) [%]	Dispersion	Central age ±1σ [Ma]	MTL±SD [µm]	# length	Dpar±SD [µm]	U [ppm]
		lat.	long.															
Tunnel																		
PK 650	Mont Blanc shear zone	6.86680	45.89724	1280	41	0.738	329	22.151	9879	6.663	3311	87	0.02	3.9±0.2	13.27±1.39	100	1.50±0.12	37
PK 1150	Mont Blanc shear zone	6.87341	45.89113	1285	35	0.579	146	16.238	4096	6.671	3311	100	0.00	4.2±0.4	n.d.	n.d.	1.50±0.11	28
2170-2113	Pre-Variscan basement	6.87924	45.88612	1293	45	1.136	437	33.664	12947	6.623	3311	47	0.14	4.0±0.2	13.00±1.85	58	1.51±0.10	60
PK 2736	Mont Blanc granite	6.88307	45.88225	1299	31	0.698	129	20.455	3783	6.678	3311	100	0.00	4.0±0.4	n.d.	n.d.	1.58±0.14	36
PK 4250	Mont Blanc granite	6.89466	45.87119	1313	50	0.385	33	11.382	975	6.352	3118	99	0.00	3.8±0.7	n.d.	n.d.	1.31±0.10	21
PK 5710	Mont Blanc granite	6.90259	45.86399	1323	8	0.310	15	9.039	438	7.162	3397	94	0.00	4.4±1.1	n.d.	n.d.	1.45±0.10	14
5406	Mont Blanc granite	6.92185	45.85700	1331	24	0.255	30	6.389	751	6.172	3311	96	0.01	4.4±0.8	n.d.	n.d.	1.51±0.13	16
4630	Mont Blanc granite	6.91632	45.85137	1338	33	0.223	28	7.819	980	6.631	3311	98	0.00	3.4±0.7	n.d.	n.d.	1.31±0.15	16
3783	Mont Blanc granite	6.92276	45.84496	1346	50	0.402	43	10.805	1157	6.616	3311	98	0.01	4.4±0.7	n.d.	n.d.	1.30±0.15	20
2903	Mont Blanc granite	6.92958	45.83888	1354	50	0.384	66	9.306	1599	6.128	3013	90	0.00	4.5±0.6	11.98±2.73	49	1.51±0.14	17
1500	Mont Blanc granite	6.94031	45.82878	1367	42	0.437	69	9.626	1521	6.639	3311	97	0.00	5.3±0.7	n.d.	n.d.	1.37±0.16	16
Surface																		
CGP22	Mont Blanc shear zone	6.87871	45.88671	2587	50	4.775	607	87.883	11171	6.746	3118	95	0.01	6.5±0.3	13.70±1.70	100	1.58±0.12	160
CGP23	Mont Blanc shear zone	6.87151	45.88993	2266	50	1.203	633	23.636	12433	7.013	3397	84	0.05	6.3±0.3	13.66±1.48	100	1.58±0.11	40
CGP24	Mont Blanc shear zone	6.86917	45.89337	1978	48	0.718	380	13.436	7114	6.713	3118	100	0.00	6.4±0.4	13.06±1.72	47	1.56±0.11	23
CGP25	Mont Blanc shear zone	6.86530	45.89639	1664	50	0.626	385	13.402	8243	6.680	3118	99	0.00	5.5±0.3	12.50±2.22	100	1.54±0.10	23
CGP26	Mont Blanc shear zone	6.85847	45.90031	1277	30	0.875	143	30.508	4986	6.970	3397	99	0.00	3.5±0.3	n.d.	n.d.	1.66±0.11	50
CGP27	Mont Blanc granite	6.90179	45.86937	3416	17	0.596	52	11.233	980	6.991	3397	99	0.00	6.6±1.0	n.d.	n.d.	1.44±0.08	19
CGP28	Mont Blanc granite	6.90695	45.85665	3213	41	0.437	77	8.508	1498	7.034	3397	100	0.00	6.4±0.8	n.d.	n.d.	1.49±0.13	14
CGP29	Mont Blanc granite	6.92781	45.84991	3403	35	1.108	180	19.638	3190	6.647	3118	98	0.02	6.7±0.5	n.d.	n.d.	1.39±0.12	32
CGP30	Mont Blanc granite	6.88758	45.87835	3750	32	0.807	92	14.940	1703	7.119	3397	96	0.01	6.8±0.8	13.59±1.59	45	1.41±0.06	21
CGP32	Mont Blanc granite	6.95043	45.82815	2121	24	0.853	82	16.281	1565	6.533	3196	98	0.00	6.1±0.7	n.d.	n.d.	1.48±0.11	28
CGP33	Mont Blanc granite	6.93877	45.83881	2733	26	1.095	110	20.106	2020	6.547	3196	100	0.00	6.3±0.6	n.d.	n.d.	1.44±0.09	48
CGP34	Mont Blanc granite	6.93978	45.83732	2620	16	0.625	42	10.951	736	6.562	3195	99	0.00	6.6±1.1	n.d.	n.d.	1.48±0.07	28
CGP35	Mont Blanc granite	6.94126	45.83397	2406	23	0.694	110	13.582	2154	6.576	3196	97	0.00	6.0±0.6	n.d.	n.d.	1.63±0.11	24
CGP36	Mont Blanc granite	6.94551	45.83235	2272	50	0.726	133	13.902	2545	6.590	3196	100	0.00	6.1±0.6	n.d.	n.d.	1.52±0.11	26
CGP37	Mont Blanc granite	7.04402	45.87163	1845	25	0.395	72	9.047	1649	6.604	3196	99	0.00	5.1±0.6	n.d.	n.d.	1.50±0.10	15
CGP38	Mont Chétif mylonite	6.96317	45.80246	1280	16	0.237	13	10.862	596	6.618	3196	96	0.00	2.6±0.7	n.d.	n.d.	1.44±0.11	20
CGP39	Helvetic Mesozoic sed.	6.91749	45.80622	1658	50	3.724	469	97.913	12330	6.632	3196	99	0.00	4.5±0.2	12.94±1.69	52	1.67±0.11	196
MRP 253	Mont Blanc granite	6.93345	45.84386	3310	9	1.040	23	16.963	375	7.077	3397	99	0.00	7.7±1.7	n.d.	n.d.	1.51±0.09	29

Latitude and longitude coordinates are given in the WGS 84 datum; ρs (ρi) are spontaneous (induced) track densities (10^5 tracks/cm^2); Ns (Ni) is number of counted spontaneous (induced) tracks; ρd is dosimeter track density (10^5 tracks/cm²); Nd is number of tracks counted on dosimeter; P(χ^2) is probability obtaining Chi-square value (χ^2) for n degree of freedom (where n is number of crystals minus 1); dispersion is a real number that is zero if all the data are identical, and increases as the data becomes more diverse; age ±1s is central age ±1 standard error [*Galbraith and Laslett*, 1993]; MTL is mean track length and SD the standard deviation of track length distribution; Dpar is etch pit diameter of fission tracks, averaged from 4 measurements per analysed grain, and reported here as average with standard deviation for all measured grains. Ages were calculated using zeta calibration method [*Hurford and Green*, 1983], glass dosimeter CN-5, and zeta value of 354.92 ± 7.03 yr/cm² (Glotzbach).

Table 2: Composition of measured apatite samples from the Mont Blanc massif and from Durango apatite, with averages from totally 208 electron microprobe analyses.

Sample	n	F		Cl		OH (calc.)	SiO_2		Ce_2O_3		SrO		P_2O_5		CaO		Σ	Σ corrected	Dpar
		Oxide	Ion	Oxide	Ion	Ion	Oxide	Ion	Oxide	Ion	Oxide	Ion	Oxide	Ion	Oxide	Ion			
CGP22	10	3.34±0.20	0.89±0.05	0.01±0.01	0.00±0.00	0.11±0.05	0.13±0.10	0.01±0.01	0.08±0.06	0.00±0.00	0.02±0.02	0.00±0.00	42.65±0.74	3.03±0.02	54.66±0.35	4.91±0.04	100.89±1.11	99.48±1.05	1.58±0.12
CGP23	10	3.39±0.15	0.90±0.04	0.05±0.03	0.01±0.00	0.09±0.04	0.02±0.01	0.00±0.00	0.09±0.02	0.00±0.00	0.02±0.02	0.00±0.00	44.44±0.35	3.09±0.01	54.14±0.16	4.77±0.03	102.15±0.41	100.71±0.39	1.58±0.11
CGP24	10	3.38±0.12	0.90±0.03	0.07±0.02	0.01±0.00	0.09±0.03	0.03±0.02	0.00±0.00	0.08±0.02	0.00±0.00	0.02±0.02	0.00±0.00	44.96±0.34	3.11±0.01	53.99±0.19	4.72±0.02	102.53±0.50	101.09±0.47	1.56±0.11
CGP25	10	3.54±0.21	0.94±0.05	0.03±0.01	0.00±0.00	0.06±0.05	0.02±0.01	0.00±0.00	0.07±0.01	0.00±0.00	0.03±0.01	0.00±0.00	45.71±0.37	3.13±0.01	53.81±0.37	4.67±0.03	103.22±0.54	101.72±0.52	1.54±0.10
CGP26	10	3.29±0.39	0.87±0.10	0.04±0.02	0.01±0.00	0.12±0.10	0.02±0.01	0.00±0.00	0.06±0.02	0.00±0.00	0.02±0.02	0.00±0.00	45.37±1.11	3.16±0.06	51.92±1.47	4.58±0.14	100.72±1.09	99.33±1.13	1.66±0.11
CGP27	17	3.87±0.25	1.03±0.07	n.d.	0.00±0.00	-0.03±0.07	0.23±0.34	0.02±0.03	0.21±0.05	0.01±0.00	0.01±0.01	0.00±0.00	44.27±0.67	3.08±0.02	53.75±0.52	4.74±0.04	102.35±0.97	100.71±0.89	1.44±0.08
CGP28	10	3.74±0.18	0.99±0.05	n.d.	0.00±0.01	0.01±0.05	0.22±0.08	0.02±0.02	0.20±0.04	0.01±0.00	n.d.	0.00±0.00	42.26±0.56	3.05±0.02	52.71±0.16	4.82±0.04	99.12±0.67	97.55±0.62	1.49±0.13
CGP29	10	4.19±1.06	1.11±0.27	0.01±0.01	0.00±0.02	-0.11±0.27	0.31±0.22	0.03±0.02	0.30±0.16	0.01±0.01	n.d.	0.00±0.00	42.99±1.15	3.07±0.03	52.57±0.65	4.76±0.05	100.39±1.46	98.62±1.30	1.39±0.12
CGP30	10	4.06±0.13	1.08±0.04	n.d.	0.00±0.03	-0.08±0.04	0.41±0.28	0.03±0.02	0.33±0.13	0.01±0.00	n.d.	0.00±0.00	43.62±0.74	3.06±0.02	53.79±0.53	4.78±0.04	102.22±0.92	100.51±0.88	1.41±0.06
MRP 253	8	3.46±0.23	0.93±0.07	0.01±0.01	0.00±0.04	0.07±0.07	0.25±0.17	0.02±0.01	0.13±0.07	0.00±0.00	0.02±0.02	0.00±0.00	42.81±1.19	3.05±0.05	52.89±1.06	4.82±0.1	99.56±1.88	98.10±1.86	1.51±0.09
PK 650	6	3.52±0.15	0.93±0.04	0.02±0.00	0.00±0.05	0.06±0.04	0.02±0.01	0.00±0.00	0.06±0.02	0.00±0.00	0.03±0.01	0.00±0.00	45.45±0.38	3.12±0.01	54.20±0.22	4.7±0.02	103.29±0.54	101.81±0.51	1.50±0.12
PK 1150	8	3.54±0.10	0.94±0.03	0.01±0.01	0.00±0.06	0.06±0.03	0.01±0.01	0.00±0.00	0.10±0.01	0.00±0.00	n.d.	0.00±0.00	44.91±0.18	3.10±0.01	54.07±0.24	4.73±0.02	102.65±0.29	101.16±0.28	1.50±0.11
PK 4250	7	4.15±0.54	1.23±0.35	n.d.	0.00±0.07	-0.24±0.35	0.46±0.35	0.04±0.03	0.19±0.08	0.01±0.00	n.d.	0.00±0.00	41.73±1.15	3.00±0.04	53.01±0.81	4.89±0.06	99.56±1.98	97.81±1.88	1.31±0.10
PK 5710	8	4.21±0.16	1.12±0.04	n.d.	0.00±0.08	-0.12±0.04	0.22±0.18	0.02±0.02	0.18±0.06	0.01±0.00	n.d.	0.00±0.00	42.40±0.49	3.02±0.02	54.33±0.39	4.9±0.03	101.34±0.64	99.57±0.61	1.45±0.10
1500	9	3.74±0.26	0.99±0.07	n.d.	0.00±0.09	0.01±0.07	0.20±0.18	0.02±0.02	0.14±0.05	0.00±0.00	0.02±0.01	0.00±0.00	43.53±0.84	3.06±0.02	54.28±0.45	4.82±0.05	101.91±1.40	100.33±1.31	1.37±0.16
2170-2113	10	3.40±0.12	0.90±0.03	0.02±0.00	0.00±0.10	0.09±0.03	0.02±0.01	0.00±0.00	0.09±0.02	0.00±0.00	n.d.	0.00±0.00	43.48±0.34	3.09±0.01	52.88±0.31	4.76±0.02	99.89±0.59	98.45±0.57	1.51±0.10
2903	8	3.34±0.14	0.89±0.04	0.01±0.01	0.00±0.11	0.11±0.04	0.14±0.06	0.01±0.00	0.15±0.07	0.00±0.00	n.d.	0.00±0.00	45.76±0.44	3.13±0.01	53.79±0.45	4.65±0.03	103.19±0.74	101.78±0.69	1.51±0.14
3783	6	3.80±0.26	1.01±0.07	n.d.	0.00±0.12	-0.01±0.07	0.64±0.37	0.05±0.03	0.21±0.10	0.01±0.00	n.d.	0.00±0.00	43.55±0.65	3.05±0.02	53.77±0.52	4.77±0.03	101.98±0.85	100.38±0.77	1.30±0.15
4630	11	4.00±0.13	1.06±0.05	n.d.	0.00±0.13	-0.06±0.05	0.24±0.20	0.02±0.01	0.14±0.12	0.00±0.00	n.d.	0.00±0.00	45.52±0.74	3.12±0.02	53.61±0.57	4.65±0.03	103.51±1.06	101.83±1.04	1.31±0.15
5406	10	4.09±0.29	1.09±0.07	0.01±0.00	0.00±0.14	-0.09±0.07	0.25±0.06	0.02±0.02	0.17±0.04	0.01±0.00	n.d.	0.00±0.00	41.43±0.52	2.99±0.01	54.36±0.44	4.97±0.03	100.31±1.07	98.59±0.99	1.51±0.13
Durango	20	3.61±0.09	0.95±0.03	0.41±0.02	0.06±0.00	-0.01±0.03	0.48±0.05	0.04±0.00	0.71±0.04	0.02±0.00	0.05±0.02	0.00±0.00	42.78±0.75	3.04±0.02	53.46±0.33	4.8±0.05	101.64±0.81	100.52±0.34	1.63±0.11

Chemical compostion in oxide weigth percent and numer of atoms per formula unit (apfu). n is the number of measurements; n.d. means not detected, with detection limits in ppm: F 140, Cl 40, SiO_2 100,Ce_2O_3 180, SrO 170, P_2O_5 470, CaO 105; * corrected for OH^- anions.

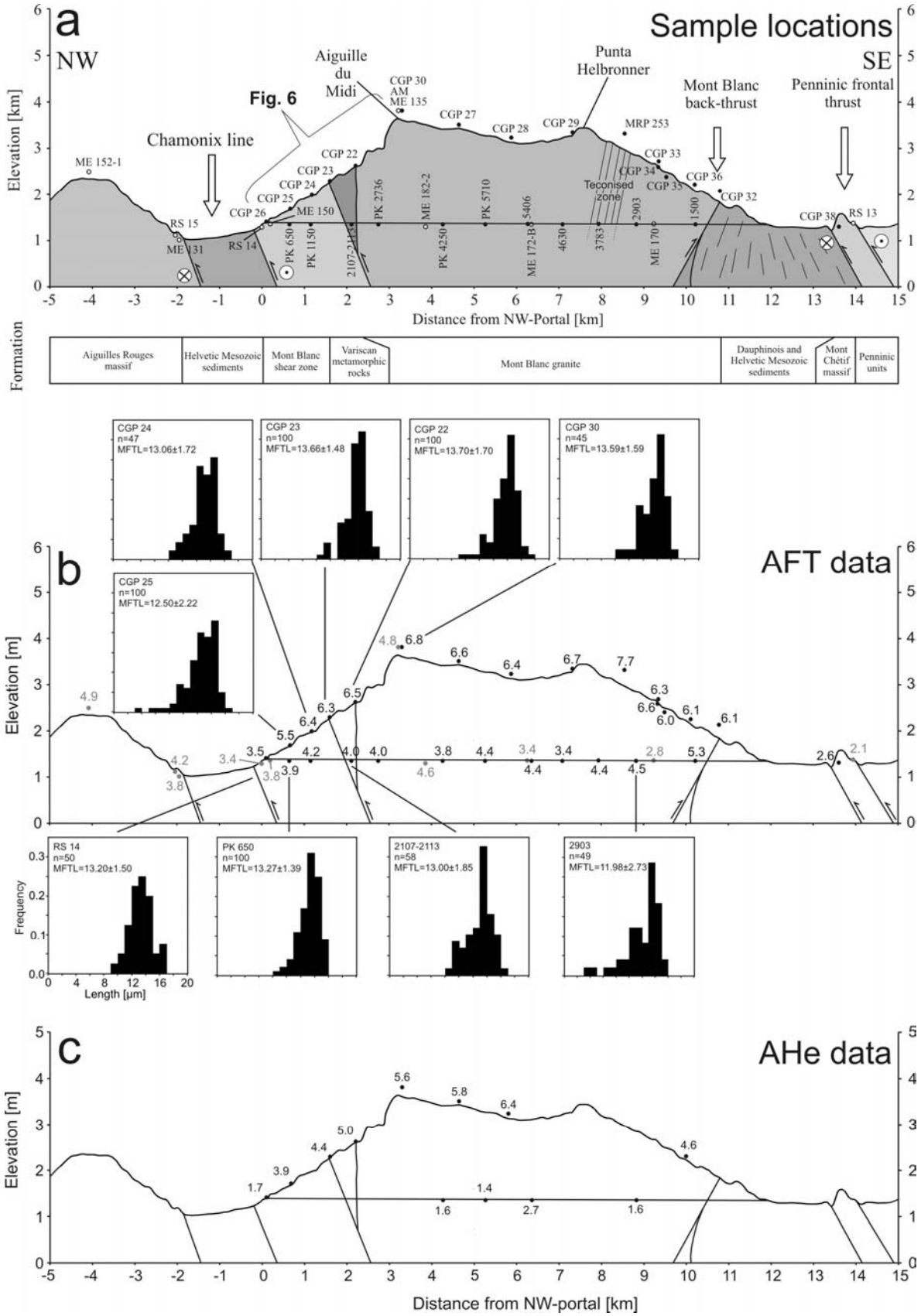

Figure 3: (a) Geological profile along the MB tunnel with own (black dots) and published (open circles) samples [*Carpéna*, 1992; *Seward and Mancktelow*, 1994, *Rahn,* 2001; *Leloup et al.*, 2005]. Samples located outside the transect are displayed in Figure 2. Structural interpretation is based on the study of *Leloup et al.* [2005]. (b) Published (grey) and new (black) AFT ages, and unprojected track length distributions. (c) AHe ages.

Table 3: Single-grain apatite (U-Th-[Sm])/He ages from the Mont Blanc tunnel and a surface line directly above the tunnel, and Durango.

Sample	AFT-age ±1σ [Ma]	Th [ng]	1σ error [%]	U [ng]	1σ error [%]	U [ppm]$	Sm [ng]	1σ error [%]	Th/U	Sm/U+Th	4He [ncc]	error [%]	TAU [%]§	uncorrected AHe age [Ma]*	Ft	corrected AHe age [Ma]	AHe error [Ma]		average AHe age ± error [Ma]#
CGP 22#3	6.5±0.3	0.0786	2.3	0.1089	2.3	21	n.d.	n.d.	0.7	n.d.	0.038	0.9	3.4	2.5	0.65	3.8	0.4		5.0±1.0
CGP 22#6		0.3288	3.2	0.3989	3.2	84	n.d.	n.d.	0.8	n.d.	0.255	0.9	4.6	4.4	0.75	5.9	0.6		
CGP 22#11		0.1264	2.7	0.2133	2.7	101	n.d.	n.d.	0.6	n.d.	0.104	0.9	3.9	3.5	0.69	5.1	0.5		
CGP 23#1	6.3±0.3	0.0078	2.0	0.1530	2.0	38	1.0194	2.0	0.1	6.3	0.067	1.2	3.7	3.6	0.76	4.5 (4.7)	0.5		4.4±0.3
CGP 23#8		0.0148	2.5	0.0926	2.5	25	n.d.	n.d.	0.2	n.d.	0.035	1.5	3.9	3.0	0.72	4.2	0.4		
CGP 23#9		0.0074	2.0	0.0737	2.0	29	0.5834	2.0	0.1	7.2	0.027	1.8	3.9	2.9	0.68	4.1 (4.3)	0.4		
CGP 23#10		0.0054	2.0	0.0424	2.0	16	0.3018	2.0	0.1	6.3	0.017	2.5	4.3	3.3	0.67	4.6 (4.9)	0.5		
CGP 23#11		0.0153	2.7	0.0947	2.7	11	n.d.	n.d.	0.2	n.d.	0.044	1.4	4.1	3.7	0.79	4.7	0.5		
CGP 25#2	5.5±0.3	0.0154	2.0	0.0417	2.0	11	0.2245	2.0	0.4	3.9	0.031	4.2	5.4	5.8	0.71	7.8 (8.1)	0.9	e	3.9±0.8
CGP 25#3		0.0123	2.0	0.0300	2.0	13	0.2455	2.0	0.4	5.8	0.009	7.9	8.6	2.3	0.67	3.3 (3.5)	0.4		
CGP 25#8		0.0032	2.0	0.0294	2.0	14	0.2115	2.0	0.1	6.5	0.011	8.9	9.6	3.1	0.66	4.5 (4.8)	0.6		
CGP 26#1	3.5±0.3	0.0162	2.7	0.1897	2.7	24	n.d.	n.d.	0.1	n.d.	0.036	1.3	4.0	1.5	0.78	2.0	0.2		1.7±0.5
CGP 26#2		0.0231	2.4	0.1946	2.4	24	n.d.	n.d.	0.1	n.d.	0.042	1.3	3.6	1.7	0.79	2.2	0.2		
CGP 26#3		0.0250	3.2	0.1523	3.2	18	n.d.	n.d.	0.2	n.d.	0.015	2.7	5.3	0.8	0.79	1.0	0.1		
CGP 26#6		0.0305	2.6	0.1085	2.6	18	n.d.	n.d.	0.3	n.d.	0.015	2.7	4.5	1.1	0.76	1.4	0.2		
CGP 27#4	6.6±1.0	0.0344	2.0	0.0094	2.0	8	0.5371	2.0	3.7	12.3	0.022	1.0	3.6	10.3	0.58	14.2 (17.8)	1.5	e	5.8±0.6
CGP 27#7		0.0581	2.2	0.1587	2.2	82	n.d.	n.d.	0.4	n.d.	0.131	0.9	3.2	6.3	0.72	8.7	0.9	e	
CGP 27#13		0.0924	2.0	0.0298	2.0	41	0.8817	2.0	3.1	7.2	0.022	1.0	3.6	3.5	0.56	5.4 (6.2)	0.6		
CGP 27-2#2		0.0237	2.0	0.0055	2.0	4	0.3322	2.0	4.3	11.4	0.018	1.0	3.6	13.5	0.59	18.3 (22.8)	1.9	e	
CGP 27-2#4		0.0319	2.0	0.0112	2.0	4	0.7052	2.0	2.8	16.4	0.012	10.0	10.6	5.3	0.67	6.1 (8.0)	0.9		
CGP 28#2	6.4±0.8	0.0602	3.9	0.0174	3.9	9	n.d.	n.d.	3.5	n.d.	0.038	4.8	7.3	9.9	0.64	15.5	1.8	e	6.4±0.8
CGP 28#5		0.1399	3.2	0.0523	3.2	23	n.d.	n.d.	2.7	n.d.	0.042	4.5	6.4	4.1	0.64	6.4	0.8		
CGP 28#6		0.0846	3.7	0.0240	3.7	11	n.d.	n.d.	3.5	n.d.	0.041	4.8	7.1	7.6	0.64	11.9	1.4	e	
CGP 30#1	6.8±0.8	0.1860	3.5	0.0502	3.5	19	n.d.	n.d.	3.7	n.d.	0.079	2.8	5.7	7.0	0.69	10.1	1.2	e	5.6±0.7
CGP 30#3		0.1533	2.7	0.0525	2.7	25	n.d.	n.d.	2.9	n.d.	0.061	3.5	5.2	5.7	0.67	8.5	1.0	e	
CGP 30#7		0.1670	4.1	0.0493	4.1	39	n.d.	n.d.	3.4	n.d.	0.037	3.9	7.0	3.4	0.61	5.6	0.7		
CGP 36#1	6.1±0.6	0.0020	2.0	0.0041	2.0	2	0.0466	2.0	0.5	7.7	0.022	1.1	3.6	40.2	0.68	54.6 (59.1)	5.6	e	4.6±0.8
CGP 36#5		0.0528	2.0	0.0248	2.0	16	0.6247	2.0	2.1	8.0	0.016	1.3	3.7	3.5	0.59	5.2 (6.0)	0.5		
CGP 36#18		0.0858	2.0	0.0385	2.0	11	1.4371	2.0	2.2	11.6	0.027	1.1	3.6	3.8	0.72	4.4 (5.3)	0.5		
CGP 36#20		0.0768	2.0	0.0479	2.0	20	0.9682	2.0	1.6	7.8	0.021	1.1	3.6	2.6	0.67	3.5 (3.9)	0.4		
CGP 36#23		0.0491	2.0	0.0287	2.0	20	0.5011	2.0	1.7	6.4	0.018	1.2	3.7	3.8	0.68	5.1 (5.6)	0.5		
PK 4250#1	3.8±0.7	0.1342	3.5	0.0427	3.5	21	n.d.	n.d.	3.1	n.d.	0.015	8.8	10.1	1.6	0.63	2.6	0.3		1.6±0.1
PK 4250#2		0.0694	5.1	0.0225	5.1	14	n.d.	n.d.	3.1	n.d.	0.004	31.1	31.9	0.9	0.61	1.5	0.5		2.8±0.2
PK 4250#8		0.1121	3.3	0.0334	3.3	27	n.d.	n.d.	3.4	n.d.	0.007	18.1	18.7	1.0	0.6	1.7	0.3		
PK 4250#4		0.1265	2.0	0.0378	2.0	20	1.1176	2.0	3.3	6.8	0.009	1.3	3.7	1.1	0.65	1.5 (1.7)	0.2		
PK 4250#12		0.0295	2.0	0.0082	2.0	5	0.5526	2.0	3.6	14.7	0.004	29.7	29.9	2.3	0.62	2.9 (3.7)	0.9		
PK 5710#1	4.4±1.1	0.0513	2.0	0.0175	2.0	17	0.8269	2.0	2.9	12.0	0.003	13.4	13.8	0.8	0.67	0.9 (1.1)	0.2		1.4±0.6
PK 5710#3		0.1303	2.0	0.0674	2.0	52	0.8118	2.0	1.9	4.1	0.015	2.8	4.5	1.2	0.66	1.8 (1.9)	0.2		
PK 5710#7		0.0773	2.0	0.0221	2.0	17	0.8187	2.0	3.5	8.2	0.017	2.4	4.2	3.6	0.69	4.5 (5.2)	0.5	e	
5406#2	4.4±.08	0.0935	5.2	0.0348	5.2	21	n.d.	n.d.	2.7	n.d.	0.011	1.2	7.5	1.6	0.64	2.5	0.3		2.7±0.2
5406#5		0.1169	3.4	0.0448	3.4	21	n.d.	n.d.	2.6	n.d.	0.026	1.0	5.0	2.9	0.67	4.4	0.5		4.3±0.2
5406#6		0.0407	4.9	0.0182	4.9	12	n.d.	n.d.	2.2	n.d.	0.009	4.1	8.0	2.8	0.63	4.5	0.5		
5406#8		0.0981	3.6	0.0422	3.6	21	n.d.	n.d.	2.3	n.d.	0.015	2.8	5.8	1.9	0.66	2.8	0.3		
5406-2#1		0.0747	2.0	0.0297	2.0	21	1.1380	2.0	2.5	10.9	0.017	1.7	3.9	3.0	0.61	4.1 (4.9)	0.4		
5406-2#5		0.0525	2.0	0.0350	2.0	21	0.9558	2.0	1.5	10.9	0.011	2.2	4.1	2.0	0.61	2.8 (3.3)	0.3		
2903#1	4.5±0.6	0.0348	5.1	0.0181	5.1	13	n.d.	n.d.	1.9	n.d.	0.010	2.4	7.6	3.1	0.65	4.8	0.6	e	1.6±0.2
2903#6		0.0321	4.4	0.0162	4.4	10	n.d.	n.d.	2.0	n.d.	0.012	2.1	6.5	4.2	0.64	6.5	0.8	e	
2903#12		0.0402	2.5	0.0196	2.5	12	n.d.	n.d.	2.0	n.d.	0.003	6.1	7.1	1.0	0.63	1.6	0.2		
Durango#1		4.1242	2.0	0.2231	2.0	n.d.	2.8200	2.0	18.5	0.6	4.327	0.9	3.6	29.2	1.00	29.2 (29.8)	0.3		29.4±1.5
Durango#2		4.6434	2.0	0.2570	2.0	n.d.	3.5023	2.0	18.1	0.7	4.811	0.9	3.6	28.7	1.00	28.7 (29.3)	0.3		
Durango#3		1.7037	2.0	0.0856	2.0	n.d.	1.3701	2.0	19.9	0.8	1.911	0.9	3.6	31.5	1.00	31.5 (32.3)	0.4		
Durango#4		4.6607	2.0	0.2220	2.0	n.d.	3.7101	2.0	21.0	0.8	4.598	1.0	3.6	28.0	1.00	28.0 (28.6)	0.3		

$ U concentration was estimated based on the determined crystal volume and measured U content, assuming an apatite density of 3.2 g/cm³; § 1σ total analytical error; * For aliquots with Sm measurements single-grain (U-Th)/He (in brackets) and (U-Th-Sm)/He ages are reported; # Average AHe age with standard deviation reported for samples with more than one reproducing single-grain AHe ages, otherwise single-grain AHe ages with total analytical error are reported; n.d. not determined; e excluded age, for details see text.

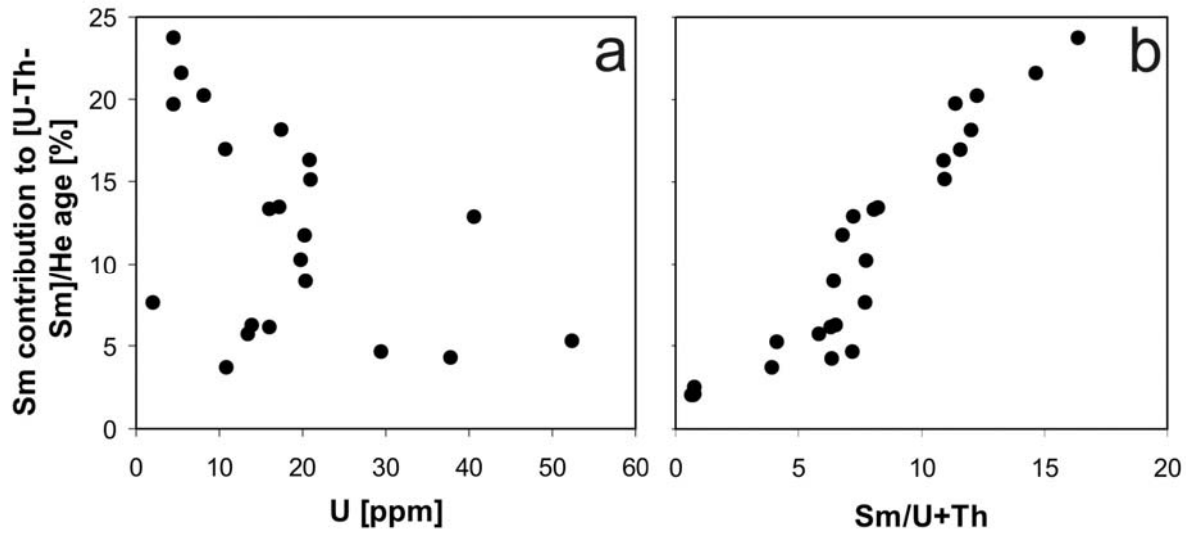

Figure 4: Percentage of Sm contribution to single grain apatite (U-Th-Sm)/He ages as a function of U concentration (a) and the ratio of Sm/U+Th (b).

5 Interpretation

Our AFT ages along the MB tunnel transect show some discrepancies with the data of *Leloup et al.* [2005]. The majority of their presented AFT ages agree well with those from other studies and our data, especially in the NW transect. However, our AFT data reveal slightly increasing ages to the southeast, whereas *Leloup et al.* [2005] report a trend to younger ages toward the southeast. Our sample from the Aiguille du Midi (CGP 30) yielded an AFT age of 6.8±0.8 Ma, which differs significantly from their published age of 4.8±0.8 Ma [*Leloup et al.*, 2005] from the same location. This discrepancy may be explained by poor sample quality and low U content (Ed Sobel, personal communication 2007). As our dataset is more densely positioned and show lower analytical errors, the data of *Leloup et al.* [2005] are not included in our interpretation:

(1) Along the whole analyzed section, we find no detectable jump in ages across fault structures. This suggests that none of the crossed faults experienced significant vertical movements since ~4 Ma, see detailed discussion below (section 7.1).

(2) AFT and AHe ages along the tunnel show no correlation with the topography above (Figure 5). This indicates that the closure isotherms of the AFT and the AHe systems were flat-lying, when the samples cooled through the apatite fission track partial annealing zone (APAZ) and the helium partial retention zone (PRZ). Accordingly, no corrections for exhumation rates derived from age elevation relations should be necessary. The problem of isotherm perturbation is further discussed below (section 7.2).

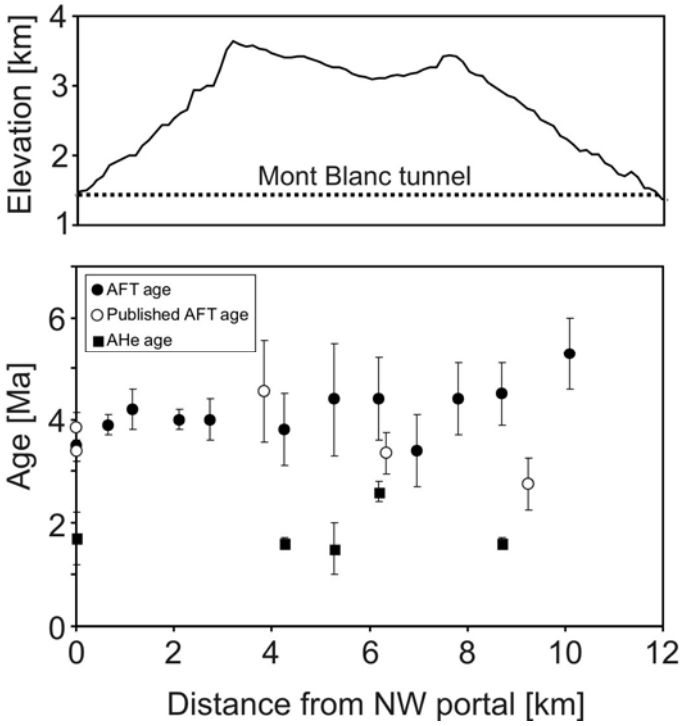

Figure 5: AFT ages and AHe ages along the MB tunnel and corresponding topography.

(3) AFT and AHe ages from the MB massif (Figure 3), spanning a total vertical distance of ~2.5 km, are positively correlated with sample elevations. The AER plot of the more densely sampled NW MB massif shows a break-in-slope at ~6 Ma and 2 km for the AFT data (Figure 6), separating an upper part characterized by a steep slope from a lower part characterized by a flat slope. The upper part gives an exhumation rate of 2.5±0.5 km/Ma before ~6 Ma, in line with relatively unshortened MTL (>13.6 µm). AHe and AFT ages for the highest part of the profile (CGP 27, 28 and 30) are similar (AFT: 6.4-6.8 Ma and AHe: 5.6-6.4 Ma), which also argues for rapid cooling through the temperature range between ~110°C and 40°C before ~6 Ma. Surface AHe ages show a concave-up trend with elevation, which typically developed after a fast exhumation event [*Wolf et al.*, 1998].

Samples between 2.0 km and 1.6 km (below the break-in-slope) yielded MTL between 13.06 and 12.50 µm, indicating that this part of the AER plot remained for a prolonged time (≥2.5 Myr, between ~6 and ~3.5 Ma) within the APAZ. The youngest (3.5±0.3 Ma) and lowest sample of the profile yielded again a longer MTL (13.2±1.5 µm), indicating that exhumation accelerated again after ~3 Ma. From this samples we derive exhumation rates >1 km /Myr between 3 Ma and present, assuming onset of rapid and continuous exhumation at ~3 Ma, an AFT closure temperature of 110°C and a geothermal gradient of 20-30°C/km. This estimation is in agreement with the corresponding AHe age (1.7±0.5 Ma).

We interpret our thermochronological data along the NW flank of the MB massif as an exhumed former APAZ (e.g., [*Gleadow and Fitzgerald*, 1987]), reflecting episodic exhumation with rapid exhumation (2.5±0.5 km/Ma) before ~6 Ma, followed by an episode of slow exhumation from ~6 to ~3 Ma, and again accelerated exhumation (>1 km/Ma) after ~3 Ma. This exhumation history is consistent with all presented thermochronological data along the MB transect, suggesting that this part as a whole was exhumed approximately at the same time with same rates. In addition, derived rates of exhumation agree well with those described by *Leloup et al.* [2005], although their data do not resolve the exact timing of exhumation.

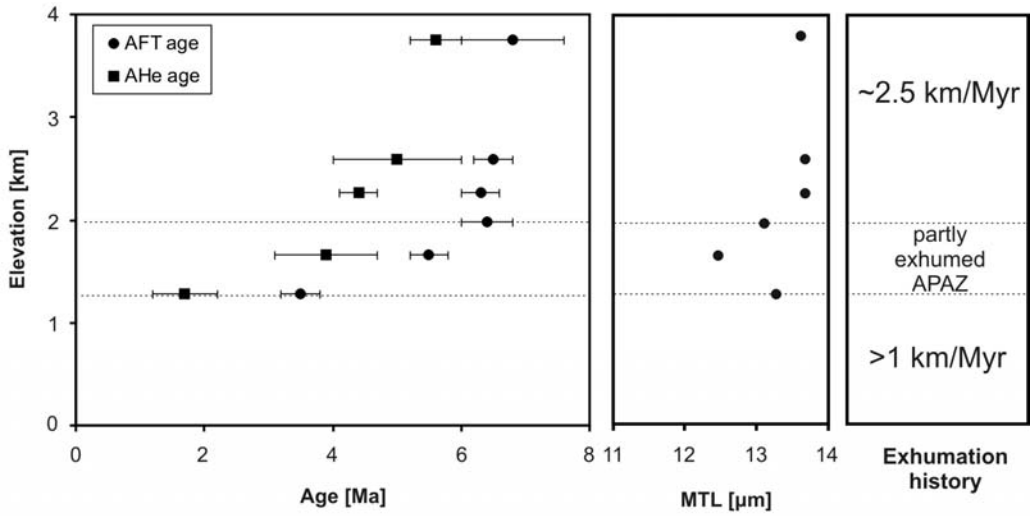

Figure 6: AFT and AHe ages, unprojected MTL, and deduced exhumation history from samples of the elevation profile along the NW flank of the MB massif.

(4) The trend to older AFT ages and shorter MTL toward the SE (Figure 5) suggests that the exhumed former APAZ, as documented along the profile at the NW flank, was slightly tilted (few hundred meters or less than 2°) toward the SE. AHe ages along the tunnel show no tilting, suggesting that tilting occurred between ~4 and ~1.5 Ma.

5.1 Thermal modeling

We tested whether all data (AFT ages, AHe ages and track length data) are consistent with the proposed exhumation history from the AER. TT paths were determined for each sample location on the elevation profile, which were then used for forward modeling of the corresponding thermochronological data and afterwards checked statistically (Figure 7). Only 25% of the modeled data statistically do not fit the measured data (GOF<0.05). This misfit can be completely attributed to the variability of single-grain AHe ages. The majority (75%), however, shows statistically acceptable or good results (GOF≥0.05), indicating that both fission track data and AHe ages are in accordance with an episodic exhumation history of the MB massif. Inverse modeling of the AFT and AHe data emphasized these findings, e.g. envelopes of tT paths with a GOF≥0.5 for sample CGP 25 show the same cooling history as predicted by the AER (Fig. 7).

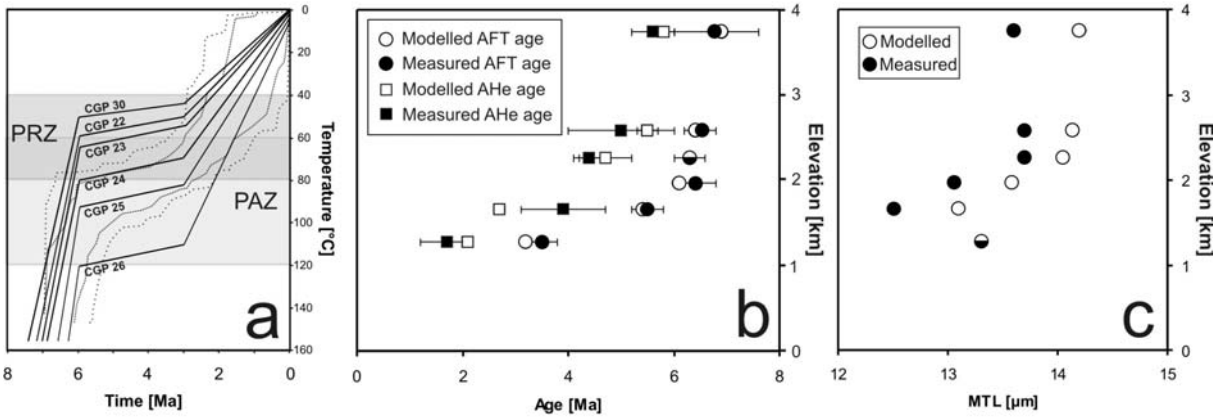

Figure 7: Predicted tT paths for individual sample locations of the elevation profile and envelopes (closely dashed line: GOF>0.5, broader dashed line: GOF>0.05) of inverse modeled tT path for sample CGP 25 (a), modeled and measured AFT ages, AHe ages (b) and unprojected MTL (c) from samples of the elevation profile along the NW flank of the MB massif.

6 Discussion

In this section we discuss our results in terms of the structural-kinematic and geodynamic evolution and estimate the paleo-relief of the MB massif.

6.1 Neogene activity along fault structures

The role of fault structures for the Late Neogene exhumation history of the MB massif was elaborated in two differing structural-kinematic evolution models by *Leloup et al.* [2005] and *Rolland et al.* [2007]. According to *Leloup et al.* [2005] two major shear zones control the exhumation of the MB massif. Between 12 and 4 Ma the MB massif was thrust top to the NW along the Mont Blanc shear zone (MBsz) onto the Aiguilles Rouges massif, with a total vertical displacement between 4 and 8 km. Evidence for this movement are the difference in the erosional levels of the Aiguilles Rouges and MB massif [*Leloup et al.*, 2005], and a jump in ZFT ages between the massifs (Figure 2). *Leloup et al.* [2005] proposed that after 4 Ma the MB massif was backthrust top to the SE along the Mont Blanc back thrust, because their AFT data show a trend to younger ages toward the thrust in the SE. Indeed, their age pattern is strongly influenced by a single 2.8 Ma age (Fig. 3b).
Our new data corroborate the cessation of activity along the MBsz after ~4 Ma, because AFT ages in the NW part of the tunnel all cluster around 4 Ma, with no offset across the MBsz (Figure 3). Regarding the age pattern along the tunnel, however, our data – which are more closely spaced and show lower analytical uncertainties than those of *Leloup et al.* [2005] – reveal exactly the opposite trend as their data, with AFT ages becoming slightly older toward the Mont Blanc back thrust in the SE. Therefore our data do not support the idea of southeastward directed backthrusting of the MB massif after 4 Ma. This does not mean that we doubt the structural interpretation of the MB back thrust proposed by *Leloup et al.* [2005], but the timing of activity is not well constrained. Maybe this structure was active before ~6 Ma during the observed fast exhumation event. Furthermore, we can exclude significant vertical displacements along other fault zones within the MB massif after ~6 Ma, because of the uniform age pattern along the tunnel and on top of the MB massif. We can also exclude continuous exhumation of the MB massif for the last ~16 Ma, as proposed by *Rolland et al.* [2007], because our data clearly indicate episodic exhumation of the MB massif during the last 6.5 Myr. We suggest that the main activity of faults within the massif and flanking the massif must have taken place before ~6 Ma, this includes also the activity of the MB back thrust.
We infer that Late Neogene exhumation of the MB massif was not caused by fault activity within the massif. The ZFT age pattern (Figure 2) [*Michalski and Soom*, 1990; *Seward and Mancktelow*, 1994; *Fügenschuh and Schmid*, 2003] suggests NW thrusting of the MB massif along fault structures between the MB and Aiguilles Rouges massifs, and probably also SE thrusting along the MB back thrust. Young activity of the PFT is evidenced by AFT ages of 2.8 Ma (CGP 38) and 2.1 Ma [*Seward and Mancktelow*, 1994, Sample RS 13], obtained for two samples from a tectonic slice (Mont Chétif massif) within the PFT (for location, see Figure 3). In line with structural investigations [*Perello et al.*, 1999], Fügenschuh (personal communication, 2007) proposed that the Mont Chétif massif was probably squeezed out by transpressional dextral movements along the PFT.

6.2 Implications for the perturbation of isotherms

In areas with pronounced relief the shallow isotherms may be perturbed, following the topography in a damped fashion. The isotherms become compressed below valleys and

widened below ridges [e.g., *Stüwe et al.*, 1994]. This effect may influence the interpretation of low-temperature thermochronological results, causing an overestimation of exhumation rates derived from AER [*Craw et al.*, 1994; *Stüwe et al.*, 1994; *Mancktelow and Grasemann*, 1997; *House et al.*, 1998, 2001; *Stüwe and Hintermüller*, 2000; *Braun*, 2002; *Foeken et al.*, 2007]. On the other hand, warping of isotherms provides the unique potential to gather information about the paleo-relief evolution [*House et al.*, 1998, 2001; *Braun*, 2002; *Foeken et al.*, 2007]. Ages of samples collected at the same elevation can be used to reconstruct the paleo-shape of the critical isotherm [*House et al.*, 1998]. Whether or not isotherms are perturbed depends on different geological and geomorphic parameters, such as relief amplitude and wavelength, or exhumation rate.

In this study we sampled the nearly horizontal MB tunnel (1330±50 m), which runs under pronounced topography characterized by a wavelength of ~14 km and a relief of ~3 km (Figure 3). For such a topography, *Stüwe et al.* [1994] suggested a perturbation effect on the 100°C isotherm in the range of 0.2 and 0.8 km for exhumation rates of 0.5 and 1 km/Myr, respectively. The corresponding perturbation of the 70°C isotherm is between 0.8 and 1.5 km, calculated with the program 'TERRA' [*Ehlers et al.*, 2005]. Thus for an exhumation rate of 1 km/Myr the difference in AFT age along the tunnel should be less than 1 Myr, probably hidden within the 1σ error of the corresponding samples (0.2-1.1 Ma). In fact, the AFT age pattern along the tunnel shows no correlation with overburden; ages vary around 4 Ma (3.8±0.7 to 5.3±0.7 Ma) (Figure 5).

AHe ages within the tunnel are between 1.5 and 2.6 Ma. Although only few AHe ages are available, it can be concluded that these are not correlated with overburden (Figure 5). Except one age (2.6 Ma) in the centre of the tunnel, all ages are in the narrow range of 1.4 and 1.7 Ma. This implies that the PRZ was approximately flat at that time. Sample CGP 26, from the NW portal, yields a 'surprisingly' young age of 1.7 Ma for a sample located in the valley. Under steady state topography we would expect to observe the youngest ages below ridges and the oldest ages under valleys [*Stüwe et al.*, 1994]. The inconsistency between the uniform age pattern along the tunnel and the suggested age difference (~1.5 Myr, for a perturbation of 0.8-1.5 km of the 70°C isotherm) expected under steady state topography demands a further explanation.

Evidently, there is no measurable perturbation of the paleo-isotherms as induced by recent/steady state topography of the MB massif. Possible explanations are: (1) The paleo-topography changed from flat to the recent one during the last 4 Ma, implying very fast incision of the present-day valleys. (2) The positions of isotherms are the result of advective heat flow controlled by fault movements, which led to fast exhumation of the valleys. We exclude this explanation, because no age jumps are visible along the sampled transect. (3) Convective heat flow, as it is typical for pronounced topography, led to an overall reduction of the perturbation of the isotherms, and may cause flat isotherms [*Whipp and Ehlers*, 2007]. At present cold waters penetrates a tectonized zone exposed at high elevations near Punta Helbronner in the southeastern MB massif (for location see Fig. 3), resulting in a downward movement of near surface isotherms in the vicinity of this zone [*Maréchal et al.*, 1999]. Both AFT and AHe data do not show any correlation with this infiltration zone (Fig. 3), emphasizing the assumption that this heat flow regime is a very young feature (<12 ka) [*Maréchal et al.*, 1999].

Therefore we suggest that flat isotherms are the result of a post-4 Ma or probably even post-1.5 Ma relief formation, which we discuss below (section 7.4).

6.3 Late exhumation pulses of the ECM

The exhumation histories of the MB massif and other ECM for the last 8 Myrs were correlated with regional geodynamic events. Exhumation rates from other ECM were taken

from a compilation by *Bogdanoff et al.* [2000] and replenished by new data [*Rahn*, 2001; *Reinecker et al*., pending successful revision].
Figure 8 shows accordance and discrepancies of calculated exhumation rates of the ECM. Striking features are: (1) high exhumation rates (~2.5 km/Myr) of the MB massif before ~6 Ma, (2) generally slow exhumation (≤0.5 km/Myr) of all ECM between ~6 and ~3 Ma and (3) acceleration in exhumation rates at ~3 Ma to values around 1 km/Myr, except for the Gotthard massif. We discuss possible geodynamic processes, which are able to explain the observed exhumation histories of the ECM, as follows:
(1) The MB massif experienced rapid exhumation before ~6 Ma. At the same time, other ECM show slow exhumation (Figure 8). Deduced exhumation rates from a compilation of published fission track ages in the central and Western Alps partly show an increase at the same time but the rates are clearly lower; values range from 0.2 to 0.7 km/Myr [*Vernon et al*., 2008]. This suggests that the observed rapid exhumation event before ~6 Ma is thus restricted to the MB area.
The continuous SW movement of the internal Penninic units SE of the MB massif bounded by the Rhône-Simplon fault zone [*Grasemann and Mancktelow*, 1993; *Steck and Hunziker*, 1994] led to dextral movements along the W-SW continuation of the Rhône-Simplon normal fault (Chamonix line and PFT, see Figure 1) [*Perello et al.*, 1999; *Leloup et al.*, 2005] and slightly transpressional movements in the MB massif [*Bistacchi and Massironi*, 2000; *Bistacchi et al.*, 2000; *Seward and Mancktelow*, 1994].
Leloup et al. [2005] suggest top to NW thrusting between the Aiguilles Rouges and MB massifs between ~12 and ~4 Ma, visible in a jump in ZFT ages (Figure 2). According to our data this event must have occurred prior to ~6 Ma. We favor a model in which transpressional movements led to vertical pop-up and rapid exhumation of the MB massif, resulting in NW thrusting between the Aiguilles Rouges and MB massifs and SE thrusting along the MB back thrust. Evidently, this structural-kinematic model needs to be reviewed by thermochronometers with higher closure temperatures, e.g. fission track or (U-Th)/He dating of zircons.
(2) All ECM are characterized by slow exhumation rates (≤0.5 km/Myr) between ~6 and ~3 Ma. *Willett et al.* [2006] suggested that increased sediment yield from the Alps was induced by the base-level drop caused by the Messinian salinity crisis between 5.59 and 5.5 Ma [*Krijgsman et al.*, 2002]. Maximum incision and erosion during this event and associated exhumation was suggested for the Southern Alps [*Willett et al.*, 2006]. *Cederbom et al.,* [2004] proposed that the increase in sediment flux to the forelands after ~5 Ma [*Kuhlemann*, 2000] was the result of a climate change with an increase in atmospheric moisture related to the intensification of the Atlantic Gulf Stream at 4.6 Ma [*Haug et al.*, 2005]. The thermochronological data from the ECM show no increase in exhumation rates that could be either attributed to the Messinian salinity crises or to an intensification of the Atlantic Gulf Stream. If these events had any influence on the Alpine erosion history its influence has been restricted to the other regions except the external Alps.
(3) Thermochronological data of all ECM, except for the Gotthard massif, suggest an acceleration in exhumation rates at ~3 Ma (Figure 8). At approximately the same time, the folding in the Jura Mountains ended [*Becker*, 2000], and global cooling led to extensive glaciation in the Northern Hemisphere starting at 2.8 Ma [e.g., *St. John and Krissek*, 2002; *Fauquette and Bertini*, 2003; *Lisiecki and Raymo*, 2005; *Klotz et al.*, 2006]. Probably glaciation in the Alps initiated at the same time, but certainly at 0.87 Ma widespread glaciation affected the whole alpine belt [*Muttoni et al.*, 2003; *Haeuselmann et al.*, 2007], resulting in increased sediment flux into the forelands [*Kuhlemann*, 2000]. Since the ECM were already uplifted to high mountainous elevations around 3 Ma [*Kuhlemann*, 2003], large glaciers formed early and led to deep incision and associated exhumation of the massifs during the last 3 Myrs, suggesting a climatic control for the acceleration in exhumation rates.

The Western Alps are characterized by orogen-parallel and orogen-perpendicular Neogene extensional movements (Figure 1) [*Sue et al.*, 2007, and references therein]. Most prominent are the normal displacements along the Rhône-Simplon fault [e.g., *Keller et al.*, 2006] and the reactivation of orogen-parallel thrusts (PFT, Briançonnais front, Internal Houiller fault) as faults with a normal component [e.g., *Malusà et al.*, 2005]. The exact timing of the change from orogen-parallel to orogen-perpendicular extension is not well constrained, however, based on ZFT and AFT ages *Fügenschuh and Schmid* [2003] suggest a reactivation of the Internal Houiller fault as a normal fault after 5 Ma, in accordance with a proposed change in the direction of extension in the Pliocene [*Sue et al.*, 2007]. All ECM except the Gotthard massif are located adjacent to major normal faults, and were thus subject to tectonic denudation/unroofing. This would explain why all westernmost ECM (Aar, Mont Blanc, Belledone, Pelvoux, Argentera) show an increase in exhumation rates at ~3 Ma. *Bogdanoff et al.* [2000] suggested that the activation of orogen-parallel normal faults caused the latest mainly Pleistocene cooling event.

We favor a model in which a combination of both forces, normal faulting <5 Ma and glaciation induced erosion <3 Ma led to enhanced exhumation of the ECM at ~3 Ma. Evidently, the controlling force (tectonic/climate) can differ in space, time and magnitude controlled by the local geology and geomorphology. For instance, the Gotthard massif is characterized by steady exhumation rates [*Schaer et al.*, 1975; *Wagner et al.*, 1977; *Glotzbach et al.,* 2008], unaffected by late Neogene orogen-perpendicular extension. Concerning the high elevation, deep carved valleys and the absence of vertical displacements along fault structures within and adjacent to the MB massif, we suggest that exhumation of the MB massif since ~3 Ma was most likely caused by glaciation induced erosion.

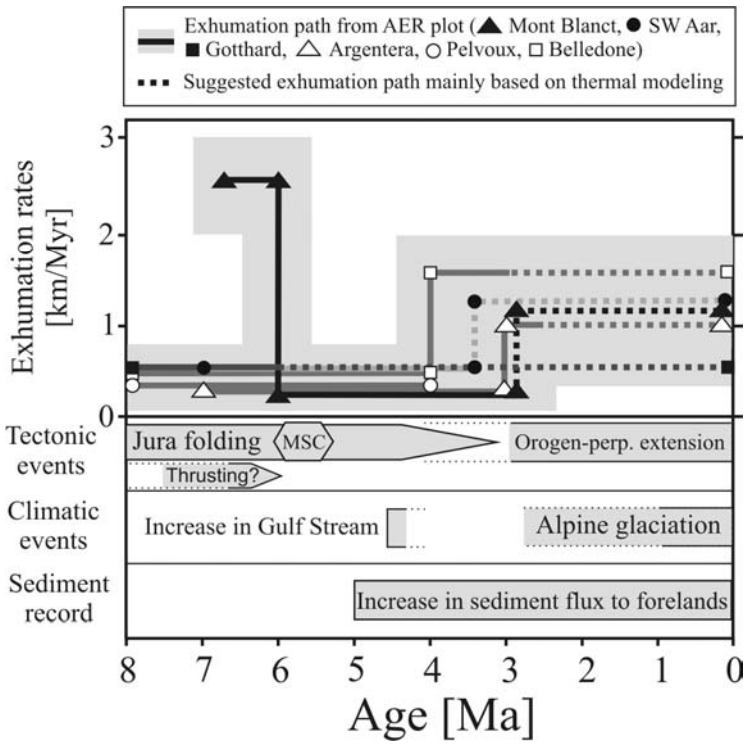

Fig. 8: Exhumation history of ECM and geodynamic events. Exhumation histories are deduced from AER plots of different authors: Mont Blanc (this study), Aar [*Reinecker et al.*, pending successful revision], Gotthard [*Wagner et al.*, 1977], Argentera [*Bogdanoff et al.*, 2000], Pelvoux [*Seward et al.*, 1999], Belledone [*Lelarge*, 1993]. Note that the given exhumation history owns an error in age of ±0.5 Ma (average 1σ error of used AFT ages). Timing of geodynamic events: MSC (Messinian salinity crisis) [*Krijgsman et al.*, 2002], Jura folding [*Becker*, 2000], orogen-perpendicular extension and normal faulting [*Fügenschuh and Schmid*, 2003; *Sue et al.*, 2007], Alpine glaciation [e.g., *St. John and Krissek*, 2002], increase in the Atlantic Gulf Stream [*Haug et al.,* 2005], increased sediment flux to forelands [*Kuhlemann*, 2000].

6.4 Relief evolution model for the Mont Blanc tunnel transect

Low-temperature thermochronology data are affected by surface processes, and therefore may provide indirect information on the paleo-relief and its evolution. Here we present a relief evolution model that is mainly based on the interpretation of the AER.
Samples CGP 27, 28 and 30 yield nearly identical AFT (6.4-6.8 Ma) and AHe ages (5.6-6.4 Ma) indicating rapid cooling through APAZ and PRZ. Rapid cooling is also supported by long MTL in sample CGP 30 (13.6±1.6 μm). We conclude that the currently high regions of the MB massif (elevations >3.4 km, e.g. Aiguille du Midi) were already exhumed to near-surface positions at around ~6 Ma. The upper boundary of the paleo-APAZ at ~6 Ma approximately corresponded to the position of the break in slope observed in the AER plot (Figure 6) at a present day elevation of ~2 km. Lower samples were within the APAZ at that time, while at ~6 Ma the MB summit was already cooled/exhumed to temperatures <40°C. The bottom of the present-day Chamonix valley, however, was then at temperatures >80°C, suggesting that the relief was less pronounced at ~6 Ma (Figure 9). The AER plot predicts slow exhumation from ~6 to ~3 Ma, indicating that recent relief along the sampled transect did not evolve prior to ~3 Ma. This is in accordance with flat-lying paleo-isotherms around 4 Ma (section 7.3, Figure 5). The timing of increased valley incision can be bracketed by the AFT age of 3.5 Ma and the AHe of 1.7 Ma for sample CGP 26, and an age of ~3 Ma is supported by thermal modeling (Fig. 7). Regarding the uniform AHe ages, which indicate flat isotherms around 1.5 Ma along the tunnel transect, a great fraction of relief formation must have occurred after ~1.5 Ma. We propose that enhanced valley incision is linked to the initiation of Alpine glaciation, which was most extensive since 0.87 Ma [*Muttoni et al.*, 2003; *Haeuselmann et al.*, 2007], but probably affected the MB massif since ~3 Ma.

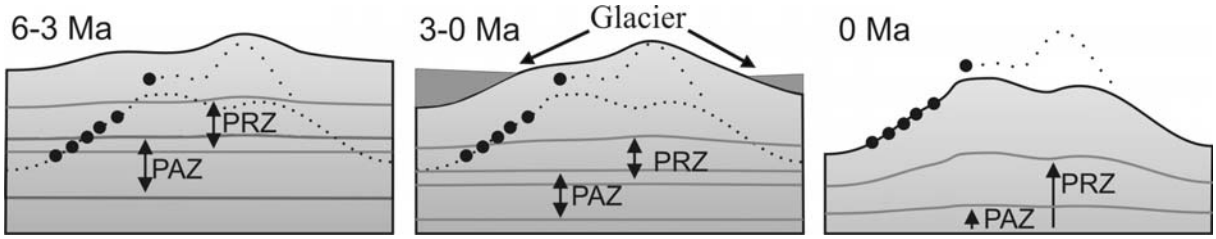

Figure 9: Relief evolution model for the MB tunnel transect. Black dots mark the sample locations of the elevation profile, fine dotted line corresponds to the recent topography along the transect and wider spaced dotted line is the topography across the MB summit.

7 Conclusions

Low-temperature thermochronological data on samples along the MB road tunnel transect reveals new insights in the thermal, structural-kinematic, and exhumation history as well as relief evolution of the MB massif. In addition, our new (U-Th-Sm)/He data strongly underlines the necessity of measuring Sm for AHe dating.
- Apatite (U-Th-Sm)/He dating show that ages are in average 12% younger than corresponding (U-Th)/He ages. Crystals with high Sm/U+Th ratios reveal up to 24% younger ages, demonstrating that Sm measurements are required for exact AHe age calculations.
- There is no measurable perturbation of paleo-isotherms due to topography along the sampled transect. Measured AFT and AHe age patterns along the MB tunnel are interpreted to be the result of a less pronounced paleo-relief between ~6 and ~1.5 Ma.

- Thermochronological data along the sampled transect show no jump in ages demonstrating that vertical displacement along major faults within the MB massif in Late Neogene time must have been small or absent.
- AFT and AHe data indicate episodic exhumation for the MB massif with fast exhumation before ~6 Ma, slow exhumation between ~6 and ~3 Ma, and accelerated exhumation since ~3 Ma.
- Comparisons with exhumation histories of other ECM reveal the following: (1) Localized fast exhumation of the MB massif prior to ~6 Ma was probably related to top to NW and minor top to SE thrusting, (2) slow exhumation rates between ~6 and ~3 Ma for all ECM indicating that the base level drop and rapid incision related to the Messinian salinity crisis at ~5 Ma, as reported for the Southern Alps, and an increase in atmospheric moisture at 4.6 Ma did not affect the ECM, and (3) late Neogene accelerated cooling and exhumation at ~3 Ma correlates with both the initiation of Alpine glaciation and ongoing normal displacements along orogen-parallel faults.
- We present a relief evolution model for the MB massif. Relief was less pronounced between ~6 and ~3 Ma, but became considerable enhanced by rapid valley incision related to climate change and Alpine glaciation after ~3 Ma and in particular after ~1.5 Ma.

Acknowledgments

This study was partly funded by the German Science Foundation (DFG), project SP 673/2-2. Gerlinde Höckh, Dorothea Mühlbayer-Renner, and Dagmar Kost (Universität Tübingen) are gratefully acknowledged for their help with mineral separation. Dr. Thomas Wenzel (Universität Tübingen) provided support during electron microprobe analysis. We thank the reviewers E. Sobel and P. van der Beek, and the associate editor T. Ehlers for their critical and constructive comments, which helped improving this manuscript.

References

Becker, A. (2000), The Jura Mountains - an active foreland fold-and-thrust belt?, *Tectonophysics*, 321, 381-406.

Bistacchi, A., E. Eva, M. Massironi, and S. Solarino (2000), Miocene to Present kinematics of the NW-Alps: evidences from remote sensing, structural analysis, seismotectonics and thermochronology, *J. Geodynamics*, 30, 205-228.

Bistacchi, A., and M. Massironi (2000), Post-nappe brittle tectonics and kinematic evolution of the north-western Alps: an integrated approach, *Tectonophysics*, 327, 267-292.

Bogdanoff, S., A. Michard, M. Mansour, and G. Poupeau (2000), Apatite fission track analysis in the Argentera massif: evidence of contrasting denudation rates in the External Crystalline Massifs of the Western Alps, *Terra Nova*, 12, 117-125.

Braun, J. (2002), Quantifying the effect of recent relief changes on age-elevation relationships, *Earth Planet. Sci. Lett.*, 200, 331-343.

Buiter, S. J. H., R. Govers, and M. J. R. Wortel (2002), Two-dimensional simulations of surface deformation caused by slab detachement, *Tectonophysics*, 354, 195-210.

Burtner, R. L., A. Nigrini, and R. A. Donelick (1994), Thermochronology of Lower Cretaceous source rocks in the Idaho-Wyoming thrust belt, *AAPG Bull.*, 78, 1613-1636.

Carlson, W. D., R. A. Donelick, and R. A. Ketcham (1999), Variability of apatite fission-track annealing kinetics: I. Experimental results, *Am. Mineral.*, 84, 1213-1223.

Carpéna, J. (1992), Fission Track Dating of Zircon: Zircons from Mont Blanc Granite (French-Italian Alps), *J Geol.*, 100, 411-421.

Cederbom, C. E., H. D. Sinclair, F. Schlunegger, and M. K. Rahn (2004), Climate-induced rebound and exhumation of the European Alps, *Geology*, 32, 709-712.

Champagnac, J. D., P. Molnar, R. S. Anderson, C. Sue, and B. Delacou (2006a), Quaternary erosion-induced isostatic rebound in the western Alps, *Geology*, 35, 195-198.

Champagnac, J. D., C. Sue, B. Delacou, P. Tricart, C. Allanic, and M. Burkhard (2006b), Miocene lateral extrusion in the inner western Alps revealed by dynamic fault analysis, *Tectonics*, 25, TC3014, doi:10.1029/2004TC001779.

Craw, D., P. O. Koons, D. Winslow, C. P. Chamberlain, and P. Zeitler (1994), Boiling fluids in a region of rapid uplift, Nanga Parbat Massif, Pakistan, *Earth Planet. Sci. Lett.*, 128, 169-182.

Danišík, M. (2005), Cooling history and relief evolution of Corsica (France) as constrained by fission track and (U-Th)/He thermochronology, *Tuebinger Geowissenschaftliche Arbeiten*, 72, 1-130.

Dunkl, I. (2000), Trackkey: a windows program for calculation and graphical presentation of fission track data, *Comput. Geosci.*, 28, 3-12.

Ehlers, T. A., T. Chaudhri, S. Kumar, C. W. Fuller, S. D. Willett, R. A. Ketcham, M. T. Brandon, D. X. Belton, B. P. Kohn, A. J. W. Gleadow, T. J. Dunai, and F. Q. Fu (2005), Computational tools for low-temperature thermochronometer interpretation, *Rev. Mineral. Geochem.*, 58, 589-622.

Ehlers, T. A., and K. A. Farley (2003), Apatite (U-Th)/He thermochronometry: methods and applications to problems in tectonic and surface processes, *Earth Planet. Sci. Lett.*, 206, 1-14.

England, P., and P. Molnar (1990), Surface uplift, uplift of rocks, and exhumation of rocks, *Geology*, 18, 1173-1177.

Farley, K. A. (2002), (U-Th)/He dating: Techniques, calibrations, and applications, *Rev. Mineral. Geochem.*, 47, 819-843.

Farley, K. A., R. A. Wolf, and L. T. Silver (1996), The effects of long alpha-stopping distances on (U-Th)/He dates, *Geochem. Cosmochim. Acta*, 60, 4223-4229.

Fauquette, S., and A. Bertini (2003), Quantification of the northern Italy Pliocene climate from pollen data: evidence for a very peculiar climate pattern, *Boreas*, 32, 361-369.

Foeken, J. P. T., C. Persano, F. M. Stuart, and M. ter Voorde (2007), Role of topography in isotherm perturbation: Apatite (U-Th)/He and fission track results from the Malta tunnel, Tauern Window, Austria, *Tectonics*, 26, TC3006, doi:10.1029/2006TC002049.

Frey, M., and R. Mählmann Ferreiro (1999), Alpine metamorphism of the Central Alps, *Schweiz. Mineral. Petrogr. Mitt.*, 79, 135-154.

Frisch, W. (1979), Tectonic progradation and plate tectonic evolution of the Alps, *Tectonophysics*, 60, 121-139.

Fügenschuh, B., and S. M. Schmid (2003), Late stages of deformation and exhumation of an orogen constrained by fission-track data: A case study in the Western Alps, *Geol. Soc. Am. Bul.*, 115, 1425-1440.

Galbraith, R. F., and G. M. Laslett (1993), Statistical models for mixed fission track ages, *Nucl. Tracks and Radiat. Meas.*, 21, 459-470.

Gallagher, K., R. Brown, and C. Johnson (1998), Fission Track analysis and its application to geological problems, *Annu. Rev. Earth Planet. Sci.*, 26, 519-572.

Gleadow, A. J. W. (1981), Fission-track dating methods: What are the real alternatives?, *Nucl. Tracks and Radiat. Meas.*, 5, 3-14.

Gleadow, A. J. W., and P. G. Fitzgerald (1987), Uplift history and structure of the Transantarctic Mountains: new evidence from fission track dating of basement apatites in the Dry Valleys area, southern Victoria Land, *Earth Planet. Sci. Lett.*, 82, 1-14.

Glotzbach, C., C. Spiegel, J. Reinecker, M. Rahn, and W. Frisch (2008), What perturbs isotherms? An assessment using fission track thermochronology and thermal modelling

along the Gotthard transect, Central Alps, in *Thermochronological methods: from paleotemperature constraints to landscape evolution models*, edited by Lisker et al., Geol. Soc. Spec. Publ., in press.

Grasemann, B., and N. S. Mancktelow (1993), Two-dimensional thermal modelling of normal faulting: the Simplon Fault Zone, Central Alps, Switzerland, *Tectonophysics*, 225, 155-165.

Haeuselmann, P., D. E. Granger, P.-Y. Jeannin, and S.-E. Lauritzen (2007), Abrupt glacial valley incision at 0.8 Ma dated from cave deposits in Switzerland, *Geology*, 35, 143-146.

Haug, G. H., A. Ganopolski, D. M. Sigman, A. Rosell-Mele, G. E. A. Swann, R. Tiedemann, S. L. Jaccard, J. Bollmann, M. A. Maslin, M. J. Leng, and G. Eglinton (2005), North Pacific seasonality and the glaciation of North America 2.7 million years ago, *Nature*, 433, 821-825.

House, M. A., B. P. Wernicke, and K. A. Farley (1998), Dating topography of the Sierra Nevada, California, using apatite (U-Th)/He ages, *Nature*, 396, 66-69.

House, M. A., B. P. Wernicke, and K. A. Farley (2001), Paleo-Geomorphology of the Sierra Nevada, California, from (U-Th)/He ages in apatite, *Am. J. Sci.*, 301, 77-102.

Hubard, M., and N. S. Mancktelow (1992), Lateral displacement during Neogene convergence in the western and central Alps, *Geology*, 20, 943-946.

Hurford, A. J., and P. F. Green (1982), A users' guide to fission track dating calibration, *Earth Planet. Sci. Lett.*, 59, 343-354.

Hurford, A. J., and P. F. Green (1983), The Zeta age calibration of fission-track dating, *Chem. Geol. (Isotope Geoscience Section)*, 41, 285-317.

Jouanne, F., Ménard, G. and X. Darmendrail (1995), Present-day vertical displacements in the north-western Alps and southern Jura Mountains: Data from leveling comparisons, *Tectonics*, 14, 606-616.

Kahle, H.-G. (1997), Recent crustal movements, geoid and density distribution; contribution from integrated satellite and terrestrial measurements, in *Results of NRP 20; deep structure of the Swiss Alps*, edited by O. A. Pfiffner, et al., pp. 251-259, Birkhaeuser Verlag, Basel.

Keller, L. M., B. Fügenschuh, M. Hess, B. Schneider, and S. M. Schmid (2006), Simplon fault zone in the western and central Alps: Mechanism of Neogene faulting and folding revisited, *Geology*, 34, 317-320.

Ketcham, R. A. (2005), Forward and inverse modelling of low-temperature thermochronology data, *Rev. Mineral. Geochem.*, 58, 275-314.

Ketcham, R. A., A. Carter, R. A. Donelick, J. Barbarand, and A. J. Hurford (2007a), Improved measurement of fission-track annealing in apatite using c-axis projection, *Am. Mineral.*, 92, 789-798.

Ketcham, R. A., A. Carter, R. A. Donelick, J. Barbarand, and A. J. Hurford (2007b), Improved modeling of fission-track annealing in apatite, *Am. Mineral.*, 92, 799-810.

Klotz, S., S. Fauquette, N. Combourieu-Nebout, D. Uhl, J.-P. Suc, and V. Mosbrugger (2006), Seasonality intensification and long-term winter cooling as a part of the Late Pliocene climate development, *Earth Planet. Sci. Lett.*, 241, 174-187.

Krijgsman, W., B.-V. M.-M., R. Flecker, F. J. Hilgen, T. J. Kouwenhoven, D. Merle, F. Orszag-Sperber, and J.-M. Rouchy (2002), The onset of the Messinian salinity crisis in the Eastern Mediterranean (Pissouri Basin, Cyprus), *Earth Planet. Sci. Lett.*, 194, 299-310.

Kuhlemann, J. (2000), Post-collisional sediment budget of circum-Alpine basins (Central Europe), *Mem. Ist. Geol. Mineral. Univ. Padova*, 52, 1-91.

Kuhlemann, J. (2003), Global Cenozoic relief formation and mountain uplift in convergent plate margins, *N. Jb. Geol. Palaeont. Abh.*, 230, 215-256.

Labhart, T. P. (1977), *Aarmassiv und Gotthardmassiv*, 173 pp., Gebr. Borntraeger, Berlin.

Lelarge, L. (1993), Thermochronogie par la méthode des traces de fission d'une marge passive (Dôme de Ponta Grossa, SE Brésil) et au sein d'une chaîne de collision (zone externe de l'Arc alpin, France), Unpublished thesis, Université Joseph Fourier, Grenoble.

Leloup, P. H., N. Arnaud, E. R. Sobel, and R. Lacassin (2005), Alpine thermal and structural evolution of the highest external crystalline massif: The Mont Blanc, *Tectonics*, 24, 1-26.

Lisiecki, L. E., and M. E. Raymo (2005), A Pliocene-Pleistocene stack of 57 globally distributed benthic δ18O records, *Paleoceanography*, 30, PA1003, doi:10.1029/2004PA001071.

Malusà, M. G., R. Polino, M. Zattin, G. Bigazzi, S. Martin, and F. Piana (2005), Miocene to Present differential exhumation in the Western Alps: Insights from fission track thermochronology, *Tectonics*, 24, TC3004, doi:10.1029/2004TC001782.

Mancktelow, N. S., and B. Grasemann (1997), Time-dependent effects of heat advection and topography on cooling histories during erosion, *Tectonophysics*, 270, 167-195.

Maréchal, J.-C., P. Perrochet, and L. Tacher (1999), Long-term simulations of thermal and hydraulic characteristics in a mountain massif: The Mont Blanc case study, French and Italian Alps, *Hydrogeol. J.*, 7, 341-354.

Michalski, I., and M. Soom (1990), The Alpine thermo-tectonic evolution of the Aar and Gotthard massifs, Central Switzerland: Fission Track ages on zircon and apatite and K-Ar mica ages, *Schweiz. Mineral. Petrogr. Mitt.*, 70, 373-387.

Molnar, P. (2004), Late Cenozoic increase in accumulation rates of terrestrial sediment: How might climate change have affected erosion rates?, *Annu. Rev. Earth Planet. Sci.*, 32, 67-89.

Muttoni, G., C. Carcano, E. Garzanti, M. Ghielmi, A. Piccin, R. Pini, S. Rogledi, and D. Sciunnach (2003), Onset of major Pleistocene glaciations in the Alps, *Geology*, 31, 989-992.

Naeser, C. W. (1978), *Fission track dating*, U.S. Geol. Surv. Open File Rep. 76-190.

Perello, P., F. Piana, and G. Martinotti (1999), Neo-Alpine structural features at the boundary between the Penninic and Helvetic domains (Prè S. Didiér - Entrèves, Aosta valley, Italy), *Eclogae Geol. Helv.*, 92, 347-359.

Rahn, M. K. (2001), The metamorphic and exhumation history of the Helvetic Alps, Switzerland, as revealed by apatite and zircon fission tracks, unpublished habil. thesis, 140 pp., Albert-Ludwigs-Universitaet Freiburg, Freiburg.

Reinecker, J., M. Danišík , C. Schmid , C. Glotzbach , M. Rahn , W. Frisch , C. Spiegel (pending successful revision), Tectonic control on the late stage exhumation of the Aar Massif (Switzerland): Constraints from apatite fission track and (U-Th)/He data, *Tectonics*, doi:10.1029/2007TC002247R.

Reiners, P. W., T. A. Ehlers, and P. K. Zeitler (2005), Past, present and future of Thermochronology, *Rev. Mineral. Geochem.*, 58, 1-18.

Ring, U., M. T. Brandon, S. D. Willett, and G. S. Lister (1999), Exhumation processes, *Spec. Publ. Geol. Soc.*, 154, 1-27.

Rolland, Y., M. Corsini, M. Rossi, S. F. Cox, G. Pennacchioni, N. Mancktelow, and A. M. Boullier (2007), Comment on "Alpine thermal and structural evolution of the highest external crystalline massif: The Mont Blanc" by P. H. Leloup, N. Arnaud, E. R. Sobel, and R. Lacassin, *Tectonics*, 26, TC2015, doi:10.1029/2006TC001956.

Schaer, J. P., G. M. Reimer, and G. A. Wagner (1975), Actual and ancient uplift rate in the Gotthard region, Swiss Alps: A comparison between precise levelling and Fission-Track Apatite age, *Tectonophysics*, 29, 293-300.

Schmid, S. M., O. A. Pfiffner, N. Froitzheim, G. Schönbron, and E. Kissling (1996), Geophysical-geological transect and tectonic evolution of the Swiss-Italian Alps, *Tectonics*, 15, 1036-1064.

Seward, D., M. Ford, J. Burgisser, H. Lickorish, E. A. Williams, and L. D. Meckel (1999), Preliminary results of fission-track analyses in the southern Pelvoux area, SE France, paper presented at 3rd Workshop on Alpine Geological Studies, Mem. Sci. Geol. Padova.

Seward, D., and N. S. Mancktelow (1994), Neogene kinematics of the central and western Alps: Evidence from fission-track dating, *Geology*, 22, 803-806.

St. John, K., and L. A. Krissek (2002), The late Miocene to Pleistocene ice-rafting history of southeast Greenland, *Boreas*, 31, 28-35.

Steck, A., and J. Hunziker (1994), The Tertiary structural and thermal evolution of the Central Alps - compressional and extensional structures in an orogenic belt, *Tectonophysics*, 238, 229-254.

Stüwe, K., and M. Hintermüller (2000), Topography and isotherms revisited: the influence of laterally migrating drainage divides, *Earth Planet. Sci. Lett.*, 184, 287-303.

Stüwe, K., L. White, and R. Brown (1994), The influence of eroding topography on steady-state isotherms. Application to fission track analysis, *Earth Planet. Sci. Lett.*, 124, 63-74.

Sue, C., B. Delacou, J. D. Champagnac, C. Allanic, P. Tricart, and M. Burkhard (2007), Extensional neotectonics around the bend of the Western/Central Alps: an overview, *Int. J. Earth Sci.*, 96, 1101-1129.

Sue, C., F. Thouvenot, and J. Fréchet (1999), Widespread extension in the core of the western Alps revealed by earthquake analysis, *J. Geophys. Res.*, 104, 25611-25622.

Sue, C., and P. Tricart (2002), Widespread post-nappe normal faulting in the Internal Western Alps: a new constraint on arc dynamics, *Geol. Soc. Spec. Publ.*, 159, 61-70.

Vernon, A. J., P. A. van der Beek, H. D. Sinclair, and M. K. Rahn (2008) Increase in late Neogene denudation of the European Alps confirmed by isoage analysis of a fission-track database, *Earth Planet. Sci. Lett.*, doi:10.1016/j.epsl.2008.03.053, in press.

von Raumer, J. F., and F. Neubauer (1993), *Pre-Mesozoic Geology in the Alps*, Springer, Berlin.

Wagner, G., and P. van den Haute (1992), *Fission-Track Dating*, 285 pp., Kluwer Academic, Boston.

Wagner, G. A., G. M. Reimer, and E. Jäger (1977), Cooling ages derived by apatite fission track, mica Rb-Sr and K-Ar dating: the uplift and cooling history of the Central Alps, *Mem. Ist. Geol. Mineral. Univ. Padova*, 30, 1-27.

Whipp, D. M., and T. A. Ehlers (2007), Influence of Groundwater flow on thermochronometer-derived exhumation rates in the central Nepalese Himalaya, *Geology*, 35, 851-854.

Willett, S. D., F. Schlunegger, and V. Picotti (2006), Messinian climate change and erosional destruction of the central European Alps, *Geology*, 34, 613-616.

Wolf, R. A., K. A. Farley, and D. M. Kass (1998), Modeling of the temperature sensitivity of the apatite (U-Th)/He thermochronometer, *Chem. Geol.*, 148, 105-114.

What perturbs isotherms? An assessment using fission track thermochronology and thermal modelling along the Gotthard transect, Central Alps

C. Glotzbach[1], C. Spiegel [1,2], J. Reinecker[1], M. Rahn[3] and W. Frisch[1]

[1] Institute of Geoscience, University Tübingen, Sigwartstr. 10, 72076 Tuebingen, Germany (e-mail: christoph.glotzbach@uni-tuebingen.de)

[2] Now at FB 5 – Geoscience, University Bremen, Postfach 330 440 28334 Bremen, Germany

[3] Institute of Mineralogy-Geochemistry, University Freiburg, Albertstr. 23b, 79104 Freiburg, Germany

Abstract: Interpretation of low-temperature thermochronological data usually relies on assumptions on the shape of isotherms. Recently, a number of thermal modelling approaches investigate and predict the theoretical influence of topography on isotherms. The application and proof of these predictions is not well confirmed by measured data. Here we present apatite fission track (AFT) data from samples collected along the Gotthard road tunnel and its corresponding surface line to test these predictions. AFT ages broadly cluster around 6 Ma along the tunnel. No correlation of tunnel ages with superimposed topography is seen, which means that topography induced perturbation of isotherms under given boundary conditions (topographic wavelength: 12 km, relief 1.5 km, exhumation rate: 0.45 km/Myr) can be neglected for the interpretation of AFT ages. Thus in areas characterized by similar topographies and exhumation rates apparent exhumation rates deduced from age elevation relationship (AER) of AFT data need no correction for topography induced perturbation of isotherms. 3D numerical thermal modelling was carried out incorporating thermally relevant parameters and mechanisms, such as topography, geology, thermal conductivities and heat production. Modelling reveals a strong influence on the shape of isotherms caused by spatially variable thermal parameters, especially heat production rates. Therefore, not only topography has to be considered for interpreting low-temperature thermochronological data, but also other parameters like heat production rates.

1 Introduction

First geological applications of low-temperature thermochronology commonly assumed that critical isotherms (e.g. 110 °C for apatite fission track) remain horizontal in relation to topography (Schaer et al. 1975). Thermal modelling, however, predicts that in areas with pronounced relief near-surface isotherms will be influenced by topography with compressed isotherms beneath valleys and wider-spaced isotherms beneath ridges (e.g. Stüwe et al. 1994). The impact for the interpretation of low-temperature thermochronological data, especially apatite fission track (AFT) and (U-Th)/He data was investigated recently (Stüwe et al. 1994; Mancktelow & Grasemann 1997; House et al. 1998; Stüwe & Hintermüller 2000; House et al. 2001; Braun 2002; Foeken et al. 2007). On the other hand, bending of isotherms carries potential information to reveal minimum ages of topography and the evolution of palaeorelief (House et al. 1998; House et al. 2001; Braun 2002; Foeken et al. 2007).

A widely used technique to derive exhumation rates utilizes the correlation of ages of a single isotopic system, e.g. AFT or apatite (U-Th)/He, with elevation, the so called age elevation relationship (AER) (Wagner & Reimer 1972; Schaer et al. 1975; Stüwe et al. 1994). The great advantage, in contrast to the mineral-pair method (Wagner et al. 1977), is that no estimation of the geothermal gradient has to be made. However, this proxy is only valid under certain assumptions (e.g. Parrish 1983): (1) during and after passing the closure isotherm all samples followed a vertical exhumation pathway and no tectonic displacement exists between

samples, (2) all samples are kinetically uniform and (3) the closure isotherm is fixed with respect to some geographical reference horizon, e.g. sea level.
A drawback of many studies is that sample profiles are rather horizontal than vertical, and thus deduced exhumation rates from such profiles are affected by topography induced perturbation of isotherms. The magnitude of isotherm perturbation increases with topographic wavelength, relief and exhumation rate (Stüwe et al. 1994). Hence, in mountainous regions the assumption that AFT relevant isotherms are flat is probably not fulfilled. In this case only vertical profiles (along a borehole or steep cliff) give correct values of exhumation rates. Resulting apparent exhumation rates of AER plots from 'near'-vertical profiles have to be corrected for the effect of isotherm perturbation due to topography. This leads to the question of the geomorphic and structural-kinematic boundary conditions that cause isotherm perturbation. Based on numerical modelling and analytical solutions (Stüwe et al. 1994; Mancktelow & Grasemann 1997; Stüwe & Hintermüller 2000; Braun 2002), exhumation rates of $\geq$0.5 km Ma^{-1} along with a topographic wavelength of $\geq$10 km and a relief of $\geq$2 km are threshold values for perturbing the 110 °C isotherm.
The aim of this study is to estimate the perturbation of isotherms under a given framework of exhumation rate, topographic wavelength, relief amplitude, rock properties and geothermal gradient by applying AFT thermochronology. AFT age variations along the tunnel transect give evidence whether the 110 °C isotherm was perturbed and if so, to what extent.
For this we sampled the Gotthard road tunnel as well as the corresponding surface line directly above the tunnel. The Gotthard road tunnel is located in central Switzerland and has a length of 16.3 km (Fig. 1). Present-day uplift rates range between 0.7 mm a^{-1} in the north and 1.1 mm a^{-1} in the south of the tunnel (Kahle 1997) (Fig. 1b, 2a). The Gotthard transect is characterized by more or less east-northeastern to west-southwestern trending ridges and valleys with a topographic wavelength of 12 km and relief of up to 1.5 km (Fig. 1b). Published exhumation rates constrained by AFT data from the Gotthard massif range between 0.45 and 0.5 km Ma^{-1} between 10 and 6 Ma (Schaer et al. 1975; Wagner et al. 1977; Michalski & Soom 1990). These values suggest that the Gotthard transect is close to the lower limit of the proposed parameter values given for 110 °C isotherm perturbation. Thus this study provides a natural benchmark to verify topography induced perturbation of isotherms predicted by existing modelling approaches.
In addition, a new 3D finite difference thermal model for predicting the positions of isotherms beneath topography is presented. Compared to previously published analytical solutions (Stüwe et al. 1994; Mancktelow & Grasemann 1997; Stüwe & Hintermüller 2000) our model provides the following advantages: (1) It incorporates 3D topography and (2) includes temporally and spatially variable parameters (e.g. thermal conductivity, internal heat production, exhumation rate, topography). Thus the model provides information about the influence of different thermal parameters on predictions of the shape of near-surface isotherms, comparable to the program 'Pecube' of Braun (2003).

2 Geological Setting

The Gotthard road tunnel crosscuts the entire Gotthard Massif (GM) and the southern part of the Aar Massif (AM). The GM forms an east-northeastern to west-southwestern trending mountain range 80 km long and up to 12 km wide (Fig. 1a). The GM and AM belong to the external massifs of the Alps. They consist of pre-Variscan poly-metamorphic basement intruded by late Variscan granitoids and covered by Late Palaeozoic to Mesozoic sedimentary rocks (Fig. 1) (e.g. Labhart 1977; Schaltegger 1994; Labhart 1999). The boundary between GM and AM is marked by the heavily tectonized Urseren-Garvera zone, built up by steeply dipping Permo-Carboniferous and Mesozoic metasediments. The sedimentary cover of the

GM and AM was mostly detached during Alpine orogeny, forming parts of the Helvetic nappes.

Peak Alpine metamorphic conditions along the tunnel were reached at around 35 to 30 Ma, with greenschist facies conditions in the north and amphibolite facies conditions in the south (Frey & Mählmann Ferreiro 1999). The post-metamorphic evolution of the study area was mainly controlled by the northward movement of the Adriatic indenter and related thrusting in the external Alps (e.g. Schmid et al. 1996). Thrusting during the 'Grindelwald stage' (22 to 12 Ma) propagated towards the foreland (Schmid et al. 1996), resulting in thrusting of the Gotthard massif upon the Tavetsch and Aar massif around 20 Ma (ductile deformation) and subsequent steepening of these structures (brittle deformation) (Wyder & Mullis 1998). It is likely that brittle deformation continues up to present, as indicated by post-glacial vertical movements that are common in the study area (Persaud & Pfiffner 2004; Ustaszewski et al. 2008).

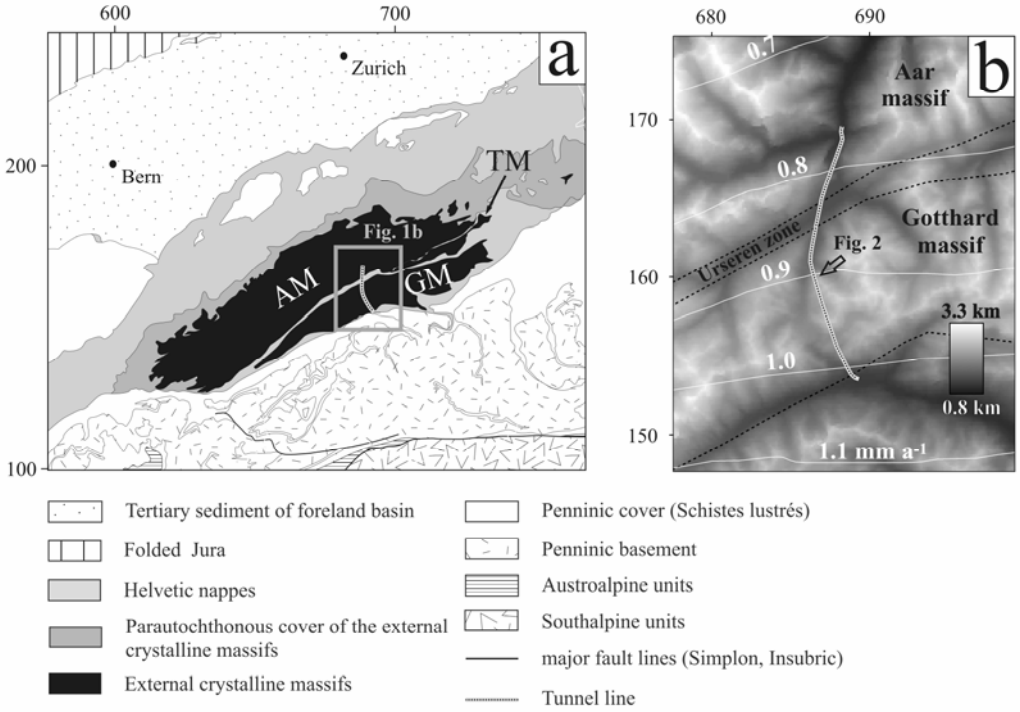

Fig. 1: (a) Geological sketch map of central Switzerland in Swiss coordinate system. The Gotthard road tunnel is located in the centre, crossing the southern part of the Aar massif (AM) and the Gotthard massif (GM). (b) Shuttle Radar Topography Mission (SRTM) digital elevation model (DEM) of the study area. Contours are measured recent rock uplift rates in mm a^{-1} from precise levellings (Kahle 1997).

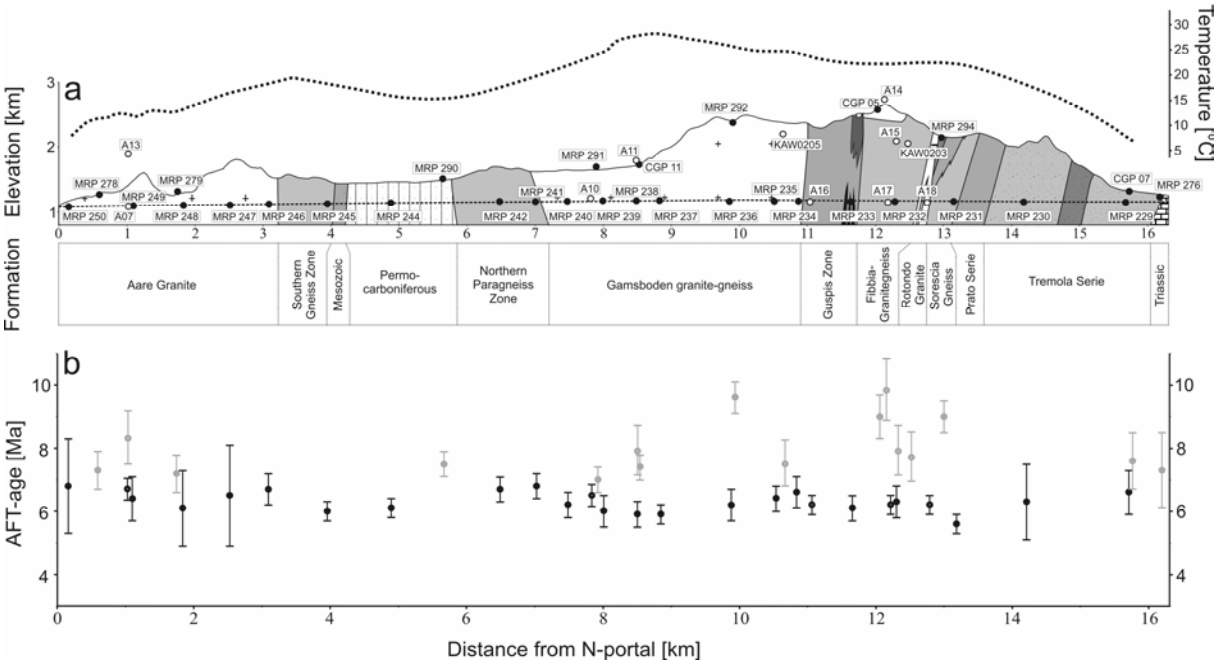

Fig. 2: (a) Geological profile along the Gotthard road tunnel (modified after Keller et al. 1987) with published (open circles) and own samples (black dots) (Schaer et al. 1975; Wagner et al. 1977). All samples are directly located on the plane of the transect, except some samples plotted between the tunnel and surface line, and above the surface line. Their distance to the plane is: 750 m (A13), 280 m (A14), 890 m (A15), 300 m (A11), 780 m (KAW0203), 420 m (KAW0205). The dotted line shows interpolated in-situ rock temperatures measured during excavation of the tunnel (Keller et al. 1987). (b) AFT ages along the tunnel (black) and on the surface (grey).

3 Inferred shape of isotherms from AFT data

The aim of this section is to investigate the perturbation of measured AFT ages under the given boundary conditions, especially with respect to topography.
Table 1 summarizes the results of AFT dating along the tunnel and the corresponding surface line. Previously published AFT data for the Gotthard area (Schaer et al. 1975; Wagner et al. 1977; Michalski & Soom 1990) are in good agreement with our data and are therefore included in our interpretations (cf. Fig. 2b).

Table 1
Apatite fission track data from the Gotthard road tunnel and a surface line directly above the tunnel.

	Sample	Geological unit	Swiss Grid (CH1903) [m] X	Y	Elevation [m]	# grains	ρ_s	N_s	ρ_i	N_i	ρ_d	N_d	$P(\chi^2)$ [%]	Dispersion	Central age ±1σ [Ma]	Dpar [µm]	U [ppm]
	Tunnel																
N	MRP 250	Aare Granite	688290	168840	1082	20	0.800	27	21.100	671	10.45	4998	13.2	0.30	6.8±1.5	1.31	16
	MRP 249	Aare Granite	688020	167940	1093	30	0.501	104	8.899	1846	6.407	3310	93.8	0.00	6.4±0.7	1.34	16
	MRP 248	Aare Granite	687770	167240	1102	10	0.429	30	8.000	559	6.424	3310	78.5	0.01	6.1±1.2	1.12	16
	MRP 247	Aare Granite	687530	166590	1110	12	0.230	17	4.037	298	6.441	3310	97.6	0.00	6.5±1.6	1.13	8
	MRP 246	Aare Granite	687340	166060	1117	60	0.527	184	9.012	3145	6.45	3118	99.9	0.00	6.7±0.5	1.24	17
	MRP 245	Southern Gneiss Zone	687060	165240	1127	49	1.942	434	37.985	8491	6.655	3311	47.2	0.04	6.0±0.3	1.63	77
	MRP 244	Permocarboniferous	686850	164330	1138	50	1.604	571	30.145	10734	6.474	3310	84.1	0.04	6.1±0.3	1.32	57
	MRP 242	Northern Paragneiss Zone	686530	162770	1157	50	0.770	360	13.266	6202	6.491	3310	51.4	0.07	6.7±0.4	1.41	23
	MRP 241	Northern Paragneiss Zone	686430	162250	1163	50	0.763	328	13.140	5649	6.6	3311	92.3	0.00	6.8±0.4	1.47	22
	MRP 240	Gamsboden Granite Gneiss	686340	161790	1168	47	1.133	315	21.050	5852	6.516	3118	99.8	0.00	6.2±0.4	1.41	37
	MRP 239	Gamsboden Granite Gneiss	686240	161280	1174	33	0.754	215	14.658	4182	6.608	3311	25.6	0.04	6.0±0.5	1.25	25
	MRP 238	Gamsboden Granite Gneiss	686280	160790	1173	35	0.900	234	17.538	4559	6.508	3310	99.4	0.00	5.9±0.4	1.21	32
	MRP 237	Gamsboden Granite Gneiss	686360	160460	1172	50	1.165	431	23.019	8519	6.549	3118	97.8	0.00	5.9±0.3	1.41	41
	MRP 236	Gamsboden Granite Gneiss	686640	159460	1168	50	0.863	161	16.091	3003	6.524	3310	74.7	0.02	6.2±0.5	1.29	28
	MRP 235	Gamsboden Granite Gneiss	686820	158830	1166	50	0.754	277	13.656	5016	6.541	3310	77.8	0.03	6.4±0.4	1.41	25
	MRP 234	Gamsboden Granite Gneiss	686920	158500	1165	50	0.821	192	15.543	3637	7.055	3397	81.3	0.00	6.6±0.5	1.41	26
	MRP 233	Guspis Zone	687160	157770	1162	50	0.419	240	7.964	4562	6.558	3310	99.5	0.00	6.1±0.4	1.57	15
	MRP 232	Fibbia Granite Gneiss	687370	157150	1160	51	0.743	212	13.843	3951	6.574	3310	66.4	0.05	6.3±0.5	1.34	25
	MRP 231	Sorescia Gneiss	687670	156340	1157	50	1.755	725	36.502	15083	6.591	3310	60.8	0.09	5.6±0.3	1.26	66
	MRP 230	Tremola Serie	688030	155380	1153	25	0.123	27	2.304	504	6.582	3118	90.5	0.00	6.3±1.2	1.51	4
S	MRP 229	Tremola Serie	688730	154050	1147	50	0.223	90	3.941	1589	6.615	3118	95.8	0.00	6.6±0.7	1.42	7
	Surface																
N	MRP 278	Aare Granite	688180	168400	1265	50	0.806	168	16.205	3376	8.277	4059	50.4	0.11	7.3±0.6	1.32	23
	MRP 279	Aare Granite	687800	167320	1315	50	0.821	171	16.885	3516	8.303	4059	7.0	0.27	7.2±0.6	1.20	23
	MRP 290	Permocarboniferous	686730	163585	1510	50	0.994	420	19.662	8305	8.354	4059	4.1	0.20	7.5±0.4	1.26	27
	MRP 291	Gamsboden Granite Gneiss	686150	161390	1690	50	1.348	499	21.959	8131	6.391	3310	71.8	0.02	7.0±0.4	1.26	40
	CGP 11	Gamsboden Granite Gneiss	686240	160740	1725	44	1.230	467	19.488	7397	6.608	3310	32.5	0.10	7.4±0.4	1.28	33
	MRP 292	Gamsboden Granite Gneiss	686650	159420	2380	50	1.446	423	22.012	6439	8.430	4059	71.3	0.06	9.6±0.5	1.31	30
	CGP 05	Rotondo Granite	687129	157340	2580	36	0.898	197	11.761	2579	6.658	3310	59.6	0.09	9.0±0.7	1.30	21
	MRP 294	Sorescia Gneiss	687640	156530	2140	50	0.896	389	11.303	4905	6.374	3310	99.9	0.00	9.0±0.5	1.28	21
	CGP 07	Tremola Serie	688851	154073	1320	23	0.459	83	7.140	1291	6.624	3310	72.7	0.16	7.6±0.9	1.31	13
S	MRP 276	Tremola Serie	689065	153820	1220	17	0.525	43	10.755	881	8.405	4059	54.6	0.01	7.3±1.2	1.59	14

ρ_s (ρ_i) are spontaneous (induced) track densities (10^5 tracks/cm2); N_s (N_i) is number of counted spontaneous (induced) tracks; ρ_d is dosimeter track density (10^5 tracks/cm²); N_d is number of tracks counted on dosimeter; $P(\chi^2)$ is probability obtaining Chi-square value (χ^2) for n degree of freedom (where n is number of crystals minus 1); dispersion is a real number, that gives an idea of the variability of the single grain age distribution, it is zero if all the data are identical, and increases as the data becomes more diverse; age ±1s is central age ±1 standard error [Galbraith and Laslett, 1993]; Dpar is etch pit diameter of fission tracks, averaged from 4 measurements per analysed grain. Ages were calculated using zeta calibration method [Hurford and Green, 1983], glass dosimeter CN-5, and zeta value of 354.92 ± 7.03 yr/cm².

To make sure that measured variations of AFT ages are in fact the result of the shape of the palaeo-isotherm the kinetic homogeneity of our apatites was tested by D_{par} measurements. D_{par} values obtained for measured samples are small and relatively uniform, varying between 1.1 and 1.6 µm (Table 1). Microprobe analyses of 15 samples from different lithologies were carried out, demonstrating that all samples are close to F-apatite end member, with Cl contents of <0.1 WT%. Furthermore, analysed elements such as Si, Mn, Ce and Sr do not show any significant variation, suggesting that apatites are kinetically uniform (for details see supplementary material p. 1, available online at http://www.geolsoc.org.uk/SUP00000).

AFT ages of samples collected at the same elevation can be used to predict the palaeoshape of the critical isotherm (House et al. 1998). All samples along the Gotthard tunnel are at ~1.1 km elevation and yield AFT ages of 6.2±0.6 Ma, overlapping within 1σ-error limits (Fig. 2b). Individual samples characterized by low U-content show larger 1σ-error, especially those from the northern and southern ends of the transect.

Surface samples yield AFT ages ranging from 7.0 to 9.6 Ma. Surface samples collected at ~1.3 km elevation along the Gotthard transect (CGP 07, MRP 276, MRP 278 and MRP 279) exhibit same ages 7.4±0.2 Ma. Thus AFT age patterns on two structural elevation levels (~1.1 km and ~1.3 km) indicate that between 6.2 and 7.4 Ma the 110 °C isotherm was flat, suggesting that topography has no visible effect on the AFT age pattern along the tunnel. Small variations in ages partly coincide with stratigraphic/tectonic boundaries (Fig. 2b), which can be explained by kinetic or physical differences (such as heat production and thermal conductivities).

Surface AFT ages show an increase with elevation (Fig. 2b and 3). Slopes of AER were calculated by weighting the ages according to their errors. Slopes and uncertainties were inverted to estimate exhumation rates with defined uncertainties (Reiners et al. 2003). Regression bands were plotted with a 95% confidence interval, which allows predicting the error of the regression lines. The AER-plot for samples of the northern flank of the Gotthard massif (MRP 237, MRP 238, CGP 11 and MRP 292) yields an apparent exhumation rate of 0.35±0.1 km Ma^{-1} for the period between 10 and 5 Ma (Fig. 3a). The horizontal and vertical distance between the samples is 1.5 and 1.2 km, respectively. Samples of the southern flank (MRP 229, MRP 276, MRP 294, CGP 07 and A14 of Schaer et al. (1975)) yield an apparent exhumation rate of 0.5±0.2 km Ma^{-1} for the period between 10 and 6 Ma (Fig. 3b). Here the horizontal and vertical distance between the samples is 4 and 1.6 km, respectively. Deduced apparent exhumation rates are in good accordance with previously published data (Schaer et al. 1975; Michalski & Soom 1990). The presented data suggest that critical isotherms are flat under the Gotthard transect and a correction for topography is not necessary.

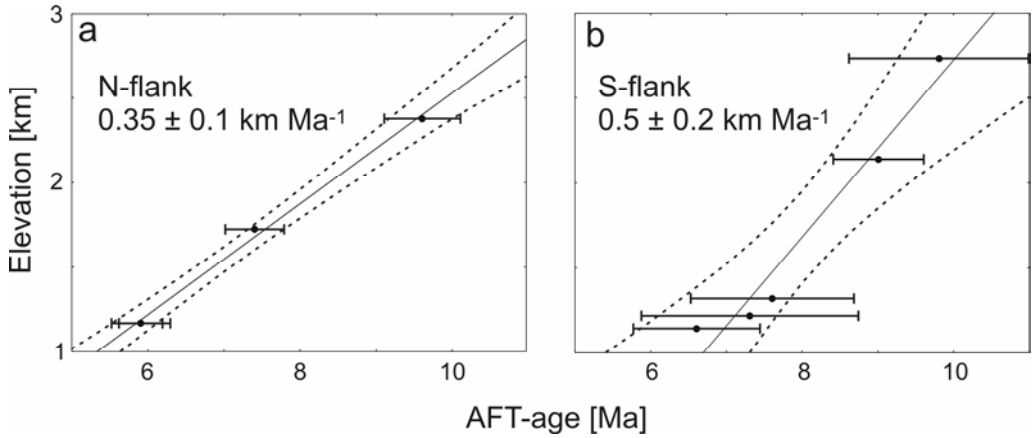

Fig. 3: AFT age elevation relationship of surface samples (a) of the northern flank (MRP 292, CGP 11, MRP 237, MRP 238) and (b) of the southern flank (A14 from Schaer et al. (1975), MRP 294, MRP 276, CGP 07, MRP 229) of the Gotthard transect.

4 Modelling the shape of isotherms

Although we demonstrated that in the specific case of the Gotthard transect no topographic correction is required, in the following section we test the theoretical influence of topography and other thermally relevant parameters on near surface isotherms. We present numerical 3D finite difference thermal models developed for a crustal block of 14 x 26 x 10 km around the Gotthard road tunnel (an overview is provided in the supplementary material p. 2). Modelling incorporates spatial and/or temporal varying parameters, namely topography, exhumation rates, thermal conductivity and heat production (for details see supplementary material p. 3). The parameter values are either taken from this study (exhumation rates) or from geophysical measurements (e.g. Busslinger & Rybach 1999). In the following, all mentioned isotherm perturbation values refer to the location of the Gotthard road tunnel transect, and are defined here as the maximum vertical deflection of the corresponding isotherm.
For simplification in the first step it is assumed that heat transfer in the crust is controlled by conduction only (Stüwe 2007). In this case Fourier's law of heat conduction can be used:

$$\frac{\partial T}{\partial t} = \kappa \cdot \nabla^2 T \tag{1}$$

where κ is the thermal diffusivity with typical values around $10^{-6} m^2 s^{-1}$, T is temperature, and t is time and ∇ is the nabla operator, describing here the spatial change of temperature in 3D (e.g. Stüwe 2007). Equation (1) is modified to account for the effect of exhumation and internal heat production due to radioactive decay, resulting in:

$$\frac{\partial T}{\partial t} = \kappa \cdot \nabla^2 T + u \cdot \frac{\partial T}{\partial z} + \frac{S}{\rho \cdot c_p} \tag{2}$$

where z is depth, S the heat production rate, ρ the rock density, and c_p the specific heat. Initial and boundary conditions necessary for the solution of the differential equation (2) are:
(1) The lower boundary of the model was placed at -10 km from the surface and was fixed with a constant vertical geothermal gradient, for which a value of 20 °C km^{-1} was used based on borehole and tunnel temperature measurements in or near the Gotthard road tunnel (Keller et al. 1987). To verify that this relatively 'shallow' lower boundary allows the deflection of isotherms caused by thermal relevant parameters (e.g. topography and exhumation), a simple 2D sinus-shaped topography was modelled analytically using the program 'TERRA' (Ehlers et al. 2005) (Fig. 4). Used parameters fit those from the Gotthard transect. Position of isotherms are unaffected by the depth of the lower boundary of the model.

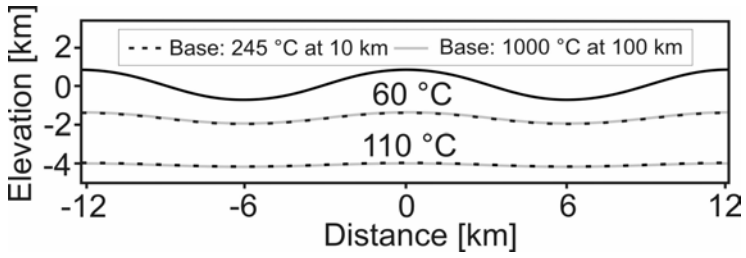

Fig. 4: Position of the 60 °C and 110 °C isotherms depending on the depth of the lower boundary. Model parameters are: steady-state topography with a wavelength of 12.5 km and an amplitude of 0.5 km, exhumation rate 0.45 km Ma^{-1}, lower boundary at -10 km/-100 km with a temperature of 245 °C/1000 °C, upper boundary fixed by topography and surface temperature calculated with 12 °C at 0 m and a lapse rate of 4.6 °C km^{-1}, thermal diffusivity 1E-6 $m^2 s^{-1}$, density 2700 kg m^{-3}, specific heat 1000 J $kg^{-1} K^{-1}$, heat production 3E-6 W m^{-3} with a skin depth of 10 km.

(2) Topography was used as an upper boundary condition, discretized with a rectangular grid and converted into air temperature, depending on elevation (Busslinger & Rybach 1999):

$$T_{\mathrm{Air}} = T_0 - \alpha \cdot h \tag{3}$$

with T_{Air} being the mean air temperature at surface, T_0 the air temperature at sea level, α the atmospheric lapse rate and h the elevation. Kohl et al. (2001) showed that ground surface temperature (GST) data collected from high elevations in Alpine terrain are best described by the model of Niethammer (1910), with T_0 = 12 °C and α = 4.6 °C km^{-1}. These values were used to calculate GST for each node based on a Shuttle Radar Topography Mission (SRTM) digital elevation model (DEM). We neglected the difference between air temperature and corresponding GST depending on exposition (slope and orientation), vegetation, snow cover and rock surface properties (e.g. Šafanda 1999). Consequently, each node of the upper boundary is composed of an elevation and a corresponding GST.
(3) Lateral boundaries were fixed with no horizontal heat flow. For simplification a uniform distance from node to node ($\Delta x=\Delta y=\Delta z$) of 132.9 m was used, according to the spatial resolution of the input DEM. Thus the total mesh was built up by 1.55 million nodes.
A simplified geological model was used for the modelling, considering five geological units: Aar massif, Urseren zone, Tavetsch massif, Gotthard massif and Schistes lustrés (Fig. 1, Table 2). Vertical boundaries between individual geological units were assumed, consistent with high dip angles observed at the surface and during tunnel construction (Fig. 2a). The geological units are characterized by different physical and thermal properties. The foliation developed during Alpine metamorphism results in a pronounced anisotropic thermal conductivity of all geological units, with ratios of up to 1.5 between maximum ($k \parallel$) and minimum ($k \perp$) values within one unit (Kappelmeyer & Haenel 1974; Kohl et al. 2001). Input thermal conductivities are listed in Table 2. Rock radioactivity measurements within the tunnel (Keller et al. 1987) were used to calculate the total heat production related to radioactive decay of uranium, thorium and potassium (Turcotte & Schubert 1982, equation (4-6)). Resulting heat production values range from 7.54 x 10^{-11} to 2.56 x 10^{-9} W kg^{-1} for individual geological units with 1.22 x 10^{-9} W kg^{-1} as an average value. Modelling was carried out either with individual values or an averaged heat production rate extrapolated to the surroundings of the Gotthard road tunnel (Table 2). Tunnelling and geophysical investigations revealed that the Aar and Gotthard massifs continue towards depth, possibly by more than 10 km (Pfiffner & Heitzmann 1997). Therefore heat production rates are assumed to be constant with depth. Modelling was conducted assuming both a steady-state and time-varying topography and a constant exhumation rate of 0.45 km Ma^{-1} (mean value of the AER plots in Fig. 3). To account for a time-varying topography nodes were added/removed and temperature adjusted (according to equation (3)) at the upper boundary during the modelling progress. For instance, a change in elevation from 0 to 2000 m in 2 Ma, is implemented by adding one node (132.9 m) every 0.133 Ma (reaching an elevation of 1994 m after 2 Ma).
A simple 2D thermal model was numerically calculated and compared with an analytical solution calculated with the program 'TERRA' (Ehlers et al. 2005) (Fig. 5), proving the correctness of the used finite difference thermal model approach.

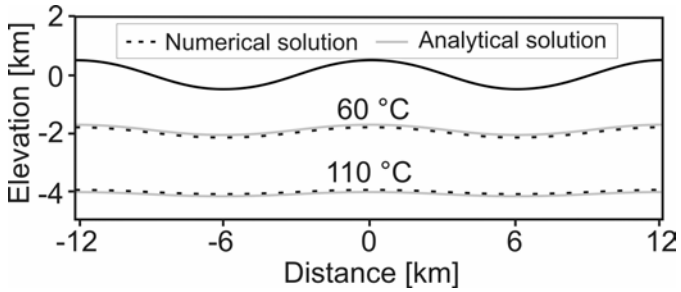

Fig. 5: Comparison between analytical solution from thermal modelling program TERRA (Ehlers et al. 2005) and the numerical model presented in this study, for a simple 2D model. Model parameters are the same as in Fig. 4, except a lower boundary at -10 km with a temperature of 220 °C.

From several performed model runs, we present five solutions, which differ by the assumed thermal conductivity, heat production and topographic evolution (Table 3). Models 1 to 3 were calculated until reaching a steady-state temperature field, which takes around 5 Ma depending on the parameterisation. Models 4 and 5 were calculated with an initial steady-state temperature field, subsequently adapted during the modelling progress due to a changing topography.

Table 2
Geological units with their anisotropic thermal conductivities (k) parallel and perpendicular to schistosity and heat production values.

Geological unit	$k_{\parallel}$ [W/m*K]	$k_{\perp}$ [W/m*K]	Heat production [10^{-9} W/kg]
Aar massif	3.66[1]	2.83[1]	1.57-1.92
Gotthard massif	4.43[1]	2.95[1]	0.51-1.50
Tavetsch massif	3.61[1]	2.79[1]	1.92
Urseren-Garvera zone	3.10[1]	2.45[1]	1.17
Schistes lustrés	3.10[2]	2.40[2]	0.51

[1]Kohl et al. (2001), [2]Kappelmeyer and Haenel (1974)

Table 3
Input parameters of individual model runs

Model Nr.	Topography	Thermal conductivity [W/K*m]	Heat production [10^{-9} W/kg]	Rock uplift rate [km/Myr]	Surface uplift rate [km/Myr]	Exhumation rate [km/Myr]
1	recent, steady-state	2.7	1.22	0.45	0.0	0.45
2	recent, steady-state	anisotropic cf. Table 2	1.22	0.45	0.0	0.45
3	recent, steady-state	anisotropic cf. Table 2	anisotropic cf. Table 2	0.45	0.0	0.45
4	0 m to recent, increasing	anisotropic cf. Table 2	anisotropic cf. Table 2	0.45	0.10 to 0.27	0.18 to 0.35
5	decreasing	2.7	1.22	0.45	-0.10 to -0.22	0.55 to 0.67

To evaluate the influence of thermally relevant parameters (e.g. topography) on low-temperature thermochronology in the following models, a closure temperatures of 110 °C and 60 °C were assumed for the apatite fission track (e.g. Rahn & Grasemann 1999) and (U-Th)/He system (e.g. Ehlers & Farley 2003), respectively. AFT age differences along the tunnel are predicted, using forward modelling of AFT ages with the program HeFTy (Ketcham et al. 2007) based on measured kinetic parameters (D_{par}) and generated time temperature (tT) path for selected localities. Therefore, during modelling progress the temperatures of selected localities were read out every 10 ka, yielding nearly continuous tT paths.
Fig. 6 shows the predicted steady-state 110 °C isotherm for different model runs and the contours of the corresponding 2D shape of the 60 °C and 110 °C isotherms along the Gotthard road tunnel.

The benefit of model 1 is that we can estimate the net influence of the topography on a chosen isotherm, because all other input parameters are spatially uniform. The modelled 110 °C isotherm clearly demonstrates that small topographic features have no influence on the isotherm (Stüwe et al. 1994; Mancktelow & Grasemann 1997). Thus, according to model 1, the shape of the isotherm follows the topography in a strongly dampened fashion (Stüwe et al. 1994) and is clearly deformed beneath the Gotthard massif, with a perturbation of 250 m. Resulting maximum AFT age difference along the tunnel is 0.5 Ma (modelled ages range from 6 to 5.5 Ma).

Incorporating spatially variable and anisotropic thermal conductivities (model 2) results in an overall deeper 110 °C isotherm, because average input thermal conductivities are higher than those used for model 1. The shape of the 110 °C isotherm in model 2 is similar to that from model 1, apart from a smaller isotherm perturbation of only 150 m (Fig. 6). Areas characterized by low-thermal conductivities (Urseren zone and Schistes lustrés, cf. Fig. 1) accumulate heat which bulge the 110 °C isotherm. We conclude that the observed differences and anisotropy of thermal conductivities along the Gotthard road tunnel (Table 2) do only weakly influence the shape of the near-surface isotherms. For models 1 and 2, the corresponding perturbation of the 60 °C isotherm is more or less twice as high as compared to the perturbation of the 110 °C isotherm. However, the resulting AFT age difference along the tunnel is only 0.2 Ma (modelled ages range from 6.7 to 6.5 Ma).

From model 3, a laterally variable heat production was added, resulting in a more complex 110 °C isotherm shape. Interestingly, the pronounced topography of the Gotthard massif, forming an east-northeastern to west-southwestern trending ridge in the southern tunnel section, is not mirrored by the 110 °C isotherm. Evidently, differences in heat production values are capable to blur the effect of topography. As demonstrated by model run 1, the net topographic effect is small. Thus, for model 3 the perturbation of the 110 °C can be nearly completely attributed to the spatial variation of heat production, which here was assumed to persist to the depth of 10 km. Due to the lateral decrease in total heat production rate, the shape of the 110 °C isotherm along the tunnel profile shows a steady decrease to the south with a perturbation of 550 m. The 60 °C isotherm runs more or less horizontally up to tunnel kilometre 12 and then decreases towards the south with a total perturbation of 450 m. For this model run, variations of AFT ages in the range of 1.2 Ma (modelled ages range from 7.6 to 6.4 Ma) along the tunnel are predicted. The perturbation effect of topography and heat production at that depth becomes less pronounced in the northern part of the transect. Thus, differences in heat production are capable to compensate (northern section) and to amplify (southern section) the perturbation of isotherms due to topography (Fig. 6).

A palaeotopographic evolution with increasing relief after 5 Ma, assuming isotropic thermal parameters, would result in flat isotherms at the time the AFT samples cross the 110 °C isotherm, following the observation of model 1. In the extreme case that the palaeotopography is flat at that time, resulting AFT ages along the tunnel are all the same. Incorporating spatial variable heat production rates (model 4) results in increased isotherm perturbation with depth, with perturbation values of the 60 °C and 110 °C isotherm of 250 and 500 m, respectively (Fig. 6).

To investigate the effect of a possible palaeotopographic evolution with higher relief and peak elevations in Late Miocene times (6 Ma), which decrease to the present, model 5 was carried out assuming initial maximum elevations of 5 km and a relief of 3 km. The shape of resulting isotherms is comparable to that of model 1, however, with more pronounced isotherm perturbations of 450 m (110 °C) and 750 m (60 °C). The doubling of the vertical isotherm perturbation with respect to model 1 corresponds to a doubling in the FT age difference along the tunnel.

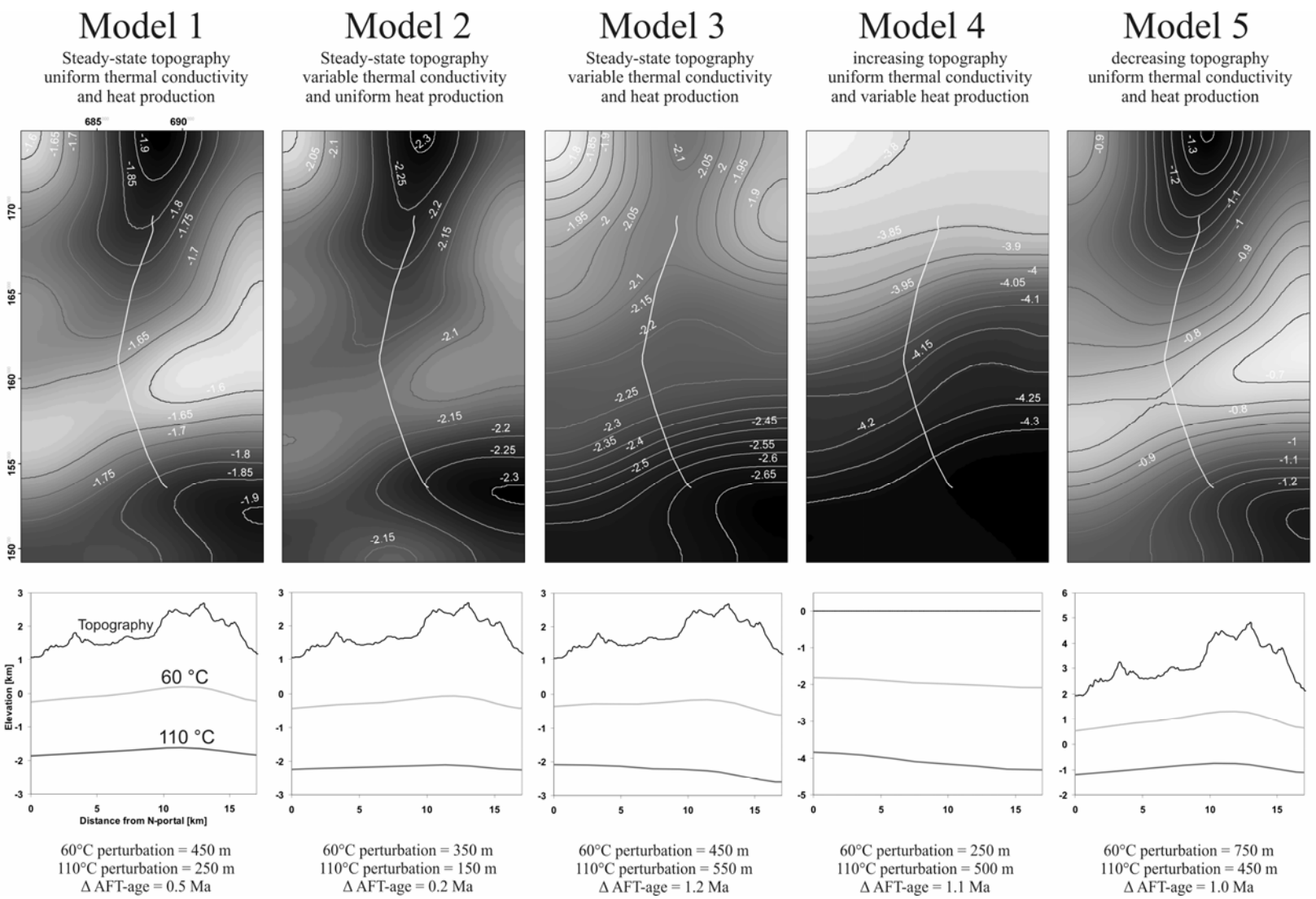

Fig. 6: 3D models of the 110 °C isotherms with contours in meters below sea level calculated with parameters listed in Tables 2 and 3. The Gotthard road tunnel is marked by the white line. The corresponding position of the 60 °C and 110 °C isotherms with topography is shown in the graphs below. Δ AFT describes the variation of AFT ages along the tunnel transect, predicted by the different model runs.

5 Influence of advective heat transport on low-temperature isotherms

To investigate the impact of heat advection due to faulting on isotherms and AFT ages simple 2D numerical modelling was carried out. A flat topography was assumed with two crustal blocks exhumed with rates of 0.5 and 1 km Ma^{-1} (Fig. 7a). Assuming steady-state conditions and an exhumation rate of 0.5 km Ma^{-1}, the 110 °C isotherm is at a depth of ~3 km. Initiation of a perpendicular fault and increased exhumation (1 km Ma^{-1}) on one side of the fault results in a perturbation of isotherms depending on the duration of displacement. Short-term movements (<0.1 Ma) result in a less pronounced perturbation of the isotherm across the fault (<50 m) and a displacement of the crustal blocks of <50 m. For small displacements heat advection approximates relative rock uplift (Fig. 7b); hence advective heat flow dominates the temperature field. For long-term movements, however, the role of diffusion increases. Thus the perturbation of the 110 °C isotherm is small as compared to the displacement (e.g. for a duration of 1 Ma, a perturbation of 200 m corresponds to a relative displacement of 500 m). Infinite displacement results in a maximum possible isotherm perturbation of ~320 m.

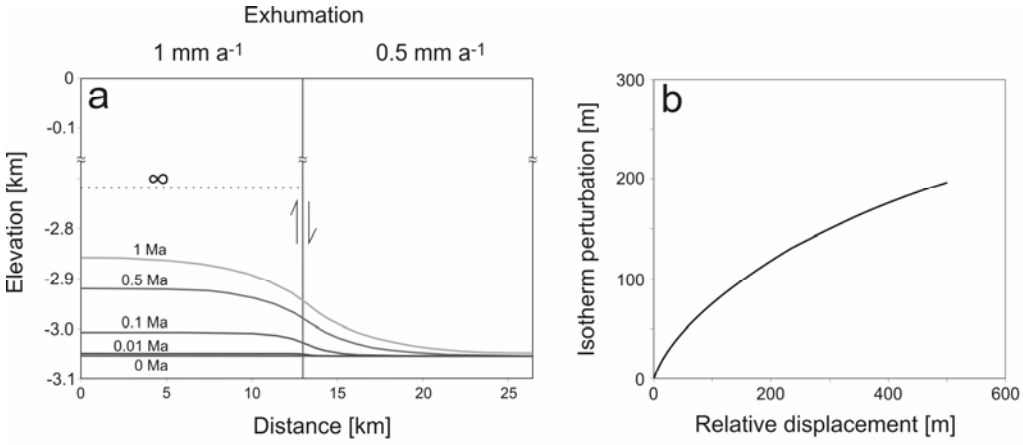

Fig. 7: (a) 2D numerical model with two crustal blocks separated by a perpendicular fault. Crustal blocks differ in their rock uplift rates and resulting exhumation rate assuming steady-state topography. Calculated 110 °C isotherms for different time steps (0, 0.01, 0.1, 0.5 and 1 Ma) are displayed. The total shift of the 110 °C isotherm after infinite time is indicated by a dashed line. (b) Relationship between perturbation of the 110 °C isotherm and relative displacement along the fault.

6 Discussion

In the following some essential requirements for the investigation of isotherm perturbation due to topography are discussed. Additionally we discuss the measured AFT age pattern in the light of the modelled predictions of isotherm perturbation.

6.1 Advective and convective heat transport

In addition to discussed thermally relevant parameters (e.g. heat production), near-surface temperatures are affected by advective and convective heat transport. Therefore, an important prerequisite for investigations on isotherm perturbations is that advective and convective heat transport must be negligible or quantifiable over geological time scales.
Advective heat transport may be caused by deformation and spatial differences in rock uplift rates. Studies on brittle deformation structures and hydrothermal mineral precipitation along the Gotthard road tunnel showed that the main phase of brittle faulting had ceased before the

structural level of the tunnel samples cooled below 190 °C (Luetzenkirchen 2002). First order precise levelling of the Swiss national levelling network revealed only a slight gradient of present-day vertical movements within the area of the Gotthard massif (Fig. 1b), with rates of 0.8 to 1.0 mm a^{-1} (Kahle 1997). On a smaller scale, however, remote sensing analysis, field work and numerical modelling demonstrate the activity of uphill facing scarps in the Urseren valley as a response to isostatic vertical movements after the last Ice Age (Dahinden 2001; Persaud & Pfiffner 2004; Hampel & Hetzel 2006; Ustaszewski et al. 2008). AFT ages along the Gotthard road tunnel show no jumps in ages (Fig. 2b), thus a differential vertical displacement of individual crustal blocks has been small and is hidden within the 1σ-error of the AFT ages. Assuming an exhumation rate of 0.5 km Ma^{-1} and an average AFT error of 0.6 Ma, only a vertical displacement of >300 m along a fault would be significant. We conclude that vertical displacements along fault zones were small and therefore can be neglected for the last 6 Ma. Simple 2D thermal modelling of movements along a single vertical fault show that a displacement of 300 m is capable to generate a perturbation of the 110 °C isotherm of ~150 m (Fig. 7). We cannot exclude that mass advection along the Gotthard transect possibly led to a perturbation of isotherms of <150 m, which in magnitude is close to the net topography induced isotherm perturbation (see models 1 and 2, Fig. 6).
Convective heat transport may play an important role for the total heat transport in high mountainous areas (e.g. Whipp & Ehlers 2007). During construction of the Gotthard road tunnel, water inflow measurements were carried out, with maximum in-situ measured rock temperatures of 32 °C (Fig. 2a) (Keller et al. 1987; Luetzenkirchen 2002). Except an area in the central Gamsboden granite-gneiss, which is assumed to be affected by a near surface convective hydrothermal circuit (Pastorelli et al. 2001; Luetzenkirchen 2002), measured rock temperatures are correlated to topography.
We conclude that advective and convective heat transport are negligible, and that conductive heat transport is dominating and controls the temperature distribution in the upper crust of the study area.

6.2 Predicted vs. observed ages

A striking characteristic comparing the modelled shape of isotherms and measured AFT ages along the Gotthard transect is the incompatibility of the most complex model 3, including spatially variable thermal conductivities and heat production rates. A possible explanation could be that measured radioactivities in rocks of the Gotthard road tunnel and resulting heat production rates are not representative for the entire lithologic unit and thus cannot be extrapolated straightforward. Alternatively, perturbation of isotherms may be compensated due to spatially variable exhumation rates increasing to the south, which is likely when the deduced exhumation rates are considered. Mean exhumation rates between 10 and 6 Ma are higher on the southern flank of the Gotthard massif as compared to the northern flank (Fig. 3). The present-day uplift rates show the same trend (Kahle 1997). Repeating model run 3 with exhumation rates increasing from north (0.45 km Ma^{-1}) to south (0.55 km Ma^{-1}) results in an AFT age pattern similar to that measured for the surface and tunnel samples (Fig. 8). These exhumation rates are optimized to match the measured AFT ages and AER derived exhumation rates. Thus small spatial differences in exhumation rates are able to compensate and mask the perturbation of isotherms due to other thermal parameters. Therefore we conclude that measured AFT age variations along the Gotthard road tunnel (6.2±0.6 Ma) do not preclude any presented model or palaeotopographic evolution. The Gotthard transect, however, is characterized by steady exhumation rates (Schaer et al. 1975; Wagner et al. 1977) and more or less vertically oriented tectonic structures and boundaries (Fig. 1b), facilitating the generation of a steady-state topography with spatially invariant ridges and valleys (Willett & Brandon 2002). But steady-state conditions are rarely achieved, especially concerning the

Late Neogene climate change and increased frequency in climatic oscillations (Whipple & Meade 2006). Most likely positive feedbacks between climate change, weathering, erosion and isostatic rebound led to increased relief during the last million years (e.g. England & Molnar 1990; Molnar & England 1990). However, resolving the latest Neogene (<5 Ma) exhumation history of the Gotthard massif is beyond the scope of this paper and needs apatite (U-Th)/He data.

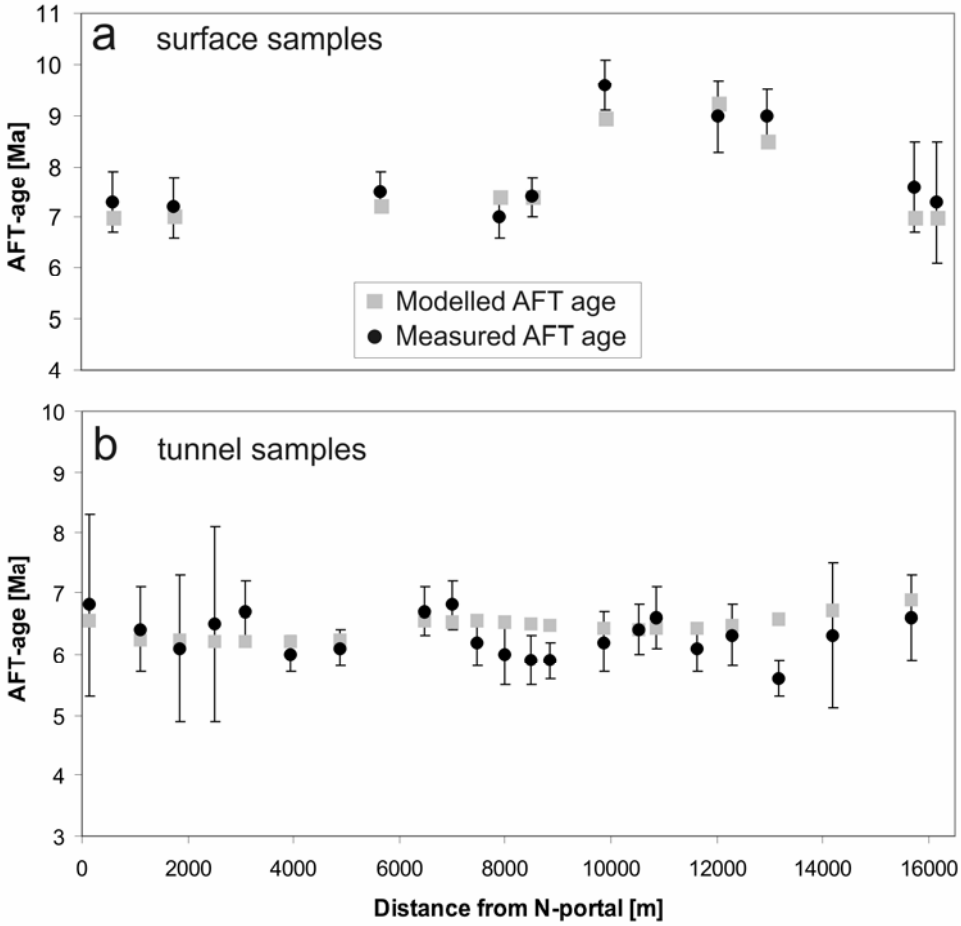

Fig. 8: Measured AFT ages (black dots, with 1σ age errors) and modelled AFT ages (grey squares) of (a) surface samples and (b) tunnel samples. Model parameters are that of model 3, but with the assumption that exhumation rates linearly increase from north (0.45 km Ma^{-1}) to south (0.55 km Ma^{-1}).

7 Conclusions

Apatite fission track data along the Gotthard road tunnel and its corresponding surface line are compared with 3D numerical thermal modelling results. Modelling allows to investigate the interplay and relative importance of 3D topography, spatially variable thermal conductivities, heat production rates, and exhumation rates on the shape of low-temperature isotherms. Additionally, the possible impact of advective and convective heat transport was investigated. The following conclusions were obtained:

- AER of AFT ages yield exhumation rates of 0.35±0.1 km Ma^{-1} (northern flank of the Gotthard transect) and 0.5±0.2 km Ma^{-1} (southern flank), similar to previously published data (Schaer et al. 1975; Michalski & Soom 1990).
- Measured AFT ages from tunnel samples are around 6.2 Ma (5.6 to 6.8 Ma) with no significant trend. A perturbation of AFT ages due to topography, with young ages correlating

with maximum overburden, is not visible along the Gotthard road tunnel. Because AFT age errors range from 5-25% (0.3-1.6 Ma), a perturbation of ~0.6 Ma will mostly remain hidden behind the data scatter.
- Modelling reveals that spatially variable heat production and exhumation rates strongly influence the shape of near-surface isotherms and need to be considered for the interpretation of low-temperature thermochronological data. In the specific case of the Gotthard transect the modelled perturbation of the 110 °C isotherm is in the range of 150 to 550 m (corresponding difference of AFT ages along the tunnel is between 0.3 to 1.2 Ma), depending on the input parameters and boundary conditions.
- This study illustrates that topography-induced perturbation of isotherms can be neglected for the interpretation of AFT ages under the given boundary conditions (topographic wavelength: 12 km, relief: 1.5 km, exhumation rate: 0.45 km Ma^{-1}) and petrophysical parameters of the Gotthard transect, such as thermal conductivities.

Acknowledgments

This study was funded by the German Science Foundation (DFG), project SP 673/2. Gerlinde Höckh, Dorothea Mühlbayer-Renner, and Dagmar Kost (Universität Tübingen) are gratefully acknowledged for mineral separation. Thanks also to T. Wenzel (Universität Tübingen) for his support during electron microprobe analysis. M. Zattin and P. van der Beek are thanked for their constructive reviews of this manuscript.

References

Braun, J., 2002. Quantifying the effect of recent relief changes on age-elevation relationships. Earth and Planetary Science Letters, 200: 331-343.

Braun, J., 2003. Pecube: a new finite-element code to solve the 3D heat equation including the effects of a time-varying, finite amplitude surface topography. Computers & Geosciences, 29: 787-794.

Burtner, R.L., Nigrini, A. and Donelick, R.A., 1994. Thermochronology of Lower Cretaceous source rocks in the Idaho-Wyoming thrust belt. AAPG Bulletin, 78(10): 1613-1636.

Busslinger, A. and Rybach, L., 1999. Felstemperaturprognose für tiefliegende Tunnel. TUNNEL, 1: 24-32.

Dahinden, T., 2001. Verschiebungsmessungen im Gotthardgebiet. Diploma thesis, ETH Zürich.

Dunkl, I., 2000. Trackkey: a windows program for calculation and graphical presentation of fission track data. Computers & Geosciences, 28(1): 3-12.

Ehlers, T.A. et al., 2005. Computational tools for low-temperature thermochronometer interpretation. Reviews in Mineralogy & Geochemistry, 58: 589-622.

Ehlers, T.A. and Farley, K.A., 2003. Apatite (U-Th)/He thermochronometry: methods and applications to problems in tectonic and surface processes. Earth and Planetary Science Letters, 206: 1-14.

England, P. and Molnar, P., 1990. Surface uplift, uplift of rocks, and exhumation of rocks. Geology, 18: 1173-1177.

Foeken, J.P.T., Persano, C., Stuart, F.M. and ter Voorde, M., 2007. Role of topography in isotherm perturbation: Apatite (U-Th)/He and fission track results from the Malta tunnel, Tauern Window, Austria. Tectonics, 26.

Frey, M. and Mählmann Ferreiro, R., 1999. Alpine metamorphism of the Central Alps. Schweizerische Mineralogische und Petrographische Mitteilungen, 79(1): 135-154.

Galbraith, R.F. and Laslett, G.M., 1993. Statistical models for mixed fission track ages. Nuclear Tracks and Radiation measurements, 21: 459-470.
Gleadow, A.J.W., 1981. Fission-track dating methods: What are the real alternatives? Nuclear Tracks and Radiation measurements, 5(1/2): 3-14.
Hampel, A. and Hetzel, R., 2006. Response of normal faults to glacial-interglacial fluctuations of ice and water masses on Earth's surface. Journal of Geophysical Research, 111.
House, M.A., Wernicke, B.P. and Farley, K.A., 1998. Dating topography of the Sierra Nevada, California, using apatite (U-Th)/He ages. Nature, 396: 66-69.
House, M.A., Wernicke, B.P. and Farley, K.A., 2001. Paleo-Geomorphology of the Sierra Nevada, California, from (U-Th)/He ages in apatite. American Journal of Science, 301: 77-102.
Hurford, A.J. and Green, P.F., 1982. A users' guide to fission track dating calibration. Earth and Planetary Science Letters, 59: 343-354.
Hurford, A.J. and Green, P.F., 1983. The Zeta age calibration of fission-track dating. Chemical Geology (Isotope Geoscience Section), 41: 285-317.
Kahle, H.-G., 1997. Recent crustal movements, geoid and density distribution; contribution from integrated satellite and terrestrial measurements. In: O.A. Pfiffner, P. Lehner, P. Heitzmann, S. Müller and A. Steck (Editors), Results of NRP 20; deep structure of the Swiss Alps. Birkhaeuser Verlag, Basel, pp. 251-259.
Kappelmeyer, O. and Haenel, R., 1974. Geothermics with Special Reference to Application. Geoexploration Monographs. Gebrüder Bornträger, 238 pp.
Keller, F., Wanner, H. and Schneider, T.R., 1987. Geologischer Schlussbericht Gotthard-Strassentunnel. Beiträge zur Geologie der Schweiz: Geotechnische Serie 70, Bern, 67 pp.
Ketcham, R.A., Carter, A., Donelick, R.A., Barbarand, J. and Hurford, A.J., 2007. Improved modeling of fission-track annealing in apatite. American Mineralogist, 92: 799-810.
Kohl, T., Signorelli, S. and Rybach, L., 2001. Three-dimensional (3-D) thermal investigation below high Alpine topography. Physics of the Earth and Planetary Interiors, 126: 195-210.
Labhart, T.P., 1977. Aarmassiv und Gotthardmassiv. Sammlung geologischer Führer, 63. Gebr. Bornträger, Berlin, 173 pp.
Labhart, T.P., 1999. Aarmassiv, Gotthardmassiv und Tavetscher Zwischenmassiv: Aufbau und Entstehungsgeschichte. In: S. Löw and R. Wyss (Editors), Vorerkundung und Prognose der Basistunnels am Gotthard und am Lötschberg. A. A. Balkema, Rotterdam, pp. 31-43.
Luetzenkirchen, V.H., 2002. Structural geology and hydrogeology of brittle fault zones in the central eastern Gotthard massif, Switzerland. PhD thesis, ETH Zürich.
Mancktelow, N.S. and Grasemann, B., 1997. Time-dependent effects of heat advection and topography on cooling histories during erosion. Tectonophysics, 270: 167-195.
Michalski, I. and Soom, M., 1990. The Alpine thermo-tectonic evolution of the Aar and Gotthard massifs, Central Switzerland: Fission Track ages on zircon and apatite and K-Ar mica ages. Schweizerische Mineralogische und Petrographische Mitteilungen, 70: 373-387.
Molnar, P. and England, P., 1990. Late Cenozoic uplift of mountain ranges and global climate change: chicken or egg? Nature, 346: 29-34.
Naeser, C.W., 1978. Fission track dating. U.S. Geological Survey Open-File Report: 76-190.
Niethammer, G., 1910. Die Wärmeverteilung im Simplon. Ecologae Geologicae Helvetiae, 11: 96-120.
Parrish, R.R., 1983. Cenozoic thermal evolution and tectonics of the Coast Mountains of British Columbia, 1. Fission track dating, apparent uplift rates, and patterns of uplift. Tectonics, 2(6): 601-631.

Pastorelli, S., Marini, L. and Hunziker, J.-C., 2001. Chemistry, isotope values (δD, δ18O, δ34SSO4) and temperatures of the water inflows in two Gotthard tunnels, Swiss Alps. Applied Geochemistry, 16: 633-649.

Persaud, M. and Pfiffner, O.A., 2004. Active deformation in the eastern Swiss Alps: post-glacial faults, seismicity and surface uplift. Tectonophysics, 385: 59-84.

Pfiffner, O.A. and Heitzmann, P., 1997. Geological interpretation of the seismic profiles of the Central Traverse (lines C1, C2 and C3-north), In: (Pfiffner et al. 1997) Deep Structure of the Swiss Alps: results of NRP 20. 115-122.

Rahn, M.K. and Grasemann, B., 1999. Fission track and numerical thermal modeling of differential exhumation of the Glarus thrust plane (Switzerland). Earth and Planetary Science Letters, 169: 245-259.

Reiners, P.W. et al., 2003. Post-orogenic evolution of the Dabie Shan, eastern China, from (U-Th)/He and Fission-Track Thermochronology. American Journal of Science, 303: 489-518.

Šafanda, J., 1999. Ground surface temperature as a function of slope angle and slope orientation and its effect on the subsurface temperature field. Tectonophysics, 306: 367-375.

Schaer, J.P., Reimer, G.M. and Wagner, G.A., 1975. Actual and ancient uplift rate in the Gotthard region, Swiss Alps: A comparison between precise levelling and Fission-Track Apatite age. Tectonophysics, 29: 293-300.

Schaltegger, U., 1994. Unravelling the pre-Mesozoic history of Aar and Gotthard massifs (Central Alps) by isotopic dating - a review. Schweizerische Mineralogische und Petrographische Mitteilungen, 74: 41-51.

Schmid, S.M., Pfiffner, O.A., Froitzheim, N., Schönbron, G. and Kissling, E., 1996. Geophysical-geological transect and tectonic evolution of the Swiss-Italian Alps. Tectonics, 15: 1036-1064.

Stüwe, K., 2007. Geodynamics of the Lithosphere - Quantitative Description of Geological Problems. Springer-Verlag, Berlin, 493 pp.

Stüwe, K. and Hintermüller, M., 2000. Topography and isotherms revisited: the influence of laterally migrating drainage divides. Earth and Planetary Science Letters, 184: 287-303.

Stüwe, K., White, L. and Brown, R., 1994. The influence of eroding topography on steady-state isotherms. Application to fission track analysis. Earth and Planetary Science Letters, 124: 63-74.

Turcotte, D.L. and Schubert, G., 1982. Geodynamics - Applications of Continuum Physics to Geological Problems. John Wiley & Sons, New York, 450 pp.

Ustaszewski, M., Hampel, A. and Pfiffner, O.A., 2007. Formation of active composite faults in the Swiss Alps: the complex interplay of tectonics, gravitation and postglacial unloading. Geophysical Research Abstracts, 9.

Wagner, G.A. and Reimer, G.M., 1972. Fission track tectonics: The tectonic interpretation of fission track apatite ages. Earth and Planetary Science Letters, 14: 263-268.

Wagner, G.A., Reimer, G.M. and Jäger, E., 1977. Cooling ages derived by apatite fission track, mica Rb-Sr and K-Ar dating: the uplift and cooling history of the Central Alps. Mem. Ist. Geol. Mineral. Univ. Padova, 30: 1-27.

Whipp, D.M. and Ehlers, T.A., 2007. Influence of Groundwater flow on thermochronometer-derived exhumation rates in the central Nepalese Himalaya. Geology, 35: 851-854.

Whipple, K.X. and Meade, B.J., 2006. Orogen response to changes in climatic and tectonic forcing. Earth and Planetary Science Letters, 243: 218-228.

Willett, S.D. and Brandon, M.T., 2002. On steady states in mountain belts. Geology, 30: 175-178.

Wyder, R.F. and Mullis, J., 1998. Fluid impregnation and development of fault breccias in the Tavetsch basement rocks (Sedrun, Central Swiss Alps). Tectonophysics, 194: 89-107.

Supplementary data

What perturbs isotherms? An assessment using fission track thermochronology and thermal modelling along the Gotthard transect, Central Alps

Apatite composition (weight-%) of 15 samples from the Gotthard road tunnel and corresponding surface transect and from Durango, with averages and standard deviations calculated from totally 320 electron microprobe analyses

Sample	n	F	Cl	SiO_2	MnO	Ce_2O_3	SrO	P_2O_5	CaO	Dpar
MRP 229	10	3.23±0.19	0.100±0.020	0.030±0.010	na	0.04±0.02	bd	44.00±0.61	54.68±0.37	1.42±0.09
MRP 231	49	3.70±0.10	bd	0.012±0.020	0.054±0.014	na	0.036±0.043	43.90±0.50	54.90±0.70	1.26±0.11
MRP 232	49	3.45±0.19	0.013±0.006	0.023±0.044	0.103±0.039	na	0.040±0.028	43.80±0.40	54.80±0.30	1.34±0.13
MRP 233	9	2.72±0.19	0.028±0.004	0.010±0.010	na	0.04±0.01	0.040±0.020	40.81±0.56	54.65±0.32	1.57±0.15
MRP 234	10	3.88±0.22	bd	0.120±0.090	na	0.11±0.05	bd	43.69±0.77	54.15±0.57	1.41±0.10
MRP 236	10	4.02±0.18	bd	0.150±0.100	na	0.13±0.05	bd	41.11±1.00	54.12±0.60	1.29±0.14
MRP 239	10	4.03±0.23	bd	0.040±0.050	na	0.06±0.02	bd	44.46±0.50	54.58±0.28	1.25±0.10
MRP 241	7	3.48±0.08	bd	0.030±0.020	na	0.02±0.02	0.020±0.020	43.62±0.40	54.71±0.10	1.47±0.09
MRP 242	10	3.62±0.19	bd	0.040±0.010	na	0.05±0.03	0.020±0.020	42.40±0.24	54.87±0.25	1.41±0.09
MRP 244	49	3.47±0.19	bd	0.057±0.071	0.071±0.046	na	0.100±0.065	43.60±0.40	54.90±0.40	1.32±0.14
MRP 245	5	3.27±0.10	bd	0.250±0.120	na	0.19±0.09	0.080±0.030	42.85±0.78	54.43±0.42	1.63±0.10
MRP 247	12	4.09±0.11	bd	0.210±0.080	na	0.16±0.08	0.020±0.010	44.58±0.48	54.01±0.35	1.13±0.14
MRP 248	10	4.15±0.23	bd	0.160±0.140	na	0.14±0.04	bd	43.99±0.36	54.04±0.25	1.12±0.12
MRP 249	10	3.75±0.22	0.006±0.005	0.150±0.040	na	0.21±0.05	0.020±0.020	43.65±0.77	54.48±0.26	1.34±0.12
MRP 291	50	4.03±0.22	bd	0.025±0.098	0.520±0.290	na	0.012±0.016	43.40±0.40	54.10±0.60	1.26±0.12
Durango	20	3.61±0.09	0.410±0.020	0.480±0.050	0.010±0.010	0.71±0.04	0.050±0.020	42.78±0.75	53.46±0.33	1.63±0.11

n is the number of measurements; na means not measured; bd means below detection, with detection limits in ppm:
F 140, Cl 40, SiO2 100, Ce2O3 180, SrO 170, P2O5 470, CaO 105

Shaded relief overview of the 3D finite difference model of the Gotthard transect with coordinates of the Swiss reference system. Different colours refer to the involved geological units: Aar massif, Gotthard massif, Tavetsch massif, Urseren zone and Schistes lustrées.

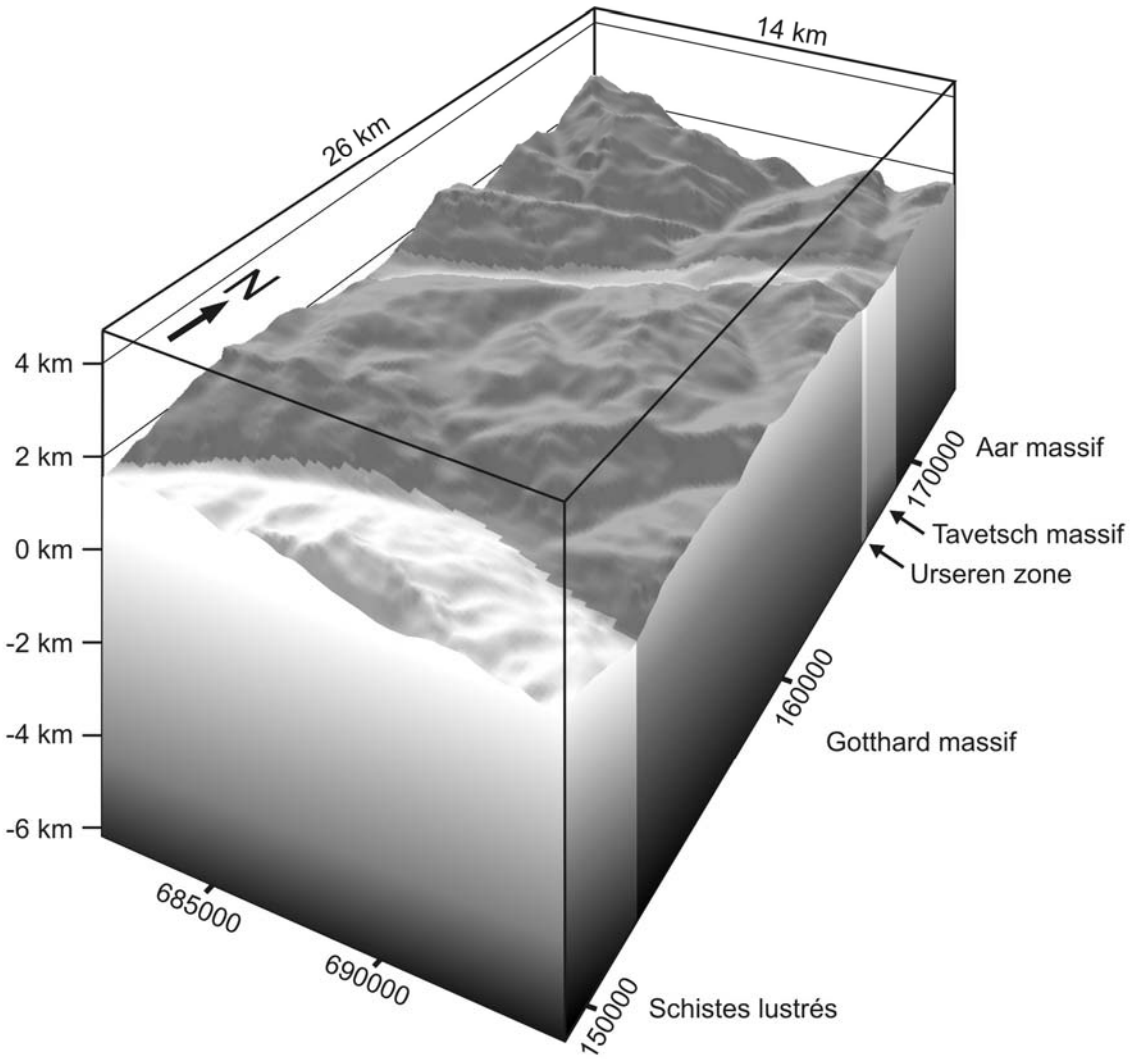

Geometrical, physical and thermal parameters used for numerical modelling

Parameter	**Description**	**Value**	**Unit**
T	temperature	variable	°C
t	time	variable	s
x,y,z	Cartesian coordinates	variable	m
$\Delta x,\Delta y,\Delta z$	nodes spacing	132.9	m
S	heat production	see Table 2	W/kg
u	exhumation rate	0.45	km/Myr
ρ	density	2 700	kg/m³
c_p	specific heat	1 000	J/kg*K
k	thermal conductivity	see Table 2	W/K*m
T_0	air T at sea level	11.88	°C
α	atmospheric lapse rate	0.0046	°C/m
G_B	vertical bottom geothermal gradient	20	°C/km

Tectonic control on the late stage exhumation of the Aar Massif (Switzerland): Constraints from apatite fission track and (U-Th)/He data

John Reinecker[1], Martin Danišík[1], Claudia Schmid[1], Christoph Glotzbach[1], Meinert Rahn[2], Wolfgang Frisch[1], Cornelia Spiegel[3]

[1] Institute for Geosciences, University of Tübingen, Sigwartstrasse 10, 72076 Tübingen, Germany
[2] Mineralogical-Geochemical Institute, University of Freiburg, Albertstrasse 23b, 79104 Freiburg, Germany
[3] FB5 - Geosciences, University of Bremen, Postfach 330440, 28334 Bremen, Germany
corresponding author: reinecker@uni-tuebingen.de

Abstract
We examine the hypothesis that Pliocene exhumation of the external massifs in the Central Alps is controlled by climatic change. New thermochronological data from the western Gastern-Aar massif are used to investigate timing, extent, and reasons for Neogene exhumation. Our data reveal that exhumation was constant with 0.5 km/Myr over the last 10 Myr in the north. In the southern part, exhumation was in the same order until ~3.5 Ma but then increased gradually towards the south to values of up to 1.2 km/Myr, resulting in overall northward tilting of the western Aar massif. We explain accelerated exhumation in the south after ~3.5 Ma mainly by tectonic denudation along the Rhône-Simplon fault and discuss changes in deep crustal configuration, which may have triggered south directed normal faulting of the hanging wall. We propose that the Rhône river got structurally trapped by the Rhône-Simplon normal fault zone, which additionally enhanced erosion in the south of the Aar massif. Climatic forcing may have an impact in the very late stage of exhumation due to Alpine glaciation in the late Pliocene.

1. Introduction

A threefold increase in global terrigenous sediment accumulation rates in the latest Neogene [*Hay et al.*, 1988] has been attributed alternatively to climatic or tectonic forcing [*Molnar and England*, 1990; *Raymo and Ruddiman*, 1992]. The increase in Pliocene sedimentation rates in the European Alps [*Kuhlemann et al.*, 2002] was attributed to accelerated erosion of the Alpine hinterland, particularly of the Alpine external massifs, which in turn has been explained by climatic reasons. *Cederbom et al.* [2004] described increased exhumation of the foreland during the Late Miocene / Early Pliocene, and suggested that the increased exhumation of the foreland was caused by accelerated erosion of the Alps and subsequent isostatic rebound of the underlying plate. According to these authors, erosion was an effect of increased precipitation due to the increased atmospheric moisture in Eurasia. *Willett et al.* [2006] argued for accelerated exhumation during the latest Miocene due to base-level drop in response to the Messinian Salinity Crisis. High erosion was sustained by subsequent increase in precipitation during the early Pliocene.
The aim of our study is to examine the hypothesis that the exhumation of the external massifs (in particular the Gastern-Aar massif, Central Switzerland) during the Pliocene is mainly forced by climatic change. We use fission track and (U-Th)/He dating on apatites from a transect along the recently excavated, 35 km long Lötschberg NEAT ("Neue Eisenbahn-Alpentransversale") base tunnel to investigate timing, extent, and reasons for Pliocene exhumation. Our results contribute to the discussion on control mechanisms for the increase in sediment accumulation rates during the latest Neogene.

2. Geologic Setting and Previous Work

The Gastern-Aar massif in Central Switzerland is the largest of the Alpine external crystalline massifs, which form a discontinuous belt in the Central and Western Alps (Fig. 1). The external crystalline massifs are part of the pre-Alpine European crust. The Gastern-Aar massif comprises two units: the Aar massif sensu stricto (Altkristallin, Bietschhorn granite, and Baltschieder granodiorite; Fig. 2) and the smaller Gastern massif (Lauterbrunnen crystalline and Gastern granite) in the northwest. The Altkristallin and the Lauterbrunnen crystalline consists of migmatites and pre-Variscan gneisses, with a complex polymetamorphic evolution [e.g., *Abrecht*, 1994; *Schaltegger*, 1994], whereas the granitoids are Late Variscan sub-alkaline intrusive bodies. During the late Alpine orogenic cycle, the Gastern-Aar massif was overthrust by Helvetic and Penninic nappes, leading to an anchi- to low epizonal metamorphic overprint with increasing temperatures from north to south, reaching peak metamorphism around 35-30 Ma [*Frey and Ferreiro-Mählmann*, 1999]. Subsequent doming of the entire nappe stack induced large scale bending of the formerly flat lying Helvetic basal thrust (Fig. 2B and 3A; [*Herwegh and Pfiffner*, 2005]).

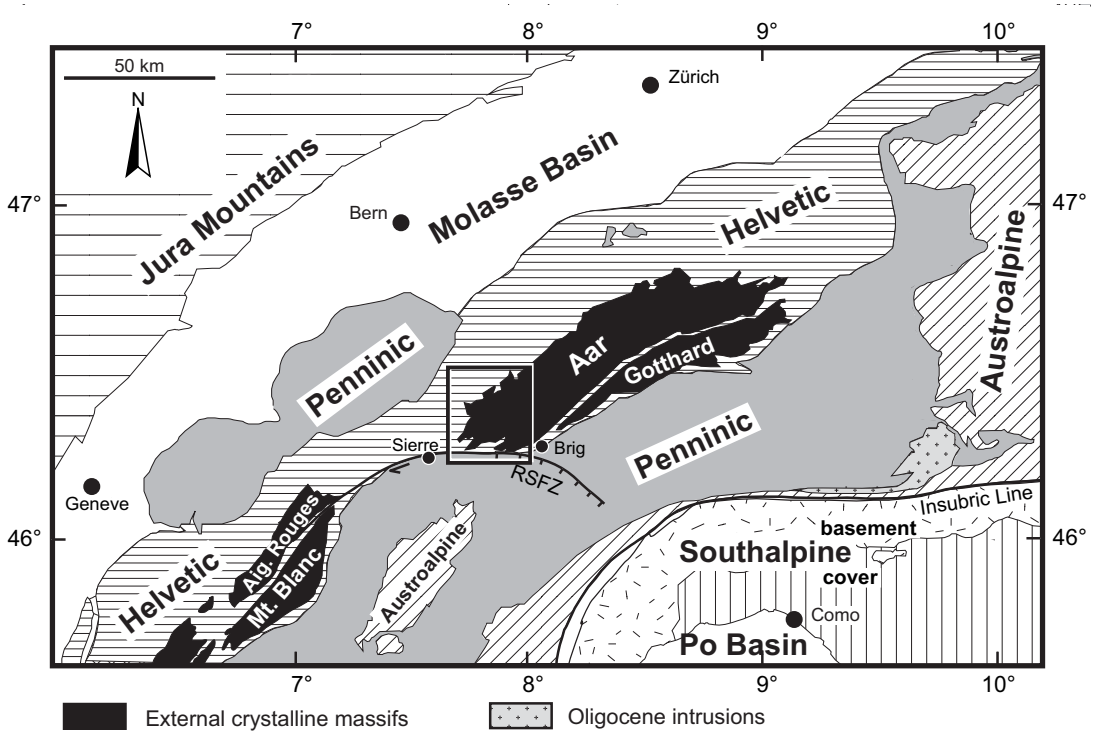

Figure 1: Simplified tectonic map of the Central Alps. The black square indicates the study area in the southwestern part of the Aar massif.

For the tectonic evolution, three fault zones are of major importance in our study area: (i) the Helvetic basal thrust, (ii) the Rote-Kuh-Gampel fault, and (iii) the Rhône-Simplon fault south of the Lötschberg transect, one of the most important and still active tectonic structures in the Central Alps [e.g., *Steck and Hunziker*, 1994; *Seward and Mancktelow*, 1994; *Maurer et al.*, 1997; *Sue et al.*, 2007] (Fig. 3A). The Rhône-Simplon fault zone follows the basal Penninic thrust beneath the Rhône valley.

The crystalline section of the Lötschberg NEAT tunnel is situated between 640 to 840 m above sea level. Approximately 500 m above and fairly parallel to the Lötschberg base tunnel runs the old railway tunnel. The local relief along the transect is ~2 km and the topographic wavelengths is ~10 km (Fig. 2B). Recent surface uplift rates from repeated precise leveling

across the Gastern-Aar massif are in the order of 0.7 mm/yr in the north and 1.4 mm/yr in the south [*Kahle et al.*, 1997].
Apatite fission track (AFT) studies of the Gastern-Aar massif region have been performed by *Schaer et al.* [1975], *Wagner et al.* [1977], *Soom* [1990], and *Michalski and Soom* [1990]. These yielded AFT ages between 7 and 2 Ma, decreasing from north to south and from east to west. The ages suggest a relatively steady exhumation rate of about 0.8 km/Myr during the last 7 Myr. In the following we extend the work of these authors and present new AFT and (U-Th)/He data (AHe) from along the Lötschberg transect in order to refine the late-stage exhumation history.

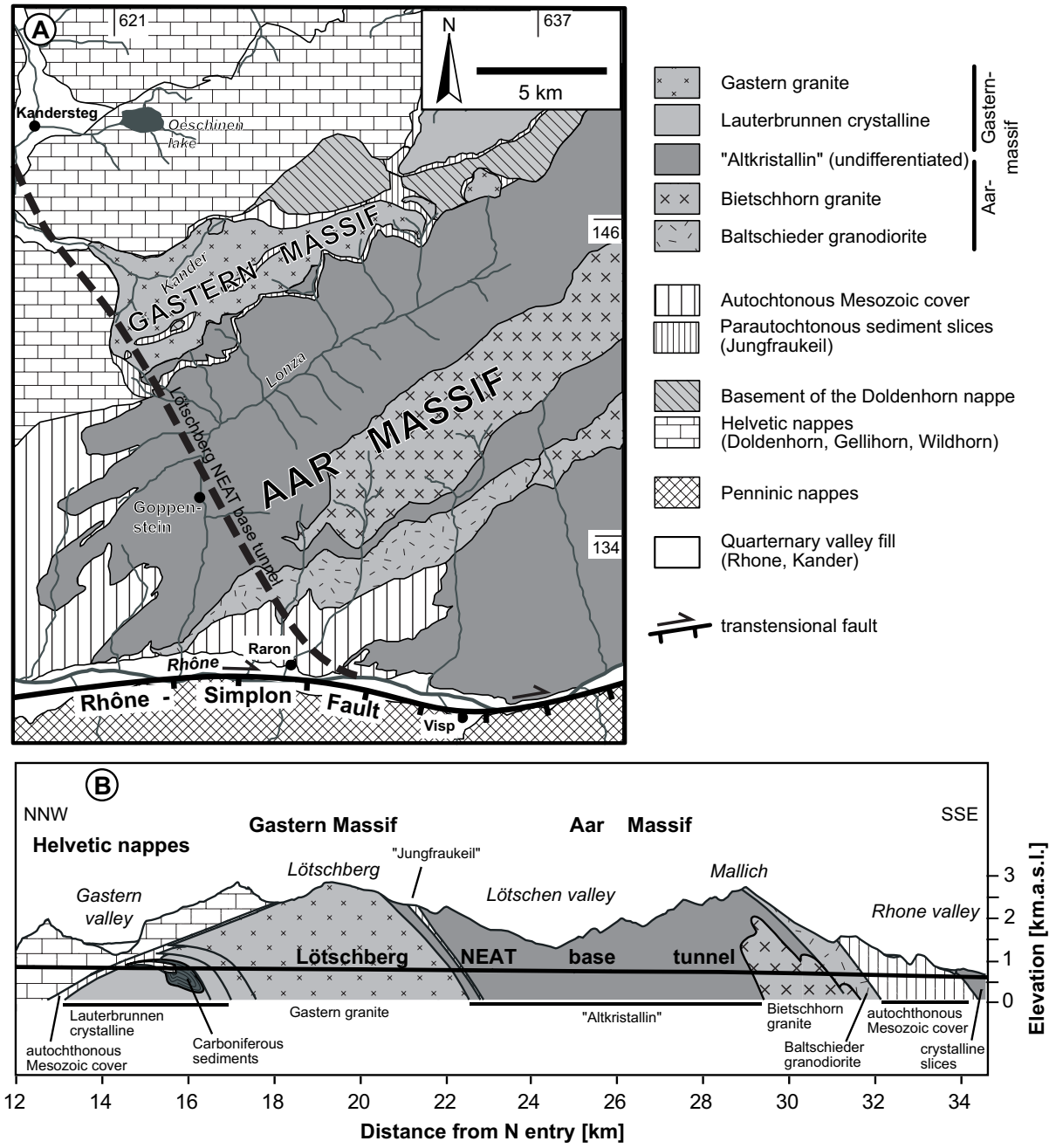

Figure 2: (A) Geological map of the southwestern (Gastern-)Aar massif and **(B)** profile along the studied transect [after *Ziegler et al.*, 2006]. Coordinates in (A) refer to the Swiss grid system.

3. Sampling strategy and analytical techniques

Combining AFT and AHe thermochronology typically monitors the thermal evolution of exhuming rocks between ~110 and 40 °C. 25 rock samples were taken from the Lötschberg NEAT tunnel, from the old Lötschberg railway tunnel, from reconnaissance drillings, and the surface directly above the base tunnel (Fig. 2 and 3A, Table 1) for AFT and AHe thermochronology. Kinetic variability of apatite was checked by Dpar measurement of all analyzed samples [*Burtner et al.*, 1994] and additionally by electron microprobe analysis of selected samples.

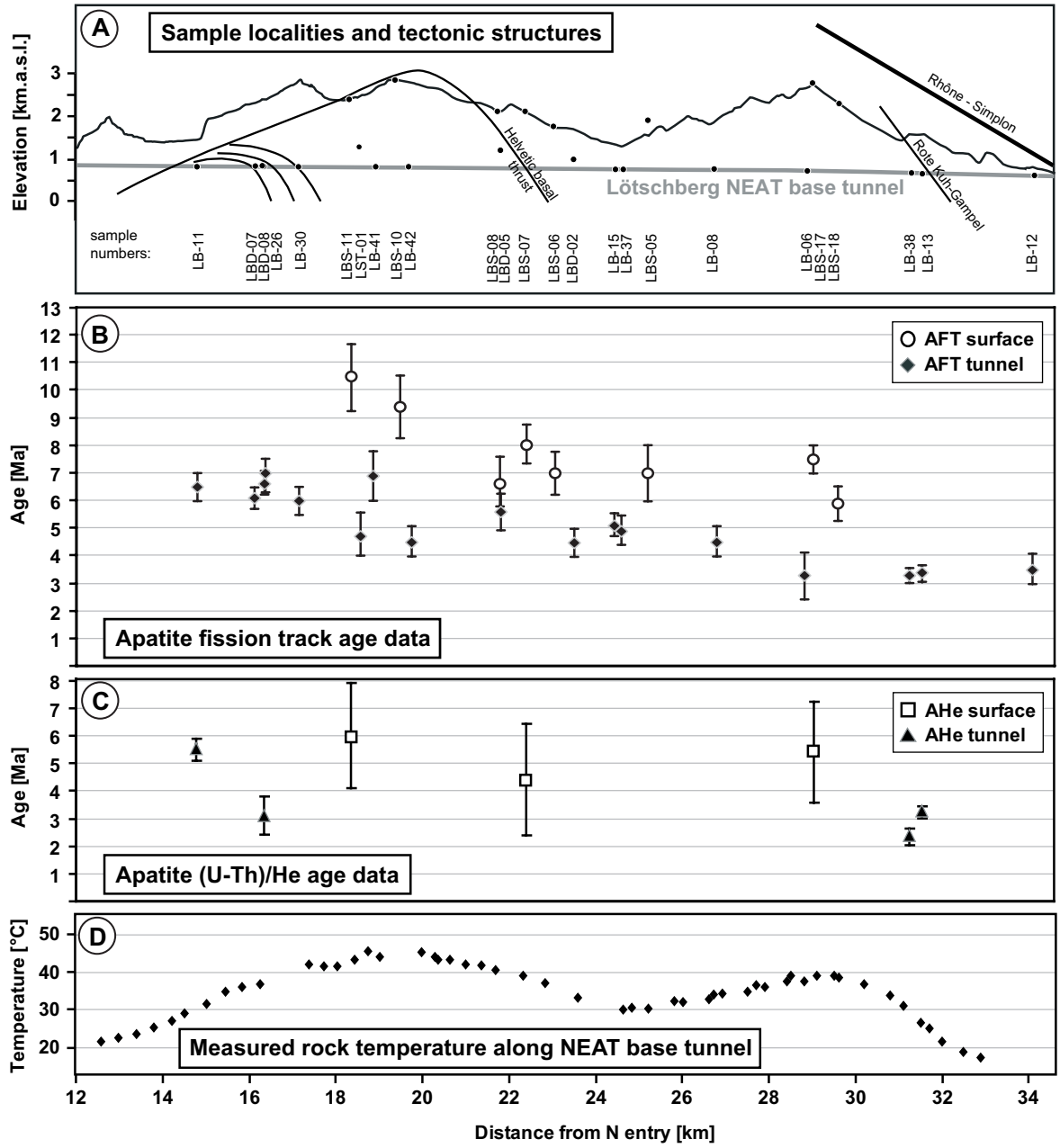

Figure 3: (A) Sample locations and main tectonic structures, **(B)** apatite fission track (AFT) ages (with 1σ error), and **(C)** apatite (U-Th)/He (AHe) ages (with standard deviation) along the transect. **(D)** Rock temperatures measured in the base tunnel [after pers. comm. with H.-J. Ziegler, R. Ottiger, F. Giovanoli, and M. Weh]. Note, that there is no indication of anomalous high or low temperatures due to water inflow except in the very south. Here cooling due to groundwater flow along the Rote-Kuh-Gampel fault and the adjacent autochthonous Mesozoic cover is evident.

Table 1: Results of apatite fission track thermochronology. Track lengths were mainly measured on Cf-irradiated samples.

Sample	Localition / Tm*	Coordinates[§]		Elevation	Lithology	U	Cryst.[$]	Spontaneous		Induced		Dosimeter		$P(\chi^2)$[#]	Dispersion	FT age[€]	Mean track length ± SD [µm]		No. of	D_{par}[ö]
		Easting	Northing	[m]		[ppm]		ρ_s	(N_s)	ρ_i	(N_i)	ρ_d	(N_d)	(%)		[Ma ± 1σ]		(c-axis projected)	tracks	[µm]
tunnel and drilling samples																				
LB-06	NEAT tunnel / 28826	626500	132870	684	gneiss	16	23	0.19	(17)	9.018	(806)	7.931	(7713)	67	0.02	**3.3 ± 0.8**	12.61 ± 1.17	(13.56 ± 0.89)	12	1.39
LB-08	NEAT tunnel / 26796	625480	134690	704	gneiss	68	25	1.322	(99)	38.319	(2869)	6.645	(6290)	96	0.00	**4.5 ± 0.5**	n.d.	n.d.	n.d.	1.71
LB-11	NEAT tunnel / 14779	618920	144760	826	granitoid	49	25	1.406	(216)	33.586	(5161)	7.972	(7713)	92	0.00	**6.5 ± 0.5**	11.97 ± 1.92	(13.29 ± 1.44)	101	1.73
LB-12	NEAT tunnel / 34049	629875	128975	646	gneiss	24	25	0.392	(56)	17.222	(2459)	7.967	(7855)	39	0.09	**3.5 ± 0.5**	n.d.	n.d.	n.d.	1.66
LB-13	NEAT tunnel / 32412	625700	130000	641	granodiorite	93	25	1.452	(144)	66.024	(6548)	8.054	(7713)	74	0.02	**3.4 ± 0.3**	12.43 ± 2.26	(13.70 ± 1.59)	75	1.63
LB-15	NEAT tunnel / 24426	624280	136760	729	gneiss	113	15	2.509	(236)	75.043	(7060)	7.891	(7713)	25	0.14	**5.1 ± 0.4**	n.d.	n.d.	n.d.	1.71
LB-26	NEAT tunnel / 16353	619850	143530	810	granite	53	25	1.539	(192)	34.316	(4281)	8.062	(7855)	67	0.01	**7.0 ± 0.6**	12.97 ± 1.48	(14.41 ± 0.91)	62	1.81
LB-30	NEAT tunnel / 17131	620330	142900	804	granite	32	25	0.92	(163)	23.919	(4238)	7.991	(7855)	78	0.01	**6.0 ± 0.5**	n.d.	n.d.	n.d.	1.73
LB-37	NEAT tunnel / 24589	624370	136610	728	gneiss	41	25	0.882	(140)	28.305	(4491)	8.027	(7855)	79	0.00	**4.9 ± 0.5**	n.d.	n.d.	n.d.	1.93
LB-38	NEAT tunnel / 31256	627750	130750	666	granodiorite	64	25	0.922	(145)	43.425	(6826)	7.955	(7855)	82	0.01	**3.3 ± 0.3**	n.d.	n.d.	n.d.	1.62
LB-41	NEAT tunnel / 18846	621390	141520	786	granite	22	25	0.647	(67)	14.349	(1485)	7.855	(7624)	44	0.07	**6.9 ± 0.9**	n.d.	n.d.	n.d.	1.93
LB-42	NEAT tunnel / 19736	621920	140820	777	granite	54	24	1.156	(75)	39.676	(2574)	7.864	(7624)	81	0.00	**4.5 ± 0.5**	n.d.	n.d.	n.d.	1.62
LBD-02	drill core "Goltschried", SB 95/23	624040	137840	914	gneiss	61	25	1.174	(74)	40.435	(2548)	7.846	(7624)	84	0.00	**4.4 ± 0.5**	n.d.	n.d.	n.d.	1.66
LBD-05	drill core "Jungfraukeil", SB 93/15	623410	138980	1155	gneiss	38	20	0.938	(77)	25.924	(2129)	7.838	(7624)	36	0.12	**5.6 ± 0.7**	n.d.	n.d.	n.d.	1.79
LBD-07	NEAT tunnel / 16257	619800	143610	810	granitoid	102	25	2.719	(372)	69.492	(9507)	7.979	(7855)	14	0.07	**6.1 ± 0.4**	n.d.	n.d.	n.d.	1.74
LBD-08	NEAT tunnel / 16332	619850	143530	810	granitoid	93	25	2.71	(426)	64.138	(10082)	8.098	(7855)	96	0.00	**6.7 ± 0.4**	n.d.	n.d.	n.d.	1.69
LST-01	old railway tunnel / 7700	621630	141590	1250	granite	77	29	1.59	(60)	43.705	(1649)	6.111	(5999)	2	0.47	**4.8 ± 0.8**	n.d.	n.d.	n.d.	1.46
surface samples																				
LBS-05	In steinigen Gräbun	625000	136280	1850	amphibolite	43	25	1.278	(70)	23.037	(1262)	6.151	(5999)	46	0.25	**7.0 ± 1.0**	n.d.	n.d.	n.d.	1.88
LBS-06	Dornbach	623650	137820	1720	gneiss	33	25	0.931	(98)	21.263	(2238)	8.110	(7855)	39	0.16	**7.0 ± 0.8**	n.d.	n.d.	n.d.	1.50
LBS-07	Fleischweng, Restialp	623240	138400	2090	gneiss	47	25	1.807	(179)	33.882	(3357)	7.809	(7713)	51	0.03	**8.1 ± 0.7**	13.32 ± 1.47	(14.53 ± 1.12)	58	1.85
LBS-08	Kummenalp	623010	139090	2070	gneiss	18	25	0.538	(62)	12.549	(1445)	8.050	(7855)	50	0.04	**6.7 ± 0.9**	n.d.	n.d.	n.d.	1.73
LBS-10	Lötschenpass	621770	141060	2830	granite	50	30	1.982	(114)	27.692	(1593)	6.230	(5999)	11	0.25	**9.4 ± 1.1**	14.12 ± 1.30	n.d.	28	1.77
LBS-11	Lötschegletscher	621120	142000	2364	granite	21	22	1.079	(94)	12.373	(1078)	6.211	(5999)	99	0.00	**10.5 ± 1.2**	12.63 ± 2.58	(14.15 ± 1.49)	100	1.90
LBS-17	Mallich	626540	132780	2700	granodiorite	83	25	2.594	(330)	54.495	(6932)	8.086	(7855)	45	0.06	**7.5 ± 0.5**	12.99 ± 2.08	(14.47 ± 1.11)	100	1.86
LBS-18	W Färricha	626980	132490	2280	granodiorite	58	25	1.284	(119)	33.816	(3135)	8.038	(7855)	77	0.02	**5.9 ± 0.6**	n.d.	n.d.	n.d.	1.82

Note: Track densities (ρ) are given in 10^5 tr/cm^2; number of tracks counted (N) shown in brackets. *Tm: metres along tunnel from N entry. [§]Coordinates according to Swiss geodetic reference system. [$]Cryst.: number of dated apatite crystals. [#]$P(\chi^2)$: probability obtaining χ^2-value for n degree of freedom (where n = no. crystals - 1). [€]Central ages calculated using dosimeter glass CN 5 with ζ_{CN5} = 389.59 ± 8.39 yr/cm². [ö]D_{par}: etch pit diameter at surface parallel to c-axis. n.d.: not determined

3.1. Apatite fission track thermochronology

We have used the external detector method [*Naeser*, 1976; *Gleadow*, 1981] and the zeta calibration approach [*Hurford and Green*, 1982, 1983] for dating apatite samples. Apatite concentrates were prepared using standard magnetic and heavy liquid separation techniques. For fission track analysis, apatites were mounted in epoxy, ground and polished to reveal internal surfaces. Afterwards the mounts were etched with 5 M HNO_3 for 20 s at 20 ± 1 °C to reveal spontaneous tracks. Irradiation was carried out at the FRM-II reactor in Garching (TU München, Germany). Subsequently, mica detectors were etched to reveal induced tracks using 40 % HF at 20 ± 1 °C for ~35 min. Fission track analysis was carried out with an optical microscope (Zeiss Axioscope 2) under 1000x magnification using a dry objective. Ages are calculated with a zeta of 389.59 ± 8.39 yr/cm² (J. Reinecker) determined with dosimeter glass CN5 and Durango and Fish Canyon Tuff age standards. Calculation, visualization and statistics were performed with Trackkey 4.2g [*Dunkl*, 2000]. All apatite fission track ages are displayed as central ages and errors as ± 1σ [*Galbraith and Laslett*, 1993].

Because of the young ages and low U contents of most apatites, samples were irradiated with ^{252}Cf-derived fission fragments, thus forming additional etching channels and increase the number of etched confined tracks [*Donelick and Miller*, 1991]. ^{252}Cf-irradiation was performed at the University of Melbourne, Australia. Exposure time was 2.5 hours; distance from ^{252}Cf-source was 16 mm.

3.2. Apatite (U-Th)/He thermochronology (AHe)

Helium analyses were carried out in the Thermochronology Laboratory at the University of Tübingen. Apatite crystals were hand-picked under a stereomicroscope from apatite concentrates used for AFT analysis following strict selection procedures, with respect to morphology, size and purity of the crystals [*Farley*, 2002]. Afterwards the crystals were inspected at 200x magnification under cross-polarized light for inclusions (all dated crystals were free of visible inclusions). Each selected crystal was digitally photographed and measured. Six to nine single and multiple crystal aliquots were prepared per sample. In multiple aliquots, only grains with average radii in a close size range were selected so that the standard deviation of the alpha recoil correction factors [*Farley et al.*, 1996] was less than 0.5%. Grains were then loaded into degassed stainless steel capsules or Pt-tubes, which in turn were loaded into a resistance furnace or diode laser module connected to the He extraction line. After pumping to $<9 \times 10^{-6}$ Pa ($<9 \times 10^{-8}$ mbar), apatite grains were individually degassed at ~950 °C for 8 minutes in the furnace or for 5 minutes in the laser module. ^{4}He blanks were measured by the same procedure and typical values over this study were ~0.0015 ncc ^{4}He STP. A re-extract [*Farley*, 2002] was run after each sample to verify complete outgassing of the crystals and to test the presence of optically undetected inclusions; if a sample exhibited residual gas in the re-extract, it was dismissed from further procedure. Gas released from the apatites was purified on a charcoal trap cooled by liquid nitrogen, spiked with 99.9 % pure ^{3}He, purified by a hot (~350 °C) Ti-Zr-alloy getter and introduced into a quadrupole mass spectrometer (Pfeiffer Prisma QMS-200) next to a cold Ti-Zr-alloy getter. ^{4}He/^{3}He ratios were measured by Channeltron detector operated in static mode, and were corrected for HD and ^{3}H by monitoring mass 1. Absolute ^{4}He concentrations were calculated from peak height comparison against ratios of ^{4}He standards with known volume, measured before and after sample analysis. Reproducibility of ^{4}He standards during this study was better than ~0.03 % and ~0.2 % (both 1σ) on a daily and long-term basis, respectively. The results were corrected for blanks. The analytical uncertainty for He analysis, including blank correction, precision, accuracy and reproducibility of ^{4}He standards, is reported in Table 2.

Following He measurements, the capsules or Pt-tubes were retrieved from the furnace and sent for U-Th analysis to the Scottish Universities Environmental Research Centre (SUERC)

in East Kilbride (Scotland) and for U-Th-Sm analysis to the School of Earth Sciences at the University of Melbourne (Australia). U and Th concentrations in the samples were accurate to ± 2.5% (1σ). The total analytical uncertainty (TAU) was computed as a square root of sum of squares of weighted uncertainties on U, Th, Sm, and He measurements. TAU was usually less than ~4% (1σ) and was used to calculate errors of raw (U-Th)/He ages.
Raw (U-Th)/He ages were corrected for alpha ejection (F_t correction) following conventional procedures [*Farley et al.*, 1996]. A value of 10 % was adopted for the uncertainty of F_t correction, and was used for calculating errors of corrected (U-Th)/He ages. Replicate analyses of Durango apatite of 30 analyses yielded a mean (U–Th)/He age of 30.8 with standard deviation of 2.5 Ma, which is in good agreement with the (U–Th)/He age for Durango apatite reported by *McDowell et al.* [2005].

3.3. Microprobe analysis

Chemical compositions of apatites were measured on selected crystals by electron microprobe analysis, using a JEOL Superprobe (JXA 8900RL) with a beam current of 20 nA, acceleration voltage of 15 kV and a beam diameter of 5 µm. The detection limits (within 1σ) and standard deviations are in the order of 40 ppm and 3.5 % for Cl and 140 ppm and 1.15 % for F, respectively.

4. Results

Microprobe analysis and Dpar measurements revealed that all apatites are kinetically relatively homogeneous, with average Dpar values between 1.4 and 1.9 µm (Table 1) and Cl-contents below 0.3 wt-% (Table 3).

4.1. Apatite fission track data

AFT data are reported in Table 1. Apart from sample LST-01 all AFT ages pass the χ^2-test and are treated as cooling ages. There is no correlation between Dpar and single grain ages of sample LST-01, and decomposition into distinct age clusters failed. Therefore we will omit LST-01 in the following interpretations.
Surface and tunnel AFT central ages decrease systematically from north to south and are positively correlated with elevation (Fig. 3B). AFT ages range from 7.0 to 3.2 Ma in the tunnel and 10.4 to 5.9 Ma at the surface. Isochrons deduced from the general age pattern are tilted towards the north (Fig. 4). Mean track lengths vary between 13.3 and 14.5 µm (c-axis projected, [*Ketcham et al.*, 2007]) with shorter mean track lengths in the tunnel samples (Table 1).

Table 2: Results of apatite (U-Th)/He thermochronology.

Sample	Aliquot Code	Elevation [m]	Position	AFT[§] age [Ma]	n[$]	U[&] [ng]	Error [%]	Th[#] [ng]	Error [%]	Sm* [ng]	Error [%]	Sm/(U+Th)	U/Th	^{4}He[€] [ncc]	Error [%]	Raw age [Ma]	F_t[ß]	Corrected age [Ma]	comment	Mean age ± SD [Ma]
LBS-11	LBS-11 #1	2364	surface	10.5 ± 2.4	1	0.0528	2.1	0.2674	1.2	n.d.	n.d.	n.d.	0.1975	0.049	2.3	3.5	0.76	4.6 ± 0.5	f	**6.0 ± 1.9**
	LBS-11 #3				1	0.0223	2.2	0.0983	2.6	n.d.	n.d.	n.d.	0.2269	0.014	6.7	2.7	0.67	4.0 ± 0.5	f	
	LBS-11 #21				1	0.0781	4.4	0.1118	3.6	n.d.	n.d.	n.d.	0.6987	0.038	1.0	3.0	0.70	4.3 ± 0.5		
	LBS-11 #23				1	0.0047	19.9	0.0522	6.1	n.d.	n.d.	n.d.	0.0894	0.006	1.9	2.9	0.63	4.6 ± 0.6	l	
	LBS-11 #4 #5				2	0.1199	1.6	0.4714	1.1	n.d.	n.d.	n.d.	0.2543	0.144	1.6	5.2	0.75	6.9 ± 0.7	f	
	LBS-11 #7				1	0.0853	1.8	0.7701	1.3	n.d.	n.d.	n.d.	0.1108	0.234	1.3	7.3	0.78	9.4 ± 0.2	f	
	LBS-11 #20				1	0.0296	7.0	0.1198	4.0	n.d.	n.d.	n.d.	0.2469	0.032	1.0	4.6	0.67	6.9 ± 0.8	l	
	LBS-11 #22				1	0.1322	4.0	0.1321	3.1	n.d.	n.d.	n.d.	1.0009	0.090	1.0	4.5	0.63	7.1 ± 0.8	l	
LBS-07	LBS-07 #1	2090	surface	8.1 ± 1.4	1	0.2995	1.6	0.0662	2.1	n.d.	n.d.	n.d.	4.5242	0.086	0.9	2.3	0.74	3.1 ± 0.3	f	**4.4 ± 2.0**
	LBS-07 #3				1	0.3492	2.5	0.0579	2.4	n.d.	n.d.	n.d.	6.0311	0.128	2.9	3.0	0.75	4.0 ± 0.4	f	
	LBS-07 #21				1	0.0366	3.0	0.0385	6.1	n.d.	n.d.	n.d.	0.9519	0.018	1.2	3.2	0.65	4.9 ± 0.6	l	
	LBS-07 #23				1	0.1036	2.4	0.0482	4.6	n.d.	n.d.	n.d.	2.1497	0.026	1.1	1.9	0.72	2.6 ± 0.3	l	
	LBS-07 #22				1	0.3774	4.2	0.0577	4.2	n.d.	n.d.	n.d.	6.5364	0.296	7.1	6.3	0.83	7.6 ± 1.0	l	
	LBS-07 #2				1	0.0115	4.3	0.0229	3.7	n.d.	n.d.	n.d.	0.5022	0.299	1.4	144.3	0.68	212 ± 23	f, e	
LBS-17	LBS-17 #1	2700	surface	7.5 ± 1.0	1	0.2251	2.0	0.0500	2.0	0.8019	2.0	2.9148	4.5056	0.077	3.5	2.6	0.82	3.2 ± 0.3	l	**5.4 ± 1.8**
	LBS-17 #2				1	0.2335	2.0	0.0604	2.0	0.8736	2.0	2.9728	3.8642	0.083	3.3	2.7	0.8	3.4 ± 0.4	l	
	LBS-17 #10				1	0.1003	2.0	0.0508	2.0	0.4940	2.0	3.2684	1.9748	0.060	4.3	4.2	0.83	5.1 ± 0.6	l	
	LBS-17 #15				1	0.2691	2.0	0.0963	2.0	1.0924	2.0	2.9894	2.7943	0.145	2.2	4.0	0.65	6.2 ± 0.6	l	
	LBS-17 #16				1	0.2254	2.0	0.0558	2.0	0.8332	2.0	2.9628	4.0383	0.144	2.2	4.9	0.69	7.1 ± 0.7	l	
	LBS-17 #20				1	0.2537	2.0	0.0436	2.0	1.0288	2.0	3.4609	5.8232	0.160	2.0	4.9	0.67	7.3 ± 0.8	l	
	LBS-17 #17				1	0.0957	2.0	0.0104	2.0	0.3667	2.0	3.4576	9.1984	0.176	1.9	14.4	0.71	20.3 ± 2.1	l, e	
	LBS-17 #19				1	0.0002	2.0	0.0012	2.0	0.0007	2.0	0.4737	0.1530	0.091	3.0	1464.6	0.76	1927 ± 205	l, e	
LB-11	LB-11 #5	826	tunnel	6.5 ± 1.0	1	0.9962	1.5	0.0784	2.1	n.d.	n.d.	n.d.	12.7066	0.493	14.4	4.0	0.82	4.9 ± 0.9	f	**5.5 ± 0.4**
	LB-11 #1				1	1.0060	1.4	0.0680	2.7	n.d.	n.d.	n.d.	14.7941	0.587	7.9	4.8	0.84	5.7 ± 0.7	f	
	LB-11 #3				1	0.6744	1.2	0.0466	1.7	n.d.	n.d.	n.d.	14.4721	0.404	3.2	4.9	0.84	5.8 ± 0.6	f	
	LB-11 #20				1	0.3403	4.4	0.0187	6.8	n.d.	n.d.	n.d.	18.2406	0.187	11.1	4.5	0.79	5.7 ± 0.9	l	
	LB-11 #2				1	0.9755	1.6	0.0609	1.4	n.d.	n.d.	n.d.	16.0181	0.644	1.3	5.4	0.82	6.6 ± 0.7	f, e	
	LB-11 #4				1	0.3740	1.1	0.0322	3.0	n.d.	n.d.	n.d.	11.6149	0.768	1.5	16.6	0.80	20.8 ± 2.1	f, e	
	LB-11 #25				1	0.3437	4.5	0.0252	5.0	n.d.	n.d.	n.d.	13.6512	0.305	6.9	7.2	0.79	9.1 ± 1.2	l, e	
LB-26	LB-26 #2	810	tunnel	7.0 ± 1.1	1	0.1175	2.3	0.0488	3.7	n.d.	n.d.	n.d.	2.4078	0.045	11.3	2.9	0.81	3.6 ± 0.6	f	**3.1 ± 0.7**
	LB-26 #3 #9				2	0.3119	1.1	0.0632	1.6	n.d.	n.d.	n.d.	4.9351	0.128	0.9	3.3	0.82	4.0 ± 0.4	f	
	LB-26 #6				1	0.0405	3.5	0.0231	2.3	n.d.	n.d.	n.d.	1.7532	0.012	24.5	2.2	0.64	3.5 ± 0.9	f	
	LB-26 #20				1	0.0322	4.9	0.0103	13.4	n.d.	n.d.	n.d.	3.1147	0.007	1.7	1.8	0.65	2.8 ± 0.4	l	
	LB-26 #21				1	0.0161	5.0	0.0047	15.4	n.d.	n.d.	n.d.	3.4466	0.004	2.8	1.8	0.71	2.5 ± 0.3	l	
	LB-26 #22				1	0.1071	2.6	0.0459	3.4	n.d.	n.d.	n.d.	2.3335	0.020	1.1	1.4	0.66	2.1 ± 0.2	l	
	LB-26 #1 #4				2	0.1281	1.9	0.0474	3.3	n.d.	n.d.	n.d.	2.7025	0.157	1.1	9.3	0.75	12.5 ± 1.3	f, e	
	LB-26 #5 #8				2	0.0997	2.6	0.0282	2.8	n.d.	n.d.	n.d.	3.5355	0.085	1.8	6.6	0.71	9.3 ± 1.0	f, e	
	LB-26 #7				1	0.0498	2.4	0.0270	3.9	n.d.	n.d.	n.d.	1.8444	0.052	4.0	7.6	0.68	11.1 ± 1.2	f, e	
LB-38	LB-38 #1	666	tunnel	3.3 ± 0.6	1	0.1065	2.0	0.0392	2.0	0.4765	2.0	3.2698	2.7156	0.019	1.5	1.3	0.65	2.0 ± 0.2	l	**2.3 ± 0.3**
	LB-38 #2				1	0.0582	2.0	0.0227	2.0	0.2546	2.0	3.1489	2.5662	0.010	2.2	1.3	0.63	2.1 ± 0.2	l	
	LB-38 #4				1	0.1486	2.0	0.0805	2.0	0.5073	2.0	2.2143	1.8446	0.037	1.2	1.8	0.65	2.8 ± 0.3	l	
	LB-38 #16				1	0.1227	2.0	0.0486	2.0	0.5241	2.0	3.0585	2.5248	0.027	1.3	1.6	0.69	2.3 ± 0.2	l	
	LB-38 #17				1	0.1431	2.0	0.0620	2.0	0.7137	2.0	3.4802	2.3098	0.031	1.3	1.6	0.70	2.3 ± 0.2	l	
	LB-38 #3				1	0.1101	2.0	0.0433	2.0	0.4443	2.0	2.8972	2.5422	0.035	1.2	2.3	0.68	3.4 ± 0.3	l, e	
	LB-38 #5				1	0.0625	2.0	0.0267	2.0	0.2421	2.0	2.7131	2.3426	0.018	1.6	2.1	0.56	3.8 ± 0.4	l, e	
	LB-38 #9				1	0.0186	2.0	0.0074	2.0	0.0977	2.0	3.7515	2.5039	0.028	1.3	10.8	0.74	14.6 ± 1.5	l, e	
LB-13	LB-13 #7	641	tunnel	3.4 ± 0.6	1	0.2989	2.0	0.1236	2.0	1.3506	2.0	3.1971	2.4182	0.1076	0.9	2.6	0.76	3.4 ± 0.4	l	**3.2 ± 0.2**
	LB-13 #17				1	0.2639	2.0	0.1807	2.0	1.1239	2.0	2.5275	1.4602	0.0896	0.9	2.3	0.76	3.0 ± 0.3	l	
	LB-13 #22				1	0.1606	2.0	0.0915	2.0	0.7295	2.0	2.8935	1.7552	0.0475	0.9	2.1	0.64	3.3 ± 0.3	l	
	LB-13 #1				1	0.2847	2.0	0.2362	2.0	1.2569	2.0	2.4129	1.2052	0.1180	0.9	2.8	0.69	4.1 ± 0.4	l, e	
	LB-13 #2				1	0.0404	2.0	0.0135	2.0	0.2366	2.0	4.3842	2.9836	0.1049	0.9	19	0.72	26.4 ± 2.7	l, e	
	LB-13 #3				1	0.2186	2.0	0.1890	2.0	1.1556	2.0	2.8348	1.1564	0.1150	0.9	3.5	0.74	4.7 ± 0.5	l, e	
	LB-13 #6				1	0.1266	2.0	0.0717	2.0	0.5911	2.0	2.9806	1.7668	0.0443	0.9	2.5	0.65	3.8 ± 0.4	l, e	
	LB-13 #8				1	0.1440	2.0	0.0771	2.0	0.8272	2.0	3.7408	1.8689	0.0654	0.9	3.2	0.73	4.4 ± 0.4	l, e	
	LB-13 #15				1	0.2296	2.0	0.1327	2.0	1.2071	2.0	3.3325	1.7305	0.1120	0.9	3.4	0.77	4.4 ± 0.5	l, e	

[§]AFT: Apatite fission track (see Tab. 1); $n: number of dated apatite grains; &U [ng]: 238U and 235U, in nanogramm; #Th [ng]: 232Th, in nanogramm; *Sm [ng]: 147Sm, in nanogramm; € 4He [ncc]: 4He, in nanocubiccentimeters; ßFt: alpha ejection correction factor after Farley [2002]; e: not used because of erronous old age; f: degassed in furnace; l: degassed in laser module; n.d.: not determined.

Table 3: Average chemical compositions of selected apatite samples from the Lötschberg transect in weight percent and number of atoms per formula unit from electron microprobe analysis. DUR refers to the Durango apatite standard, which was repeatedly measured during the course of electron microprobe analysis.

	DUR	LB 26	LB 11	LBS 07	LBS 17	LBS 11
CaO	53.13	53.97	53.13	54.23	54.07	53.17
P_2O_5	43.91	44.06	44.10	43.99	43.63	43.92
F	3.56	3.33	4.10	2.62	3.49	3.69
Cl	0.40	0.14	0.01	0.11	0.18	0.30
SiO_2	0.46	0.04	0.01	0.08	0.15	0.05
SrO	0.04	0.02	0.01	0.04	0.02	0.01
Ce_2O_3	0.67	0.10	0.17	0.07	0.18	0.15
Σ	102.17	101.66	101.53	101.14	101.72	101.29
$\Sigma_{corr.}$[§]	100.58	100.22	99.80	100.01	100.21	99.68
Ca	9.422	9.561	9.466	9.594	9.614	9.490
P	6.152	6.167	6.208	6.149	6.129	6.193
F	1.864	1.742	2.157	1.369	1.832	1.945
Cl	0.112	0.039	0.003	0.031	0.051	0.085
Si	0.076	0.007	0.002	0.013	0.025	0.008
Sr	0.004	0.002	0.001	0.004	0.002	0.001
Ce	0.041	0.006	0.010	0.004	0.011	0.009
OH calc.	0.024	0.219	0.000	0.601	0.117	0.000
Σ	17.695	17.743	17.847	17.764	17.781	17.731
analysed grains	5	35	38	36	42	34

[§]$\Sigma_{corr.}$: corrected

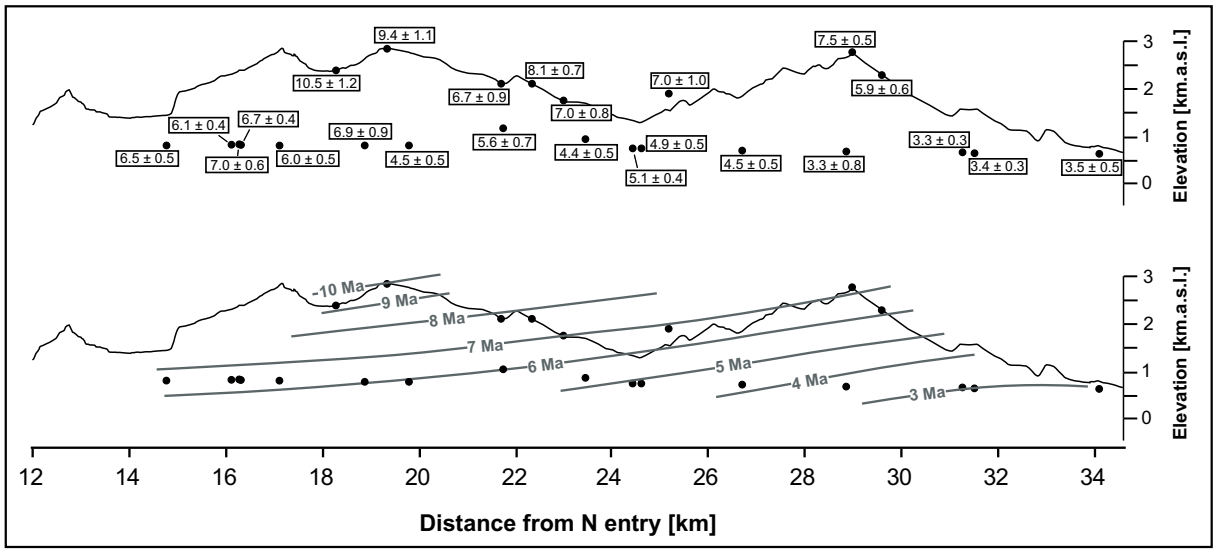

Figure 4: Reconstruction of AFT isochrons (drawn by hand) taking into account age errors and age-elevation relationships. Note that sample LST-01 was not used and AFT ages are displayed with 1σ error.

4.2. Apatite (U-Th)/He data

Apatite quality in the Lötschberg area is rather poor, often containing inclusions. Acceptable grains (without apparent inclusions or cracks when inspected under optical microscope) were

found in 7 samples. From these 46 aliquots were analyzed; results are reported in Table 2. The scatter in single grain ages within a sample may be due to heterogeneous U/Th distribution. Some aliquots obviously have erroneously old ages, which we ascribe to U-rich microinclusions (e.g. zircons) not visible under the optical microscope.
To identify "meaningful" ages, belonging to one age population we have grouped the data taking into account the corresponding AFT ages, and replication within 1σ error limits plus ~10% uncertainty related to alpha ejection correction. Groups of 2 to 4 replicating aliquots per sample could be determined (Table 2). For sample LBS-11 we have found two age groups with mean ages of 4.4 and 7.0 Ma, both younger than the corresponding AFT age of 10.4 Ma. Since we have no reasonable arguments to skip one, we have decided to report the mean age of all single grain ages younger than the corresponding AFT age. Generally, mean AHe ages range from 6 to 2 Ma with no systematic relation between age and distance along the transect, and no correlation between age and elevation in the surface samples (Fig. 3A and C).

5. Interpretation

5.1. Exhumation rates

Exhumation rates can be estimated from AFT data following two ways: (1) Age-elevation relation (AER) profiles yield paleo-exhumation rates averaged for the time between the oldest and the youngest AFT age of the profile, without the need of assuming a geothermal gradient. (2) Single AFT ages yield average cooling rates between the time of closure (the AFT age) and the present. Assuming a reasonable geothermal gradient, these average cooling rates can then be transferred into average exhumation rates. For this study, both age-elevation relations and cooling rates are used to estimate exhumation rates.

Exhumation rates derived from age-elevation relations

From three segments (i.e. Gastern, Goppenstein, and Mallich) along the transect, AER profiles were constructed (Fig. 5). From theoretical considerations the influence of the given topography has only a very minor if not a negligible effect on AFT relevant isotherms (see supplement A.1). However, to minimize potential effects of topography resulting in isotherm perturbation, the profiles were chosen as steep as possible.
Age-elevation relationships from each segment show a linear correlation of AFT ages with elevation within errors suggesting constant exhumation rates. Exhumation rates are 0.50 km/Myr ($R^2 = 0.76$) for the northern (Gastern), 0.49 km/Myr ($R^2 = 0.88$) for the central (Goppenstein), and 0.53 km/Myr ($R^2 = 0.98$) for the southern (Mallich) segment of the transect, averaged for the period between 10 – 6 Ma, 8 – 4 Ma, and 7 – 3.5 Ma, respectively (Fig. 5). The exhumation rates of the three regions are practically the same with a mean exhumation rate of ~0.5 km/Myr for the time period between 10 and 3.5 Ma.

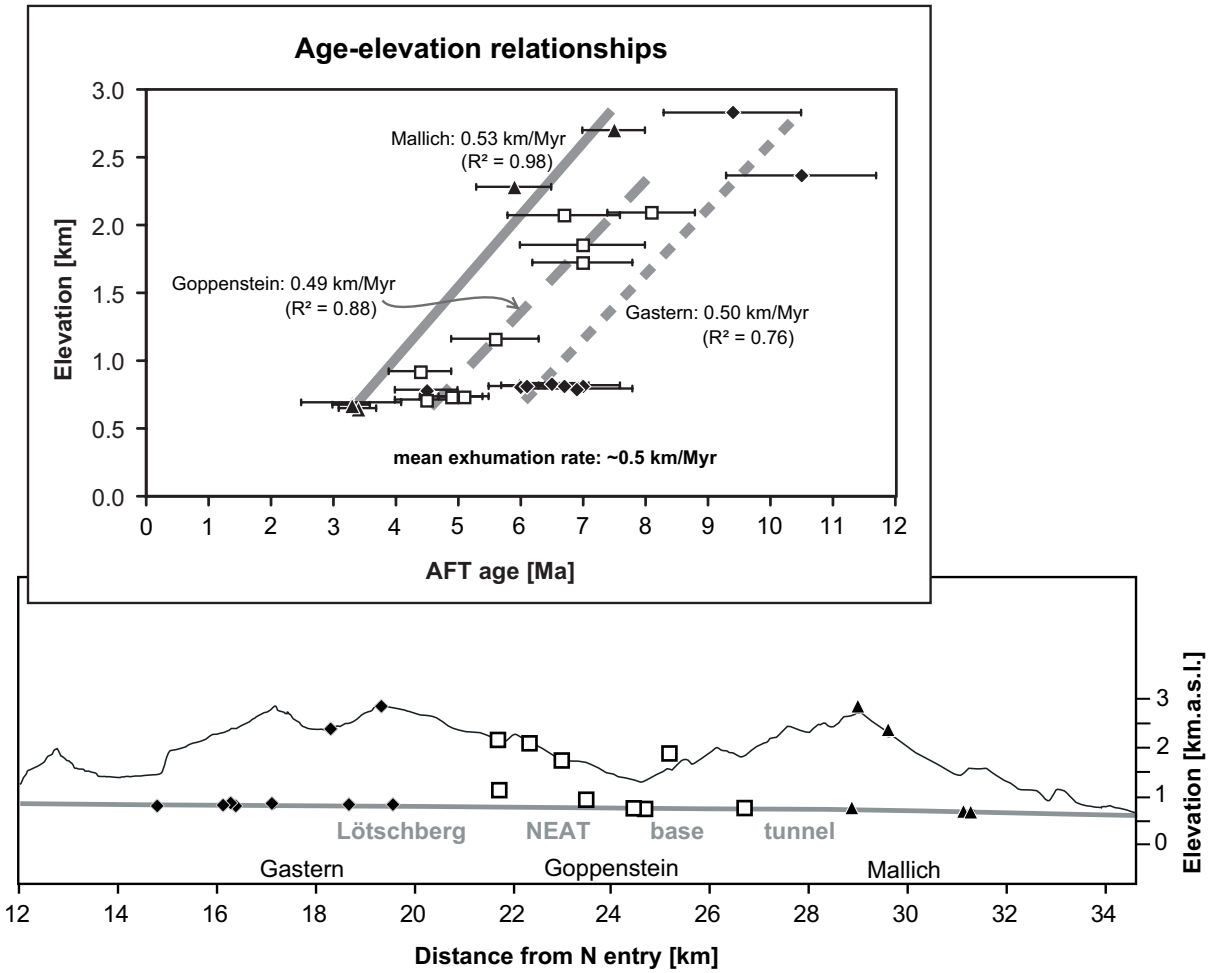

Figure 5: Exhumation rates between ~10 and 3.5 Ma, derived from age-elevation relationships (AER) of AFT data. The slopes of the AER regression lines yield a mean exhumation rate in the order of 0.5 km/Myr.

Exhumation rates derived from cooling rates

For the time interval between 3.5 Ma and today exhumation rates can only be estimated from cooling rates of single AFT samples. For each AFT cooling age we have calculated the average cooling rate from closure temperature of the AFT system (appr. 110 °C, *Rahn and Grasemann* [1999]) to present-day rock temperature. The latter are from in-situ rock temperature measurements in the tunnels (Fig. 3D). Mean annual air temperatures are taken for surface samples. To translate cooling rates into exhumation rates we have to assume a reasonable mean geothermal gradient constant for the averaged time period. Based on heat flow measurements in the old Lötschberg railway tunnel [*Clark and Niblett*,1956] and from interpolation of in-situ rock temperatures in the tunnels to surface temperatures we have calculated a present-day geothermal gradient of ~25 °C/km. (A more detailed description can be found in the supplement A.2 to this paper.)

In Figure 6 calculated exhumation rates are plotted for each sample with 1σ error of the AFT age. Exhumation rates from tunnel and surface samples are around 0.5 km/Myr in the Gastern and 0.6 km/Myr in the Goppenstein segment. The calculated exhumation rates are in the same order as those from the AER profiles with a trend to slightly higher rates towards the south. In the Mallich segment, exhumation rates are significantly increased since 3.5 Ma compared to the exhumation rate between 7 and 3.5 Ma from the AER profile and increase to the south. Maximum values are in the order of 1.2 km/Myr (calculated with a constant geothermal gradient of 25 °C/km). Exhumation rates from tunnel samples in the Mallich segment are

higher than those derived from corresponding surface samples with a “break in slope” around 3.5 Ma (i.e. the age of the tunnel sample LB06 near km 29 in Figure 6).
An increase in exhumation rates will increase heat advection and compress isotherms below surface. Therefore we have to rethink our assumption of a constant geothermal gradient of 25 °C/km. To account for isotherm compression we have recalculated the exhumation rates for the tunnel samples of the Mallich segment (all of them ≤ 3.5 Ma, the “break in slope”-age) using a geothermal gradient of 30 °C/km (filled symbols in Fig. 6). The resulting exhumation rates are now lower, but still significantly increased with maximum values of ~1.0 km/Myr.
In summary, exhumation rates derived from cooling rates and AER profiles of the Gastern and Goppenstein segment indicate more or less constant exhumation in the order of 0.5 km/Myr from 10 to 0 Ma. In contrast exhumation of the Mallich segment in the south increased significantly from 0.5 to 1.0-1.2 km/Myr (depending on the geothermal gradient) since 3.5 Ma.

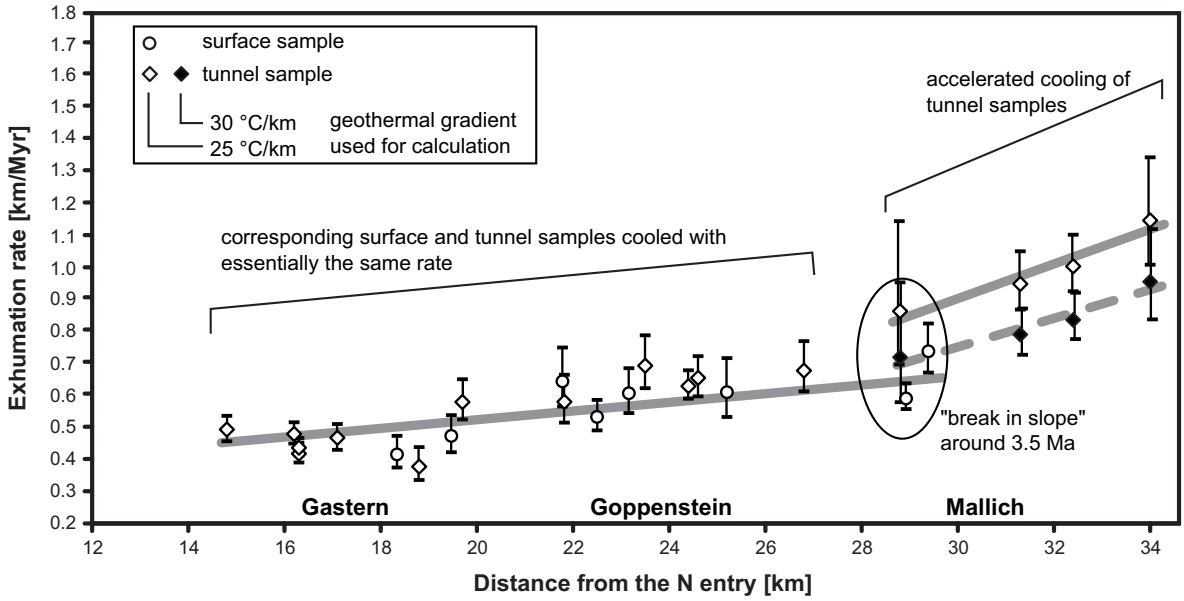

Figure 6: Exhumation rates calculated for each samples between time of AFT closure and the present. Bars indicate the range in exhumation rates taking into account the 1σ error of the AFT ages. The solid and dashed grey lines indicate the trend of mean exhumation along the transect calculated with a geothermal gradient of 25 °C/km and 30 °C/km, respectively. An increased geothermal gradient was chosen only in the footwall of the Rhone-Simplon fault. Note the increase in exhumation rates towards the south and the break in slope near km 29.

5.2. Thermal history modeling

We tested the internal consistency of our interpretations by thermal history modeling. Thermal history modeling calculates cooling paths consistent with the measured data. Thermal histories were modeled for 5 samples with special emphasis on samples with both AFT and AHe data, and track length distributions (Fig. 7). Loose constraints were taken for the modeling to allow maximum flexibility. Thermal history modeling of these samples are in line with the idea of a period of constant cooling for the time between approximately 10 and 3.5 Ma, followed by a period of accelerated cooling. Modeling results are thus consistent with thermal histories deduced from AER profiles and calculations of exhumation rates from single samples along the tunnel transect. Furthermore, thermal history modeling also shows the consistency of AFT and AHe ages.

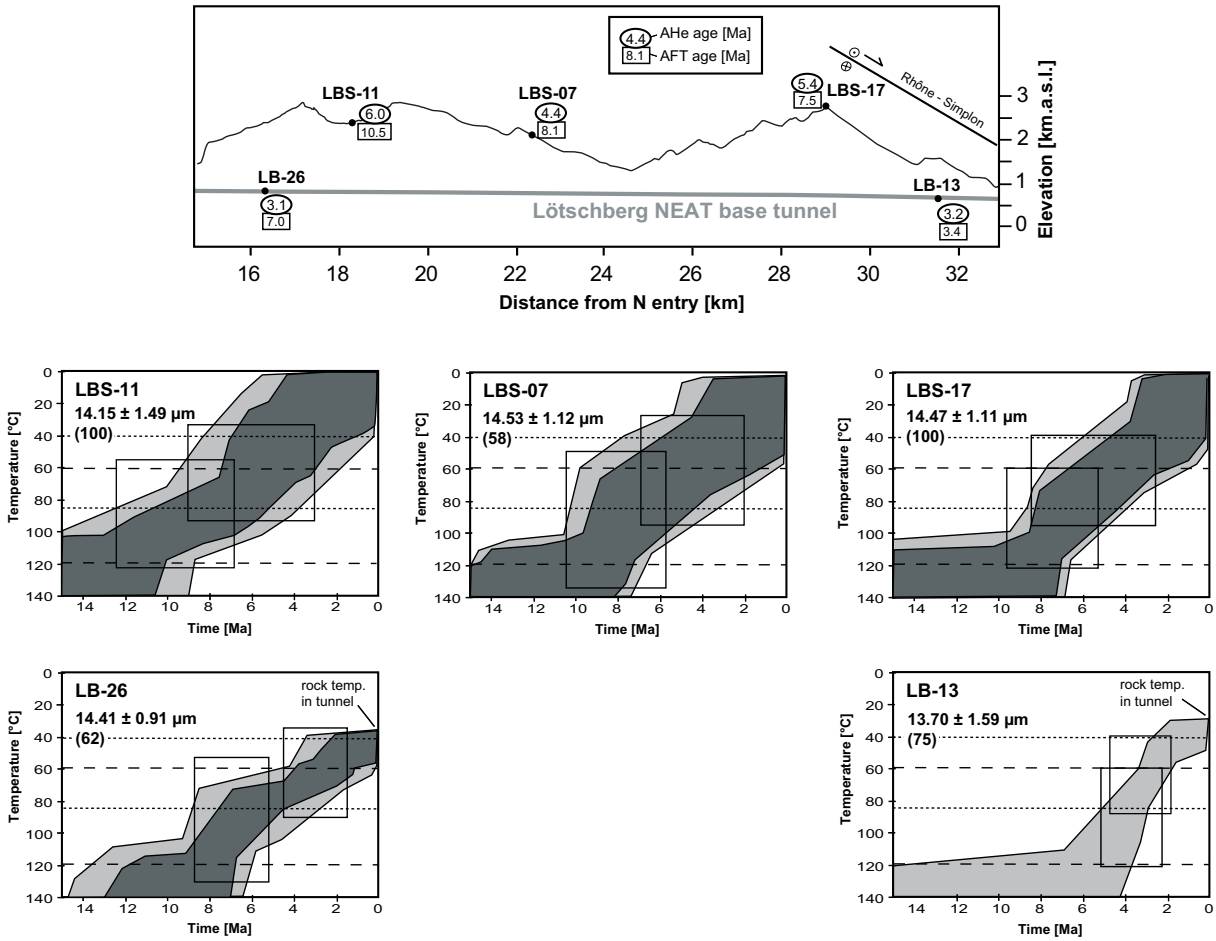

Figure 7: Thermal histories using the inverse modeling function of HeFTy [*Ketcham*, 2005] v1.3c, Monte Carlo search mode, 10,000 iterations per model run and the annealing model from *Ketcham et al.* [2007]. Model initial length was calculated from Dpar. Track length distribution with C-axis projection [*Ketcham et al.*, 2007] was used. Dark grey-shaded area: envelope of good-fit solution; light grey-shaded area: envelope of acceptable-fit solutions; boxes: model constraints. Dotted lines indicate approximate temperature bound of the AHe partial retention zone; dashed lines indicate the approximate temperature bound of the AFT partial annealing zone. Note that for sample LB-11 no acceptable time-temperature path could be modeled.

In order to further test the validity of the estimated exhumation rates and to better constrain the onset of accelerated exhumation in the south of the transect, we have performed finite difference thermal modeling following *Rahn and Grasemann* [1999]. The simplified 2D model along the transect takes into account the effect of uplift, exhumation and internal heat production. The following parameters were used: steady state topography; isotropic thermal conductivity of 3 W/mK; radioactive heat production of 1.22^{-9} W/kg (calculated with eq. (4-6) in *Turcotte and Schubert* [1982] and radioactivity measurements [*Keller et al.*, 1987]); constant heat flow of 54 mW/m^2 at the lower bound of the model at 10 km depth; and an exhumation rate of 0.5 km/Myr constant over the last 10 Myr in the north and increasing to 1.2 km/Myr around 3.5 Ma in the south. With these parameters modeled temperatures are in good accordance with measured rock temperatures (see supplement B to this paper for details). The numerical model starts with an initial geothermal gradient of 25 °C/km and fits gradually the gradient to the changing conditions. In the model the increase in exhumation rate in the south increases the geothermal gradient averaged over the last 3.5 Myr to ~28 °C/km, which fits well to our assumptions made above.

In a first step, we have calculated time-temperature paths for selected points in the transect. By using the forward modeling tool of HeFTy [*Ketcham*, 2005], AFT ages were then calculated from the time-temperature paths. The resulting AFT model-ages are displayed in Figure 8 together with the isochrons of Figure 4 for comparison with the measured AFT ages.

Except for the northernmost part of the tunnel, the modeled ages are in excellent agreement with the AFT ages observed, giving further support for our proposed exhumation history.

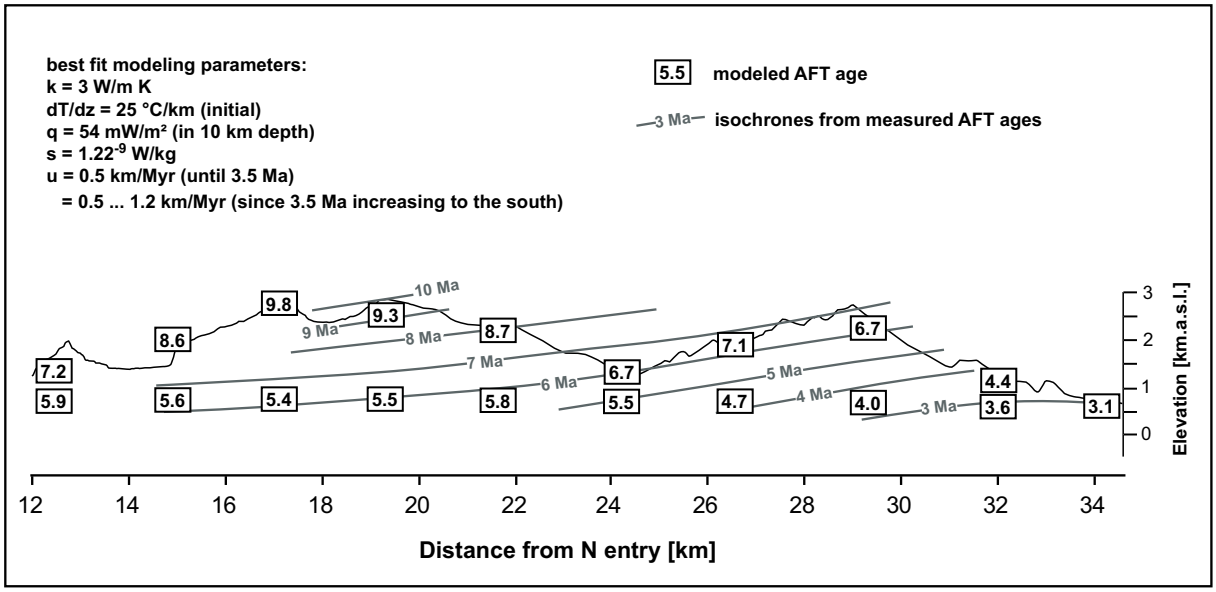

Figure 8: Comparison of modeled AFT ages with constructed isochrons from measured AFT data (from Fig. 4). A simplified 2D finite difference model was used to calculate synthetic time-temperature paths from which AFT ages are modeled by using the forward modeling function of HeFTy [*Ketcham*, 2005]. Best fit with the observed AFT data was gained by increasing the exhumation rates in the south of the transect to values of up to 1.2 km/Myr at 3.5 Ma. Abbreviations: *k* conductivity, *dT/dz* initial geothermal gradient, *q* heat flow density, *s* radioactive heat production, *u* exhumation rate.

6. Discussion

6.1. Fluid circulation

AFT and AHe systems are sensitive to circulating hot fluids. However, the present-day temperature field as deduced from in situ rock temperature measurements within the Lötschberg tunnels shows that perturbation of isotherms due to circulating fluids is very limited, except in the very south (Fig. 3D). Here we observe decreasing rock temperatures in the vicinity of the Rote-Kuh-Gampel fault. This fault separates the Baltschieder granodiorite in the north from the autochthonous Mesozoic cover in the south. The latter is intensively deformed and partly carstified, with a high potential for circulating fluids. High water influx during tunnel construction was observed here, whereas the crystalline massifs in the north are generally dryer [*Ottiger*, 2006]. The Mesozoic sedimentary sequence ("Jungfraukeil"), which separates the Gastern from the Aar massif, was found to bear water probably connected to the springs in Leukerbad, an important thermal spa ~10 km to the west. However, smaller water inflows were observed to cease after a short time [*Ottiger*, 2006], so that large-scale fluid circulation within the crystalline parts of the Gastern-Aar massif can be excluded. Rock and water temperatures are found to be in equilibrium and mirror the topography above the tunnel. Only the age reflected by sample LB-12 in the crystalline slices south of the autochthonous Mesozoic sequence, from where we have no data on fluid circulation or water and rock temperatures, may be discussed in the context of fluid-induced influence. In this case, we assumed a rock temperature of 10 °C due to its location very close to the floor of the Rhône valley with an annual air temperature in the same order. There is no evidence of thermal fluid circulation at the surface in the near vicinity. Also the age patterns (AFT and AHe) do not show irregularities within limits of errors. Therefore we consider our data not to be influenced by localized fluid circulations and regard the ages obtained to be related to regional cooling.

6.2. Faulting

Main uplift (doming) of the western Gastern-Aar massif and bending of the Helvetic basal thrust post-dates the emplacement of the overlying Helvetic nappes [*Burkhard*, 1988; *Pfiffner et al.*, 1997, Fig. 3A]. Imbrication of the crystalline basement on the northern flank of the Gastern-Aar massif and thrusting of the basement over the autochthonous Mesozoic cover and the Molasse Basin probably occurred during the same time period [*Pfiffner et al.*, 1997]. The imbrications in the north of the Lötschberg transect adjacent to the Carboniferous sediments (Fig. 2) do not cross the Helvetic basal thrust and are therefore assumed to be related to an older phase of shortening. AFT data to the north and south of these small scale thrusts do not show any offsets and thus indicate that these thrusts were not active since closure of the AFT system (Fig. 3).

6.3. Tilting of the Gastern-Aar massif

Published AFT ages within the Gastern-Aar massif show a general decreasing trend from north to south. At ~3.5 Ma, thin-skinned tectonics ceased in the Alpine foreland [*Becker*, 2000]. At the same time, exhumation accelerated in the south to values about twice as high as in the north of the transect. With a differential exhumation of 0.5 km/Myr over 3.5 Myr and ~13 km distance the total tilting is calculated to be in the order of 8° consistent with the isochrons drawn in Figure 4 (Fig. 9).

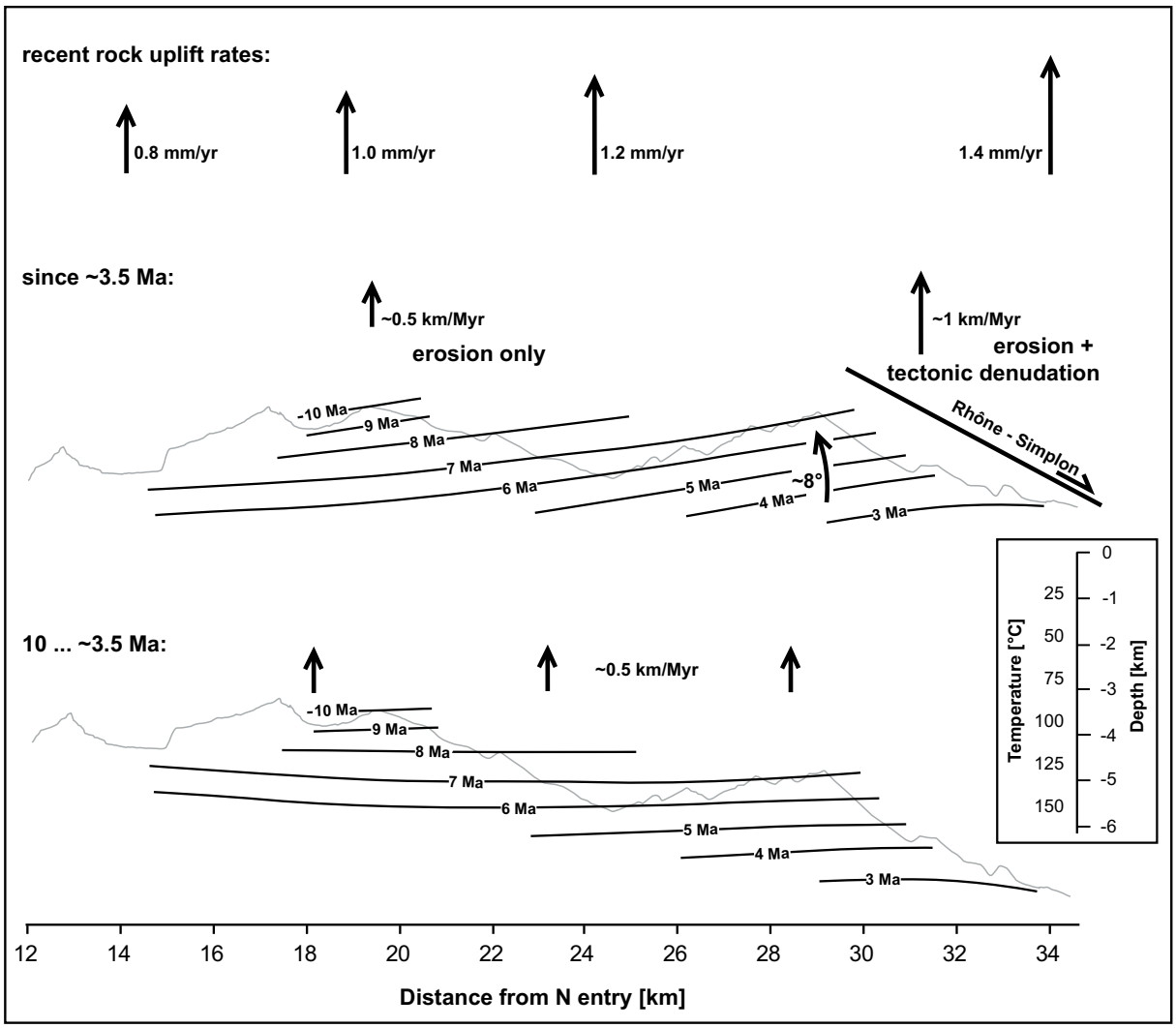

Figure 9: Proposed exhumation history of the western Aar massif with homogeneous exhumation of 0.5 km/Myr between 10 and 3.5 Ma. Subsequent increase in exhumation rate in the south results in overall tilting of the massif. Recent rock uplift [after *Kahle et al.*, 1997] is displayed for comparison.

6.4. Comparison with previous studies in the Gastern-Aar massif

To maintain internal consistency and to avoid problems arising from different laboratory calibrations, we have not included AFT data from former studies (see [*Michalski and Soom*, 1990] for data compilation and references therein) in our interpretations. Here, the interpretations from other studies are compared with our results.

Michalski and Soom [1990] used age-elevation profiles from AFT data from different areas of the Aar massif to deduce exhumation rates. In the Lötschberg area (= western Aar massif), the authors constructed two overlapping AER profiles ("Gastern Massif" and "North West Aar Massif"). The authors deduced exhumation rates in the order of 0.8 km/Myr between 7 Ma and present, which we cannot confirm from our data. Our AER profiles are vertical, constructed for distinct segments, and reveal significantly lower exhumation rates in the order of 0.5 km/Myr, remaining constant over the last 10 Myr (Fig. 5). *Michalski and Soom* [1990] deduced the same value (0.5 km/Myr) for the eastern and central Aar massif for the time interval 10-0 Ma and 10-4 Ma, respectively. After 4 Ma the exhumation rate in the central Aar massif increased to 0.8 km/Myr (calculated with a geothermal gradient of 30 °C/km; *Michalski and Soom* [1990]), a similar increase to what we see in the Mallich segment of the Lötschberg transect (Fig. 6).

6.5. Deep crustal processes (crustal wedging)

Deep crustal and upper mantle processes exert a strong influence on the geometry of an orogen, crustal tectonics, and topography. Basement uplift of the Gastern-Aar massif and horizontal shortening in response to thin-skinned thrust tectonics in the northern foreland and folding of the Jura mountains occurred since 10 Ma ('Grindelwald phase', e.g. [*Pfiffner et al.*, 1997]). *Becker* [2000] bracketed the time interval of thin-skinned foreland deformation between 9 and 3.3 Ma. If crustal wedging is responsible for shortening, thrusting, and uplift of the external massifs in conjunction with thin-skinned foreland deformation, then the cessation of the latter around 3.5 Ma also marks a change in deep crustal processes. At the same time we observe accelerated exhumation rates in the southern part of the Lötschberg transect.

Updoming and exhumation of the Gastern-Aar massif may be viewed as the result of a crustal-scale ramp fold as proposed by *Schmid et al.* [1997]. The detachment is located between lower and upper European crust and kinematically linked to the Adriatic lower crustal wedge. Presently the tip of the Adriatic lower crustal wedge is below the area of maximum rock uplift rates in the central Swiss Alps (Fig. 10A; [*Kahle et al.*, 1997; *Schmid et al.*, 1996; *Schmid and Kissling*, 2000]). The Lötschberg transect is immediately to the north of the tip of the Adriatic wedge (singularity point "S" sensu *Beaumont et al.*, [1994]), i.e., on the pro-shear side (Fig. 10B). The observed present-day uplift gradient [*Kahle et al.*, 1997] diminishing towards the north on the pro-shear side could be explained by ongoing northward propagation of the wedge along the European lower crust, which in turn would result in overall block tilting on this side. The observed increase in exhumation rates towards the south along the Lötschberg transect and the overall northward tilting would also be in line with the present-day rock uplift pattern above an indenting Adriatic wedge.

Sue et al. [2007] advocate a model of the present-day western and central Alps that is controlled by body forces in the Alpine root. Based on multi-disciplinary observations and numerical modeling, they propose that active tectonics in the western and central Alps are driven by buoyancy forces rather than by ongoing crustal shortening. Crustal shortening as a driving force was ruled out because of the drastic decrease in convergence rate between Adria and Europe in the western Alpine arc during Pliocene times (see *Sue et al.* [2007] and references therein). From a close correlation between the present-day tectonic mode and crustal thickness *Sue et al.* [2007] argue for buoyancy driven extensional post-orogenic collapse on top of an overthickened crust. The high Alpine chain tends to collapse by reactivation of preexisting structures as normal faults with orogen-perpendicular extension. A

candidate for such a fault is the Rhône-Simplon fault zone in the south of the Lötschberg transect.

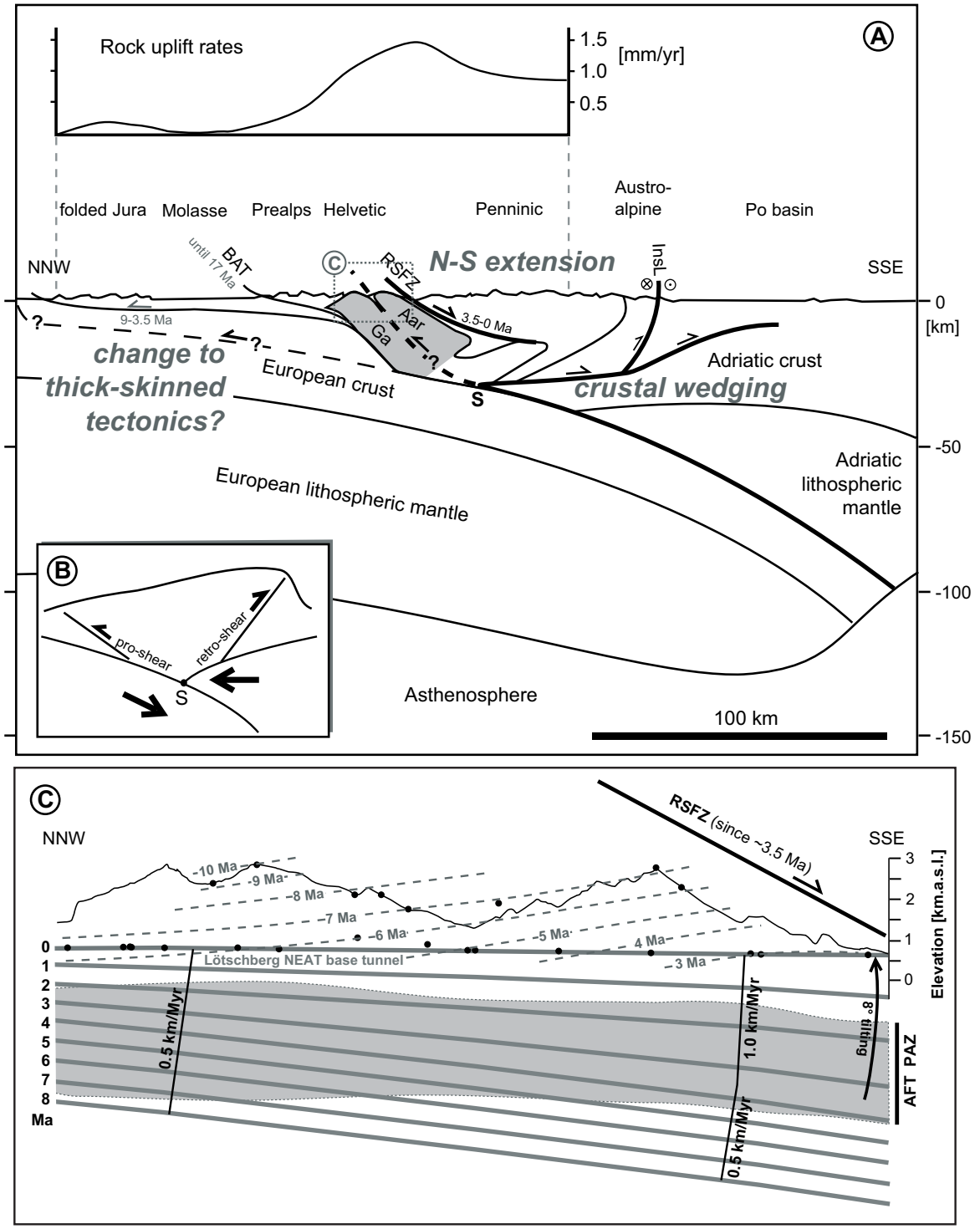

Figure 10: Synthesis of the proposed tectonic processes controlling late stage exhumation of the Gastern-Aar massif: (**A**) Simplified lithospheric scale profile through the Central Alps after *Pfiffner et al.* [1997] and *Schmid et al.* [1997] with major active structures. Ages refer to faulting activity. Grey highlighted area represents the Gastern-Aar massif. Abbreviations: *BAT* basal Alpine thrust, *RSFZ* Rhône-Simplon fault zone, *InsL* Insubric line, *Ga* Gastern massif, *Aar* Aar massif, *S* singularity point after *Beaumont et al.* [1994]. Rock uplift rates are from *Kahle et al.* [1997]. See text for further explanation. (**B**) Sketch profile describing general geometries associated with crustal wedging [*Beaumont et al.*, 1994]. (**C**) Reconstruction of the exhumation of the structural level of the Lötschberg NEAT base tunnel (grey thick lines) through space and time. Present-day surface is kept fixed for reference. AFT partial annealing zone (*PAZ*) is given by the grey area. A geothermal gradient of 25 to 30 °C/km was assumed. Dashed lines are AFT isochrons from Fig. 4. Black dots refer to the sample localities.

6.6. Normal faulting along the Rhône-Simplon fault zone and associated river capture

Dextral strike-slip faulting with a minor normal faulting component is documented for the Rhône-Simplon fault not later than 11 Ma until ~3 Ma (*Steck and Hunziker* [1994] with references therein). Paleostress data as documented by brittle kinematic indicators in both the hanging- and footwall of the Simplon fault zone revealed NE-SW extension [*Grosjean et al.*, 2004], in agreement with ductile kinematics within the Simplon fault mylonites [*Mancktelow*, 1990]. This period of dominant dextral strike-slip movement along the Rhône valley had no imprint on thermochronological data in the footwall of the Rhône-Simplon fault.

NE-SW extension was followed by N-S extension as deduced by seismotectonic and stress inversion studies [*Maurer et al.*, 1997; *Delacou et al.*, 2004; *Kastrup et al.*, 2004]. N-S extension is also observed in the structural data by *Grosjean et al.* [2004] near Brig. *Sue et al.* [2007] suggest that present-day N-S extension in the Valais area developed due to gravitational collapse and spreading of an overthickened crust from the Pliocene onward. According to the orientation of the Rhône-Simplon fault zone a change from NE-SW to N-S directed extension increases its normal-faulting component along the Rhône valley. Tectonic denudation is then more effective and the exhumation rates in the footwall increase. Also the surface uplift pattern as revealed by repeated precise leveling [*Kahle et al.*, 1997] can be explained by isostatic adjustment in response to extensional tectonics. From our data we postulate that the change from NE-SW to N-S extension in the hanging wall of the Rhône-Simplon fault zone occurred around 3.5 Ma, coeval with the onset of increased exhumation.

Fission track ages north of the Rhône valley are consistently younger than those to the south. *Soom* [1990] calculated a vertical offset in the order of 3 km for the last ~5 Myr immediately west of our transect near Sierre (Fig. 1). He also postulated an increase in normal faulting activity of the Rhône-Simplon fault zone in the Brig area since 3 Ma. Both findings are in line with our interpretation. However, it is not clear whether this increase of exhumation rates can be attributed to normal faulting (tectonic denudation) alone. River erosion may have been localized by the Rhône-Simplon fault zone due to its low erosional resistance (intense fracturing) as compared to neighboring units. Drainage systems use such weak zones, and the Rhône river may have extended its catchment along these active lines of deformation [*Schlunegger et al.*, 1998; *Kühni and Pfiffner*, 2001]. In the course of ongoing normal faulting, the Rhône river may have migrated down the normal fault zone shifting the river southward relative to the exhuming Gastern-Aar massif.

6.7. Climatic forcing

Accelerated exhumation may also be triggered by climate change. This was proposed by *Cederbom et al.* [2004] and *Willett et al.* [2006] for the Central Alps. Accelerated erosion either by increased precipitation or Alpine glaciation will lead to subsequent isostatic rebound. A significant component of the present-day rock uplift [*Kahle et al.*, 1997] in the Alps was attributed to isostatic rebound compensating for valley erosion [*Champagnac et al.*, 2007] and deglaciation [*Barletta et al.*, 2006]. Deglaciation should induce uplift mainly in the areas of maximum ice thickness, one of which was located in the Rhône valley during last glacial maximum [*Florineth and Schlüchter*, 1998]. Isostatic response to present day glacier shrinkage may account for up to half of the observed uplift [*Barletta et al.*, 2006].

Cederbom et al. [2004] and *Willet et al.* [2006] proposed a climate-driven increase in exhumation rates around 5 Ma for the central Alps. We can not confirm this 5 Ma-event with our data. Instead our data indicate constant exhumation rates for the western Aar massif between 10 and ~3.5 Ma. Moreover, palynological data from the Mediterranean realm do not reveal any indication for enhanced precipitation at the end of the Messinian salinity crisis (5.50 Ma ago [*Krijgsman et al.*, 1999]) or after it [*Fauquette et al.*, 1998, 1999; *Fauquette and Bertini*, 2003; *Warny et al.*, 2003]. At the end of the Pliocene warm period cyclic Alpine

glaciation started around 2.8 Ma [*St. John and Krissek*, 2002; *Fauquette and Bertini*, 2003; *Klotz et al.*, 2006] and intensified around 0.9 Ma [*Muttoni et al.*, 2007; *Haeuselmann et al.*, 2007]. Our data suggest an increase in exhumation around 3.5 Ma in the southern part of the transect whereas exhumation in the northern part was more or less constant since 10 Ma. The impact of Alpine glaciation after 2.8 Ma can not be resolved by the current thermochronological data. However, we may assume that glacial erosion strongly contributes to the exhumation since 0.9 Ma, when Alpine glaciation intensified with subsequent drastic increase in glacial erosion efficiency [*Muttoni et al.*, 2007; *Haeuselmann et al.*, 2007].

7. Conclusions

Our data show that exhumation was rather constant with a rate of ~0.5 km/Myr over the last 10 Myr in the north of the studied transect (Gastern and Goppenstein segment). In the south (Mallich segment), exhumation was in the same order until ~3.5 Ma but then increased gradually towards the south to values of up to 1.2 km/Myr resulting in overall tilting of the Aar massif by ~8° towards the north. We explain this exhumation pattern, and particularly the onset of rapid exhumation in the south around 3.5 Ma, by tectonic denudation in the footwall of the Rhône-Simplon fault zone. Alpine glaciation (since ~2.8 Ma, intensified since 0.9 Ma), and localized river incision (increasing with time) must have had an impact, but can not be resolved by our data. For the interaction of these different driving forces, we propose the following model:
A change in deep crustal configuration around 3.5 Ma led to an orogen-perpendicular collapse on top of an overthickened crust. At the same time movements along the Rhône-Simplon fault zone changed from dextral strike-slip (orogen-parallel) to south directed normal faulting (orogen-perpendicular). We address the increase in exhumation rates to the south of the Lötschberg transect, in the footwall of the Rhône-Simplon fault zone, to be the immediate and main effect of the tectonic denudation along the Rhône-Simplon fault zone. We propose that the Rhône river got structurally trapped by the Rhône-Simplon fault zone, which additionally enhanced erosion in the south of the Aar massif. The onset of Alpine glaciation and in particular the intensification of glacial erosion since ~0.9 Ma must have additionally contributed to the observed exhumation pattern and led to a drastically increased relief. However, from Late Miocene to Middle Pliocene we do not observe any increase in exhumation rate of the western Gastern-Aar massif, which could be addressed to climatic forcing.

Acknowledgements
Many thanks to BLS Alp Transit AG and the local construction site management for the possibility to sample while constructing the Lötschberg base tunnel and for the drilling samples. Gerlinde Höckh, Dorothea Mühlbayer-Renner, and Dagmar Kost are gratefully acknowledged for mineral separation. Thanks also to Dr. Thomas Wenzel for his support during electron microprobe analysis and Prof. Klaus Dietz for his help concerning the statistics. We appreciate the discussions and help while sampling from M. Weh, C. Dekant, F. Giovanoli, R. Ottiger, R. Hänni, A. Kuhlemann, and H.-P. Ziegler. M. Zattin and C. Cederbom gave valuable comments to an earlier version of the manuscript. Two anonymous reviewers gave helpful reviews.
This study was funded by the German Science Foundation (DFG), project SP673/2-2.
We dedicate this paper to Martin Burkhard, whose work in the Aar massif has been the basis of this study in many respects.

References

Abrecht, J. (1994), Geologic units of the Aar massif and their pre-Alpine rock associations: a critical review, *Schweiz. Mineral. Petrogr. Mitt.*, *74*, 5-27.

Barletta, V.R., C. Ferrari, G. Diolaiuti, T. Carnielli, R. Sabadini, and C. Smiraglia (2006), Glacier shrinkage and modeled uplift of the Alps, *Geophy. Res. Lett.*, *33*, L14307, doi:10.1029/2006GL026490.

Becker, A. (2000), The Jura Mountains - an active foreland fold-and-thrust belt?, *Tectonophysics*, *321*, 381-406.

Beaumont, C., P. Fullsack, and J. Hamilton (1994), Style of crustal deformation caused by subduction of the underlying mantle, *Tectonophysics*, *232*, 119-132.

Burkhard, M. (1988), L'Helvétique de la bordure occidentale du massif de l'Aar (évolution tectonique et métamorphique), *Eclogae geol. Helv.*, *81*, 63-114.

Burtner, R.L., A. Nigrini, and R.A. Donelick (1994), Thermochronology of Lower Cretaceous source rocks in the Idaho-Wyoming thrust belt, *Am. Assoc. Petrol. Geol. Bull.*, *78*, 1613-1636.

Cederbom, C.E., H.D. Sinclair, F. Schlunegger, and M.K. Rahn (2004), Climate-induced rebound and exhumation of the European Alps, *Geology*, *32*, 709-712.

Champagnac, J.D., P. Molnar, R.S. Anderson, C. Sue, and B. Delacou (2007), Quaternary erosion-induced isostatic rebound in the western Alps, *Geology*, *35*, 195-198.

Clark, S. P., and E. R. Niblett (1956), Terrestrial heat flow in the Swiss Alps, *Royal Astron. Soc. Geophys. Suppl. Monthly Notices*, *7*, 176-195.

Delacou, B., C. Sue, J.D. Champagnac, and M. Burkhard (2004), Present-day geodynamics in the bend of the western and central Alps as constrained by earthquake analysis, *Geophys. J. Int.*, *158*, 753-774.

Donelick, R.A., and D.S. Miller (1991), Enhanced TINT fission track densities in low spontaneous track density apatites using ^{252}Cf-derived fission fragment tracks: a model and experimental observations, *Nucl. Tracks Radiat. Meas.*, *18*, 301-307.

Dunkl, I. (2000), Trackkey: a windows program for calculation and graphical presentation of fission track data, *Computers & Geosciences*, *28*, 3-12.

Farley, K.A. (2002), (U-Th)/He dating: Techniques, calibrations, and applications, *Mineral. Soc. Am. Rev. Mineral. Geochem.*, *47*, 819-844.

Farley, K.A., R.A. Wolf, and L.T. Silver (1996), The effects of long alpha-stopping distances on (U-Th)/He ages, *Geochimica and Cosmochimica Acta*, *60*, 4223-4229.

Fauquette, S., and A. Bertini (2003), Quantification of the northern Italy Pliocene climate from pollen data: evidence for a very peculiar climate pattern, *Boreas*, *32*, 361-369.

Fauquette, S., J. Guiot, and J.-P. Suc (1998), A method for climate reconstruction of the Mediterranean Pliocene using pollen data, *Palaeogeography, Palaeoclimatology, Palaeoecology*, *144*, 183-201.

Fauquette, S., J-P. Suc, J. Guiot, F. Diniz, N. Feddi, Z. Zheng, E. Bessais, and A. Drivaliari (1999), Climate and biomes in the West Mediterranean area during the Pliocene, *Palaeogeography, Palaeoclimatology, Palaeoecology*, *152*, 15-36.

Florineth, U., and C. Schlüchter (1998), Reconstruction the Last Glacial Maximum (WÜRMIAN) ice surface geometry and flowlines of the Central Swiss Alps, *Eclogae Geologicae Helvetiae*, *91*, 391-407.

Frey, M., and R. Ferreiro-Mählmann (1999), Alpine metamorphism of the Central Alps, Switzerland, *Schweiz. Mineral. Petrogr. Mitt.*, *79*, 135-154.

Galbraith, R.F., and G.M. Laslett (1993), Statistical models for mixed fission track ages, *Nucl. Tracks Radiat. Meas.*, *21*, 459-470.

Gleadow, A.J.W. (1981), Fission-track dating methods: What are the real alternatives?, *Nucl. Tracks Radiat. Meas.*, *5*, 3-14.

Grosjean G., C. Sue, and M. Burkhard (2004), Late Neogene extension in the vicinity of the Simplon fault zone (central Alps, Switzerland), *Eclogae geol. Helv.*, *97*, 33-46.

Haeuselmann, P., D.E. Granger, P.-Y. Jeannin, and S.-E. Lauritzen (2007), Abrupt glacial valley incision at 0.8 Ma dated from cave deposits in Switzerland, *Geology*, *35*, 143-146.

Hay, W.W., J.L. Sloan, and C.N. Wold (1988), The mass/age distribution and composition of sediments on the ocean floor and the global rate of sediment subduction, *J. Geophys. Res.*, *93*, 14933-14940.

Herwegh, M., and O.A. Pfiffner (2005), Tectono-metamorphic evolution of a nappe stack: A case study of the Swiss Alps, *Tectonophysics*, *404*, 55-76.

Hurford, A.J., and P.F. Green (1982), A users' guide to fission track dating calibration, *Earth Planet. Sci. Lett.*, *59*, 343-354.

Hurford, A.J., and P.F. Green (1983), The zeta age calibration of fission-track dating, *Chem. Geol. (Isotope Geoscience Section)*, *41*, 285-317.

Kahle, H.G., A. Geiger, B. Buerki, E. Gubler, U. Marti, B. Wirth, M. Rothacher, W. Gurtner, G. Beutler, I. Bauersima, and O.A. Pfiffner (1997), Recent crustal movements, geoid and density distribution: Contribution from integrated satellite and terrestrial measurements, in *Deep structure of the Swiss Alps: Results of NRP 20*, Basel, Boston, Berlin, edited by O.A. Pfiffner et al., pp. 251-259, Birkhäuser, Boston, Cambridge, Mass..

Kastrup, U., M.L. Zoback, N. Deichmann, K.F. Evans, D. Giardini, and A.J. Michael (2004), Stress field variations in the Swiss Alps and the northern Alpine foreland derived from inversion of fault plane solutions, *J. Geophys. Res.*, *109*, B01402, doi:10.1029/2003JB002550.

Keller, F., H. Wanner, and T.R. Schneider (1987), Geologischer Schlussbericht Gotthard-Strassentunnel, *Beiträge zur Geologie der Schweiz: Geotechnische Serie, 70*, 67 pp., Bern.

Ketcham, R.A. (2005), Forward and inverse modeling of low-temperature thermochronometry data, *Rev. Mineral. Geochem.*, *58*, 275-314.

Ketcham, R.A., A. Carter, R.A. Donelick, J. Barbarand, and A.J. Hurford (2007), Improved measurement of fission-track annealing in apatite using c-axis projection, *Am. Mineral.*, *92*, 789-798.

Klotz, S., S. Fauquette, N. Combourieu-Nebout, D. Uhl, J.-P. Suc, and V. Mosbrugger (2006), Seasonality intensification and long-term winter-cooling as a part of the Late Pliocene climate development, *Earth Planet. Sci. Lett.*, *241*, 174-187.

Kühni, A., and O.A. Pfiffner (2001), The relief of the Swiss Alps and adjacent areas and its relation to lithology and structure: topographic analysis from a 250-m DEM, *Geomorphology*, *41*, 285-307.

Kuhlemann, J., W. Frisch, B. Szekely, I. Dunkl, and M. Kazmer (2002), Postcollisional sediment budget history of the Alps: Tectonic versus climatic control, *Int. J. Earth Sci.*, *91*, 818-837.

Krijgsman, W., F.J. Hilgen, I. Raffi, F.J. Sierro, and D.S. Wilson (1999), Chronology, causes and progression of the Messinian salinity crisis, *Nature*, *400*, 652-655.

Mancktelow, N. (1990), The Simplon Fault Zone, *Beitr. geol. Karte Schweiz*, *163* (N.F.), 74 pp..

Maurer, H.R., M. Burkhard, N. Deichmann, and A.G. Green (1997), Active tectonism in the central Alps: contrasting stress regimes north and south of the Rhone Valley, *Terra Nova*, *9*, 91-94.

McDowell, F. W., W. C. McIntosh, and K. A. Farley (2005), A precise ^{40}Ar–^{39}Ar reference age for the Durango apatite (U–Th)/He and fission-track dating standard, *Chem. Geol.*, *214*, 249-263.

Michalski, I., and M. Soom (1990), The Alpine thermotectonic evolution of the Aar and Gotthard massifs, central Switzerland: Fission track ages on zircon and apatite and K-Ar mica ages, *Schweiz. Mineral. Petrogr. Mitt.*, *70*, 373-387.

Molnar, P., and P. England (1990), Late Cenozoic uplift of mountain ranges and global climate change: chicken or egg?, *Nature*, *346*, 29-34.

Muttoni, G., C. Ravazzi, M. Breda, R. Pini, C. Laj, C. Kissel, A. Mazaud, and E. Garzanti (2007), Magnetostratigraphic dating of an intensification of glacial activity in the southern Italian Alps during Marine Isotope Stage 22, *Quaternary Research*, *67*, 161-173.

Naeser, C.W. (1976), Fission track dating, *U.S. Geol. Surv. Open-File Report*, 76-190.

Ottiger, R. (2006), Hydrogeologie Vortrieb Ferden, in *Geologie und Geotechnik der Basistunnels am Gotthard und am Lötschberg*, edited by S. Löw, pp. 167-179, vdf Hochschulverlag, Zürich.

Pfiffner, O.A., S. Sahli, and M. Stäuble (1997), Structure and evolution of the external basement uplifts (Aar, Aguilles Rouges / Mt. Blanc), in *Deep Structure of the Swiss Alps: Results of NRP 20*, edited by O.A. Pfiffner et al., pp. 139-153, Birkhäuser, Boston, Cambridge, Mass..

Rahn, M.K., and B. Grasemann (1999), Fission track and numerical thermal modeling of differential exhumation of the Glarus thrust plane (Switzerland), *Earth Planet. Sci. Lett.*, *169*, 245-259.

Raymo, M.E., and W.F. Ruddiman (1992), Tectonic forcing of late Cenozoic climate, *Nature*, *359*, 117-122.

Schaer, J., G. Reimer, and G. Wagner (1975), Actual and ancient uplift rate in the Gotthard region, Swiss Alps: a comparison between precise levelling and fission track apatite age, *Tectonophysics*, *29*, 293-300.

Schaltegger, U. (1994), Unravelling the pre-Mesozoic history of Aar and Gotthard massifs (Central Alps) by isotopic dating – a review, *Schweiz Mineral. Petrogr. Mitt.*, *74*, 41-51.

Schlunegger, F., R. Slingerland, and A. Matter (1998), Crustal thickening and crustal extension as controls on the evolution of the drainage network of the central Swiss Alps between 30 Ma and the present: constraints from the stratigraphy of the North Alpine Foreland Basin and the structural evolution of the Alps, *Basin Research*, *10*, 197-212.

Schmid, S.M., and E. Kissling (2000), The arc of the Western Alps in the light of geophysical data on deep crustal structure, *Tectonics*, *19*, 62-85.

Schmid, S.M., O.A. Pfiffner, N. Froitzheim, G. Schönborn, and E. Kissling (1996), Geophysical-geological transect and tectonic evolution of the Swiss-Italian Alps, *Tectonics*, *15*, 1036-1064.

Schmid, S.M., O.A. Pfiffner, G. Schönborn, N. Froitzheim, and E. Kissling (1997), Integrated cross section and tectonic evolution of the Alps along the Eastern Traverse, in *Deep Structure of the Swiss Alps: Results of NRP 20*, edited by O.A. Pfiffner et al., pp. 289-304, Birkhäuser, Boston, Cambridge, Mass..

Seward, D., and N. Mancktelow (1994), Neogene kinematics of the central and western Alps: Evidence from fission-track dating, *Geology*, *22*, 803-806.

Soom, M. (1990), Abkühlungs- und Hebungsgeschichte der Externmassive und der penninischen Decken beidseits der Simplon-Rhône-Linie seit dem Oligozän: Spaltspurendatierung an Apatit/Zirkon und K-Ar-Datierungen an Biotit/Muskovit (Westliche Zentralalpen), *PhD thesis*, University Bern, 119 pp.

Steck, A., and J. Hunziker (1994), The Tertiary structural and thermal evolution of the Central Alps – compressional and extensional structures in an orogenic belt, *Tectonophysics*, *238*, 229-254.

Sue, C., B. Delacou, J.D. Champagnac, C. Allanic, P. Tricart, and M. Burkhard (2007), Extensional neotectonics around the bend of the Western/Central Alps: an overview, *Int. J. Earth Sci.*, *96*, 1101-1129.

St. John, K.E.K., and L.A. Krissek (2002), The Late Miocene to Pleistocene ice-rafting history of southeast Greenland, *Boreas*, *31*, 28-35.

Turcotte, D.L., and G. Schubert (1982), Geodynamics - Applications of Continuum Physics to Geological Problems, 450 pp., New York.

Wagner, G., G. Reimer, and E. Jäger (1977), Cooling ages derived by apatite fission track, mica Rb-Sr and K-Ar dating: the uplift and cooling history of the Central Alps, *Mem. Ist. Geol. Mineral. Univ. Padua*, *30*.

Warny, S.A., P.J. Bart, and J-P. Suc (2003), Timing and progression of climatic, tectonic and glacioeustatic influences on the Messinian Salinity Crisis, *Palaeogeography, Palaeoclimatology, Palaeoecology*, *202*, 59-66.

Willett, S.D., F. Schlunegger, and V. Picotti (2006), Messinian climate change and erosional destruction of the central European Alps, *Geology*, *34*, 613-616.

Ziegler, H.-J. (2006), and Geologengruppe Lötschberg-Basistunnel, Geologisches Befundprofil Lötschberg-Basistunnel (1:50 000), in *Geologie und Geotechnik der Basistunnels am Gotthard und am Lötschberg*, edited by S. Löw, map supplement, vdf Hochschulverlag, Zürich.

Supplement to Reinecker et al. - 2007TC002247

A. Estimation of exhumation rates

The assumptions on possible perturbation of relevant isotherms and geothermal gradients below topography are critical for the deduction of exhumation rates from thermochronological data. In the following we shortly assess theoretically and numerically the influences of topography along the Lötschberg transect on AFT relevant isotherms and discuss the constraints on the geothermal gradient.

A.1. Topographic effect on isotherm perturbation along the Lötschberg transect

The problem of isotherm perturbation for cooling histories is described in detail by *Stüwe et al*. [1994] and *Mancktelow and Grasemann* [1997]. These authors also provide analytical and numerical solutions of the heat conduction/advection equation to quantify the effect of topography especially for AFT thermochronology. *Stüwe et al.* [1994] have in one example assumed steady-state topography with amplitude of 1.5 km and wavelength of 20 km. In this case isotherm perturbation is negligible for exhumation rates of 0.5 km/Myr but gets significant with higher rates. Shorter wavelengths and less relief will reduce the perturbation effect on AFT relevant isotherms. However, the present-day topography of the Lötschberg transect with 1 km amplitude and 10 km wavelength is in the order of what *Stüwe et al.* [1994] would say is not perturbing AFT relevant isotherms significantly. Considering the current relief to be very much related to intensified glacial erosion since ~0.9 Ma [*Muttoni et al.*, 2007; *Haeuselmann et al.*, 2007], we may assume that the relief was lower in former times and consequently the perturbation of isotherms was even less before ~0.9 Ma.

Mancktelow and Grasemann [1997] have incorporated time-dependent variations in isotherm geometry due to changes in exhumation rates. To gain an idea on how much the AFT relevant isotherms are affected by topography and exhumation rate we have assumed the 'worst' case with highest relief, which is the present-day topography, and compared their numerical predictions with our 'apparent' exhumation rates deduced from AER profiles. For an exhumation rate of 0.5 km/Myr the perturbation of AFT relevant isotherms is insignificant, but minor overestimation in the order of 0.17 km/Myr for 'apparent' relative to 'real' exhumation rates have to be considered for 1 km/Myr (*Mancktelow and Grasemann* [1997]; Figure S1). However, the increased exhumation rate of up to 1.2 km/Myr after ~3.5 Ma does not affect the result from AER profile of 0.5 km/Myr mean exhumation rate valid for the time interval between 10 and 3.5 Ma. *Braun* [2002] modeled the influence of surface relief changes on exhumation rates from AFT-AER and revealed that for short wavelength (<12 km) the effect is negligible even for large changes.

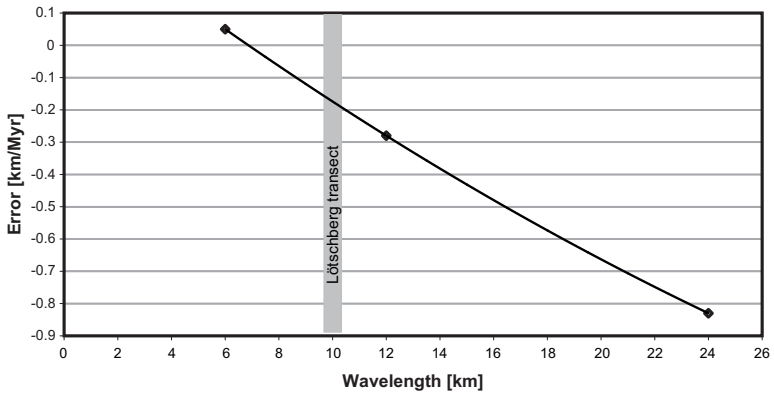

Figure S1: Error in the apparent exhumation rate for different wavelengths and a real exhumation rate of 1 km/Myr (after Mancktelow and Grasemann, 1997).

A.2. Constraining the geothermal gradient for the Lötschberg transect

Calculating exhumation rates from single AFT age data needs the assumption of a reasonable geothermal gradient to be constant over time or a good approximation of a "mean" geothermal gradient in cases were the gradient is a function of time, topography, denudation rate and fluid flow. The latter is in most cases not resolvable or unknown. So we have to search for a reasonable value for an assumed constant geothermal gradient. For a constant long-term moderate cooling history as in the northern part of the Lötschberg transect we have adopted the mean present-day near surface gradient deduced from heat-flow measurement in the old railway tunnel and from interpolation of measured rock temperatures in the tunnels to the surface (Figure S2). Surface temperatures are assumed to equal the mean annual air temperature at the given location, which are taken from the database of the Federal Office of Meteorology and Climatology MeteoSwiss [www.meteoschweiz.admin.ch/web/de/klima/klimanormwerte/]. Both estimation methods revealed approximately the same mean geothermal gradient in the order of 25 °C/km with increased near surface gradients (up to 52 °C/km) below valleys and decreased gradients beneath ridges (down to 21 °C/km) (Figure S2). The lateral change in near surface geothermal gradient is attributed to the lateral cooling effect of the present-day high relief. Water circulations within the Mesozoic sediments probably enhanced near surface cooling in the Gastern and Rhone valley (Figure S2). Beneath the Lötschen valley cooling from water circulation seems not to play an important role probably due to the lithologies.

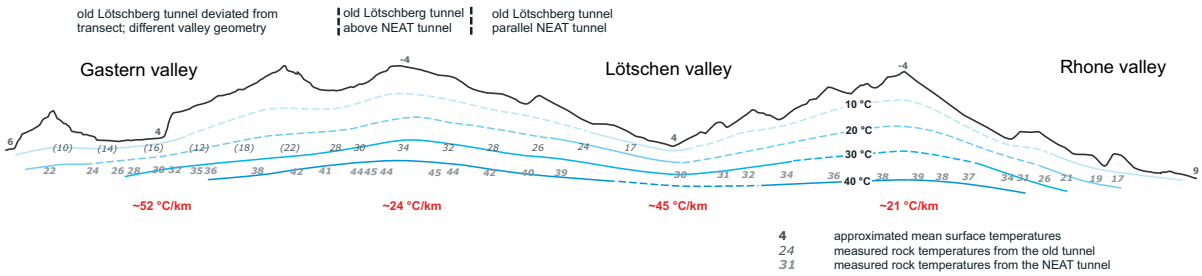

Figure S2: Isotherms and geothermal gradients along the Lötschberg transect from measured in-situ rock temperatures in the old railway tunnel and the NEAT base tunnel. Note that only the southern part of the old tunnel runs above and parallel the NEAT tunnel. The northern part of the old tunnel is outside of the transect.

Normal faulting may significantly alter the isotherms in the vicinity and across the fault zone. Generally the geothermal gradient in the footwall will be increased by the enhanced heat advection. The effect increases with increasing shear velocities and is also sensitive to the dip angle of the fault zone. Low-angle normal faults with erosion of the footwall have generally higher heat flows in the footwall [*Grasemann and Mancktelow*, 1993].

To conclude, with the present-day topography and steady-state exhumation rate of 1 km/Myr (which is the 'worst' case under consideration) AFT-relevant isotherms are perturbed by not more than ~200 m (i.e. the amplitude of perturbation). This situation, however, is not covered in time by our AER profiles. For the time interval 10 to ~3 Ma, covered by the AER profiles, the lower relief and exhumation rates will decrease the effect of heat advection and lower isotherm perturbation. Therefore the moderate exhumation rates of 0.5 km/Myr deduced from AER plots (Fig. 5) are considered realistic. In the northern part of the transect the constantly low exhumation rates hinder an increase in error even under higher relief. In the southern part we face low-angle normal faulting along the Rhône-Simplon fault zone since ~3.5 Ma, which lead to accelerated exhumation (up to 1.2 km/Myr) in the footwall. Tectonic denudation will increase the geothermal gradient in the footwall of the normal fault. We have accounted for this effect by assuming an increased gradient of 30 °C/km in the calculation of the

exhumation rate for the southern AFT samples in the footwall of the Rhône-Simplon fault (Fig. 6).
The relief increased rapidly around ~0.9 Ma, due to enhanced glacial erosion efficiency. The effect of the late increase in relief can not be assessed by our data because of low resolution.

B. Testing the validity of the 2D thermal model

To test the validity of the numerical model, which we have used to model AFT ages (see Figure 8), we modeled temperatures for 700 m above sea level (which is roughly the level of the NEAT tunnel) with the same initial parameters. The modeled and measured rock temperatures in the Lötschberg NEAT tunnel match nicely within 5 °C (Figure S3). Larger deviations of up to 10 °C are due to water circulation and subsequent cooling within the carstified Helvetic nappes. The influence from fluid flow in the autochthonous Mesozoic cover in the south seems to be negligible as the temperature field can be explained by tectonic denudation below the Rhone-Simplon fault alone.

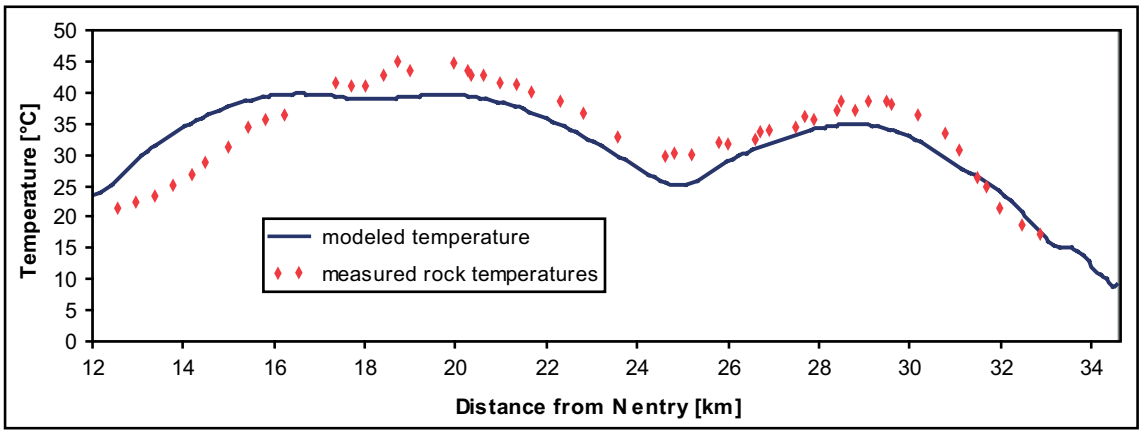

Figure S3: Modeled and measured rock temperatures in the Lötschberg NEAT tunnel.

References

Braun, J. (2002), Quantifying the effect of recent relief changes on age-elevation relationships, *Earth Planet. Sci. Lett.*, *200*, 331-343.

Grasemann, B., and N.S. Mancktelow (1993), Two-dimensional thermal modelling of normal faulting: the Simplon Fault Zone, Central Alps, Switzerland, *Tectonophysics*, *225*, 155-165.

Haeuselmann, P., D.E. Granger, P.-Y. Jeannin, and S.-E. Lauritzen (2007), Abrupt glacial valley incision at 0.8 Ma dated from cave deposits in Switzerland, *Geology*, *35*, 143-146.

Mancktelow, N.S., and B. Grasemann (1997), Time-dependent effects of heat advection and topography on cooling histories during erosion, *Tectonophysics*, *270*, 167-195.

Muttoni, G., C. Ravazzi, M. Breda, R. Pini, C. Laj, C. Kissel, A. Mazaud, and E. Garzanti (2007), Magnetostratigraphic dating of an intensification of glacial activity in the southern Italian Alps during Marine Isotope Stage 22, *Quaternary Research*, *67*, 161-173.

Stüwe, K., L. White, and R. Brown (1994), The influence of eroding topography on steady-state isotherms. Application to fission track analysis, *Earth Planet. Sci. Lett.*, *124*, 63-74.

Neogene activity along the Forcola normal fault: implications for the late-stage exhumation history of the Central Alps (Switzerland)

Nina Dörr[1,2], Cornelia Spiegel[1,2*], Martin Danišík[1], Christoph Glotzbach[1], Meinert Rahn[3], Wolfgang Frisch [1]

1: Universität Tübingen, Institut für Geowissenschaften, Sigwartstrasse 10, 72076 Tübingen, Germany
2: Universität Bremen, FB 5 – Geowissenschaften, Postfach 330 440, 28334 Bremen, Germany
3: Universität Freiburg, Mineralogisch-Geochemisches Institut, Albertstrasse 23b, 79104 Freiburg i. Brsg., Germany

Abstract

The Forcola normal fault follows a major Alpine suture zone, separating the European and the Briançonnais paleogeographic domains. In this study, we analyse rocks exposed east and west of the Forcola fault for zircon fission track, apatite fission track, and apatite (U-Th)/He thermochronology. Our aim is to better constrain the timing of activity along the Forcola fault, and and the denudation history of the Central Alps. Our data reveal that normal faulting along the Forcola fault persisted – continuously or discontinuously – until the latest Neogene. The evolution of the Forcola fault along the eastern margin of the Lepontine Dome was similar to the evolution of the Simplon fault along the western margin. Exhumation of the eastern Lepontine area was episodic, with periods of accelerated exhumation between (i) ~23 and 16 Ma, related to Miocene lateral extension, (ii) 12 and 10 Ma, coincident with a shift of the main Alpine drainage divide to the north, and (iii) between 5 and 4 Ma, associated with net exhumation of at least 1.8 km and contemporaneous with a nearly threefold increase of deposition rates in the foreland basins. Diachronous exhumation patterns along the Alps argue against a purely climatic origin of this latest exhumation period. Instead, we speculate that slab-breakoff beneath the Western Alps may explain the exhumation patterns observed.

Introduction

Understanding the late-stage evolution of an orogen is crucial for understanding topography and geomorphology of modern mountain ranges. The present-day morphology of the European Alps is the result of post-collisional processes, namely of Miocene large-scale orogen-parallel extension, and of latest-stage climatic and/or tectonic processes. The Lepontine Dome of the Central Alps is a metamorphic dome that formed during Miocene lateral extension. With present-day uplift rates of up to 1.4 mm/yr, it belongs to the most rapidly uplifting areas of the Alps. It was exhumed and unroofed along two normal faults bordering the dome to the west and to the east, the Simplon fault (Mancktelow, 1992) and the Forcola fault (Meyre et al., 1998; Fig. 1 and 2). Both fault systems are assumed as being conjugated. According to literature data, normal faulting along the Forcola fault commenced earlier (~25 Ma, Meyre et al., 1998) than along the Simplon fault (18 Ma; Grasemann and Mancktelow, 1993). While the Simplon fault is well-studied, less is known about the Forcola fault, although it is suggested to represent a major rejuvenated Alpine suture zone, separating the European and the Briançonnais paleogeographic domains.

The latest-stage exhumation history of the Alps is dominated by a nearly threefold increase in deposition rates in the foreland basins during the Pliocene (Kuhlemann, 2000; Fig. 3A). Since

* corresponding author: cornelia.spiegel@uni-bremen.de

this increase is not related to any obvious changes of the tectonic setting, it has been attributed to climatic causes (Cederbom et al., 2004; Willett et al., 2006). Cederbom et al. (2004) postulated that Pliocene climatic change caused enhanced erosion rates in the Central Alps, leading to up to 6.5 km of net erosion in the high topography areas of the Aar massif. However, independent proof for such high Pliocene erosion rates and for significant climate change in the area of the Alps at that time is lacking.
Our study aims to gain a better understanding of the processes that formed the present-day morphology of the Alps. In particular, we pursue two main goals: (i) to better constrain the timing of activity along the Forcola fault and thus the exhumation history of the Lepontine Dome, and (ii) to better understand the Pliocene exhumation and erosion period of the Central Alps. For this, we use a combination of zircon fission track, apatite fission track and apatite (U-Th)/He thermochronology, applied to rocks from both sides of the Forcola normal fault (Fig. 2). This approach allows monitoring the thermal history of the exposed rocks in the temperature range between approximately 330 to 40°C, thus documenting exhumation from about 10 km crustal depth to near-surface levels.

Geological Setting

Post-collisional evolution of the Alps
The present elongate shape of the Alps is mainly the result of large-scale Miocene lateral extension, caused by ongoing north-south convergence combined with lateral extrusion towards the unconstrained margin (Pannonian Basin) in the east (Ratschbacher et al., 1991, Frisch et al., 1998 and 2000). Orogen-parallel extension caused east-west stretching of more than 300 km for the entire Alps and led to exhumation and unroofing of the Alpine core complexes, namely the Lepontine Dome, the Tauern window and the Rechnitz window. Lateral extension started at about 23 Ma (Frisch et al., 2000). At 21 Ma, sediment discharge rates in the foreland basins strongly decreased, reflecting relief collapse (Kuhlemann, 2000; Fig. 3A), while at the same time, first Penninic detritus from the Central Alps was deposited in the North Alpine Foreland Basin (Spiegel et al., 2004). The extension period lasted until about 12 Ma (Frisch et al., 2000) and ended with the opening of the Tauern Window in the Eastern Alps (Brügel, 1998, Frisch et al., 1998) and the exposure of the Lower Penninic units of the Lepontine Dome in the Central Alps (Spiegel et al., 2000).
At about 5 Ma, foreland basin deposition rates strongly increased, indicating enhanced erosion of the Alpine hinterland (Kuhlemann, 2000; Fig. 3A). This enhanced erosion was attributed to climatic reasons by Cederbom et al. (2004) and Willett et al. (2006). Cederbom et al. (2004) related it to the shoaling and closure of the Isthmus of Panama, leading to an intensification of the Gulf Stream and thus to an increase in atmospheric moisture in Europe. Willett et al. (2006) suggested that climate change was also responsible for the end of the Messinian salinity crisis. Kuhlemann et al. (2002), by contrast, related Pliocene enhanced erosion rates to deep-seated lithospheric processes.

Geology of the study area
The Lepontine Dome comprises Lower Penninic units, which are separated from the Middle to Upper Penninic units to the west and to the east by the Simplon and Forcola normal faults, respectively. To the north it is bordered by the Aar and Gotthard massifs, while to the south it is separated from the South-Alpine units by the Periadriatic Lineament (Fig. 1). The study area is situated to both sides of the Forcola fault at the eastern margin of the Lepontine dome (Fig. 2). It comprises the Lower Penninic Adula nappe (including some samples from the Leventina nappe) west of the Forcola fault and the Middle Penninic Tambo nappe to the east of the fault. The Adula nappe represents the southern tip of the European margin and was the first part of stable Europe to enter the subduction zone during Eocene continent-continent collision

(Schmid et al., 1996), reaching peak pressures of up to 3.5 GPa during subduction (Heinrich, 1986). The Tambo nappe, by contrast, belongs to the Briançonnais paleogeographic domain and reached peak pressures of only 1.0–1.3 GPa during Alpine metamorphism (Baudin and Marquer, 1993).

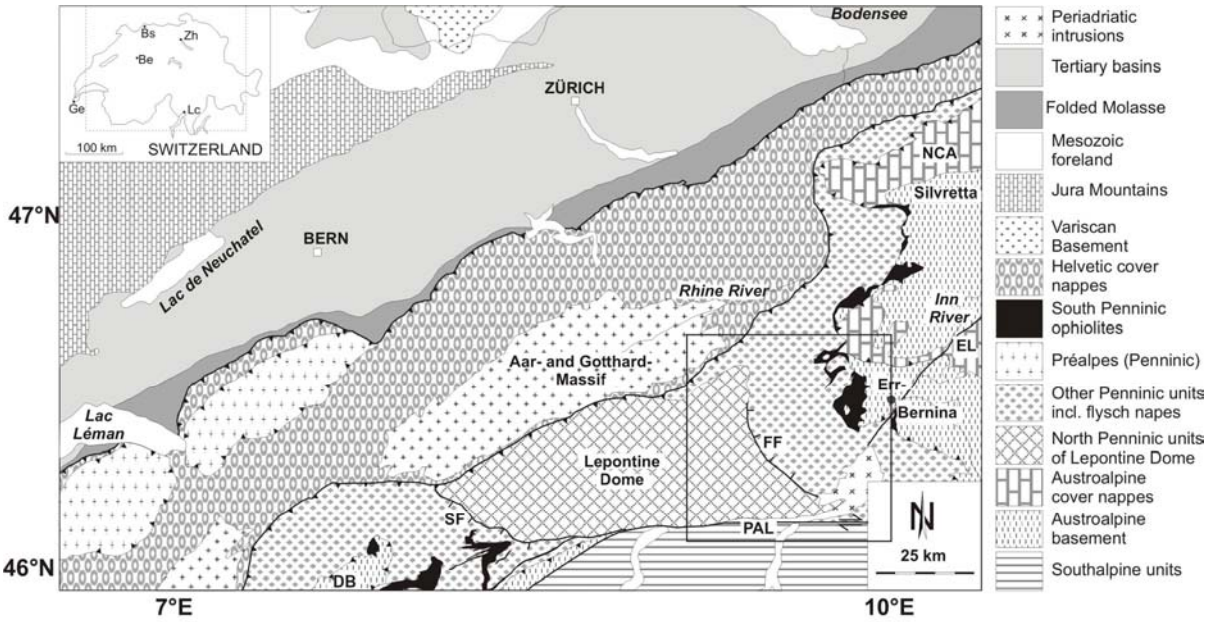

Fig. 1: Geological map of the Central Alps, showing the study area (black square) at the eastern margin of the Lepontine Dome. DB: Dent Blance nappe, EL: Engadine Line, NCA: Northern Calcareous Alps, FF: Forcola Fault, PAL: Periadriatic Lineament, SF: Simplon Fault. Inset: Be: Berne, Bs, Basel, Ge: Geneva, Lc: Locarno, Zh: Zurich.

The Forcola fault, separating the Tambo and the Adula nappe, is a ductile to brittle normal fault, dipping 40° to 50° to the north-east (Meyre et al., 1998). Total vertical displacement along the Forcola fault was at least 3 km during late-stage exhumation (Meyre et al., 1998). To the north, the Forcola fault is covered by the Mesozoic sediments of the Misox zone, which represents the remnants of the Valais trough formerly located between the European and the Briançonnais paleogeographic domains. Meyre et al. (1998) estimated that the Forcola fault was mainly active between 25 and 18 Ma. This estimate was derived from Rb-Sr and K-Ar ages (Jäger et al., 1967; Purdy and Jäger, 1976; Marquer et al., 1994) which date about the same temperature range as assumed for the deformation of the Forcola fault. The Forcola fault is considered as being conjugated with the Simplon fault at the western margin of the Lepontine Dome. The hanging wall of the Simplon fault was exhumed with an average rate of ~0.4 mm/yr since at least 25 Ma (Grasemann and Mancktelow, 1993). Displacement along the fault commenced at ~18 Ma, with most rapid movements between 18 and 15 Ma (Grasemann and Mancktelow, 1993). Assuming a fault plane dip of ~25°, total vertical displacement was ~15 km (Grasemann and Mancktelow, 1993). During the Late Neogene the Simplon fault was reactivated and is probably still active today (Seward and Mancktelow, 1994).

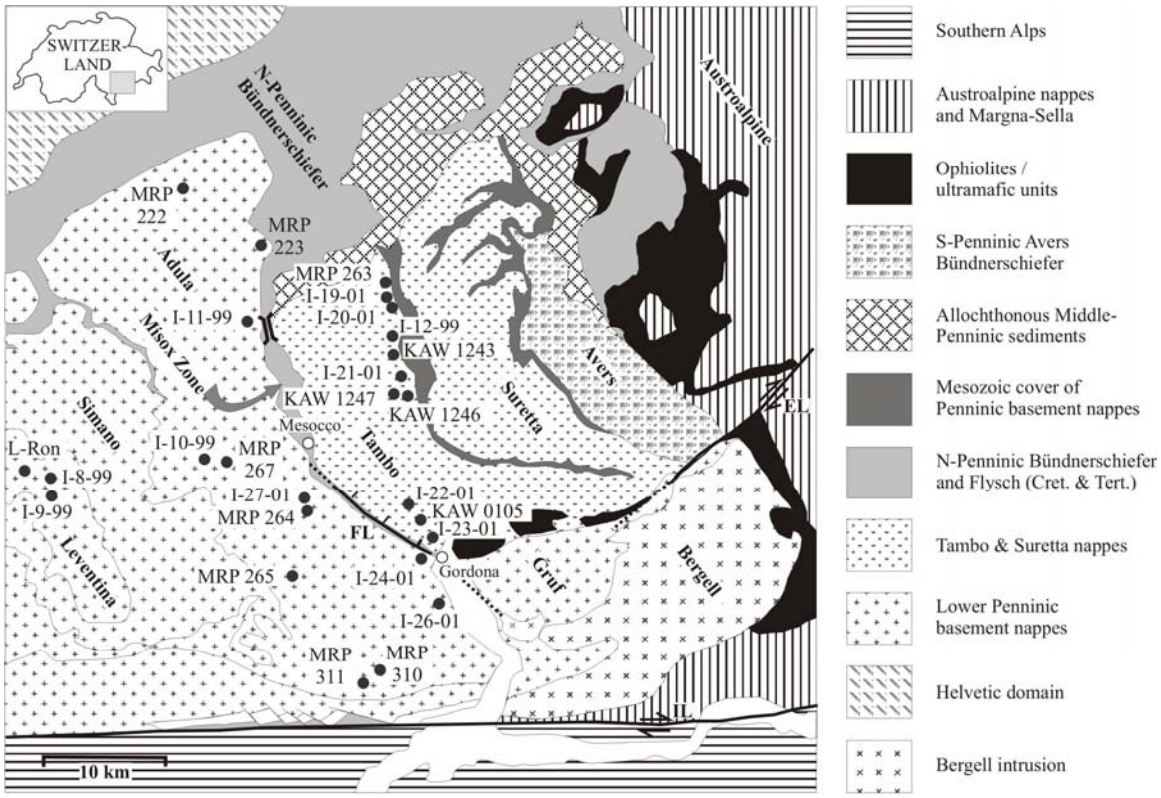

Fig. 2: Geological map of the study area, with sample locations (see also Wagner et al., 1977; Hunziker et al., 1992; Timar-Geng et al., 2004; Rahn, 2005). FL: Forcola Line, EL: Engadine Line, IL: Insubric Line. Map after Meyre et al. (1998) and Schmid et al. (1990).

Methodology

Fission Track Thermochronology:
Fission track analysis is based on spontaneous nuclear fission of ^{238}U, causing damage trails in the crystal lattice. These damage zones are called fission tracks and, when exposed to elevated temperatures, they gradually anneal with time. Fission track dating is thus sensitive to certain temperature ranges. Zircon fission track (ZFT) thermochronology monitors cooling through the temperature range between approximately 330 to 230°C (zircon partial annealing zone, ZPAZ, Tagami and Shimada, 1996). Apatite fission track (AFT) thermochronology, by contrast, records cooling through the temperature range between approximately 110 and 60°C (APAZ, apatite partial annealing zone, e.g., Brandon et al., 1998). The cooling style through this temperature range is reflected by the shortening patterns of fission tracks. Therefore, whenever possible, about 100 horizontal confined tracks have been measured for each apatite sample. Apart from time and temperature, fission track annealing is also influenced by the bulk chemical composition of the dated mineral. For apatite, the integrated effect of different anion and cation substitutions is reflected by the bulk etching velocity (Donelick, 1993; Burtner et al., 1994). Therefore, the mean diameter of etch figures on prismatic surfaces of apatite (= D_{par} value) has been measured as kinetic parameter for the annealing properties of individual apatite grains.

Apatite (U-Th)/He thermochronology:
Apatite (U-Th)/He (AHe) thermochronology is based on the ingrowth of radiogenic helium produced by the α-decay of U and Th. At temperatures >~85°C, helium diffuses out of the crystal, while at temperatures <~40°C, helium is retained and accumulates with time (Wolf et al. 1998). Between ~85 and ~40°C, helium is partially retained (helium partial retention zone – HePRZ). AHe thermochronology is thus sensitive to even lower temperatures than AFT

thermochronology and allows monitoring near-surface thermal processes. Because of the overlap of APAZ and HePRZ, AHe analysis provides independent proof for the results of AFT analysis, and vice versa. The stopping distance of a helium particle ejected from its parent isotope during radioactive decay is approximately 20 µm, leading to helium loss at the grain margins. To adjust for this effect, measured AHe ages have to be corrected. This alpha-ejection correction depends on grain size and morphology of the analysed apatite grain (Farley et al., 1996).
For AHe thermochronology, samples were first pre-selected on the basis of the grain mounts used for AFT analysis, to assess number and nature of inclusions and zoning with respect to the uranium-content. Between 2 and 6 aliquots were analysed for each of the remaining samples. Most of these were single-grain aliquots, only for sample MRP 310 we also included multi-grain aliquots. Average ages were calculated from aliquots, which revealed AHe ages younger than the corresponding AFT ages. Only AHe ages, which were based on the average of at least two aliquots were used for further interpretation.

Thermal history modelling
The results of different thermochronometers can be integrated by thermal history modelling calculating sets of potential thermal histories, which are consistent with the measured data. For this study, we used the software HeFTy (Ketcham, 2005), which is able to simultaneously model AFT and AHe data. Results of ZFT thermochronology cannot be directly included, but were used as constraints for the starting points of the modelled thermal histories. We used the annealing model of Ketcham et al. (2007), D_{par} as kinetic parameter (with 5 M etching method), and the He diffusion characteristics of Durango apatite (Farley, 2000).

Sampling and dating strategy
The samples used for this study were collected over a vertical distance of 2 km, but not from strictly vertical profiles. Instead, we chose to sample a relatively broad spatial distribution, because we wanted to assess the differential exhumation history of both sides of the Forcola fault over a broader regional scale. Also, in terms of apatite fission track ages, a relatively dense data set already exists from that area (Table 2, and compilation in Rahn, 2005). We therefore put our main focus on zircon fission track and apatite (U-Th)/He thermochronology, complemented by apatite fission track data from the literature. For AHe thermochronology and thermal history modelling, however, we only used samples, which have also been dated by AFT thermochronology.

Results of thermochronology and thermal history modelling

Results of thermochronological analysis are presented in tables 2, and 3 and figure 3. ZFT ages reveal a complex pattern (Fig. 3B). The majority of ages clusters between 23 and 16 Ma, which we interpret as reflecting a period of accelerated cooling / exhumation. With a ZFT age of ~12 Ma, the sample from the Leventina nappe is significantly younger than the other samples. Neither a systematic age-elevation relationship nor a clear jump in ages across the Forcola fault was observed, although average ages to the west of the Forcola fault are slightly younger (~18 Ma) than to the east of it (~21 Ma). Zircons yielded strong variations of the U-content, ranging from ~400 to >3000 ppm. Therefore, the ZFT age variation may also partly be explained by differences of the closure temperature of the ZFT system, resulting from differences in radiation damage.
AFT ages, by contrast, show (i) a positive correlation between sample age and elevation, and (ii) a clear age-offset across the Forcola fault. AFT ages cluster around 5 Ma west and around 10 Ma east of the Forcola fault (Fig. 3C). Mean track lengths (MTL) are only slightly

shortened and cluster around 14 μm on both sides of the Forcola fault. AFT age patterns as well as MTL suggest rapid exhumation from about 12 to 10 Ma and around 5 Ma (Fig. 3C).
Average AHe ages reveal a small but systematic age difference between rocks exposed east and west of the Forcola fault (Fig. 3D). Samples from the area west of the fault yield a positive correlation between sample age and elevation, showing rapid exhumation between 5.5 Ma and 5 Ma, slowing down at ~4 Ma, with a net exhumation of >1.8 km between 5 and 4 Ma.
ZFT, AFT, and AHe data were integrated by thermal history modelling (Fig. 4). Age patterns along the Forcola fault, as described above, suggest an episodic cooling history with periods of accelerated cooling from ~23 to 16 Ma, 12 to 10 Ma, and around 5 Ma, and periods of slower cooling in-between. Constraints for the modelling were chosen accordingly. Thermal history modelling shows that our measured data are consistent with such an episodic cooling history, and that all three thermochronological data sets are consistent with each other. The period of rapid cooling from ~12 to 10 Ma is not recorded by the samples west of the Forcola fault, as they are derived from a deeper structural level than samples east of the fault, and were still at temperatures >110°C at that time (Fig. 5). Only later they became juxtaposed with samples from east of the fault by normal faulting. Net exhumation of ~1.8 km between 5 and 4 Ma is also consistent with the modelled time-temperature path, which reveals cooling of approximately 60°C for that time interval and the best-fit solution (Fig. 4B). Furthermore, the modelled cooling histories are also consistent with an end of rapid exhumation at 4 Ma and subsequent slower cooling rates, as deduced from the AHe age-elevation relationship (Fig. 3D).

Table 1: Locations of samples included in this study

Sample	Location	Elevation (m)	Longitude	Latitude	Unit
I-09-99	Biasca	350	716,900	134,350	Leventina
I-08-99	Biasca	380	717,750	137,800	Leventina
L-Ron	Sassan	780	711,260	137,770	Leventina
I-10-99	Val Calanca	1130	730,000	137,690	Adula
I-11-99	Ps. San Bernadino	1790	732,900	150,420	Adula
I-24-01	near Gordona	290	748,400	127,400	Adula
I-26-01	San Pietro	293	749,450	125,050	Adula
MRP 265	Norantola	375	733,580	127,430	Adula
MRP 264	Soazza	470	736,610	133,850	Adula
I-27-01	Soazza	710	736,550	135,400	Adula
MRP 223	Hinterrhein	1650	734,075	153,775	Adula
MRP 222	Guraletsch	1905	728,730	159,600	Adula
MRP 267	Trescolmen	2100	733,730	139,950	Adula
MRP 311	Cima dello Stagn	2280	736,200	119,150	Adula
MRP 310	Sass della Vacca	2290	737,370	120,155	Adula
I-23-01	Mese	555	747,800	129,400	Tambo
KAW 0105	Truzzo	590	748,600	134,550	Tambo
KAW 1243	Motta	760	747,450	142,500	Tambo
I-22-01	Olmo	1005	747,720	133,950	Tambo
KAW 1246	Prestone	1020	747,550	138,950	Tambo
I-12-99	Campodolcina	1345	746,540	144,100	Tambo
I-21-01	Starleggia	1602	745,200	141,750	Tambo
I-20-01	Monte Spluga	1945	745,390	150,790	Tambo
I-19-01	Monte Spluga	1962	745,200	151,000	Tambo
KAW 1247	Prestone	1980	745,500	140,850	Tambo
MRP 263	Ps. di Spluga	2120	745,060	151,980	Tambo

Table 2: Results from Fission Track Thermochronology

Sample	Mineral	nappe	counted grains	U-cont. (ppm)	spontaneous		induced		$P\chi^2$	dosimeter		Centr. age (Ma ± 1σ)	MTL (µm)	S.D. (µm)	n
					ρ_s	n_s	ρ_i	n_i	(%)	ρ_d	n_d				
Newly generated data from this study															
I-9-99	Zircon	Leventina	18	3040	165	919	253	1407	53	3.07	3793	11.6 ± 0.6	n.d.	n.d.	n.d.
I-8-99	Zircon	Leventina	25	566	57	1130	82	1618	85	5.38	9989	21.8 ± 0.9	n.d.	n.d.	n.d.
I-10-99	Zircon	Adula	25	404	34	733	60	1275	78	5.67	9989	18.9 ± 1.0	n.d.	n.d.	n.d.
I-11-99	Zircon	Adula	17	1704	136	968	145	1027	2	3.14	3793	17.0 ± 1.1	n.d.	n.d.	n.d.
I-24-01	Zircon	Adula	17	2378	193	1389	226	1625	0	3.49	3793	17.2 ± 1.2	n.d.	n.d.	n.d.
I-24-01	Apatit	Adula	17	17	0.44	27	16.53	1019	90	11.54	5529	5.7 ± 1.1	13.72	1.81	37
I-26-01	Zircon	Adula	16	2113	158	1061	207	1391	33	3.63	3793	16.0 ± 0.8	n.d.	n.d.	n.d.
I-27-01	Zircon	Adula	9	1707	178	614	174	600	0	3.74	3793	22.0 ± 2.2	n.d.	n.d.	n.d.
I-27-01	Apatite	Adula	20	44	1.28	153	44.27	5294	94	12.57	5529	6.8 ± 0.6	13.72	1.94	100
I-12-99	Zircon	Tambo	25	727	74	1141	102	1563	91	5.13	9989	21.7 ± 0.9	n.d.	n.d.	n.d.
I-19-01	Zircon	Tambo	19	803	95	825	72	618	34	3.25	3793	25.2 ± 1.6	n.d.	n.d.	n.d.
I-19-01	Apatite	Tambo	20	28	1.23	128	23.06	2397	98	10.25	5539	10.2 ± 1.0	n.d.	n.d.	n.d.
I-20-01	Zircon	Tambo	12	1079	90	364	98	394	37	3.28	3793	17.6 ± 1.4	n.d.	n.d.	n.d.
I-21-01	Zircon	Tambo	14	1340	129	694	124	668	99	3.35	3793	20.2 ± 1.2	n.d.	n.d.	n.d.
I-21-01	Apatite	Tambo	20	32	1.55	203	28.43	3736	92	10.76	5529	10.9 ± 0.8	14.11	1.64	100
I-22-01	Zircon	Tambo	18	1535	153	1089	142	1010	49	3.39	3793	21.2 ± 1.1	n.d.	n.d.	n.d.
I-23-01	Zircon	Tambo	13	1643	155	639	152	629	41	3.46	3793	20.4 ± 1.3	n.d.	n.d.	n.d.
Data included in this study from the literature															
L-Ron	Apatite	Leventina	20	n.d.	0.3	16	9.5	491	53	10.36	8739	5.9 ± 1.7	14.04	1.62	18
MRP 267	Apatite	Adula	20	n.d.	1.2	107	43.4	3952	76	10.38	2530	4.8 ± 0.5	14.15	1.56	100
MRP 223	Apatite	Adula	20	n.d.	0.7	107	29	2292	90	11.28	2750	4.8 ± 0.7	13.40	1.5	100
MRP 264	Apatite	Adula	20	n.d.	0.4	39	41.9	1218	60	10.59	2581	5.8 ± 1.0	13.18	1.89	100
MRP 266	Apatite	Adula	20	n.d.	0.6	38	13.2	885	69	10.45	2547	7.7 ± 1.3	14.04	1.31	59
MRP 222	Apatite	Adula	20	n.d.	0.12	171	31.3	4376	80	13.29	4146	8.9 ± 0.8	13.94	1.33	100
MRP 311	Apatite	Adula	20	n.d.	0.7	64	13.7	1303	89	9.61	2343	8.1 ± 1.1	14.28	1.3	100
MRP 310	Apatite	Adula	20	n.d.	0.5	35	6.7	514	92	9.54	2326	11.2 ± 2.0	13.93	1.34	100
MRP 265	Apatite	Adula	20	n.d.	1.1	98	36	3230	79	10.52	2564	5.5 ± 0.6	13.95	1.48	100
MRP 263	Apatite	Tambo	20	n.d.	3.2	281	34.5	3025	18	10.66	2598	16.9 ± 1.3	13.27	1.65	100
KAW 1243	Apatite	Tambo	300	n.d.	0.04	24	0.71	421	6	6.56	7788	12.7 ± 2.7	n.d.	n.d.	n.d.
KAW 1247	Apatite	Tambo	200	n.d.	0.16	64	2.69	1062	13	6.56	7788	13.4 ± 2.1	n.d.	n.d.	n.d.
KAW 1246	Apatite	Tambo	200	n.d.	1.95	769	43.51	2750	3	6.56	7788	9.9 ± 0.6	12.9	1.71	100

Fission track ages of this study were calculated using dosimeter glasses CN-2 with ζCN-2 = 116 ± 2 for zircon, and dosimeter glass CN-5 with ζCN-5 = 373 ± 8 for apatite. Dating was performed according to the external detector method (Gleadow, 1981) and the zeta calibration approach (Hurford and Green, 1983). MTL = mean track lengths. n = number of counted tracks, r = track density (x10^5 tracks/cm²). $P\chi^2$ is the probability of obtaining χ^2 value for n degress of freedom (where n = number of crystals - 1). Literature data was taken from Wagner et al., 1977, Hunziker et al., 1992, Timar-Geng et al., 2004, and Rahn, 2005.

Table 3: Results from apatite (U-Th)/He thermochronology

Sample name	n	Th (ng)	U (ng)	^{4}He (ncc)	TAE (%)	Th/U	raw age (Ma)	Ft	corr. age (Ma)	± error (Ma)	mean age (Ma)	S.E. of mean (Ma)	S.D. (Ma)
I-08-99#1	1	0.059	0.031	0.013	5.2	1.883	2.3	0.63	3.7	0.4			
I-08-99#2	1	0.018	0.044	0.015	7.1	0.412	2.5	0.62	4.1	0.5	**3.2**	0.7	1.2
I-08-99#3	1	0.028	0.040	0.009	4.5	0.681	1.5	0.80	1.9	0.2			
I-10-99#3	1	0.061	0.021	0.022	7.1	2.915	5.2	0.73	*7.1*	*0.9*			
I-11-99#4	1	0.029	0.022	0.008	7.2	1.339	2.2	0.68	*3.2*	*0.4*			
I-19-01#2	1	0.060	0.065	0.034	7.1	0.924	3.6	0.72	5.0	0.6			
I-19-01#3	1	0.028	0.111	0.073	5.3	0.252	5.1	0.83	6.2	0.7			
I-19-01#5	1	0.043	0.148	0.155	5.3	0.289	8.1	0.74	*11.0*	*1.2*	**6.6**	0.7	1.4
I-19-01#6	1	0.030	0.147	0.117	5.3	0.202	6.3	0.87	7.2	0.8			
I-19-01#7	1	0.022	0.051	0.038	7.1	0.433	5.6	0.69	8.2	1.0			
I-21-01#1	1	0.032	0.129	0.088	5.3	0.249	5.3	0.81	6.6	0.7			
I-21-01#2	1	0.022	0.035	0.020	7.1	0.622	4.0	0.65	6.2	0.8			
I-21-01#3	1	0.027	0.073	0.036	7.1	0.372	3.7	0.69	5.4	0.7	**6.0**	0.3	0.6
I-21-01#4	1	0.029	0.075	0.055	7.1	0.383	5.5	0.84	6.6	0.8			
I-21-01#5	1	0.022	0.054	0.029	7.1	0.402	4.0	0.74	5.4	0.7			
I-22-01#1	1	0.035	0.021	0.021	7.1	1.658	5.8	0.74	7.8	1.0	**7.2**	0.6	0.9
I-22-01#4	1	0.049	0.023	0.021	7.1	2.121	5.0	0.75	6.6	0.8			
I-24-01#1	1	0.014	0.024	0.006	6.5	0.594	1.9	0.65	3.0	0.4			
I-24-01#2	1	0.024	0.036	0.012	4.3	0.670	2.5	0.68	3.6	0.4	**3.4**	0.2	0.4
I-24-01#3	1	0.041	0.064	0.022	4.9	0.633	2.4	0.66	3.7	0.4			
I-27-01#1	1	0.037	0.084	0.030	4.3	0.442	2.7	0.59	4.5	0.5			
I-27-01#2	1	0.099	0.280	0.166	3.3	0.353	4.5	0.80	5.7	0.6			
I-27-01#3	1	0.040	0.093	0.041	4.7	0.429	3.3	0.78	4.2	0.5	**4.0**	0.5	1.1
I-27-01#4	1	0.059	0.079	0.023	5.1	0.745	2.0	0.79	2.6	0.3			
I-27-01#5	1	0.056	0.052	0.017	5.2	1.077	2.1	0.702	3.0	0.3			
I-27-01#7	1	0.051	0.196	0.076	4.6	0.259	3.0	0.76	4.0	0.4			
MRP222#1	1	0.140	0.149	0.067	3.1	0.940	3.0	0.75	4.1	0.4			
MRP222#2	1	0.085	0.111	0.075	4.4	0.766	4.7	0.75	6.3	0.7			
MRP222#3	1	0.087	0.098	0.075	6.5	0.884	5.2	0.78	6.6	2.8	**5.3**	0.5	1.2
MRP222*10	1	0.074	0.094	0.043	4.1	0.790	3.2	0.73	4.4	0.5			
MRP222*20	1	0.129	0.092	0.043	4.2	1.404	2.9	0.72	4.0	0.4			
MRP222*30	1	0.070	0.087	0.039	4.4	0.804	3.2	0.51	6.2	0.7			
MRP223#1	1	0.031	0.039	0.015	6.2	0.813	2.7	0.66	4.1	0.5			
MRP223#4	1	0.042	0.095	0.056	4.1	0.435	4.4	0.74	5.9	0.6			
MRP223#6	1	0.028	0.024	0.010	6.2	1.142	2.7	0.46	5.8	0.7	**5.3**	0.6	1.0
MRP223#7	1	0.028	0.022	0.024	6.4	1.299	7.0	0.57	*12.2*	*1.4*			
MRP223#8	1	0.027	0.042	0.028	5.5	0.633	4.8	0.65	*7.4*	*0.8*			
MRP264#1	1	0.091	0.020	0.024	5.4	4.591	4.8	0.73	*6.6*	*0.8*			
MRP264#3	1	0.020	0.040	0.019	7.0	0.514	3.6	0.84	*4.3*	*0.5*			
MRP310#10	1	0.055	0.024	0.008	5.0	2.323	1.8	0.64	2.8	0.3			
MRP310#6#7	2	0.046	0.054	0.030	4.9	0.857	3.9	0.84	4.6	0.5	**5.0**	1.2	2.5
MRP310#8	1	0.061	0.014	0.008	5.9	4.357	2.2	0.54	4.1	0.5			
MRP310#9#2	2	0.058	0.024	0.023	5.3	2.419	5.0	0.59	8.5	1.0			
MRP311#2	1	0.113	0.021	0.089	4.4	5.383	15.4	0.77	*20.1*	*2.2*			
MRP311#3	1	0.027	0.026	0.015	5.8	1.025	3.8	0.62	6.1	0.7			
MRP311#4	1	0.080	0.018	0.020	5.4	4.442	4.4	0.61	7.2	0.8	**5.4**	1.2	2.2
MRP311#5	1	0.114	0.019	0.080	6.3	5.994	14.4	0.68	*21.3*	*2.5*			
MRP311#8	1	0.171	0.054	0.021	3.6	3.199	1.8	0.62	2.9	0.3			

TAE = Total analytical error, S.E. = standard error, S.D. = standard deviation. Numbers in italics have been excluded from interpretation

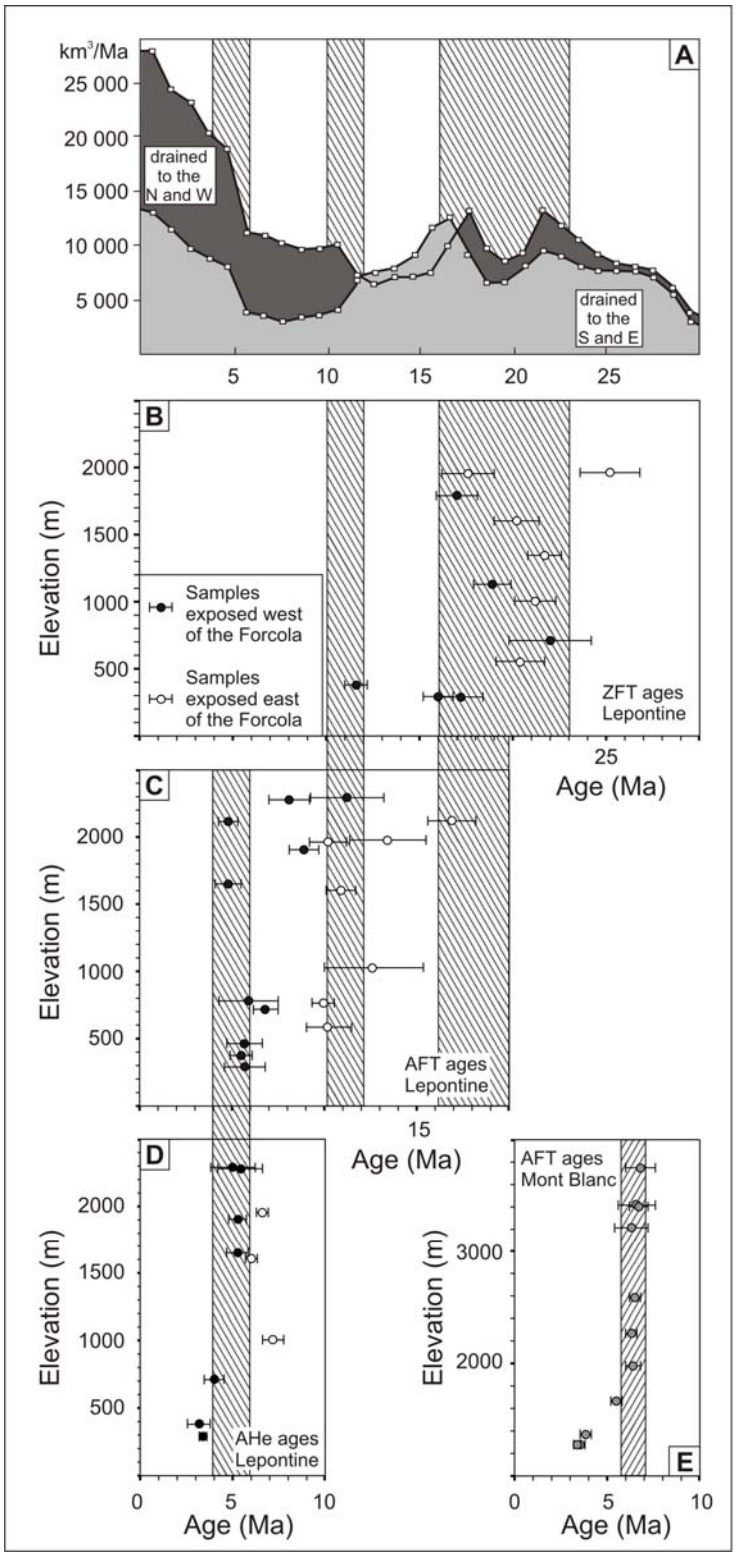

Fig. 3: Relation between results of thermochronology and the sediment budget of circumalpine basins. Hatched patterns mark time intervals which we interpret as periods of accelerated cooling. **A**: Sediment budget of the Central and Western Alps, separated for areas draining to the north and west (dark grey) and to the south and east (light grey). After Kuhlemann (2000). **B, C, D**: ZFT, AFT, and AHe ages of the eastern margin of the Lepontine Dome, plotted against sample elevation. Plot C includes data from Wagner et al., 1977; Hunziker et al., 1992; Timar-Geng et al., 2004, and Rahn, 2005, table 2). **E**: AFT ages from the northwestern flank of the Mont Blanc massif (Western Alps), plotted against sample elevation. Data from Glotzbach et al. (in review).

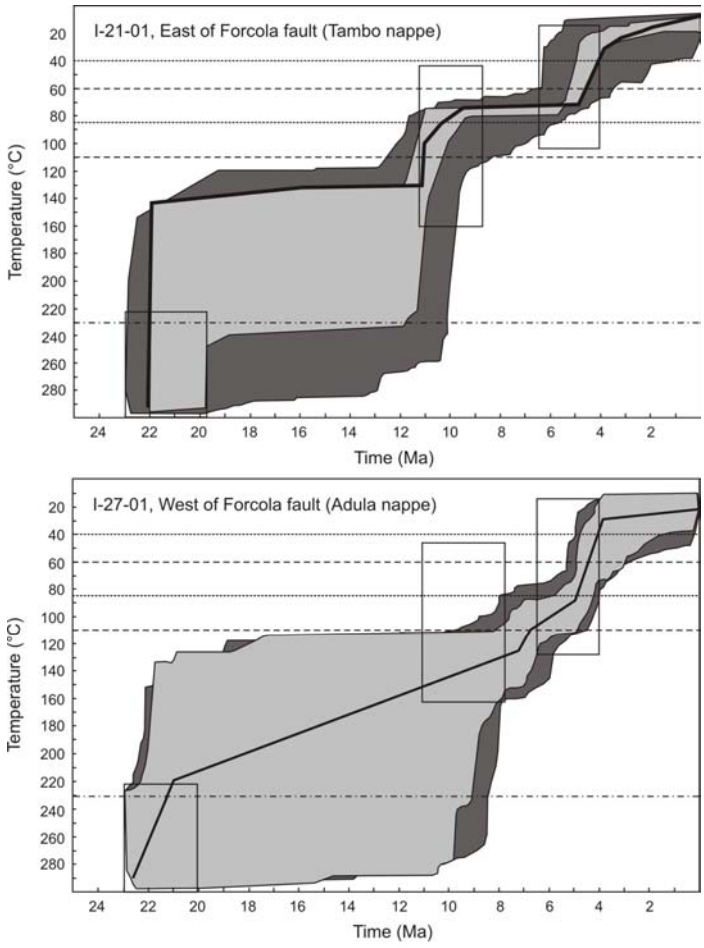

Fig. 4: Thermal history modelling of select samples from the Tambo nappe (east of the Forcola fault) and the Adula nappe (west of the Forcola fault), testing the proposed episodic cooling history on the basis of AFT and AHe thermochronology. Dpar I-21-01: 2.31 μm, Dpar I-27-01: 2.05 μm). Modelling was carried out with the program HeFTy (Ketcham, 2005). Thick black line: best fit solution, light grey areas: good fit solutions, dark grey areas: acceptable fit solutions, black squares: constraints. Dashed lines show temperature ranges of the zircon and apatite partial annealing zones and of the helium partial retention zone.

Activity along the Forcola normal fault

With no clear difference between rocks exposed to the east and to the west of the Forcola the ZFT age pattern argues against significant displacement along the Forcola fault between ~ 23 and 16 Ma. ZFT thermochronology, however, gives no evidence about activity along the Forcola fault prior to 23 Ma, when the presently exposed structural level was still situated at a crustal depth below the ZPAZ (Fig. 5). If normal faulting commenced or resumed after 16 Ma, as suggested by the AFT and AHe ages, one would expect that this later displacement would result in a disturbance of the ZFT age pattern, with older ZFT ages east and younger ZFT ages west of the Forcola fault. To explain the ZFT ages observed, we propose the following exhumation history: (i) between ~23 and 16 Ma, the area of the present-day Forcola fault experienced accelerated exhumation, resulting in a similar ZFT age signature of a larger crustal segment. This is supported by the clustering of ZFT ages between ~23 and 16 Ma, and is consistent with the modelled thermal history, (ii) displacement along the Forcola fault commenced / resumed after 16 Ma., and (iii) total vertical displacement related to the post-16 Ma activity of the Forcola was minor compared to the net exhumation during the 23 to 16 Ma rapid cooling period. Otherwise we would again observe a jump in ZFT ages across the Forcola fault. According to this interpretation, the eastern margin of the Lepontine Dome (Forcola area) would have experienced a similar thermal evolution as its western margin

(Simplon area), with a period of rapid exhumation after approximately 25 Ma, followed by the onset of vertical displacement at about 18 Ma (see Grasemann and Mancktelow, 1993).
AFT and AHe ages show a clear jump across the Forcola fault, indicating that normal faulting was – continuously or discontinuously – active until the latest Neogene (at least 3 Ma, Fig. 5). This is much longer than previously assumed (Meyre et al., 1998), but again consistent with the history along the western margin of the Lepontine Dome, where late Neogene reactivation of the Simplon fault was observed by Seward and Mancktelow (1994). From the AFT age pattern, a minimum vertical displacement of 1.1 km between ~10 and 5 Ma is deduced, assuming that the rock units presently juxtaposed to the east and to the west of the Forcola were formerly a continuous crustal section.

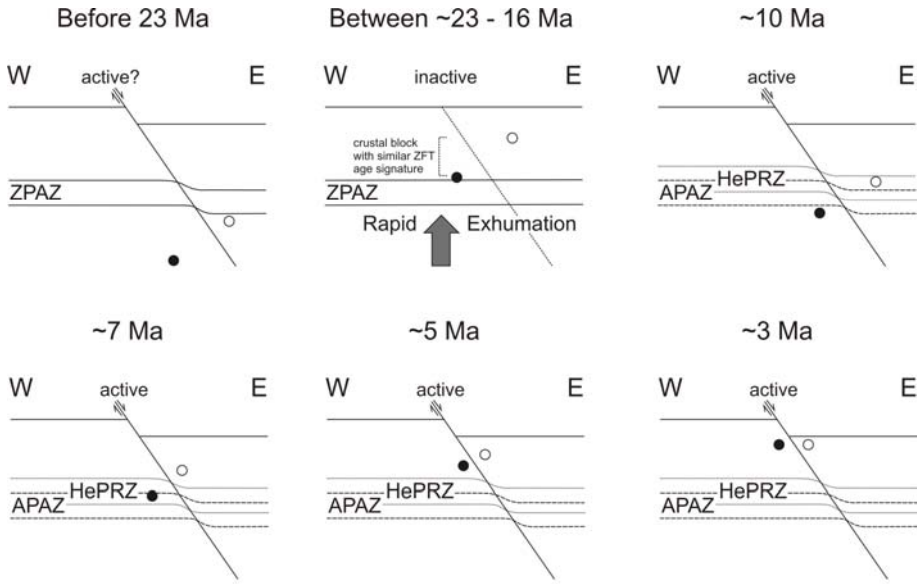

Fig. 5: Exhumation history of the presently exposed structural level east (white dot) and west (black dot) to the Forcola fault, relative to the temperature ranges of the zircon partial annealing zone (ZPAZ), apatite partial annealing zone (APAZ) and helium partial retention zone (HePRZ). Not to scale.

Late-stage exhumation history of the Central Alps

Our data reveal an episodic cooling history for the eastern margin of the Lepontine Dome, with periods of accelerated cooling / exhumation from ~23 to 16 Ma, 12 to 10 Ma, and around 5 Ma. The cooling episode between ~23 to 16 Ma coincides with the onset of the lateral extension period, which was the strongest geomorphic reorganization in post-collisional times, resulting in the collapse of the relief and more than 300 km of east-west stretching (Frisch et al., 2000). A strong exhumation pulse at ~21 Ma is also evidenced by the simultaneous occurrence of Penninic detritus in all fan systems of the Swiss Molasse Basin (Spiegel et al., 2002 & 2004). Exhumation / doming, relief collapse, and renewed doming are also reflected by the sediment budget, showing first increasing deposition rates between 25 and 21 Ma, followed by a drastic decrease at 21 Ma, and again a strong increase after 20 Ma (Fig. 3A, Kuhlemann et al., 2000 and 2002).
The 12 to 10 Ma period of accelerated exhumation also seems to be related to tectonic and geomorphic changes in the Central Alps. At that time, lateral extension ended, which resulted in a renewed build-up of relief. Main thrusting activity in the Central Alps switched to the north, initiating thrusting in the Jura Mountains (Kälin, 1997; Becker, 2000). This resulted in the shift of the main Alpine drainage divide to the north, as evidenced by the sediment budget data of circum-Alpine basins (Kuhlemann et al., 2001, Fig. 3A).

Another period of rapid exhumation, associated with net exhumation of >1.8 km, took place between 5 and 4 Ma. The end of rapid exhumation at 4 Ma is concurrent with the end of folding in the Jura Mountains (Becker, 2000) and with the decrease of active deformation in the Western and Central Alps. This supports the suggestion of Willett et al. (2006) that the shift from orogenic construction to orogenic destruction occurred at ~4 Ma.
Onset of rapid exhumation at ~5 Ma was contemporaneous with a nearly threefold increase in foreland basin deposition rates (Fig. 3A–. It should be kept in mind, however, that the 1.6 to 1.8 km of exhumation estimated here cannot be attributed solely to erosion, but partly to tectonic denudation since our data are derived from the footwall of an active normal fault). No obvious changes of the tectonic setting at ~5 Ma are described in the literature, so increased deposition rates in the foreland basins have been explained by climatic changes, namely enhanced precipitation rates (Cederbom et al., 2004, Willett et al., 2006). Palynonlogical data, however, give no evidence for changes in precipitation rates at that time (Fauquette et al., 1998 and 1999; Fauquette and Bertini, 2003; Warny et al., 2003). Climate-driven exhumation may be distinguished from tectonically driven exhumation by the cooling pattern along the orogen: as a response to climatic changes, one would expect simultaneous exhumation along the entire orogen, whereas for tectonic changes, a differential exhumation pattern would be expected.
In this context we like to compare age-elevation relationships from the eastern Lepontine Dome in the Central Alps (Fig. 3B, C, D) and from the northwestern flank of the Mont Blanc massif in the Western Alps (Fig. 3E; Glotzbach et al., in review). The 5 - 4 Ma exhumation pulse cannot be verified in the Mont Blanc area. Instead, rapid exhumation took place there between ~7 and 6 Ma, i.e., 2 myr earlier. Even though these two profiles may not be representative for the entire Alps, our data are consistent with those of Vernon et al. (2006), who has computed the exhumation history of the entire Western and Central Alps, based on a compilation of all FT ages of that area. These authors also found that the late Neogene exhumation pulse shifted from the Western Alps to the Central Alps. Furthermore, deposition patterns in the circum-Alpine foreland basins show that the Pliocene increase in sedimentation rates was much more pronounced in the Western and Central Alps, as compared to the Eastern Alps, and started earlier in the west than in the east (Kuhlemann et al., 2002). This time shift in both, foreland basin deposition rates and hinterland exhumation argues against a (purely) climatic origin of Late Neogene accelerated exhumation and erosion.
An alternative explanation would be a relatively young slab-breakoff beneath the Western Alps, as postulated by Lippitsch et al. (2003) on the basis of high-resolution teleseismic tomography. Accelerated Late Miocene to Pliocene exhumation may be the surface expression of this slab-breakoff, starting beneath the Western Alps and propagating towards the east. Earlier slab breakoff beneath the Central Alps during the Oligocene also resulted in accelerated exhumation, particularly in the Bergell area of the Central Alps (von Blanckenburg and Davis, 1995). According to the data of Lippitsch et al. (2003), the sunken young slab is currently at a depth of approximately 150 km beneath the Western Alps. Assuming a free sinking rate of ~2 cm/yr (Hafkenscheid et al., 2006), slab breakoff should have occurred at ~7.5 Ma, which would be consistent with the onset of accelerated exhumation at ~7 km in the Western Alps. Whether this scenario is realistic, however, remains to be tested by geophysical modelling.

Conclusions

For this study we analysed samples exposed to the east and west of the Forcola normal fault by zircon fission track, apatite fission track, and apatite (U-Th)/He thermochronology, in order to gain insights into timing and activity of the Forcola fault and into the late-stage exhumation history of the Lepontine Dome of the Central Alps. Our data revealed the following:

- ZFT age patterns and thermal history modelling suggest that the eastern Lepontine Dome was rapidly exhumed between ~23 to 16 Ma, presumably related to the onset of Miocene lateral extension.
- Net exhumation between 23 and 16 Ma must have been larger than later vertical displacement along the Forcola fault.
- Faulting activity (continuous or discontinuous) along the Forcola persisted until at least 3 Ma, much longer than previously assumed.
- Exhumation of the eastern Lepontine Dome was episodic, with periods of accelerated exhumation between ~23 and 16 Ma, 12 and 10 Ma, and 5 and 4 Ma.
- The eastern margin of the Lepontine Dome (Forcola area) experienced a similar evolution as its western margin (Simplon area), with relatively rapid exhumation after 25 Ma, onset (or re-start) of normal faulting after 17 Ma, and continuous or discontinuous fault activity until the latest Neogene.
- Rapid exhumation between ~5 and 4 Ma was associated with net exhumation of >1.8 km, consistent with enhanced deposition rates in the foreland basins (Kuhlemann, 2000).
- The slow-down of exhumation rates after 4 Ma was contemporaneous with the cessation of the Jura folding and thus with the decrease of active deformation in the Central Alps, which presumably marked the transition from orogenic construction to orogenic destruction (Willet et al. 2006).
- Exhumation patterns along the Alps argue against a purely climatic control of Pliocene rapid exhumation. Instead, we speculate that late slab breakoff beneath the Western Alps may be responsible for the exhumation patterns observed.

Acknowledgements

This study was financed by the German Science Foundation. Thanks to Gerlinde Höckh, Dagmar Mühlbayer-Renner and Dagmar Kost for sample processing, to Per Jeisecke for preparing the thin sections, and to Lars Behnke and Joachim Kuhlemann for support during sampling.

References

Baudin, T., and Marquer, D. (1993), Métamorphisme et déformation dans la nappe de Tambo (Alpes Centrales, Suisses); évolution de la substitution phengitique au cours de la déformation alpine, *Schweiz. Mineral. Petrogr. Mitt., 73*, 285-299.

Becker, A. (2000), The Jura Mountains – an active foreland fold-and-thrust belt? *Tectonophysics, 321/4*, 381-406.

Brandon, M.T., Roden-Tice, M.K., and Garver, J.I. (1998), Late Cenozoic exhumation of the Cascadia accretionary wedge in the Olympic Mountains, Northwest Washington Stat. *GSA Bulletin,* 110/8, 985-1009.

Brügel, A. (1998), Provenances of alluvial conglomerates from the Eastalpine foreland: Oligo-Miocene denudation history and drainage evolution of the Eastern Alps [Ph.D. thesis], *Tübinger Geowissenschaftlich Arbeiten, Reihe A40*, 1-168.

Burtner R., Nigrini, A., and Donelick, R. (1994), Thermochronology of Lower Cretaceous source rocks in the Idaho-Wyoming thrust belt. *AAPG Bulletin,* 78/ 10, 1613-1636.

Cederbom, Ch., Sinclair, H., Schlunegger, F., and Rahn, M. (2004), Climate-induced rebound and exhumation of the European Alps, *Geology*, 32/8, 709-712.

Donelick, R. (1993), Apatite etching characteristics versus chemical composition, *Nucl. Tracks Radiat. Meas*., *21*, 604.

Farley, K.A. (2000), Helium diffusion from apatite: General behavior as illustrated by Durango apatite, *J. Geophys. Res., 105,* 2903-2914.

Farley, K.A., Wolf, R.A., and Silver, L.T. (1996), The effects of long alpha-stopping distances on (U-Th)/ He ages: Geochim. et Cosmochim. Acta, v. 60, p. 4223–4229.

Fauquette, S., and Bertini, A. (2003), Quantification of the northern Italy Pliocene climate from pollen data: evidence for a very peculiar climate pattern, *Boreas, 32*, 361-369.

Fauquette, S., Guiot, J., and Suc, J-P. (1998), A method for climate reconstruction of the Mediterranean Pliocene using pollen data, *Palaeogeography, Palaeoclimatology, Palaeoecology, 144*, 183-201.

Fauquette, S., Suc, J-P., Guiot, J., Diniz, F., Feddi, N., Zheng, Z., Bessais, E., and Drivaliari, A. (1999), Climate and biomes in the West Mediterranean area during the Pliocene, *Palaeogeography, Palaeoclimatology, Palaeoecology, 152*, 15-36.

Frisch, W., Kuhlemann, J., Dunkl, I., and Brügel, A. (1998), Palinspastic reconstruction and topographic evolution of the Eastern Alps during late Tertiary tectonic extrusion, *Tectonophysics, 297*, 1-15.

Frisch W., Dunkl, I., and Kuhlemann, J. (2000), Post-collisional large-scale extension in the Eastern Alps, *Tectonophysics, 327*, 239-265.

Glotzbach, Ch., Reinecker, J., Danisik, M., Rahn, M., Frisch, W., and Spiegel, C. (in review), Neogene exhumation history of the Mont Blanc massif, Western Alps, *Tectonics*.

Grasemann, B., and Mancktelow, N. (1993), Two-dimensional thermal modelling of normal faulting: the Simplon fault zone, Central Alps, Switzerland, *Tectonophysics, 225*, 155-165.

Hafkenscheid, E., Wortel, M., and Spakman, W. (2006), Subduction history of the Tethyan region derived from seismic tomography and tectonic reconstructions, *J. Geophys. Res., 111*, B08401.

Heinrich, C. (1986), Eclogite facies regional metamorphism of hydrous mafic rocks in the Central Alpine Adula nappe, *J. Petrol., 27*, 123-154.

Hunziker, J., Desmons, J., and Hurford, A. (1992), Thirty-two years of geochronological work in the Central and Western Alps: A review on seven maps*, Mém. Géologie (Lausanne), 13*, 59 pp.

Jäger, E., Niggli, E., and Wenk, E. (1967), Rb-Sr Altersbestimmungen an Glimmern der Zentralalpen. *Beitr. Geol. Karte Schweiz NF 134.*

Kälin, D. (1997), Litho- und Biostratigraphie der mittel- bis obermiozänen Bois de Raube Formation (Nordwestschweiz), *Eclogae Geol. Helv.*, *90*, 97-114.

Ketcham, R. (2005), Forward and inverse modeling of low-temperature thermochronometry data. *Reviews in Mineralogy, 58*, 275-314.

Ketcham, R., Carter, A., Donelick, R., Barbarand, J., and Hurford, A. (2007), Improved modeling of fission-track annealing in apatite, *Amer. Mineral., 92,* 799-810.

Kuhlemann, J. (2000), Post-collisional sediment budget of circum-Alpine basins, *Mem. Sci. Geol. Padova, 52/1*, 1-91.

Kuhlemann, J., Frisch, W., Dunkl, I., Székely, B., and Spiegel, C. (2001), Miocene shifts of the drainage divide in the Alps and their foreland basin, *Z. Geomorph., 45/2*, 239-265.

Kuhlemann, J., Frisch, W., Szekely, B., Dunkl, I., and Kazmer, M. (2002), Postcollisional sediment budget history of the Alps: Tectonic versus climatic control, *Int. J. Earth Sc., 91*, 818–837.

Lippitsch, R., Kissling, E., and Ansorge, J. (2003), Upper mantle structure beneath the Alpine orogen from high-resolution teleseismic tomography, *J. Geophys. Res. 108*, doi 10.1029/2002JB002016.

Marquer, D., Baudin, T., Peucat, J.-J., and Persoz, F. (1994), Rb-Sr mica ages in the Alpine shear zones of the Truzzo Granite: Timing of the tertiary Alpine p T deformation in the Tambo nappe (Central Alps, Switzerland). *Eclogae Geol. Helv., 87*, 225-239.

Meyre, C., Marquer, D., Schmid, S., and Ciancaleoni, L. (1998), Syn-orogenic extension along the Forcola fault: Correlation of Alpine deformations in the Tambo and Adula nappes (Eastern Penninic Alps), *Eclogae Geol. Helv., 91*, 409-420.

Purdy, J., and Jäger, E. (1976), K-Ar ages on rock-forming minerals from the Central Alps. *Mem. Ist Geol. Min. Univ. Padova, 30*, 32pp.

Rahn, M. (2005), Apatite fission track ages from the Adula nappe: late-stage exhumation and relief evolution, *Schweiz. Min. Petr. Mitt., 85*, 233-245.

Ratschbacher, L., Merle, O., Davy, P., and Cobbold, P. (1991), Lateral extrusion in the Eastern Alps, part 1: boundary conditions and experiments scaled for gravity, *Tectonics, 10*, 245-256.

Schmid, S., Rück, P., and Schreurs, G. (1990), The significance of the Schams nappes for the reconstruction of the paleotectonic and orogenic evolution of the Penninic zone along the NFP-20 East traverse (Grisons, eastern Switzerland), *Mém . Soc. Géol. France, 156*, 263-287.

Schmid, S., Pfiffner, A., Froitzheim, N., Schönborn, G., and Kissling, E. (1996), Geophysical-geological transect and tectonic evolution of the Swiss-Italian Alps. *Tectonics, 15*, 1036-1064.

Seward, D., and Mancktelow, N. (1994), Neogene kinematics of the Central and Western Alps: evidence from fission track dating, *Geology, 22*, 803-806.

Spiegel, C., Kuhlemann, J., Dunkl, I., Frisch, W., von Eynatten, H., and Kadosa, B. (2000), Erosion history of the Central Alps: evidence from zircon fission track data of the foreland basin sediments, *Terra Nova, 12*, 163-170.

Spiegel, C., Siebel, W., Frisch, W., and Berner, Z. (2002), Sr and Nd isotope ratios and trace element geochemistry of detrital epidote as provenance indicators: implications for the reconstruction of the exhumation history of the Central Alps, *Chem. Geol., 189*, 231-250.

Spiegel, C., Siebel, W., Kuhlemann, J., and Frisch, W. (2004), Toward a comprehensive provenance analysis: a multi-method approach and its implications for the evolution of the Central Alps, *GSA Special Paper, 378*, 37-50.

Tagami, T., and Shimada, C. (1996), Natural long-term annealing of the zircon fission track system around a granitic pluton, *J. Geophys. Res., B 101/4*, 8245-8255.

Timar-Geng, Z., Grujic, D., and Rahn, M. (2004). Deformation of the Leventina-Simano nappe boundary, Central Alps, Switzerland, *Eclogae Geol. Helv., 97*, 265-278.

Vernon, A., van der Beek, P., Rahn, M., and Sinclair, H. (2006), Denudation of the Western Alps during Mio-Pliocene times constrained by low-temperature thermochronometers, *AGU Fall meeting*, Abstract # T11A-0422.

von Blanckenburg, F., and Davies, J.H. (1995), Slab breakoff: A model for syncollisional magmatism and tectonics in the Alps, *Tectonics, 14/1*, 120-131.

Wagner, G., Reimer, G., and Jäger, E. (1977), Cooling ages derived by apatite fission track, mica Rb-Sr and K-Ar dating: the uplift and cooling history of the Central Alps. *Mem. Ist. Geol. Mineral. Univ. Padova, 30,* 27 pp.

Warny, S.A., Bart, P.J., and Suc, J-P. (2003), Timing and progression of climatic, tectonic and glacioeustatic influences on the Messinian Salinity Crisis, *Palaeogeography, Palaeoclimatology, Palaeoecology, 202,* 59-66.

Willett, S.D., Schlunegger, F., and Picotti, V. (2006), Messinian climate change and erosional denudation of the central European Alps, *Geology, 34/8*, 613-616.

Wolf, R.A., Farley, K.A., and Kass, D.M. (1998), A sensitivity analysis of the apatite (U-Th)/He thermochronometer, *Chem. Geol. 148*, 105-114.

Exhumation history of the central Gotthard and Aar massifs: Constraints from low-temperature thermochronology

C. Glotzbach[1,1], J. Reinecker[1], M. Danišík[1], M. Rahn[2], W. Frisch[1] and C. Spiegel[3]

[1] Institut für Geowissenschaften, Universität Tübingen, Germany
[2] Mineralogisch-Geochemisches Institut, Universität Freiburg, Germany
[3] FB 5 – Geowissenschaften, Universität Bremen, Germany

Abstract In this study apatite and zircon fission track and apatite (U-Th)/He data are used to reconstruct the exhumation history of the central Aar and Gotthard massif. Age elevation profiles and thermal history modelling suggest that the study area was exhumed fast at ~15 Ma with a rate of ~1 km/Myr. Subsequently, exhumation rates continuously decreased to moderate and steady exhumation since ~9 Ma (~0.5 km/Myr). Probably at ~1 Ma exhumation accelerated again, however, this event could not be well resolved with the data. Fast exhumation at ~15 Ma is most likely linked with the ongoing indentation of the Adriatic wedge, which caused thrusting in the Aar massif and related uplift and exhumation in the hangingwall. The data suggest nearly steady exhumation rates since ~9 Ma, unaffected by major exogenic and endogenic forces that occurred during the last 6 Myr (e.g. Messinian Salinity Crisis, increase in the Atlantic Gulf Stream and related intensification of precipitation, initiation of Alpine glaciation and orogen-perpendicular extension), which clearly affected adjacent regions, e.g. the SW Aar massif. Therefore, we suggest that deep seated processes (e.g. isostatic uplift of an overthickened crust) exclusively correspond to the observed exhumation rate of ~0.5 km/Myr since ~9 Ma, which can be seen as a 'background' exhumation rate for the Central Alps. We explain the slightly higher recent rock uplift rates compared to the long-term exhumation rates as the result of isostatic movements caused by unloading effects, which led to short term fluctuations of rock uplift rates.

1. Introduction

The Central Alps are a unique field laboratory for investigating feedbacks and interrelations between tectonics and climate and their impact and responds to near surface processes (cooling, erosion, exhumation) (e.g., Willett et al., 2006a). Measured rates of these processes vary temporally and spatially in the Central Alps, including seismicity (Pavoni et al., 1997), recent rock uplift rates (Kahle, 1997) and cooling and exhumation rates (e.g., Hurford, 1986; Seward and Mancktelow, 1994; Wagner et al., 1977).
Tectonic processes in the Central Alps such as slab-breakoff (von Blanckenburg and Davies, 1995) and indentation of a crustal wedge (Pfiffner et al., 1997) control the pattern and rate of exhumation since the Late Paleogene. Persaud and Pfiffner (2004) suggested that ongoing compression in the Alps contributes to the observed exhumation pattern.
A primary climatic control of the Late Neogene exhumation history of the Central Alps was suggested by some authors, which interpret the increase in sediment flux after ~5 Ma to the forelands (Kuhlemann, 2000) as the result of a climate change to wetter conditions (Cederbom et al., 2004; Willett et al., 2006b). In addition, modelling approaches demonstrate the importance of glacially and erosion induced rebound effects on the exhumation history (Barletta et al., 2006; Champagnac et al., 2006). For instance, Champagnac et al. (2006)

[1] Corresponding author. Institut für Geowissenschaften, Universität Tübingen, Sigwartstr. 10, D-72076 Tübingen, Germany. Tel. +49 7071 2975240. Fax +49 7071 5059. E-mail addresses: christoph.glotzbach@uni-tuebingen.de

suggested that about 50% of the observed vertical motion of the Western Alps is related to isostatic rebound of enhanced Quaternary erosion rates resulting from glaciation.
The strong coupling of different processes was demonstrated by modelling and field observations in the Central Alps, e.g., the relation between glacial shrinkage after the last Ice Age, isostatic rebound and reactivation of post glacial fault structures in the Central Alps (Hampel and Hetzel, 2006; Persaud and Pfiffner, 2004; Ustaszewski et al., 2007).
The aim of this study is to unravel the Neogene exhumation history of the central Gotthard and Aar massifs (GM and AM, respectively) by low-temperature thermochronology (zircon and apatite fission track, and apatite (U-Th)/He thermochronology). The data are used to investigate the impact of different endogenic and exogenic forces in controlling the exhumation pattern of the study area and of the Central Alps. For this purpose the Gotthard road tunnel as well as the corresponding surface line was sampled (Gotthard transect). This sampling strategy allows observing horizontal and vertical age trends across the southeastern AM and GM, and to derive spatial and temporal cooling and exhumation rates.

2 Geological Setting

The Central Alps formed in response to convergent movements in the Mediterranean region resulting in the southward subduction of the Penninic ocean during the Tertiary (e.g., Frisch, 1979). During this orogeny the European continental margin was overthrust by the African continental margin (Austroalpine domain) and continental and oceanic crust fragments of the Penninic domain were squeezed in-between (Steck and Hunziker, 1994). Penninic and Helvetic units were thrust northwards, resulting in the deep burial of the now exposed external crystalline massifs (ECM). The ECMs (Aar, Gotthard, Tavetsch, Mont Blanc, Aiguilles Rouges, Belledone, Argentera, Pelvoux) are exposed orogen parallel at the footwall of the Penninic frontal thrust. They consist of pre-Variscan poly-metamorphic basement intruded by late Variscan granitoids and are covered by Palaeozoic to lower Tertiary sedimentary rocks (Labhart, 1977; von Raumer and Neubauer, 1993). Peak metamorphic conditions were reached at the Eocene-Oligocene boundary (35-30 Ma).
In this study we investigate a transect crossing the GM and the southern part of the AM (Fig. 1). The boundary between the GM and AM is marked by Permo-Carboniferous and Mesozoic sediments of the heavily tectonized Urseren-Gavera-zone. To the east the Tavetsch massif outcrop in between the Urseren-Gavera-zone (Fig. 1) The AM and the GM experienced greenschist facies metamorphism, whereas rocks outcropping in the southern part of the GM reached amphibolite facies conditions (Frey and Ferreiro Mählmann, 1999; Frey et al., 1976). Recent rock uplift rates, determined by precise leveling (Gubler, 1976; Kahle, 1997), increase to the south, with rates of >1 mm/y in the central Lepontine dome, and maximum rates of >1.5 mm/y in the area of Brig and Chur (Fig. 1). The study area is situated in between these maxima, and is characterized by recent rock uplift rates between 0.8 and 1.0 mm/y.

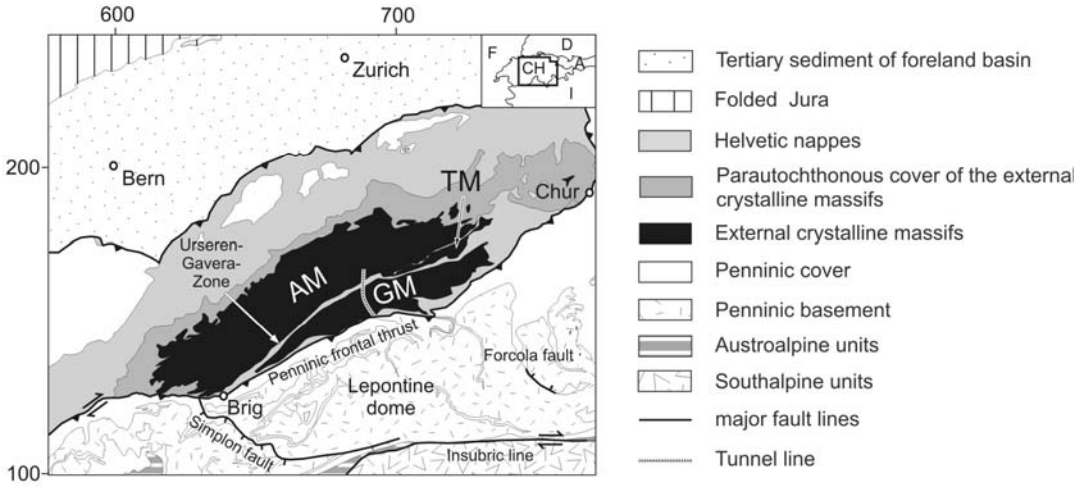

Fig. 1: Geological sketch map of central Switzerland. Coordinates refer to the Swiss reference system. Abbreviations: AM Aar massif, GM Gotthard massif, TM Tavetsch massif

3 Available thermochronological constraints

Published zircon fission track (ZFT) ages of the AM range from 12 Ma in the southeast to 103 Ma in the northwest (Michalski and Soom, 1990; Soom, 1989), indicating that ZFT system was only partially reset during Alpine metamorphism at the northwestern margin of the massif. Penninic rocks in the southeast surrounding of the GM show a uniform ZFT age pattern between 11 and 14 Ma (Dörr, 2007; Hurford, 1986; Steiner, 1984), whereas ages increase towards the eastern Lepontine area with ages of 17-25 Ma. No ZFT ages for the GM exist so far.

Apatite fission track (AFT) ages of the GM vary between 4.5 and 10.3 Ma, similar to AFT ages of the adjacent AM and Penninic nappes (Hurford, 1986; Rahn, 2005; Schaer et al., 1975; Steiner, 1984; Timar-Geng et al., 2004; Wagner and Reimer, 1972; Wagner et al., 1977). AFT ages in the GM, with elevations around 2 km, become continuously older from southwest to northeast (Wagner et al., 1977). No variations in ages is visible over geological boundaries (e.g. Gavera-Urseren-Zone and Penninic frontal thrust (Hurford, 1986)). Based on the interpretation of age elevation profiles (AER) and mineral pairs, several authors report exhumation rates of ~0.45 km/Myr during late Miocene times for the central AM and GM (Hurford, 1986; Schaer et al., 1975; Wagner et al., 1977).

Recently published apatite (U-Th)/He (AHe) ages of the eastern Lepontine dome range from 3.2 to 7.2 Ma (Dörr, 2007) (Fig. 2).

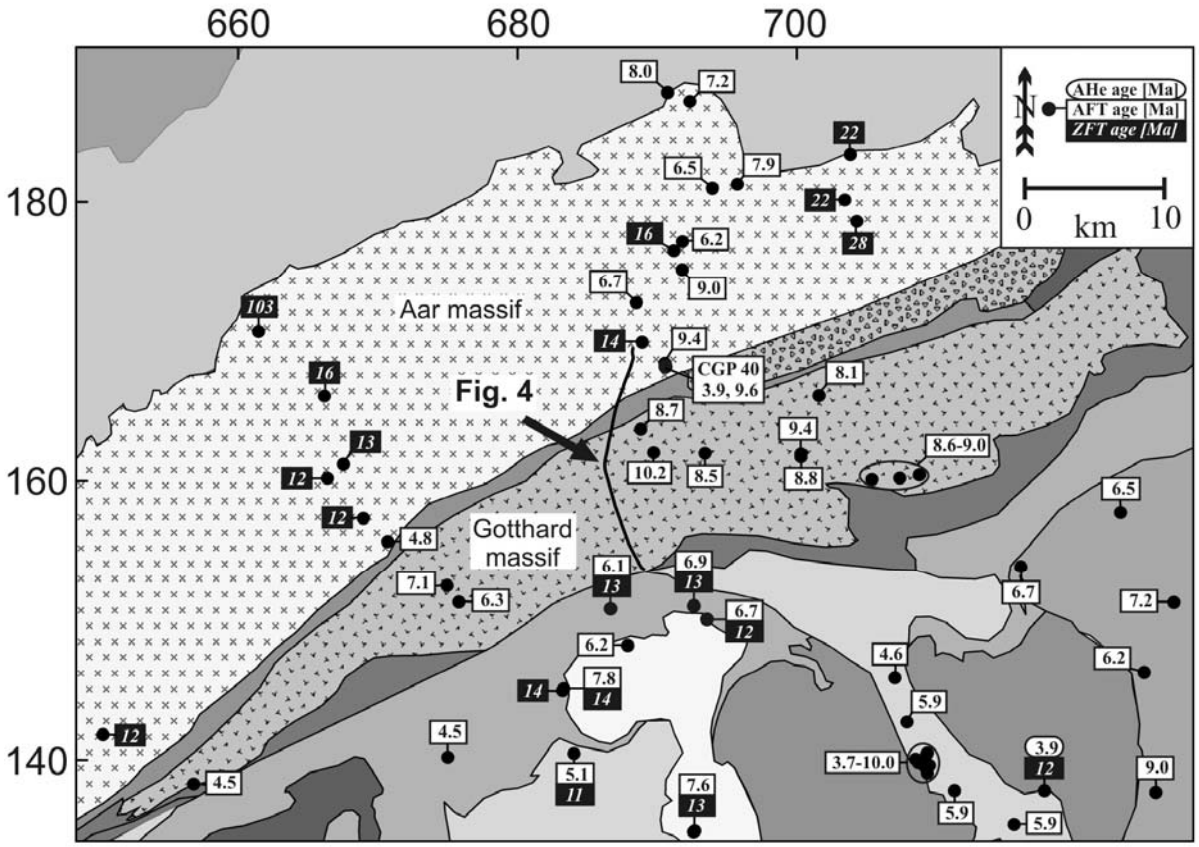

Fig. 2: Published ZFT, AFT and AHe ages in the central AM, GM and surrounding regions (Dörr, 2007; Hurford, 1986; Michalski and Soom, 1990; Rahn, 2005; Schaer et al., 1975; Soom, 1989; Timar-Geng et al., 2004; Wagner et al., 1977). Samples in close vicinity are grouped with ellipses. Own sample locations and ages form the Gotthard transect (black line) are reported in Fig. 4, except sample CGP 40, which is shown here. Coordinates are in Swiss reference system (km).

4. Methods

4.1 Fission track analytical procedure

Apatite and zircon concentrates were separated using standard magnetic and heavy liquid techniques. Apatites were mounted in epoxy and zircons in PFA TeflonTM, and their surfaces were ground and polished. Apatite mounts were etched with 5M HNO3 for 20s at 20°C and zircon mounts with a eutectic melt of KOH-NaOH for 27-130 hours at 215°C (Zaun and Wagner, 1985). Irradiation was carried out at the FRM-II reactor in Garching (TU München, Germany). Mica detectors were etched to reveal induced tracks using 40% HF at 20°C for 40 min. Fission track counting was carried out with an optical microscope (Zeiss Axioscope 1) under 1000x magnification using a dry lense for AFT analysis and an oil immersion lense for ZFT analysis. Samples were dated by the external detector method (Gleadow, 1981; Naeser, 1978) using the zeta calibration approach (Hurford and Green, 1982; Hurford and Green, 1983). Age calculation, visualization and statistics were carried out with Trackkey 4.2g program (Dunkl, 2000). Details about the AFT methodology can be found, e.g., in Wagner and Van den haute (1992), Gallagher et al. (1998) or Reiners et al. (2005).
Because of low uranium contents and young ages, all apatite samples were irradiated by a Cf source in Melbourne (Australia), to enhance the number of etchable confined tracks. Measured Dpar values (mean of 4 measurements of each crystal) were complemented by electron microprobe analysis (University of Tübingen, Germany) on selected crystals, using a

JEOL Superprobe with a beam current of 30 nA, an acceleration voltage of 15 kV and a beam diameter of 10 μm.

4.2 (U-Th)/He analytical procedure

Helium analyses were carried out in the thermochronology laboratory of the University of Tübingen (Germany). Apatite crystals were hand-picked under a stereomicroscope taking into account morphology, size and purity of the crystals. Crystals were inspected at 200x magnification under cross-polarized light for inclusions (all dated crystals were apparently free of visible inclusions). Each selected crystal was digitally photographed parallel and perpendicular to its crystallographic c axis and measured. The crystals were loaded into Pt tubes and degassed by laser. U-Th analyses were conducted at the Scottish Universities Environmental Research Centre (SUERC) in East Kilbride (Scotland), and U-Th-Sm analyses were conducted at the University of Melbourne (Australia). Details about instrumentation and analytics are given in Danišík (2005).
The total analytical uncertainty (TAU) was computed as the square root of the sum of squares of weighted uncertainties on U, Th, (Sm), and He measurements. TAU was usually less than ~4% (1σ) and was used to calculate errors of raw (U-Th)/He ages. Raw (U-Th)/He ages were corrected for the helium loss at the grain margins (alpha-ejection correction) (Farley et al., 1996). A value of 10% was adopted as the uncertainties of alpha-ejection corrections, and was used to calculate the error of corrected (U-Th/He ages. Details about the methodology can be taken from elsewhere (e.g., Ehlers and Farley, 2002).

4.3 Thermal modeling

Time-temperature (tT) paths for individual samples were determined using inverse modeling of AFT and AHe data. Modeling was carried out with the program HeFTy v. 1.3c (Ketcham, 2005) based on the multikinetic annealing model of Ketcham et al. (2007b) and with c axis projected track length data (Ketcham et al., 2007a). TT-paths were statistically evaluated and categorized by a value of goodness of fit (GOF), in which a ‘good’ result corresponds to a value of 0.5, an ‘acceptable’ result corresponds to a value of 0.05, and a GOF of 1 is the optimum. For details we refer to Ehlers et al. (2005) and Ketcham (2005).
The input parameters for each sample used in this study are its central FT age with 1σ error, the predicted tT-path, and if available the c axis projected track length distribution, the single-grain AHe ages and, as a kinetic parameter, the Dpar value.

5. Results

ZFT, AFT and AHe thermochronology was conducted to tunnel and surface samples from the Gotthard transect, locations are given in Table 1.

Table 1: Sample locations

Sample	Geological unit	Swiss Grid (CH1903) [m]		Elevation
		X	Y	[m]
Surface samples				
CGP03	Prato Serie	687821	155880	2250
CGP04	Sorescia Gneiss	687674	156335	2130
CGP05	Rotondo granite	687129	157340	2580
CGP06	Guspis Zone	687155	157760	2520
CGP07	Tremola Series	688851	154073	1320
CGP08	Gamsboden Granite Gneiss	686901	158498	2370
CGP09	Gamsboden Granite Gneiss	686830	158864	2370
CGP10	Gamsboden Granite Gneiss	686345	160420	1890
CGP11	Gamsboden Granite Gneiss	686240	160740	1725
CGP12	Gamsboden Granite Gneiss	686240	161700	1680
CGP13	Gamsboden Granite Gneiss	686425	162157	1650
CGP14	Northern Paragneiss Zone	686507	162791	1740
CGP15	Permocarboniferous	686870	164359	1470
CGP16	Southern Gneiss Zone	687081	165208	1500
CGP17	Southern Gneiss Zone	687327	166101	1620
CGP18	Aare Granite	687529	166589	1800
CGP19	Aare Granite	687884	168027	1650
CGP20	Aare Granite	688290	168840	1150
CGP21	Aare Granite	687593	166834	1650
CGP40	Aare Granite	690625	168100	2390
CGP41	Aare Granite	687700	167813	1280
CGP43	Gamsboden Granite Gneiss	685888	159588	1903
CGP44	Guspis Zone	686888	157978	2320
CGP45	Fibbia Granite Gneiss	686400	156887	2091
Tunnel samples				
MR P 229	Tremola Serie	688730	154050	1147
MR P 231	Sorescia Gneiss	687670	156340	1157
MR P 232	Fibbia Granite Gneiss	687370	157150	1160
MR P 233	Guspis Zone	687160	157770	1162
MR P 234	Gamsboden Granite Gneiss	686920	158500	1165
MR P 235	Gamsboden Granite Gneiss	686820	158830	1166
MR P 236	Gamsboden Granite Gneiss	686640	159460	1168
MR P 237	Gamsboden Granite Gneiss	686360	160460	1172
MR P 238	Gamsboden Granite Gneiss	686280	160790	1173
MR P 239	Gamsboden Granite Gneiss	686240	161280	1174
MR P 240	Gamsboden Granite Gneiss	686340	161790	1168
MR P 241	Northern Paragneiss Zone	686430	162250	1163
MR P 242	Northern Paragneiss Zone	686530	162770	1157
MR P 244	Permocarboniferous	686850	164330	1138
MR P 245	Southern Gneiss Zone	687060	165240	1127
MR P 246	Aare Granite	687340	166060	1117
MR P 247	Aare Granite	687530	166590	1110
MR P 248	Aare Granite	687770	167240	1102
MR P 249	Aare Granite	688020	167940	1093
MR P 250	Aare Granite	688290	168840	1082
MR P 278	Aare Granite	688180	168400	1265
MR P 291	Gamsboden Granite Gneiss	686150	161390	1690
MR P 292	Gamsboden Granite Gneiss	686650	159420	2380
MR P 294	Sorescia Gneiss	687640	156530	2140
GSS3800	Sorescia Gneiss	687440	156920	1158
GSS8220	Gamsboden Granite Gneiss	686260	161160	1173
GSN4840	Permocarboniferous	686970	164960	1135

5.1 ZFT data

ZFT ages were measured on 17 tunnel samples and 18 surface sample, yielding ages between 13.5 and 21.0 Ma (Table 2, Fig. 4). Almost all samples pass the chi-square ($\chi 2$) test, indicating that reported ages represent single age populations. Only one sample (CGP 08) fails the chi-square test.
Raman spectroscopic measurements reveal very narrow bands ('full width at half maximum' of 1 to 6 cm-1 the 1000 cm-1) typical for well crystallized zircons (e.g., Nasdala et al., 2004; Nasdala et al., 2001).

Table 2: ZFT ages from the Gotthard transect

Sample	#grains	ρs	Ns	ρi	Ni	ρd	Nd	P(χ^2) [%]	ZFT age ±1σ [Ma]	U [ppm]
CGP03	40	45.888	1422	61.184	1896	3.055	1480	16	16.9±1.2	620
CGP04	40	45.613	1499	50.299	1653	3.140	1480	97	21.0±1.4	557
CGP05	40	74.921	1708	116.548	2657	3.045	1480	32	14.5±1.0	1193
CGP06	40	72.601	1433	96.464	1904	3.084	1480	98	17.2±1.2	1130
CGP08	40	93.257	1583	150.283	2551	3.053	1480	1	14.0±0.9	1539
CGP09	40	100.668	1222	148.861	1807	3.151	1480	41	15.8±1.1	1469
CGP10	40	70.811	1796	107.281	2721	3.105	1480	25	15.2±1.0	1299
CGP11	20	102.326	717	157.985	1107	3.066	1480	77	14.7±1.1	1586
CGP12	40	85.808	1609	177.270	3324	5.068	3711	99	15.5±0.7	1227
CGP13	40	70.213	1372	106.240	2076	3.099	1480	75	15.1±1.0	1132
CGP14	40	35.597	1342	42.998	1621	3.083	1480	99	18.9±1.3	464
CGP15	20	103.579	1109	156.072	1109	3.070	1480	92	15.1±1.1	1582
CGP16	40	35.370	747	58.855	1243	3.056	1480	25	13.6±1.1	609
CGP17	40	69.857	1303	106.099	1979	3.088	1480	99	15.0±1.0	1040
CGP18	20	77.901	838	117.689	1266	3.132	1480	93	15.3±1.1	1213
CGP19	40	64.624	1435	97.319	2161	3.066	1480	93	15.4±1.0	1076
CGP20	20	64.974	731	101.061	1137	3.107	1480	60	14.8±1.1	1048
CGP21	20	52.944	1045	81.011	1599	3.119	1480	8	14.9±1.1	870
MRP 231	40	47.011	1197	99.796	2541	5.039	3711	100	15.1±0.7	699
MRP 232	40	76.599	1270	174.307	2890	5.055	3711	73	14.0±0.7	1058
MRP 233	40	22.212	1883	28.110	2383	3.027	1480	88	17.7±1.2	314
MRP 234	40	96.299	1264	215.530	2829	5.031	3711	100	14.2±0.7	1351
MRP 235	40	73.756	1696	119.897	2757	3.090	1480	45	14.1±0.9	1350
MRP 236	20	75.126	734	166.423	1626	5.023	3711	60	14.3±0.8	1057
MRP 237	40	107.270	1408	229.320	3010	5.075	3711	98	15.0±0.7	1347
MRP 238	40	70.321	1388	114.652	2263	3.105	1480	74	14.1±1.0	1186
MRP 239	40	82.362	1520	191.384	3532	5.063	3711	65	13.7±0.6	1221
MRP 240	40	79.900	1463	188.491	3460	5.051	3711	96	13.5±0.6	1162
MRP 241	40	64.938	1474	133.488	3030	5.056	3711	93	15.5±0.7	975
MRP 244	20	63.087	716	96.041	1090	3.140	1480	91	15.3±1.2	1089
MRP 245	40	41.858	694	96.261	1596	5.046	3711	100	13.8±0.8	587
MRP 246	40	74.723	1556	169.567	3531	5.022	3711	8	13.9±0.6	1104
MRP 247	44	72.451	1666	167.951	3862	5.036	3711	99	13.7±0.6	1077
MRP 248	41	57.535	1323	129.856	2986	5.048	3711	74	14.1±0.7	1126
MRP 249	40	72.946	1519	156.073	3250	5.053	3711	100	15.0±0.7	974

ρs (ρi) is the spontaneous (induced) track density (10^5 tracks/cm^2); Ns (Ni) is the number of counted spontaneous (induced) tracks; ρd is the dosimeter track density (10^5 tracks/cm^2); Nd is the number of tracks counted on the dosimeter; P(χ^2) is the probability of obtaining Chi-square values (χ^2) for n degree of freedom (where n is number of crystals minus 1); ZFT age ±1σ is central age ±1 standard error (Galbraith and Laslett, 1993); Ages were calculated using the zeta calibration method (Hurford and Green, 1983), glass dosimeter CN-2, and a zeta value of 126±4 yr/cm² calculated with Buluk Tuff and Fish Canyon Tuff zircon age standards.

5.2 AFT data

AFT ages of all tunnel samples and 10 surface samples were previously published by Glotzbach et al. (2008). In addition, in this study AFT ages were measured on 21 surface samples (Table 3, Fig. 4). All AFT ages are displayed as central ages and errors as ±1σ (Galbraith and Laslett, 1993). Dpar values obtained for measured samples are small and relatively uniform, varying between 1.35 and 1.71 μm (Table 2). Microprobe analyses of 13 samples have been carried out, demonstrating that all samples are close to F-apatite end members (Table 4). Furthermore, analyzed elements such as Si, Ce and Sr do not show any significant variation, suggesting that apatites are kinetically uniform.

Table 3: AFT ages of the Gotthard transect

Sample	# grains	ρs	Ns	ρi	Ni	ρd	Nd	P(χ^2) [%]	Central age ±1σ [Ma]	Dpar [μm]	U [ppm]
CGP 03	50	2.115	876	32.873	13616	6.943	3118	0	7.9±0.3	1.47±0.10	58
CGP 04	41	1.664	442	25.019	6647	6.910	3118	100	8.1±0.5	1.63±0.11	48
CGP 06	35	0.447	178	6.407	2552	6.877	3118	100	8.5±0.7	1.38±0.10	10
CGP 08	50	1.738	328	18.988	3583	6.845	3118	100	11.1±0.7	1.50±0.11	33
CGP 09	50	1.392	548	17.243	6788	6.592	3311	29	9.4±0.5	1.44±0.10	30
CGP 10	43	1.469	537	24.194	8844	6.584	3311	39	7.1±0.4	1.47±0.10	41
CGP 12	32	1.672	251	30.252	4541	6.812	3118	97	6.7±0.5	1.42±0.08	50
CGP 13	23	2.232	345	36.196	5594	6.576	3311	21	7.2±0.4	1.54±0.11	67
CGP 14	50	0.750	500	8.624	5752	6.568	3311	65	10.1±0.5	1.55±0.12	16
CGP 15	50	2.145	652	35.951	10928	6.561	3311	99	6.9±0.3	1.49±0.11	77
CGP 16	50	2.955	637	54.009	11641	6.553	3311	34	6.4±0.3	1.71±0.10	100
CGP 17	15	0.474	51	9.185	988	6.545	3311	34	6.0±0.9	1.35±0.13	16
CGP 18	8	0.788	30	11.078	422	6.779	3118	98	8.5±1.6	1.42±0.12	28
CGP 19	23	0.569	79	5.793	805	6.537	3311	6	11.4±1.4	1.44±0.16	12
CGP 20	50	0.527	103	8.543	1671	6.529	3311	67	7.1±0.7	1.48±0.12	15
CGP 21	22	0.526	96	9.031	1648	6.521	3311	76	6.7±0.7	1.38±0.09	19
CGP 40	21	0.702	97	14.096	1949	6.646	3196	18	5.9±0.6	1.37±0.09	24
CGP 41	25	0.614	68	7.162	793	6.660	3196	100	10.1±1.3	1.46±0.08	14
CGP 43	15	3.158	168	37.504	1995	6.689	3196	99	10.0±0.8	1.66±0.14	66
CGP 44	25	0.283	58	2.777	570	6.703	3196	98	12.1±1.7	1.57±0.10	5
CGP 45	25	1.603	214	23.516	3140	6.717	3196	100	8.1±0.6	1.44±0.10	41

ρs (ρi) is the spontaneous (induced) track density (10^5 tracks/cm²); Ns (Ni) is the number of counted spontaneous (induced) tracks; ρd is the dosimeter track density (10^5 tracks/cm²); Nd is the number of tracks counted on the dosimeter; P(χ^2) is the probability obtaining Chi-square value (χ^2) for n degree of freedom (where n is the number of crystals minus 1); dispersion is a real number that is zero if all the data are identical, and increases as the data becomes more diverse; Dpar is the etch pit diameter of fission tracks, averaged from 4 measurements per analysed grain. Ages were calculated using the zeta calibration method (Hurford and Green, 1983), glass dosimeter CN-5, and a zeta value of 355±7 yr/cm² calculated with Durango and Fish Canyon Tuff apatite standards.

Table 4: Composition of measured apatite samples from the Gotthard transect and from Durango apatite, with averages from totally 146 electron microprobe analyses.

Sample	n	F		Cl		OH^- (calc.)	SiO_2		Ce_2O_3		SrO		P_2O_5		CaO		Σ	Σ corrected*	Dpar
		Oxide	Ion	Oxide	Ion	Ion	Oxide	Ion	Oxide	Ion	Oxide	Ion	Oxide	Ion	Oxide	Ion			
CGP 04	10	3.32±0.14	0.85±0.03	0.03±0.01	0.00±0.00	0.12±0.04	0.10±0.09	0.01±0.01	0.04±0.02	0.00±0.00	0.05±0.02	0.00±0.00	44.97±0.47	3.09±0.01	54.57±0.19	4.75±0.03	103.07±0.61	101.67±0.58	1.63±0.11
CGP 08	10	3.41±0.22	0.89±0.06	0.01±0.01	0.00±0.00	0.09±0.06	0.11±0.05	0.01±0.01	0.11±0.01	0.00±0.00	n.d.	0.00±0.00	44.45±0.46	3.09±0.01	53.82±0.29	4.74±0.02	101.91±0.69	100.47±0.69	1.50±0.11
CGP 09	5	3.61±0.06	0.93±0.02	n.d.	0.00±0.00	0.04±0.02	0.08±0.04	0.01±0.00	0.08±0.02	0.00±0.00	n.d.	0.00±0.00	44.56±0.17	3.08±0.01	54.59±0.24	4.78±0.02	102.94±0.12	101.41±0.14	1.44±0.10
CGP 10	3	3.94±0.07	1.04±0.02	n.d.	0.00±0.00	-0.05±0.02	0.09±0.06	0.01±0.01	0.10±0.02	0.00±0.00	n.d.	0.00±0.00	43.36±0.41	3.06±0.02	54.26±0.21	4.84±0.04	101.76±0.22	100.10±0.19	1.47±0.10
CGP 12	10	4.10±0.23	1.07±0.06	0.01±0.01	0.00±0.00	-0.09±0.07	0.04±0.03	0.00±0.00	0.10±0.02	0.00±0.00	n.d.	0.00±0.00	44.56±0.40	3.1±0.01	53.71±0.41	4.73±0.03	102.51±0.86	100.78±0.84	1.42±0.08
CGP 13	9	3.97±0.09	1.06±0.02	0.01±0.01	0.00±0.00	-0.06±0.02	0.02±0.01	0.00±0.00	0.09±0.02	0.00±0.00	n.d.	0.00±0.00	43.16±0.70	3.04±0.01	54.42±0.26	4.88±0.03	101.68±0.65	99.80±0.27	1.54±0.11
CGP 14	10	3.41±0.16	0.88±0.05	0.01±0.01	0.00±0.00	0.09±0.05	0.04±0.02	0.00±0.00	0.09±0.09	0.00±0.00	0.02±0.01	0.00±0.00	45.17±1.34	3.12±0.05	53.71±1.00	4.69±0.13	102.44±0.65	101.00±0.62	1.55±0.12
CGP 15	9	3.55±0.16	0.91±0.04	n.d.	0.00±0.00	0.06±0.04	0.15±0.15	0.01±0.01	0.13±0.12	0.00±0.00	0.09±0.07	0.00±0.00	44.94±0.36	3.09±0.01	54.59±0.22	4.75±0.02	103.45±0.25	101.96±0.26	1.49±0.11
CGP 16	8	3.18±0.16	0.85±0.04	0.01±0.01	0.00±0.00	0.16±0.04	0.40±0.13	0.03±0.01	0.31±0.06	0.01±0.00	0.04±0.04	0.00±0.00	41.49±0.35	2.99±0.01	54.41±0.22	4.96±0.02	99.85±0.51	98.51±0.47	1.71±0.10
CGP 17	10	4.13±0.17	1.09±0.06	n.d.	0.00±0.00	-0.10±0.05	0.08±0.05	0.01±0.00	0.13±0.04	0.00±0.00	0.02±0.01	0.00±0.00	42.77±0.24	3.03±0.01	54.61±0.23	4.9±0.02	101.74±0.37	100.00±0.35	1.35±0.13
CGP 19	10	3.58±0.16	0.95±0.04	0.01±0.01	0.00±0.00	0.05±0.05	0.14±0.05	0.01±0.00	0.20±0.08	0.01±0.00	0.02±0.02	0.00±0.00	42.93±0.50	3.04±0.01	54.54±0.44	4.88±0.02	101.43±0.91	99.92±0.87	1.44±0.16
CGP 20	10	3.57±0.15	0.94±0.03	0.01±0.01	0.00±0.00	0.05±0.04	0.17±0.15	0.01±0.01	0.23±0.11	0.01±0.00	0.03±0.02	0.00±0.00	43.40±0.56	3.05±0.01	54.43±0.33	4.84±0.03	101.84±0.75	100.33±0.67	1.48±0.12
CGP 21	22	4.02±0.22	1.14±0.06	0.01±0.03	0.00±0.00	-0.11±0.06	0.17±0.14	0.02±0.02	0.20±0.09	0.01±0.00	0.03±0.02	0.00±0.00	42.26±1.40	2.98±0.01	54.33±0.49	5.01±0.03	101.01±1.53	99.79±1.67	1.38±0.09
Durango	20	3.61±0.09	0.95±0.03	0.41±0.02	0.06±0.00	-0.01±0.03	0.48±0.05	0.04±0.00	0.71±0.04	0.02±0.00	0.05±0.02	0.00±0.00	42.78±0.75	3.04±0.02	53.46±0.33	4.8±0.05	101.64±0.81	100.52±0.34	1.63±0.11

Chemical compostion in oxide weight percent and numer of atoms per formula unit (apfu); n is the number of measurements; n.d. means not detected, with detection limits in ppm: F 140, Cl 40, SiO2 100,Ce2O3 180, SrO 170, P2O5 470, CaO 105; * corrected for OH- anions.

AFT ages range from 5.9 to 12.1 Ma and show no clear correlation with sample elevation. AFT ages along the sampled transect show a complex pattern, with nearly uniform ages around 6.2 Ma along the tunnel (Glotzbach et al. 2008), whereas surface samples yield scattered ages (5.9-12.1 Ma). Most samples pass the chi-square ($\chi 2$) test, indicating that these ages represent single populations (Table 2). Samples CGP 03, 19 and 40 are characterized by low values of $\chi 2$ probabilities and high dispersions, typical for samples with more than one age population. Identification of significant age components was done with PopShare (Dunkl and Székely, 2002). Best-fit peaks for sample CGP 03 (6.0±0.4 and 8.3±2.7 Ma) and for CGP 19 (9.8±0.9 and 15.4±11.1 Ma) overlap with each other, whereas CGP 40 yields two well-defined age components with 3.9±1.0 and 9.6±2.4 Ma (errors are SD) (Fig. 3). No correlation between Dpar values and AFT age groups was observed for sample CGP 40 (Fig. 3).

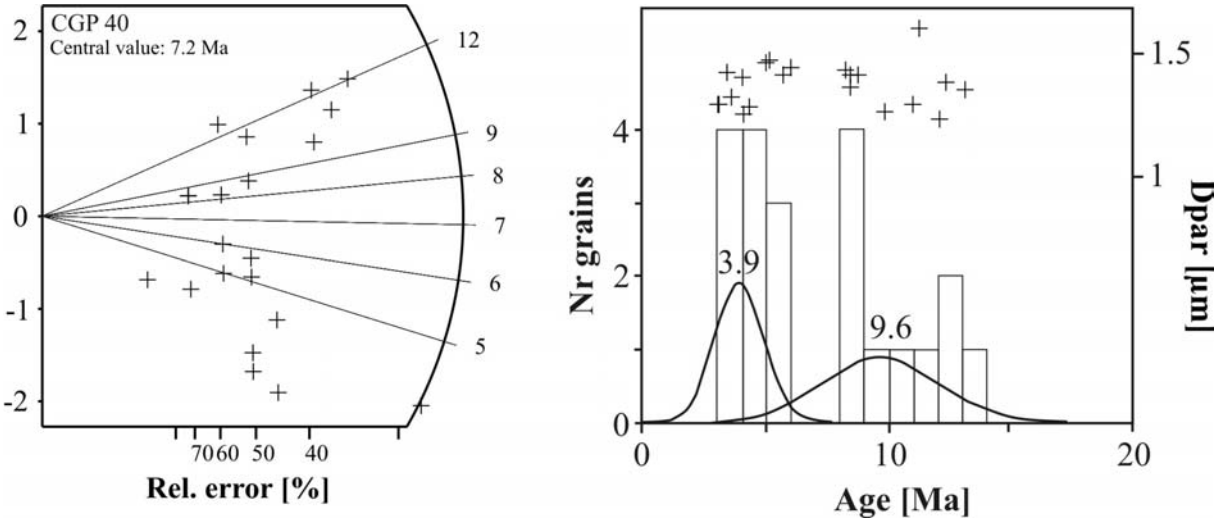

Fig. 3: Radial Plot and grain age spectrum with Dpar values for samples CGP 40 with best-fit age groups, calculated with PopShare (Dunkl and Székely, 2002).

Fission track length data was measured for surface and tunnel samples. Track length distributions are all uniform with mean confined track length (MTL) between 11.9 and 14.2 µm (Table 5, Fig. 4). Most MTL are between 13.0 and 13.5 µm. MTL show a weak correlation with sample elevation and AFT age. In the tunnel MTL vary from 13.6 to 11.9 µm. Surface samples yield MTL between 13.1 and 14.2 µm, identical with MTL measured southeast of the GM (Rahn, 2005). Measured track length distributions are typical for samples, which experienced rapid to moderate cooling through the PAZ.

Table 5: Track length data of the Gotthard transect

Sample	AFT age ±1σ [Ma]	# length	MTL±SD [µm]
CGP 04	8.1±0.5	100	14.05±1.20
CGP 06	9.0±0.7	57	13.41±1.45
CGP 07	8.5±0.7	31	13.71±1.39
CGP 08	7.6±0.9	29	13.22±1.55
CGP 09	11.1±0.7	100	14.05±1.39
CGP 11	7.4±0.4	100	13.15±1.87
CGP 14	10.1±0.5	100	13.91±1.37
CGP 16	6.4±0.3	100	13.48±1.60
CGP 20	7.1±0.7	56	13.28±1.35
MRP 231	5.6±0.3	107	11.90±2.00
MRP 232	6.3±0.5	86	12.95±1.89
MRP 233	6.1±0.4	100	13.56±1.26
MRP 235	6.4±0.4	102	13.07±1.70
MRP 236	6.2±0.5	66	12.92±1.66
MRP 238	5.9±0.4	61	12.88±1.55
MRP 240	6.2±0.4	100	13.57±1.61
MRP 242	6.7±0.4	100	13.04±1.66
MRP 244	6.1±0.3	116	13.55±1.31
MRP 245	6.0±0.3	100	13.01±1.87
MRP 250	6.8±1.5	94	13.37±2.19
MRP 291	7.0±0.4	102	13.08±1.51
MRP 292	9.6±0.5	100	14.18±1.72
MRP 294	9.0±0.5	100	14.16±1.12
GSS3800	n.d.	36	13.38±1.54
GSS8220	n.d.	100	13.12±1.59
GSN4840	n.d.	100	13.55±1.23

n.d. means not determined

6.4.3 AHe data

In total 44 single apatite crystals from 10 surface and 5 tunnel samples were analysed by (U-Th)/He and (U-Th-Sm)/He thermochronology, respectively (Table 6). Following the approach proposed by Fitzgerald et al. (2006) we used the central AFT age as criteria to identify outliers of single grain (U-Th)/He ages. 9 grains yield apatite (U-Th)/He (AHe) ages older than the corresponding AFT age, and are therefore not incorporated in our interpretation. We assume that these 'too old' ages can be ascribed to He implanted by mineral and fluid inclusions (Lippolt et al., 1994), not visible under 200x magnification and/or phases adjacent to or enclosing the apatite grains, e.g. zircon. Mean AHe ages were calculated for samples with more than one measured crystal, otherwise single grain AHe ages are reported (Table 6, Fig. 4). In this study we used the degree of replication of single grain AHe ages as a proxy for the reliability of the resulting mean AHe age. Samples characterized by single grain AHe age samples with poorly replicating single grain ages are not considered in the interpretation, but are shown for completeness in all figures in grey colour.

Surface samples yield AHe ages between 2.9 to 9.6 Ma. The youngest sample (CGP 17) is located in the SE Aare granite and oldest ages were found for the high elevated samples of the southern transect (CGP 08 and MRP 292). AHe ages along the tunnel are younger than corresponding ages of the surface samples, however, ranging between 2.4 to 5.5 Ma. Again a sample from the SE Aare granite yielded the youngest age.

Table 6: AHe ages of the Gotthard transect

Sample	AFT-age ±1σ [Ma]	Th [ng]	1σ error [%]	U [ng]	1σ error [%]	Sm [ng]	1σ error [%]	Th/U	Sm/Th+U	4He [ncc]	error [%]	TAU [%]§	uncorrected AHe age [Ma]	Ft$	corrected AHe age [Ma]*	1σ error		average AHe age ±SD [Ma]
CGP 08#2	11.1±0.7	0.0204	4.4	0.0085	7.3	n.d.	n.d.	2.4	n.d.	0.014	2.6	8.9	8.7	0.62	14.0	1.6	e	9.6±0.6
CGP 08#4		0.0273	3.8	0.0475	4.3	n.d.	n.d.	0.6	n.d.	0.046	0.9	5.8	7.1	0.71	10.0	1.1		
CGP 08#5		0.0244	4.5	0.0596	4.1	n.d.	n.d.	0.4	n.d.	0.045	1.2	6.2	5.7	0.62	9.2	1.0		
CGP 11#2	7.4±0.4	0.0517	3.9	0.0542	3.8	n.d.	n.d.	1.0	n.d.	0.025	0.9	5.5	3.1	0.62	5.0	0.5		5.0±0.5
CGP 16#3	6.4±0.3	0.3122	2.3	0.2037	2.3	n.d.	n.d.	1.5	n.d.	0.112	1.0	3.4	3.3	0.69	4.8	0.5		4.9±0.3
CGP 16#5		0.4798	2.2	0.2305	2.7	n.d.	n.d.	2.1	n.d.	0.118	1.0	3.6	2.8	0.60	4.7	0.5		
CGP 16#8		0.4398	1.9	0.1936	3.0	n.d.	n.d.	2.3	n.d.	0.123	0.9	3.7	3.4	0.65	5.2	0.5		
CGP17#3	6.0±0.9	0.0046	2.0	0.0124	2.0	0.2131	2.0	0.4	12.5	0.033			18.9	0.74	25.5 (28.9)		e	2.9±0.5
CGP17#5		0.0231	2.0	0.0293	2.0	0.8719	2.0	0.8	16.6	0.010			2.0	0.60	3.3 (4.0)			
CGP17#6		0.0406	2.0	0.0198	2.0	0.8648	2.0	2.1	14.3	0.007			1.6	0.63	2.6 (3.2)			
CGP18#8	8.5±1.6	0.0061	2.0	0.0118	2.0	0.4140	2.0	0.5	23.2	0.009			4.7	0.63	7.4 (9.4)			6.2±1.9
CGP18#9		0.0139	2.0	0.0170	2.0	0.4440	2.0	0.8	14.4	0.007			2.6	0.64	4.1 (4.9)			
CGP18#10		0.0367	2.0	0.0165	2.0	0.6744	2.0	2.2	12.7	0.016			4.5	0.63	7.2 (8.8)			
CGP 19#1+4	11.4±1.4	0.0483	3.7	0.0171	2.6	n.d.	n.d.	2.8	n.d.	0.018	2.2	5.0	5.3	0.65	8.2	0.9		7.3±3.4
CGP19#2		0.0263	2.0	0.0093	2.0	0.3611	2.0	2.8	10.2	0.004			1.8	0.63	2.9 (3.4)			
CGP19#3		0.0349	2.0	0.0144	2.0	0.3385	2.0	2.4	6.9	0.013			4.2	0.62	6.8 (7.7)			
CGP19#5		0.0392	5.0	0.0122	4.3	n.d.	n.d.	3.2	n.d.	0.017	2.2	7.0	6.7	0.60	11.1	1.3		
CGP20#7	7.1±0.7	0.0185	2.0	0.0208	2.0	0.3816	2.0	0.9	9.7	0.015			4.6	0.66	7.0 (7.9)			5.2±2.5
CGP20#9		0.0506	2.0	0.0151	2.0	0.5209	2.0	3.4	7.9	0.008			2.1	0.62	3.5 (4.0)			
CGP21#1	6.7±0.7	0.0644	2.0	0.0267	2.0	1.2079	2.0	2.4	13.3	0.016			2.6	0.67	3.9 (4.9)			3.9±0.4
CGP21#4		0.0283	2.0	0.0146	2.0	0.5758	2.0	1.9	13.4	0.079			25.9	0.73	35.5 (43.7)		e	
CGP21#5		0.0037	2.0	0.0068	2.0	0.2511	2.0	0.5	23.9	0.016			14.6	0.67	21.8 (28.3)		e	
MRP229#1	6.6±0.7	0.0057	2.0	0.0103	2.0	0.0832	2.0	0.6	5.2	0.005			3.4	0.81	4.2 (4.4)			4.2±0.4
MRP229#3		0.0047	2.0	0.0039	2.0	0.1079	2.0	1.2	12.5	0.006			9.9	0.80	12.3 (15.0)		e	
MRP 234#1	6.6±0.5	0.0195	6.0	0.0311	3.9	n.d.	n.d.	0.6	n.d.	0.011	1.1	7.2	2.5	0.63	4.0	0.4		3.7±0.5
MRP 234#3		0.0659	3.5	0.0755	2.7	n.d.	n.d.	0.9	n.d.	0.025	3.6	5.7	2.3	0.69	3.4	0.4		
MRP 234#5		0.0525	3.1	0.0667	2.3	n.d.	n.d.	0.8	n.d.	0.078	0.9	4.0	8.1	0.69	11.8	1.2	e	
MRP236#2	6.2±0.5	0.0396	2.0	0.0300	2.0	0.7746	2.0	1.3	11.1	0.020			3.7	0.67	5.6 (6.5)			5.5±0.4
MRP236#8		0.0552	2.0	0.0486	2.0	0.7139	2.0	1.1	6.9	0.027			3.3	0.66	5.0 (5.5)			
MRP236#10		0.0216	2.0	0.0356	2.0	0.4717	2.0	0.6	8.2	0.019			3.5	0.60	5.9 (6.4)			
MRP236#13		0.0128	2.0	0.0248	2.0	0.2630	2.0	0.5	7.0	0.027			7.7	0.66	11.6 (12.5)		e	
MRP 242#2	6.7±0.4	0.0235	4.3	0.0192	3.8	n.d.	n.d.	1.2	n.d.	0.007	1.4	5.9	2.2	0.73	3.0	0.3		3.0±0.3
MRP 246#2	6.7±0.5	0.0705	2.0	0.0314	2.0	0.9395	2.0	2.2	9.2	0.007	1.5	3.8	1.09	0.61	1.8 (2.1)	0.2		2.4±0.6
MRP 246#6		0.1464	2.0	0.0614	2.0	1.7283	2.0	2.4	8.3	0.029	1.0	3.6	2.16	0.71	3.0 (3.5)	0.3		
MRP 246#13		0.0591	2.0	0.0247	2.0	1.3488	2.0	2.4	16.1	0.011	1.2	3.7	1.86	0.65	2.9 (3.7)	0.3		
MRP246#5		0.0537	2.0	0.0271	2.0	1.4280	2.0	2.0	17.7	0.011			1.8	0.70	2.6 (3.4)			
MRP246#14		0.0795	2.0	0.0424	2.0	1.3575	2.0	1.9	11.1	0.015			1.7	0.70	2.5 (2.9)			
MRP246#17		0.0407	2.0	0.0265	2.0	1.1094	2.0	1.5	16.5	0.005			1.0	0.67	1.5 (1.9)			
MRP 278#4	7.3±0.6	0.0831	2.7	0.0418	3.9	n.d.	n.d.	2.0	n.d.	0.025	1.7	5.1	3.3	0.70	4.7	0.5		4.9±0.2
MRP 278#5		0.0543	3.0	0.0239	5.4	n.d.	n.d.	2.3	n.d.	0.032	1.4	6.3	7.2	0.67	10.8	1.1	e	
MRP 278#6		0.0490	2.0	0.0116	2.0	0.6240	2.0	4.2	10.3	0.011	3.5	4.9	3.1	0.61	5.1 (6.2)	0.5		
MRP 292#1	9.6±0.5	0.0429	3.4	0.0572	3.4	n.d.	n.d.	0.8	n.d.	0.050	1.2	5.0	6.1	0.72	8.5	0.9		8.3±0.3
MRP 292#2		0.0586	3.2	0.0882	3.8	n.d.	n.d.	0.7	n.d.	0.073	1.0	5.1	6.0	0.74	8.0	0.9		
MRP 292#4		0.0202	4.8	0.0613	3.2	n.d.	n.d.	0.3	n.d.	0.057	1.1	5.8	7.2	0.64	11.2	1.2	e	

§ 1σ total analytical error; $ alpha ejection correction factor (Farley et al., 1996); * For aliquots with Sm measurements single-grain (U-Th)/He (in brackets) and (U-Th-Sm)/He ages are reported; # Average AHe age with standard deviation reported for samples with more than one reproducing single-grain AHe ages, otherwise single-grain AHe ages with total analytical error are reported; n.d. not determined; e excluded age.

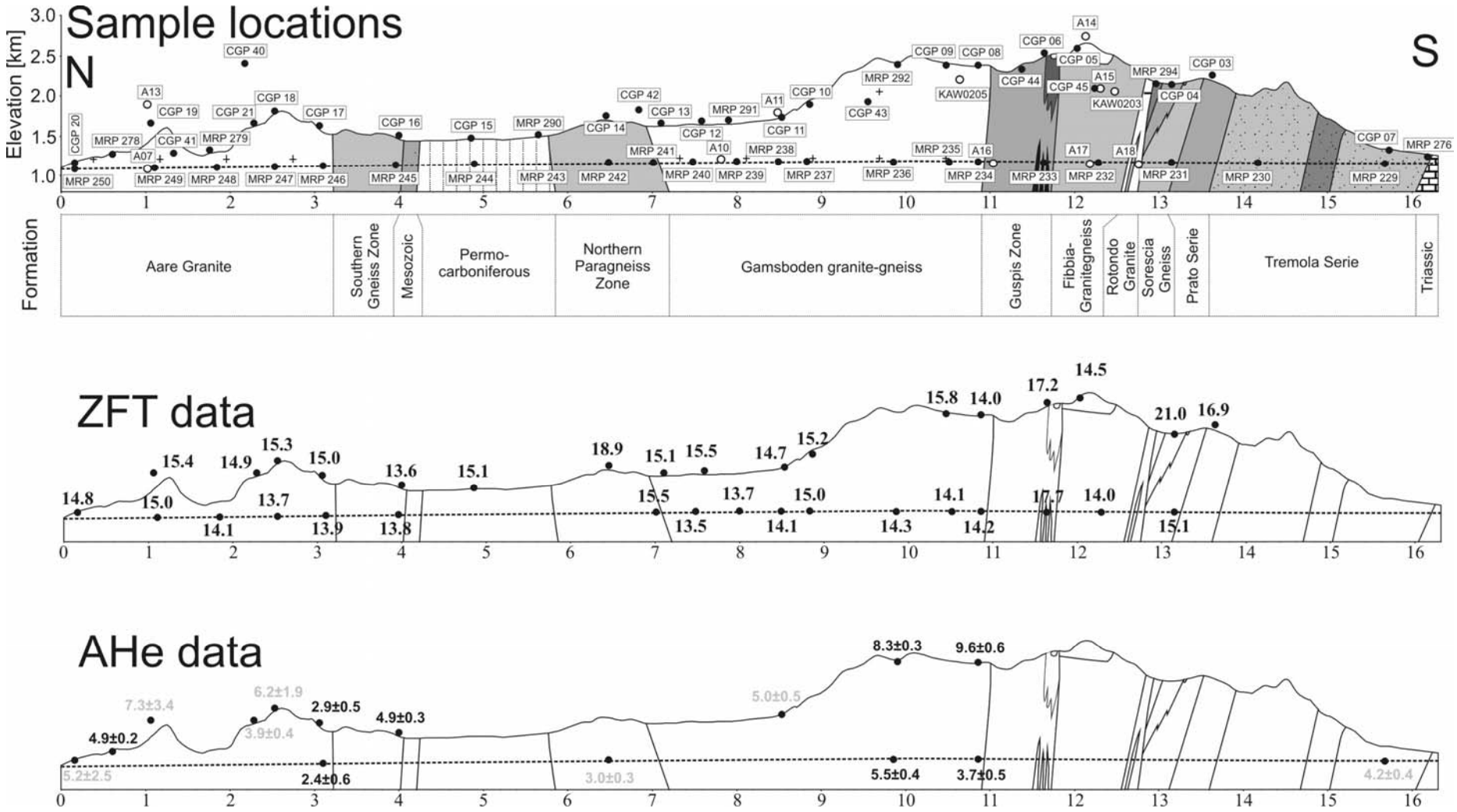
Sample locations
N
S
Elevation [km]
3.0
2.5
2.0
1.5
1.0
CGP 40
A13
CGP 19
CGP 21
CGP 18
CGP 17
CGP 20
MRP 278
CGP 41
MRP 279
A07
MRP 250
MRP 249
MRP 248
MRP 247
MRP 246
CGP 16
MRP 245
CGP 15
MRP 244
MRP 290
MRP 243
CGP 14
MRP 242
CGP 42
CGP 13
MRP 241
CGP 12
MRP 291
A10
MRP 240
MRP 239
A11
CGP 10
MRP 238
MRP 237
CGP 11
MRP 292
CGP 43
MRP 236
CGP 09
CGP 08
KAW0205
MRP 235
MRP 234
A16
CGP 06
A14
CGP 05
CGP 44
CGP 45
A15
KAW0203
MRP 294
CGP 03
CGP 04
A17
A18
MRP 233
MRP 232
MRP 231
MRP 230
CGP 07
MRP 276
MRP 229
0 1 2 3 4 5 6 7 8 9 10 11 12 13 14 15 16
Formation
Aare Granite
Southern Gneiss Zone
Mesozoic
Permo-carboniferous
Northern Paragneiss Zone
Gamsboden granite-gneiss
Guspis Zone
Fibbia-Granitegneiss
Rotondo Granite
Sorescia Gneiss
Prato Serie
Tremola Serie
Triassic
ZFT data
14.8
15.0
15.4
14.1
14.9
13.7
15.3
13.9
15.0
13.8
13.6
15.1
18.9
15.5
15.1
13.5
15.5
13.7
14.7
14.1
15.2
15.0
15.8
14.3
14.0
14.2
17.2
14.1
14.5
17.7
14.0
21.0
15.1
16.9
0 1 2 3 4 5 6 7 8 9 10 11 12 13 14 15 16
AHe data
5.2±2.5
7.3±3.4
4.9±0.2
6.2±1.9
3.9±0.4
2.9±0.5
2.4±0.6
4.9±0.3
3.0±0.3
5.0±0.5
8.3±0.3
5.5±0.4
9.6±0.6
3.7±0.5
4.2±0.4
0 1 2 3 4 5 6 7 8 9 10 11 12 13 14 15 16

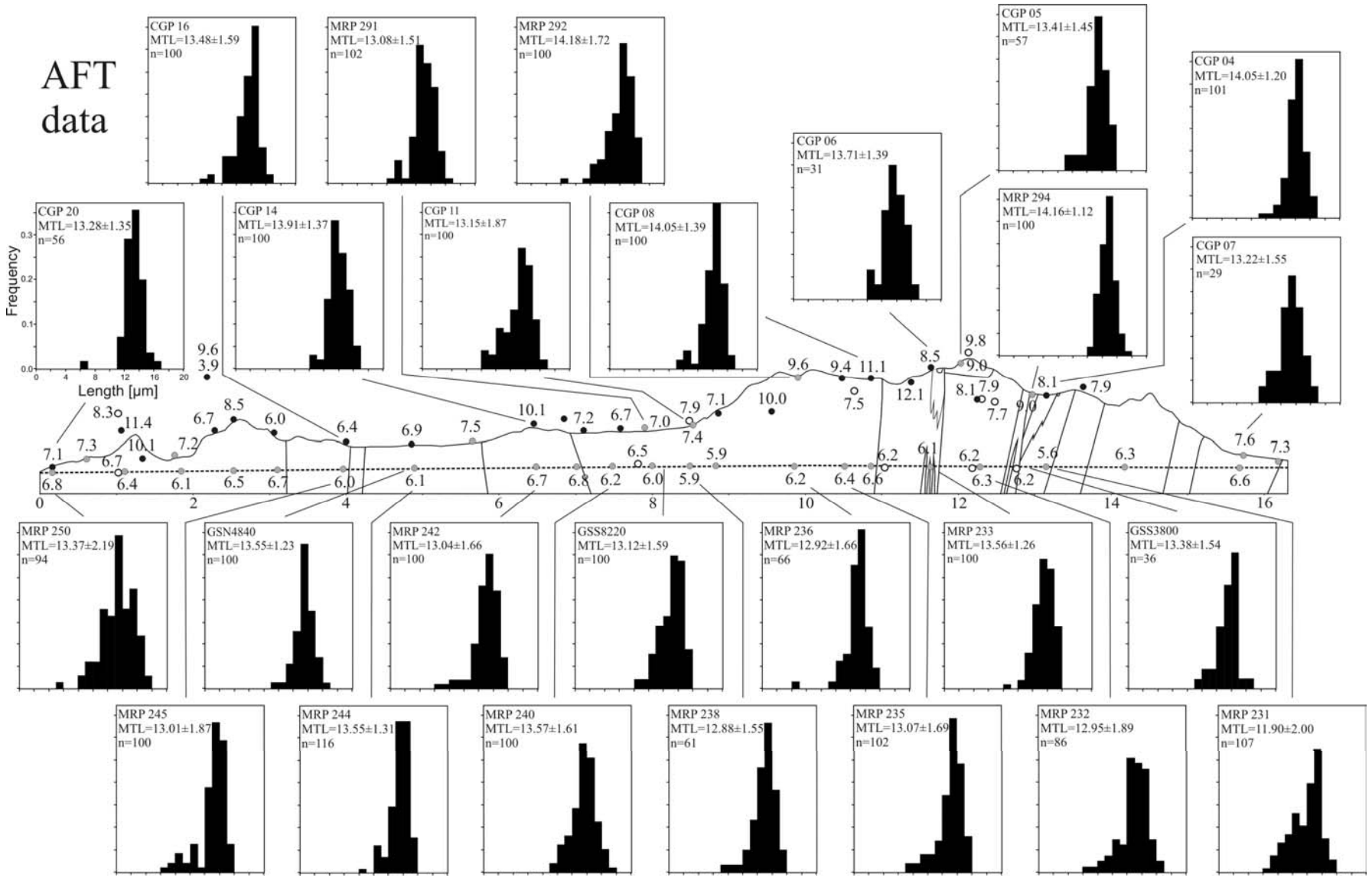

Fig. 4: Sample locations, ZFT, AFT and AHe data along the Gotthard transect. Published AFT ages are from Glotzbach et al. (2008) (grey dots), and from Schaer et al. (1975) and Wagner et al (1977) (open circles). Single grain or poorly replicating AHe ages are in grey colour.

6. Interpretation and discussion

In the following section the presented thermochronological data are interpreted and discussed in terms of their meaning for the quantification of near surface processes, including cooling and exhumation, fault activity and mass movement.
Determinations of the annealing kinetics of analyzed samples are required to quantify surface processes. Measurements of the Dpar, Cl content and FWHM (full width at half maximum) Raman bands indicate homogenous annealing properties for apatite as well as for zircon. Nevertheless, both single grain ages and central ZFT ages show a slight correlation with U content (Fig. 5). Grains/samples with low U content yield older ages. Probably even low accumulated radiation damage (<0.1 α-fluence in 10^{16}/mg) can cause differences in the annealing kinetic of ZFT (Rahn et al., 2004), so that tracks in samples with less U / radiation damage anneal at higher temperatures.

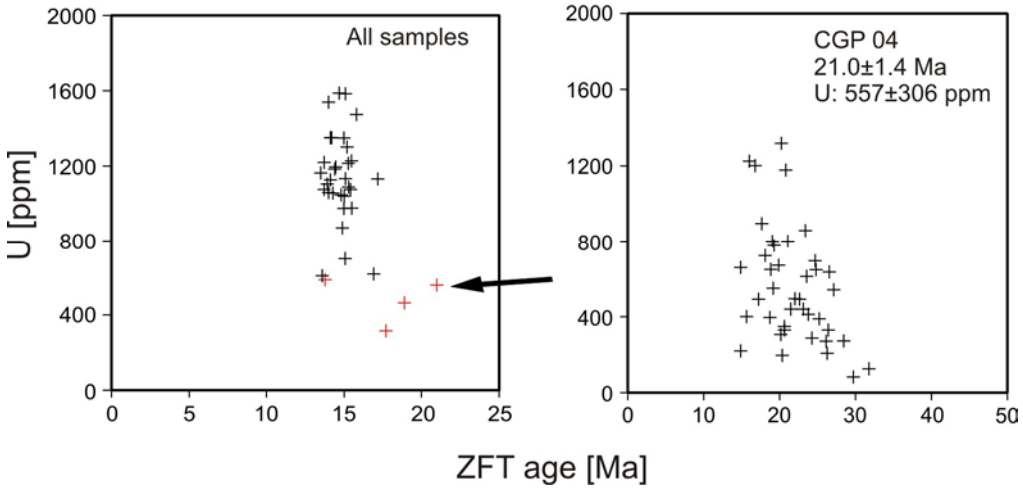

Fig. 5: Central ZFT ages plotted against their mean U contents and single grain ZFT ages plotted against their U contents for sample CGP 04.

6.1 Thermal and exhumation history

We derive exhumation rates applying inverse modelling of AFT and AHe data and using the positive correlation of ages with elevation of a single isotopic system (Schaer et al., 1975; Stüwe et al., 1994; Wagner and Reimer, 1972).
Only samples with available AFT age and length data were used for inverse modelling of cooling paths. If available, reliable AHe data were incorporated in the modelling process. Modelled tT-path of the tunnel samples are highly consistent, showing a convex upward trend, with fast to moderate cooling (20-60°C/Myr) between ~12 and ~6 Ma followed by slow cooling (5-15°C/Myr) between ~6 and ~1 Ma. Some samples reveal a clear break in slope at ~6 Ma, whereas others show a more continues decrease in cooling rates from ~6 Ma to present (Fig. 6). Comparable tT-path were modelled for surface samples, which additionally suggest that fast to moderate cooling initiated before ~11 Ma. Some samples in the tunnel and on the surface point to an increase in cooling rates around ~1 Ma with rates up to 30°C/Myr. All samples are consistent with continuous decreasing cooling rates, probably followed by an increase in cooling rates around 1 Ma.

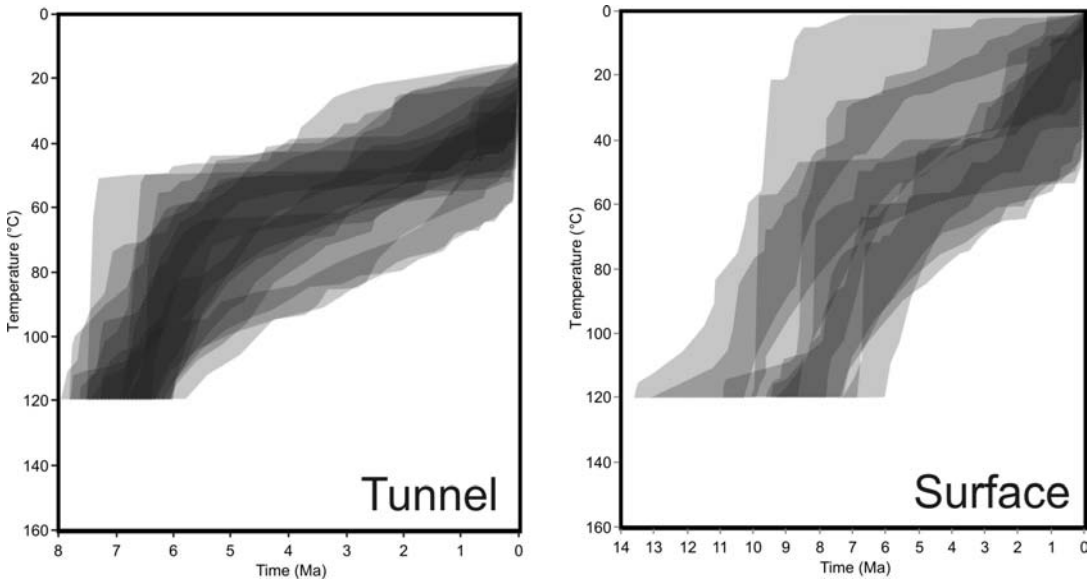

Fig. 6: Stacked statistically good tT-path of tunnel and surface samples.

Deriving exhumation rates from age elevation relationship (AER) circumvents any supposition of the geothermal gradient. Resulting exhumation rates, however, are only reliable under several assumptions (e.g., Parrish, 1983): (1) during and after passing the closure temperature all samples followed a vertical exhumation pathway and no tectonic displacement exist between sample locations, (2) all dated samples behave kinetically uniform and (3) all samples cooled through the closure temperature at the same elevation with respect to some geographical reference horizon, e.g. sea level. These assumptions are all fulfilled for AFT ages of the Gotthard transect: (1) vertical offsets are insignificant, (2) all samples are kinetically uniform and (2) paleo-isotherms were flat (Glotzbach et al., 2008).
Plotting all AFT ages against sample elevation results in a complex AER (Fig. 7). Several samples yield AFT ages >10 Ma, forming a group, which clearly differs from the other samples in the AER (Fig.7, grey shaded area). These samples were probably affected by mass-wasting processes, discussed later (section 6.3). After excluding these data and the young age component of sample CGP 40, the remaining data yield an age elevation correlation with a slope of 0.5 km/Myr between 6 and 9 Ma (Fig. 7). Slopes of AER were calculated weighting the ages according to their errors. Slopes and uncertainties were inverted to estimate exhumation rates with defined uncertainties (Reiners et al., 2003). Regression bands were plotted with a 95% confidence interval, which allows predicting the error of the regression lines, yielding an exhumation rate of 0.5±0.1 km/Myr.
Regarding the ZFT data the assumption, that all samples behave kinetically uniform and thus the thermochronometer closed at approximately the same temperature, is probably not fulfilled. Closure temperatures of single zircon grains can vary between 230-330°C (Tagami and Shimada, 1996), depending on the cooling rate and radiation damage (e.g., Rahn et al., 2004). Separating the AER plot in two parts with a threshold U value of 600 ppm removes a great fraction of scatter. Samples with a mean U content >600 ppm yield apparent exhumation rates between 0.6-3 km/Myr within the 95% confidence interval and a mean of 1 km/Myr between 14-16 Ma (Fig. 7).
Because of the poor sample quality we were not able to generate enough AHe ages for deriving meaningful exhumation rates from AER.

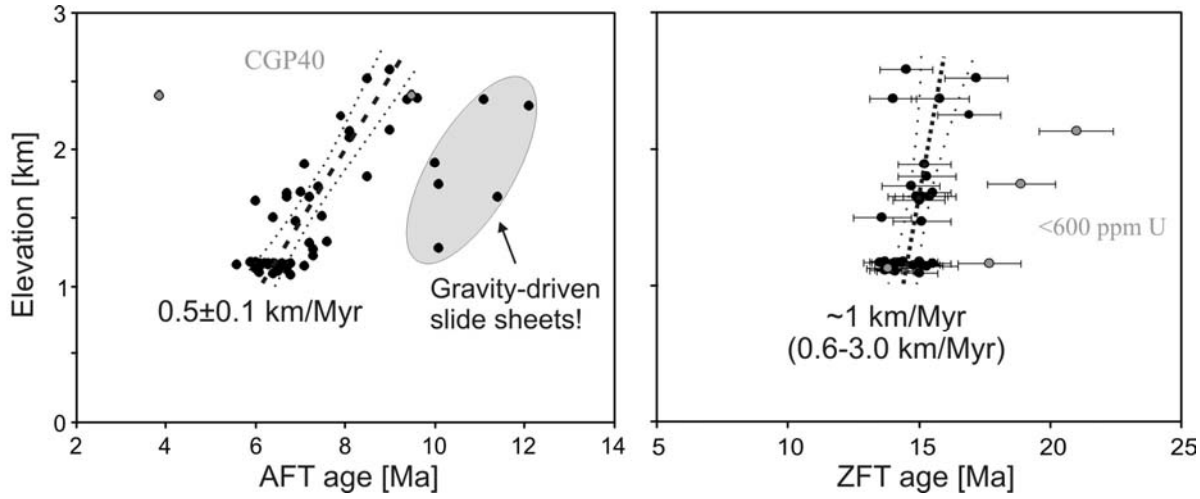

Fig. 7: AER plots of AFT and ZFT ages.

The sample strategy allows to derive spatial information about the exhumation history from several vertical profiles using the age elevation dependence of pairs of tunnel and surface samples. In most cases the error of the AFT ages is high and the elevation difference between the samples low, so that derived exhumation rates are associated with high uncertainties. We therefore do not report them here.
To sum up, inverse thermal modelling and AER plots reveal similar cooling and exhumation histories, indicating continuously decreasing rates since ~15 Ma. Exhumation rates decrease from rates around 1 km/Myr between 16-14 Ma to 0.5 km/Myr between 9-6 Ma. Probably cooling/ exhumation rates accelerated during the last Myr, as indicated by modelling and very young AHe ages in the southeastern AM.

6.2 Neogene fault activity along the Gotthard transect

The thermochronological data were used to verify the Late Neogene fault activity along the Gotthard transect. The following interpretation of the data is based on the assumption that all samples are characterized by the same closure temperature, which is likely for the AFT data (Dpar and microprobe analyses, cf. Table 2 and 3), but not necessarily for the ZFT data. The observed variation of ZFT ages along the transect can be best explained by differences in annealing kinetics. Except for one sample (MRP 233) with the lowest measured mean U content, all ZFT ages along the tunnel transect are relatively uniform. In addition, AHe and AFT ages along the tunnel show no variations in ages, thus no fault movement with significant vertical offset has occurred since ~14 Ma.
Based on microthermometric analysis of associated fluid inclusions in quartz combined with microstructural studies in the Tavetsch massif Wyder and Mullis (1998) suggested a steepening of structures and initiation of brittle deformation between 13-17 Ma, and relative uplift of the AM in relation to the GM after 9-11 Ma. In addition, remote sensing analysis, finite element modelling, precise levelling and field work demonstrate the existence of a later fracturing phase in the AM and GM, which mostly reactivated older faults and are formed due to postglacial unloading (Dahinden, 2001; Persaud and Pfiffner, 2004; Ustaszewski et al., 2007; Zangerl et al., 2006). Regarding our thermorchronological data relative displacements associated with these deformation phases are absent or small and remain hidden behind the analytical error of the methods. This interpretation is in line with structural and mineralogical studies, suggesting that the main phase of brittle deformation had ceased before the structural level of the tunnel samples cooled below 190 °C (Luetzenkirchen, 2002).

Post-glacial faults are most abundant in the Urseren valley, where they are characterized by uphill-facing scarps with horizontal slickensides that follow the distinct subvertical Alpine foliation (Fig. 7). Postglacial displacements on these faults can exceed 20 m (Eckhardt et al., 1983).
Sample CGP 40 was taken from a uphill-facing scarp (Fig. 8 and fault C4 in (Persaud, 2002)) at an elevation of 2.4 km, which correspond to the course of the Glacial trimline at an elevation of ~2.4 km (Florineth and Schlüchter, 1998). Precise leveling across this fault reveals relative vertical movements of 0.5 mm/a (profile 6 in (Dahinden, 2001)). AFT dating yield two age components with ages of 3.9 and 9.6 Ma. The older age component is identical with the adjacent sample A12 (9.4 Ma) from Schaer et al. (1975) (cf. Fig. 2). Grains from the young component are probably annealed during a thermal event at ~4 Ma or younger, which implies either strong kinetic differences between the components or a very localized heat source. Potential heat sources are (i) hydrothermal activity or (ii) frictional heating caused by earthquakes. Hydrothermal activity would lead to a broader (m- to km-scale) thermal anomaly. In contrast frictional heating produced by a single earthquake produces a very narrow zone (mm- to m-scale) with very high temperatures (>500°C). Dpar values are identical for both age components, arguing against kinetic variations within the sample and in favour for a localized heat source such as frictional heating. In shallow depth shear stress is too low to generate large earthquakes, which produce enough frictional heat (d'Alessio et al., 2003), precluding the possibility that post-glacial earthquakes led to partial annealing of sample CGP 40. Most likely sample CGP 40 was affected by frictional heating at ~4 Ma.

Fig. 8: Uphill-facing scarp (Profile 6 in Dahinden (2001)); C4 in Persaud (2002)) with an offset of 3 m. Sample CGP 40 was taken directly from the scarp adjacent to a polished surface (343°/88°) with slickensides, which reveal nearly vertical orientations. The geographical location of the sample is marked in Figure 2.

6.3 Mass-wasting processes

Mass-wasting, especially landslides, are important erosional processes in mountainous areas. Mass-wasting moves material from higher elevations to lower elevations forced by gravity, resulting in an overall lowering of relief (e.g., Davis and Friedmann, 2005). The European Alps including the study area are affected by mass-wasting processes, e.g. a 1 km² sized landslide is located directly south of Andermatt close to the studied transect (Zangerl et al., 2006).

Thermochronological data along the Gotthard transect, particularly the AFT and partly the AHe data reveals three areas characterized by distinctly older AFT ages (>10 Ma), AHe ages (>9 Ma) and long MTL (~14 µm) (Fig. 4): (i) the Aare granite (CGP 19 and 41), (ii) the northern Paragneiss zone (CGP 14) and (iii) the southern Gamsboden granite gneiss (CGP 8, 43 and 44). These areas can be distinguished from the surrounding areas by clear jumps in ages and track length distributions, both laterally and vertically. Therefore, fault activity or hydrothermal influence, which would also affect adjacent samples, cannot explain these 'old ages'. Field evidence revealed that these areas are internally intact and that their strike and dip agree with the overall trend. Most likely gravitational sliding of oversteepened slopes caused the observed pattern of the thermochronological data. This assumption, although speculative, is supported by visual analysis of Google Earth scenes, indicating that for instance samples CGP 19 and 41 are located in a slide sheet with a clear basal contact (Fig. 9).

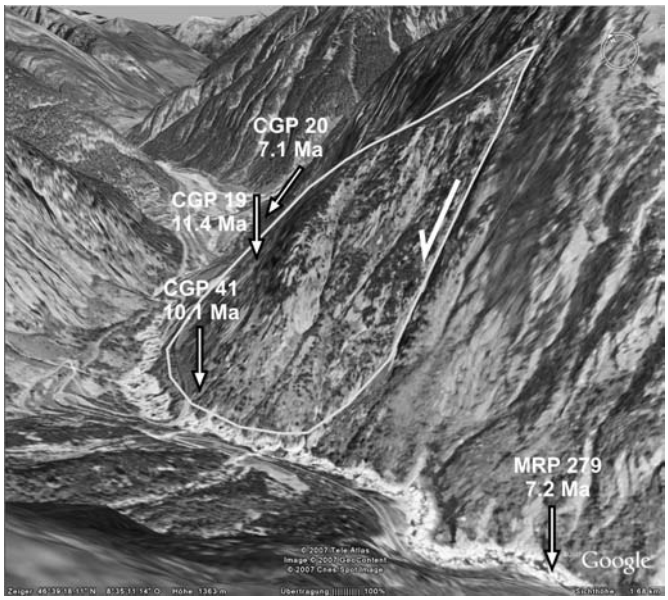

Fig. 9: Assumed gravity-driven slide sheet in the Aar granite, with AFT ages of selected samples. Picture is taken from Google Earth.

6.4 Implications for the geodynamic evolution of the Central Alps

In this chapter we discuss the observed Neogene exhumation history of the central AM and GM with regard to the geodynamic evolution of the Central Alps.

Thermochronological data indicate continuous decreasing exhumation rates since ~15 Ma for the central AM and GM, similar to what is found in the Central Alps, where fast cooling started before 20 Ma in the SE part and subsequently migrated towards NW affecting the area SE of the Gotthard massif around 18-15 Ma (Hurford, 1986; Wagner et al., 1977). Probably fast exhumation was induced by backthrusting during the 'Grindelwald phase' (22-12 Ma), which led to shortening and thrusting in the Molasse basin and in the external AM. The formation of a fan-structure in the GM (Zangerl et al., 2006) and steepening of structures in the Tavetsch massif at 17-13 Ma (Wyder and Mullis, 1998) are likely associated with thrusting along the Aar basal thrust. At the same time sediment deposition rates around the Western and Swiss Alps decreased (Kuhlemann, 2000), indicating a northward shift of the drainage divide in the Alps induced by updoming of the external massifs (Kuhlemann et al., 2001).

The derived constant exhumation history since ~9 Ma suggest that climatic and tectonic forces, especially the Messinian Salinity Crises at ~5.5 Ma (Krijgsman et al., 2002) and the increase of the Atlantic Gulf Stream at ~4.6 Ma (Haug and Tiedemann, 1998) and related

intensification of precipitation in the Alps (Cederbom et al., 2004), do not affect exhumation rates in the Central Alps.
The latest Neogene exhumation history of the study area is different from that of adjacent regions. In contrast to the central AM and GM, the southwestern AM and the area around Chur are characterised by an increase in exhumation rates around 3 Ma (Vernon et al., 2008), evident by AFT ages younger than 3 Myr (Lihou et al., 1995; Michalski and Soom, 1990). We suggest that these areas were strongly affected by climatic and tectonic forces at that time, which led to a clear erosional/exhumational response (Fig. 10). Not only tectonic forces can act very locally, climat change causing enhanced glacial/fluvial erosion could carve deep valleys and led to spatial differences in exhumation rates (i.e. rocks in or close to the major valleys will be exhumed rapidly, whereas rocks from nearby ridges will show no increase in exhumation).

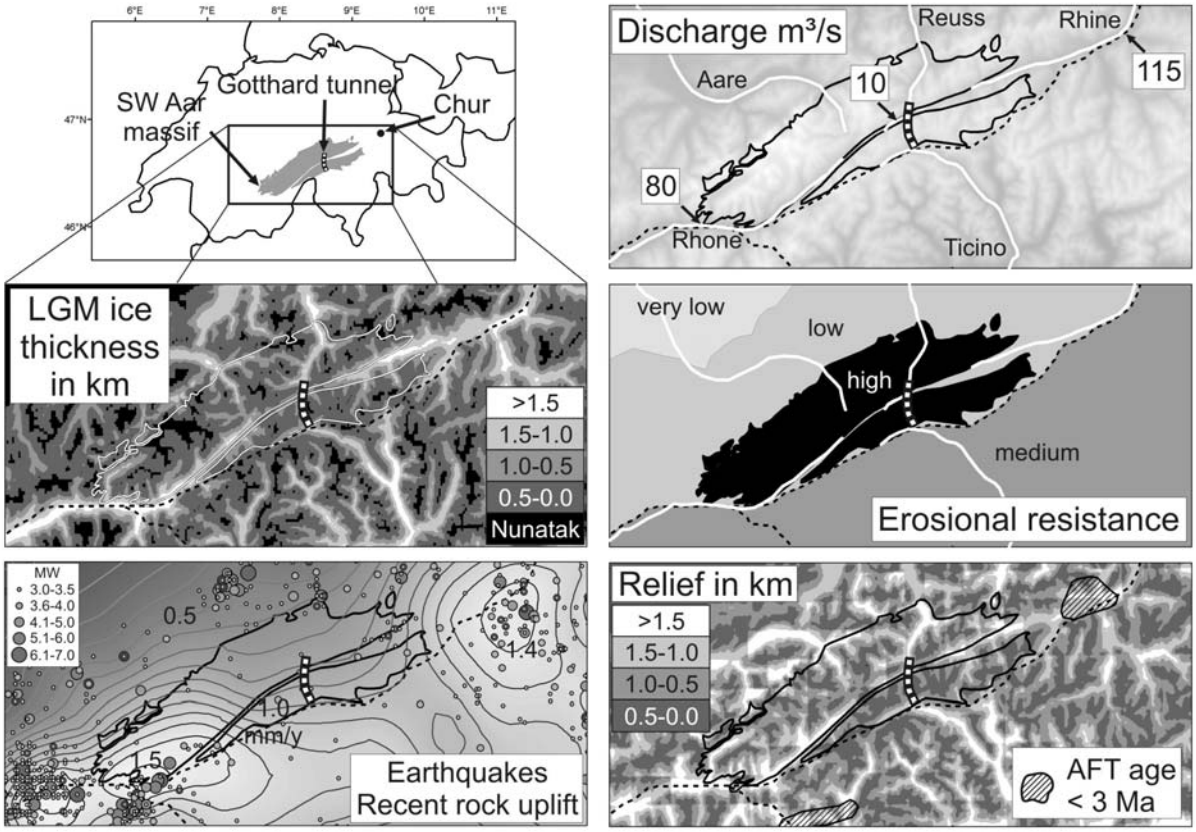

Fig. 10: Geomorphological and geological spatial differences in the Central Alps: discharge (Schlunegger and Hinderer, 2001), ice thickness of the last glacial maximum (LGM) (Kelly et al., 2004), erosional resistance (Schlunegger and Hinderer, 2001), relief, recent rock uplift (Kahle, 1997) and earthquake activity between 1000 and 2007 (Earthquake Catalogue of Switzerland).

There are several regional geologic and geomorphologic distinctions between the study area and regions, which experienced a Late Neogene increase in exhumation:
The southwestern AM and the area around Chur are characterised by high recent discharge rates (Schlunegger and Hinderer, 2001), high LGM ice thicknesses (Florineth and Schlüchter, 1998; Kelly et al., 2004), low erosional resistance of outcropping rocks, especially in the area around Chur, high recent rock uplift rates (Kahle, 1997), high density of historical earthquakes (Earthquake Catalogue of Switzerland), high relief and very young AFT ages (<3 Ma). In contrast the study area in the central AM and GM is characterised by contrary rates and values (Fig. 10).
The coincidence of areas with high glacial and fluvial erosional potential, highest recent rock uplift rates, high seismicity and very young AFT ages predict a direct coupling and positive

feedback of these processes. An important tectonic control on late Neogene exhumation was assumed by several authors, especially for areas in the footwall of the Rhône-Simplon fault and Penninic frontal thrust (e.g., Seward and Mancktelow, 1994),
We suggest that both climatic and tectonic processes were minor in the last 3 Myr in the central AM and GM, but pronounced in the Rhine and Rhône valleys. Present-day rock uplift rates (0.8-1.0 mm/y), however, are twice as high as exhumation rates since ~9 Ma (0.5±0.1 km/Myr). We explain this discrepancy by short term fluctuations of the rock uplift rates caused by isostatic movements (Barletta et al., 2006; Champagnac et al., 2006), which cannot be resolved with low-temperature thermochronology. The central AM and GM, however, are in a long term exhumational steady state since ~9 Ma, exhumed continuously with a rate of ~0.5 km/Myr. Therefore we suggest that this exhumation rate can be seen as a 'background' value for the Central Alps, resulting exclusively from deep seated long lasting processes (e.g. isostatic uplift of an overthickened crust) and related exhumation. This idea is supported by similar exhumation rates derived for the southwestern AM for the last ~10 Myr and between ~7 and ~3.5 Ma for the northern and southern Lötschberg transect, respectively (Reinecker et al., pending successful revision).

7. Conclusions

On the basis of thermochronological data (ZFT, AFT and AHe) we draw several conclusions concerning the thermal-structural evolution of the Central Alps.
- Probably mass wasting processes affected thermochronological ages in the central GM and AM.
- Thermochronological data along the Gotthard tunnel suggest negligible vertical offsets along fault structures since ~15 Ma.
- Exhumation rates for the central AM and GM continuously decrease, with fast exhumation at ~15 Ma (~1 km/Myr) and moderate steady exhumation since ~9 Ma (~0.5 km/Myr). Probably an acceleration in exhumation occurred at ~1 Ma.
- Fast exhumation around 15 Ma is related to ongoing indentation of the Adriatic wedge, which led to thrusting along the Aar basal thrust and updoming and fast exhumation of the AM and GM.
- Since ~9 Ma the central AM and GM are in a long term exhumational steady state. Isostatic movements caused by unloading effects, however, led to short term post-glacial fluctuations of rock uplift rates.
- Probably an exhumation rate of ~0.5 km/Myr can be allocated as a 'background' value for the Central Alps, exclusively forced by deep seated long lasting processes and related exhumation.

References

Barletta, V.R. et al., 2006. Glacier shrinkage and modeled uplift of the Alps. Geophysical Research Letters, 33, doi:10.1029/2006GL026490.

Cederbom, C.E., Sinclair, H.D., Schlunegger, F. and Rahn, M.K., 2004. Climate-induced rebound and exhumation of the European Alps. Geology, 32: 709-712.

Champagnac, J.D., Molnar, P., Anderson, R.S., Sue, C. and Delacou, B., 2006. Quaternary erosion-induced isostatic rebound in the western Alps. Geology, 35: 195-198.

d'Alessio, M.A., Blythe, A.E. and Bürgmann, R., 2003. No frictional heat along the San Gabriel fault, California: Evidence from fission-track thermochronology. Geology, 31: 541-544.

Dahinden, T., 2001. Verschiebungsmessungen im Gotthardgebiet, Diploma-thesis, ETH Zürich.
Danišík, M., 2005. Cooling history and relief evolution of Corsica (France) as constrained by fission track and (U-Th)/He thermochronology. Tübinger Geowissenschaftliche Arbeiten, 72: 1-130.
Davis, G.A. and Friedmann, S.J., 2005. Large-scale gravity sliding in the Miocene Shadow Valley Supradetachment Basin, Eastern Mojave Desert, California. Earth-Science Reviews, 73: 149-176.
Dörr, N., 2007. Late-stage exhumation history of the Lepontine dome: constraints from U-Th/He thermochronology, Eberhard Karls Universität Tübingen, Tübingen, 69 pp.
Dunkl, I., 2000. Trackkey: a windows program for calculation and graphical presentation of fission track data. Computers & Geosciences, 28(1): 3-12.
Dunkl, I. and Székely, B., 2002. Component analysis with visualization of fitting - PopShare, a Windows program for data analysis. Geochemica et Cosmochimica Acta, 66: 201.
Eckhardt, P., Funk, H. and Labhart, T.P., 1983. Postglazial Krustenbewegungen an der Rhein-Rhone-Linie. Mesuration, Photogrammétrie, Génie rural, 2: 43-56.
Ehlers, T.A. et al., 2005. Computational tools for low-temperature thermochronometer interpretation. Reviews in Mineralogy & Geochemistry, 58: 589-622.
Ehlers, T.A. and Farley, K.A., 2002. Apatite (U-Th)/He thermochronometry: methods and applications to problems in tectonic and surface processes. Earth and Planetary Science Letters, 206(1-2): 1-14.
Farley, K.A., Wolf, R.A. and Silver, L.T., 1996. The effects of long alpha-stopping distances on (U-Th)/He dates. Geochemica et Cosmochimica Acta, 60: 4223-4229.
Florineth, D. and Schlüchter, C., 1998. Reconstructing the Last Glacial Maximum (LGM) ice surface geometry and flowlines in the Central Swiss Alps. Eclogae Geologicae Helvetiae, 91: 391-407.
Frey, M. and Ferreiro Mählmann, R., 1999. Alpine metamorphism of the Central Alps. Schweizerische Mineralogische und Petrographische Mitteilungen, 79(1): 135-154.
Frey, M.v., Jäger, E. and Niggli, E., 1976. Gesteinsmetamorphose im Bereich der Geotraverse Basel-Chiasso. Schweizerische Mineralogische und Petrographische Mitteilungen, 56: 649-659.
Frisch, W., 1979. Tectonic progradation and plate tectonic evolution of the Alps. Tectonophysics, 60: 121-139.
Galbraith, R.F. and Laslett, G.M., 1993. Statistical models for mixed fission track ages. Nuclear Tracks and Radiation measurements, 21: 459-470.
Gallagher, K., Brown, R. and Johnson, C., 1998. Fission Track analysis and its application to geological problems. Annual Reviews Earth Planetary Science, 26: 519-572.
Gleadow, A.J.W., 1981. Fission-track dating methods: What are the real alternatives? Nuclear Tracks and Radiation measurements, 5(1/2): 3-14.
Glotzbach, C., Spiegel, C., Reinecker, J., Rahn, M.K. and Frisch, W., 2008. What perturbs isotherms? An assessment using fission track thermochronology and thermal modelling along the Gotthard transect, Central Alps. In: F. Lisker, B. Ventura and U. Glasmacher (Editors), Thermochronological methods: from paleotemperature constraints to landscape evolution models. Geological Society Special Publication, London, in press.
Gubler, E., 1976. Beitrag des Landesnivellements zur Bestimmung vertikaler Krustenbewegung in der Gotthard-Region. Schweizerische Mineralogische und Petrographische Mitteilungen, 56: 675-678.
Hampel, A. and Hetzel, R., 2006. Response of normal faults to glacial-interglacial fluctuations of ice and water masses on Earth's surface. Journal of Geophysical Research, 111.

Haug, G.H. and Tiedemann, R., 1998. Effect of the formation of the Isthmus of Panama on Atlantic Ocean thermohaline circulation. Nature, 393: 673-676.
Hurford, A.J., 1986. Cooling and uplift patterns in the Lepontine Alps South Central Switzerland and an age of vertical movement on the Insubric fault line. Contributions to Mineralogy and Petrology, 92: 413-427.
Hurford, A.J. and Green, P.F., 1982. A users' guide to fission track dating calibration. Earth and Planetary Science Letters, 59: 343-354.
Hurford, A.J. and Green, P.F., 1983. The Zeta age calibration of fission-track dating. Chemical Geology (Isotope Geoscience Section), 41: 285-317.
Kahle, H.-G., 1997. Recent crustal movements, geoid and density distribution; contribution from integrated satellite and terrestrial measurements. In: O.A. Pfiffner, P. Lehner, P. Heitzmann, S. Müller and A. Steck (Editors), Results of NRP 20; deep structure of the Swiss Alps. Birkhaeuser Verlag, Basel, pp. 251-259.
Kelly, M.A., Buoncristiani, J.-F. and Schlüchter, C., 2004. A reconstruction of the last glacial maximum (LGM) ice-surface geometry in the western Swiss Alps and contiguous Alpine regions in Italy and France. Eclogae Geologicae Helvetiae, 97: 57-75.
Ketcham, R.A., 2005. Forward and inverse modelling of low-temperature thermochronology data. Reviews in Mineralogy & Geochemistry, 58(275-314).
Ketcham, R.A., Carter, A., Donelick, R.A., Barbarand, J. and Hurford, A.J., 2007a. Improved measurement of fission-track annealing in apatite using c-axis projection. American Mineralogist, 92: 789-798.
Ketcham, R.A., Carter, A., Donelick, R.A., Barbarand, J. and Hurford, A.J., 2007b. Improved modeling of fission-track annealing in apatite. American Mineralogist, 92: 799-810.
Krijgsman, W. et al., 2002. The onset of the Messinian salinity crisis in the Eastern Mediterranean (Pissouri Basin, Cyprus). Earth and Planetary Science Letters, 194: 299-310.
Kuhlemann, J., 2000. Post-collisional sediment budget of circum-Alpine basins (Central Europe). Mem. Ist. Geol. Mineral. Univ. Padova, 52: 1-91.
Kuhlemann, J., Frisch, W., Dunkl, I., Székely, B. and Spiegel, C., 2001. Miocene shifts of the drainage divide in the Alps and their foreland basin. Zeitschrift für Geomorphologie N. F., 45(2): 239-265.
Labhart, T.P., 1977. Aarmassiv und Gotthardmassiv. Sammlung geologischer Führer, 63. Gebr. Bornträger, Berlin, 173 pp.
Lihou, J., Hurford, A.J. and Carter, A., 1995. Preliminary fission-track ages on zircon and apatites from the Sardona unit, Glarus Alps, eastern Switzerland: late Miocene-Pliocene exhumation rates. Schweizerische Mineralogische und Petrographische Mitteilungen, 75: 177-186.
Lippolt, H.J., Leitz, M., Wernicke, R.S. and Hagedorn, B., 1994. (Uranium+Thorium)/Helium dating of apatite: experience with samples from different geochemical environments. Chemical Geology, 112: 179-191.
Luetzenkirchen, V.H., 2002. Structural geology and hydrogeology of brittle fault zones in the central eastern Gotthard massif, Switzerland. PhD Thesis, ETH, Zürich.
Michalski, I. and Soom, M., 1990. The Alpine thermo-tectonic evolution of the Aar and Gotthard massifs, Central Switzerland: Fission Track ages on zircon and apatite and K-Ar mica ages. Schweizerische Mineralogische und Petrographische Mitteilungen, 70: 373-387.
Naeser, C.W., 1978. Fission track dating. U.S. Geological Survey Open-File Report: 76-190.
Nasdala, L. et al., 2004. Incomplete retention of radiation damage in zircon from Sri Lanka. American Mineralogist, 89: 219-231.

Nasdala, L. et al., 2001. Meamictisation of natural zircon: accumulation versus thermal annealing of radioactivity-induced damage. Contributions to Mineralogy and Petrology, 141: 125-144.

Parrish, R.R., 1983. Cenozoic thermal evolution and tectonics of the Coast Mountains of British Columbia, 1. Fission track dating, apparent uplift rates, and patterns of uplift. Tectonics, 2(6): 601-631.

Pavoni, N., Maurer, H.R., Roth, P. and Deichmann, N., 1997. Seismicity and seismotectonics of the Swiss Alps, In: O.A. Pfiffner, P. Lehner, P. Heitzmann, S. Mueller and A. Steck (Editors), Deep Structure of the Swiss Alps: results of NRP 20, pp. 241-250.

Persaud, M., 2002. Active Tectonics in the Eastern Swiss Alps, Bern, 115 pp.

Persaud, M. and Pfiffner, O.A., 2004. Active deformation in the eastern Swiss Alps: post-glacial faults, seismicity and surface uplift. Tectonophysics, 385: 59-84.

Pfiffner, O.A., Lehner, P., Heitzmann, P., Mueller, S. and Steck, A., 1997. Deep Structure of the Swiss Alps: results of NRP 20. Birkhäuser Verlag, 379 pp.

Rahn, M.K., 2005. Apatite fission track ages from the Adula nappe: late-stage exhumation and relief evolution. Schweizerische Mineralogische und Petrographische Mitteilungen, 85: 233-245.

Rahn, M.K., Brandon, M.T., Batt, G.E. and Garver, J.I., 2004. A zero-damage model for fission-track annealing in zircon. American Mineralogist, 89: 473-484.

Reinecker, J., Danišík, M., Schmid, C., Glotzbach, C., Rahn, M., Frisch, W. and Spiegel, C. (pending successful revision), Tectonic control on the late stage exhumation of the Aar Massif (Switzerland): Constraints from apatite fission track and (U-Th)/He data, *Tectonics*, doi:10.1029/2007TC002247R.

Reiners, P.W., Ehlers, T.A. and Zeitler, P.K., 2005. Past, present and future of Thermochronology. Reviews in Mineralogy & Geochemistry, 58: 1-18.

Reiners, P.W. et al., 2003. Post-orogenic evolution of the Dabie Shan, eastern China, from (U-Th)/He and Fission-Track Thermochronology. American Journal of Science, 303: 489-518.

Schaer, J.P., Reimer, G.M. and Wagner, G.A., 1975. Actual and ancient uplift rate in the Gotthard region, Swiss Alps: A comparison between precise levelling and Fission-Track Apatite age. Tectonophysics, 29: 293-300.

Schlunegger, F. and Hinderer, M., 2001. Crustal uplift in the Alps: why the drainage pattern matters. Terra Nova, 13: 425-432.

Seward, D. and Mancktelow, N.S., 1994. Neogene kinematics of the central and western Alps: Evidence from fission-track dating. Geology, 22: 803-806.

Soom, M., 1989. Spaltspurendatierungen entlang des NFP 20-Westprofils (Externmassive und Penninikum). Schweizerische Mineralogische und Petrographische Mitteilungen, 69: 191-192.

Steck, A. and Hunziker, J., 1994. The Tertiary structural and thermal evolution of the Central Alps - compressional and extensional structures in an orogenic belt. Tectonophysics, 238: 229-254.

Steiner, H., 1984. Radiometrische Altersbestimmungen an Gesteinen der Maggia-Decke (Penninikum der Zentralalpen). Schweizerische Mineralogische und Petrographische Mitteilungen, 64: 227-259.

Stüwe, K., White, L. and Brown, R., 1994. The influence of eroding topography on steady-state isotherms. Application to fission track analysis. Earth and Planetary Science Letters, 124: 63-74.

Tagami, T. and Shimada, C., 1996. Natural long-term annealing of the zircon fission track system around a granitic pluton. Journal of Geophysical Research, 101: 8245-8255.

Timar-Geng, Z., Grujic, D. and Rahn, M.K., 2004. Deformation at the Leventina-Simano nappe boundary, Central Alps, Switzerland. Eclogae Geologicae Helvetiae, 97: 265-278.

Ustaszewski, M., Hampel, A. and Pfiffner, O.A., 2007. Formation of active composite faults in the Swiss Alps: the complex interplay of tectonics, gravitation and postglacial unloading. Geophysical Research Abstracts, 9.

Vernon, A., van der Beek, P., Sinclair, H., Persano, C. and Stuart, F.M., 2008. Mechanisms of late Neogene exhumation of the Alps: Insights from AFT and AHe vertical profiles in the Aar massif (Switzerland) and the Lepontine Alps (Italy). Geophysical Research Abstracts, 10.

von Blanckenburg, F. and Davies, J.H., 1995. Slab breakoff: A model for syncollisional magmatism and tectonics in the Alps. Tectonics, 14: 120-131.

von Raumer, J.F. and Neubauer, F., 1993. Pre-Mesozoic Geology in the Alps. Springer, Berlin.

Wagner, G. and Van den haute, P., 1992. Fission-Track Dating. Solid earth sciences library, 6. Enke Verlag, 285 pp.

Wagner, G.A. and Reimer, G.M., 1972. Fission track tectonics: The tectonic interpretation of fission track apatite ages. Earth and Planetary Science Letters, 14: 263-268.

Wagner, G.A., Reimer, G.M. and Jäger, E., 1977. Cooling ages derived by apatite fission track, mica Rb-Sr and K-Ar dating: the uplift and cooling history of the Central Alps. Mem. Ist. Geol. Mineral. Univ. Padova, 30: 1-27.

Willett, S.D., Hovius, N., Brandon, M.T. and Fisher, D.M., 2006a. Tectonics, Climate, and Landscape Evolution. Geological Society of America Special Paper, 398.

Willett, S.D., Schlunegger, F. and Picotti, V., 2006b. Messinian climate change and erosional destruction of the central European Alps. Geology, 34: 613-616.

Wyder, R.F. and Mullis, J., 1998. Fluid impregnation and development of fault breccias in the Tavetsch basement rocks (Sedrun, Central Swiss Alps). Tectonophysics, 194: 89-107.

Zangerl, C., Loew, S. and Eberhardt, E., 2006. Structure, geometry and formation of brittle discontinuities in anisotropic crystalline rocks of the Central Gotthard Massif, Switzerland. Ecologae geol. Helv., 99: 271-290.

Zaun, P.E. and Wagner, G., 1985. Fission-track stability in zircons under geological conditions. Nucl. Tracks Radiat. Meas., 10: 303-307.

Bildungsgang

Christoph Glotzbach geb. 07.11.1978

Seit September 2005	Promotionsstudent an der Eberhard Karls Universität Tübingen mit dem Thema ‚Low-temperature thermochronology of the Central and Western Alps' unter der Leitung von Prof. Wolfgang Frisch und Prof. Cornelia Spiegel
1999-2005	Studium der Geologie/Paläontologie an der Westfälischen Wilhelms-Universität Münster, Diplomarbeit mit Thema ‚Bewertung von multispektralen, -sensoralen und -temporalen Satellitendaten im Hinblick auf ihre geologische Aussagekraft am Beispiel der intrakratonen Amadeus Becken, Finge Gorge Nationalpark (Australien)'
1998-1999	Zivildienst beim DRK in Schöppingen
1989-1998	Gymnasium in Ochtrup, Abitur 1998
1985-1989	Grundschule in Metelen